Liquid-Phase Epitaxial Growth of Highly Oriented and Crystalline MOF Thin Films: Post-Synthetic Modification and Different Applications

Zur Erlangung des akademischen Grades eines

DOKTORS DER NATURWISSENSCHAFTEN

(Dr. rer. nat.)

Fakultät für Chemie und Biowissenschaften

Karlsruher Institut für Technologie (KIT) - Universitätsbereich

genehmigte

DISSERTATION

von

M. Eng. Zhengbang Wang

aus

Xianning, Hubei, China

Dekan: Prof. Dr. Peter Roesky

Referent: Prof. Dr. Christof Wöll

Korreferent: Prof. Dr. Stefan Bräse

Tag der mündlichen Prüfung: 09.02.2015

I hereby declare, that this thesis is based on my own work and was written by me unless stated otherwise in the body of this thesis. I have properly referenced all the text and figures that are not my own.

Zhengbang Wang

06.01.2015

Abstract 8

Zusammenfassung 10

1 Introduction 12

1.1 Metal-organic frameworks (MOFs) 12

1.1.1 Design of MOFs 13

1.1.2 Preparation of MOFs 13

1.1.3 Properties and application of MOFs 14

1.2 Surface-mounted metal-organic frameworks (SURMOFs) 17

1.2.1 Preparation of SURMOFs 18

1.2.2 Techniques and method for the growth of SURMOFs 20

1.2.3 Advantages and applications of SURMOFs 27

1.3 Post-synthetic modification (PSM) 29

1.3.1 PSM of MOFs 29

1.3.2 PSM of SURMOFs 31

1.4 Objectives of this thesis 33

2 Characterization methods 35

2.1 X-ray diffraction 35

2.1.1 Theoretical background 35

2.1.2 X-ray diffractometer 36

2.1.3 Out-of-plane and in-plane XRD 37

2.2 Infrared spectroscopy 38

2.2.1 Transmission infrared spectroscopy 39

2.2.2 Infrared reflection-absorption spectroscopy 39

2.2.3 Attenuated total reflection 41

2.2.4 Ultra high vacuum infrared reflection-absorption spectroscopy 42

2.3 X-ray photoelectron spectroscopy 44

2.4 Ultraviolet-visible spectroscopy 45

2.5 Optical microscope 46

2.6 Fluorescence microscope 47

2.7 Scanning electron microscope and energy dispersive X-ray analysis 49

2.8 Atomic force microscope 50

2.9 Water contact angle measurement 52

2.10 Quartz crystal microbalance for gas molecule loading 53

2.11 Spectroscopic ellipsometry 55

3 Materials and experiments 57

3.1 Materials 57

3.2 Preparation of SAMs 57

3.3 Compounds or molecules loading in SURMOFs 58

3.4 PSM of SURMOFs 59

3.5 Theoretical calculation 61

4 Results 63

4.1 Multi-heteroepitaxial growth of SURMOF-2 series 63

4.1.1 Background 63

4.1.2 Heteroepitaxial growth of SURMOFs 64

4.1.3 Size-selected loading of nano-particles in SURMOFs 68

4.1.4 Theoretical model 71

4.1.5 Summary 73

4.2 Liquid-phase epitaxial growth of azido-based SURMOFs and their post-synthetic modification 74

4.2.1 Background 74
4.2.2 Characterization of SURMOF [$Zn_2(N_3\text{-bdc})_2$(dabco)] 75
4.2.3 PSM of [$Zn_2(N_3\text{-bdc})_2$(dabco)] SURMOFs using CuAAC 77
4.2.4 Surface modification of SURMOFs 81
4.2.5 PSM of [$Zn_2(N_3\text{-bdc})_2$(dabco)] SURMOFs using SPAAC 84
4.2.6 Summary 86

4.3 Patterning of MOF thin films using post-synthetic modification ... 87
4.3.1 Background 87
4.3.2 Deposition of MOFs on patterned SAMs modified Au-substrate and their post-synthetic modification. 88
4.3.3 Cu(I) catalyzed alkyne–azide cycloaddition controlled by photoinitiated Cu(II) reduction 92
4.3.4 Patterned decomposition of azide group 96
4.3.5 Photo-induced thiol-yne click chemistry 97
4.3.6 Multiheteroepitaxy growth of layers-patterned SURMOFs and their post-synthetic modification. 100
4.3.7 Summary 102

4.4 Tunable coordinative defects in UHM-3 SURMOFs by post-synthetic thermal treatment and their application for gas adsorption 103
4.4.1 Background 103
4.4.2 Characterization of pristine UHM-3 SURMOFs 105
4.4.3 Coordinatively unsaturated dicopper units in UHM-3 SURMOFs 107
4.4.4 Adsorption of CO_2 and coadsorption of CO and CO_2 in UHM-3 SURMOFs with defects 110
4.4.5 DFT calculations 113
4.4.6 Experimental results and discussion 115
4.4.7 Summary 117

5 Conclusions 118

6 Appendix 121

6.1 Synthesis of chemical compounds 121

6.2 Abbreviations 125

7 References 128

8 Publications 147

9 Acknowledgements 149

Abstract

The ability to control the coating of a given substrate with metal-organic frameworks (MOFs) is essential for developing advanced MOF applications. The studies for this thesis were focused on growing MOF thin films on modified substrate using liquid phase epitaxy (LPE) method. LPE is a layer-by-layer process that yields highly crystalline MOF thin films (SURMOFs) with controlled orientation and thickness. The aim was to construct functional SURMOFs, as well as, to tune their reactivity.

Heteroepitaxy has been intensively studied for the growth of conventional materials such as metals and semiconductors. However, lattice constant difference of more than 2% between two materials still remains challenging. In this context, hierarchically organized MOF-on-MOF multilayer systems with huge lattice mismatch up to 20% using a particular liquid-phase epitaxy process were successfully realized. By collaborating with Prof. Thomas Heine and Dr. Binit Lukose, a thorough theoretical analysis of the MOF-on-MOF heterojunction structure and energetics allowed identifying two main reasons for this unexpected mismatch tolerance: the healing of vacancies with residual acetate and the low elastic constant of the MOF material.

Post-synthetic modification (PSM) of MOFs allows producing new MOF configurations that cannot be obtained directly from the self-assembly synthesis process. In this thesis, two click reactions schemes, the Cu(I) catalyzed azide alkyne click reaction (CuAAC) and the strain promoted azide alkyne click reaction (SPAAC), were investigated and used to modify azide based pillar-layer SURMOF [$Zn_2(N_3\text{-bdc})_2(dabco)$]. The results demonstrated that the need of catalyst for the CuAAC in materials with nanoscale pore size is a drawback for effective conversion. Additionally, possible contaminations with cytotoxic Cu(I) ions after reaction would remain a substantial problem for biological and medical applications. Both problems could be overcome using SPAAC, where no catalyst is needed. After optimization of the reaction conditions, conversion yields of nearly 100% were achieved.

Recently, the patterning of MOF thin films has attracted considerable attention because of their application in nano- or micro-devices. In this thesis, a bottom-up approach to grow patterned SURMOF [$Zn_2(N_3\text{-bpdc})_2(dabco)$] on patterned SAMs using robot dipping method combined with a ultrasonic cleaning process was firstly demonstrated. Uniform patterned MOF thin films of high crystalline quality were obtained in high yield. In addition, the azide group on the linker allowed the further PSM with alkyne terminated dye molecule. To obtain the functional patterning of monolithic SURMOFs, PSMs were used in a controlled fashion, where the functional group was grafted locally to the MOF structure by a UV induced reaction combined with a photo mask technique. Here, the azide-alkyne click reaction and thiol-yne click chemistry were used. The azide-alkyne click reaction was initiated by the photoreduction of Cu(II) to the

active Cu(I) catalyst, whereas the thiol-yne click chemistry was induced directly by the UV light. Furthermore, heteroepitaxial growth of multilayers systems (Cu-N_3BPDC+Cu-BPDC+ Cu-N_3BPDC+Cu-BPDC+Cu-N_3BPDC+Cu-BPDC) was also used to control the localization of subsequent PSM. The results demonstrated that the pattern functionalization of MOF thin film is not limited to the two dimensions of the mounting surface but is indeed possible in 3D.

Defect-engineering in MOFs have also attracted considerable attention due to the additional reactivity of the defective sites and the possible applications in catalysis, gas adsorption, and gas separation. Here, the production of defective Cu(I) sites from a oriented, homogeneous and virtually defect-free (below 1 %) Cu(II) paddle wheel based UHM-3 SURMOFs was demonstrated using a postsynthetic thermal treatment. A quantitative analysis of the defect concentration in SURMOFs was carried out by CO adsorption and XPS measurements. The resulting defective Cu(I) sites were investigated for the adsorption of gas molecules such as CO and CO_2. The interaction of CO and CO_2 with the Cu(II) and Cu(I) sites were characterized thoroughly using XPS and IRRAS. The binding energies of these two species were determined using temperature-induced desorption. The interaction between the guest molecules and the Cu(I) and Cu(II) sites were also analyzed using density-functional theory (DFT, contributed by Prof. Thomas Heine, Dr. Andreas Mavrantonakis and Dr. Barbara Supronowicz). Surprisingly, both experiment and theory showed that the binding energy of CO_2 to Cu(I) and Cu(II) sites are essentially identical, in pronounced contrast to CO, which binds much stronger to Cu(I).

Zusammenfassung

Kontrollierte Beschichtungen gegebener Substrate mit metallorganischen Gerüstverbindungen (engl. *metal-organic frameworks, MOFs*) sind notwendig für die Entwicklung fortschrittlicher MOF-Anwendungen. Die Untersuchungen zur vorliegenden Arbeit wurden an MOF-Dünnfilmen durchgeführt, welche auf modifizierten Substraten mittels Flüssigphasenepitaxie (eng. *liquid-phase epitaxy, LPE*) gewachsen wurden. LPE ist ein Schicht-für-Schicht-Verfahren, mit welchem hochkristalline MOF-Dünnfilme (sogenannte SURMOFs) mit kontrollierter Orientierung und Dicke hergestellt werden können. Die Ziele dieser Arbeit waren die Herstellung funktioneller SURMOFs sowie das Einstellen ihrer Reaktivität.

Heteroepitaxie wurde intensiv für das Wachstum von konventionellen Materialien wie Metalle und Halbleiter untersucht. Bei der Heteroepitaxie dieser Materialien sind Unterschiede der Gitterkonstanten von mehr als 2% allerdings immer noch eine große Herausforderung. In dieser Arbeit wurden hierarchisch aufgebaute MOF-auf-MOF-Schichtsysteme mit großen Gitteranpassungen von bis zu 20% erfolgreich unter Verwendung der Flüssigphasenepitaxie realisiert. Durch die Zusammenarbeit mit Prof. Thomas Heine und Dr. Binit Lukose wurde eine gründliche theoretische Analyse der MOF-auf-MOF-Struktur ermöglicht und zwei Hauptgründe für diese unerwartet große Toleranz wurden identifiziert: ungebundenen Stellen können mit Rest-Acetat geheilt werden und die niedrige Elastizitätskonstante macht das MOF-Material flexibel.

Post-synthetische Modifikationen (PSM) von MOFs ermöglichen die Herstellung neuer MOF-Materialien, die nicht direkt synthetisiert werden können. In dieser Arbeit werden zwei Klick-Reaktionsschemata, die Cu(I)-katalysierte Azid-Alkin-Klickreaktion (CuAAC) und die *strain promoted* Azid Alkin-Klickreaktion (SPAAC), untersucht und verwendet, um SURMOFs vom Typ $[Zn_2(N_3\text{-}bdc)_2(dabco)]$ zu modifizieren. Die Ergebnisse zeigen, dass die Notwendigkeit des Katalysators für die CuAAC in Materialien mit Nanometer-großen Poren ein Nachteil für eine effektive Umwandlung darstellt. Zusätzlich sind mögliche Verunreinigungen mit zytotoxischen Cu(I)-Ionen, die nach der Reaktion im MOF verbleiben können, ein wesentliches Problem für biologische und medizinische Anwendungen. Beide Probleme können mit SPAAC, wo kein Katalysator benötigt wird, überwunden werden. Durch Optimierung der SPAAC-Reaktionsbedingungen wurden Ausbeuten von fast 100% erreicht.

Für potentielle Anwendungen in mikroskopisch kleinen Geräten ist die Strukturierung der MOF-Dünnschichten entscheidend. In dieser Arbeit wird ein *Bottom-up*-Ansatz zum Wachstum lateral gemusterter SURMOFs vom Typ $[Zn_2(N_3\text{-}bpdc)_2(dabco)]$ auf gemusterten SAMs genutzt. Diese SURMOFs wurden mit einem Roboter-gesteuerten Tauchverfahren in Kombination mit Ultraschallreinigung hergestellt und gleichmäßige, gemusterte MOF-Dünnfilme von hoher Kristallinität wurden erhalten. Darüber hinaus erlaubt die Azid-Gruppe des Linkers weitere PSM mit Alkin-funktionalisierten Farbstoffmolekülen. Um funktionelle und strukturierte SURMOFs zu erhalten, wurden PSM in kontrollierter Weise angewandt, in dem die funktionellen Gruppen in der MOF-Struktur lokal mittels einer UV-induzierte Reaktion in Kombination mit einer Fotomaskentechnik modifiziert wurden.

Hier wurden die Azid-Alkin-Klickreaktion und *Thiol-yne* Klickreaktion verwendet. Die Azid-Alkin-Klickreaktion wurde durch die Photoreduktion von Cu(II) in katalytisch aktives Cu(I) initiiert, während die *Thiol-yne* Klick-Reaktion direkt vom UV-Licht induziert wurde. Weiteres hetero-epitaktisches Wachstum von mehrlagigen Systemen (Cu-N_3BPDC + Cu-BPDC + Cu-N_3BPDC + Cu-BPDC + Cu-N_3BPDC + Cu-BPDC) wurde benutzt, um die Lokalisierung der nachfolgenden PSM zu steuern. Die Ergebnisse zeigen, dass die Funktionalisierung der MOF-Dünnschichten nicht nur auf beide laterale Dimensionen begrenzt ist, sondern tatsächlich 3-dimensionale Strukturierungen möglich sind.

Die Defekt-Konstruktion in MOFs ist auf Grund der hohen Reaktivität der Fehlstellen sehr interessant, besonders in Hinblick auf mögliche Anwendungen in der Katalyse, Gasadsorption und Gastrennung. Hier wird die Herstellung von defektreichen Cu(I)-Gebieten aus einer nahezu defektfreien Cu(II)-basierend UHM-3-SURMOF-Struktur mittels Wärmebehandlung nach der Synthese gezeigt. Die resultierenden Cu(I)-Defektstellen wurden mittels Adsorption von Gasmolekülen wie CO und CO_2 untersucht. Die Wechselwirkung von CO und CO_2 mit Cu(II)- und Cu(I)-Positionen wurde gründlich mit XPS und IRRAS charakterisiert. Die Bindungsenergien beider Spezies wurden mit temperaturabhängiger Desorption bestimmt. Die Interaktion zwischen den Gastmolekülen und den Cu(I)- und Cu(II)-Plätzen wurden mit Hilfe von Berechnungen mittels Dichtefunktionaltheorie (DFT, von Prof. Thomas Heine, Dr. Andreas Mavrantonakis und Dr. Barbara Supronowicz) analysiert. Theorie und Experiment zeigen überraschenderweise, dass die Bindungsenergie von CO_2 zu Cu(I)- und Cu(II)-Plätzen im Wesentlichen identisch sind, was im deutlichem Kontrast zu CO steht, das viel stärker zu Cu(I) bindet.

1 Introduction

1.1 Metal-organic frameworks (MOFs)

Porous materials have attracted considerable attention from a wider, interdisciplinary scientific community, because their applications range from industrial processes to household routines, and advanced uses in medicine[1], electronics[2], optics[3] and photonics[4]. In general, a porous system contains networks of minute openings and cavities. Almost all solid materials, including metals, glasses, carbons, and polymers, can exist in such a state. However, these structures are usually amorphous matter where pores have random sizes and disordered distributions. This can be a huge drawback when developing some advanced and technical applications. In contrast, ordered porous materials exhibit a couple of advantages[5, 6]: (1) Their structure can be easily determined. (2) The pore with defined topologies and dimensions are reproducible. (3) The regular pore system can be used to host guest molecules or nanoparticles that are spatially stabilized and organized by the ordered structure.

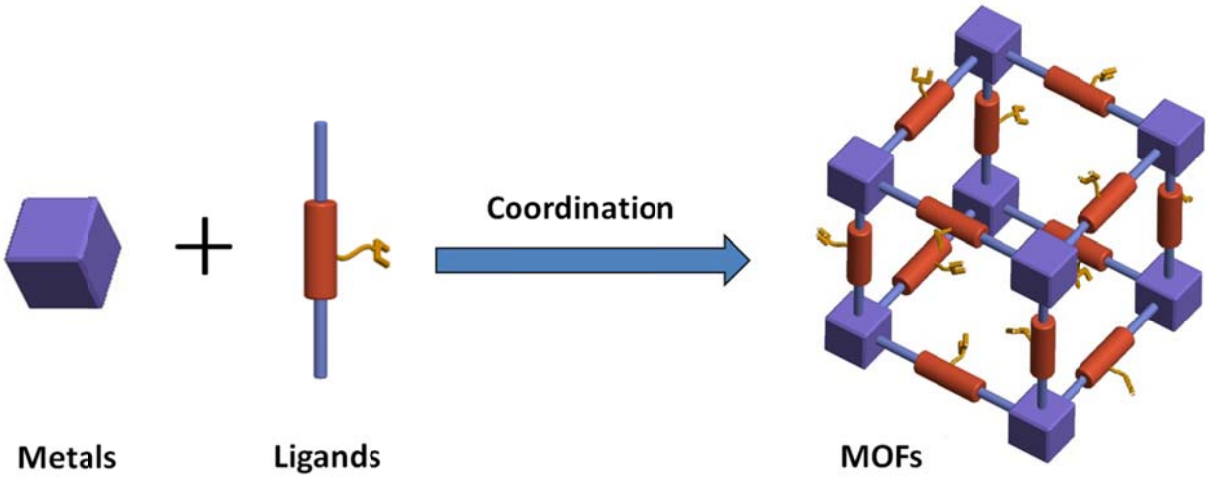

Figure 1.1: A general scheme illustrating the coordination of metal sources and organic ligands to MOFs. Cubic structure is taken for example.

Metal–organic frameworks (MOFs) are a rather new class of ordered porous materials containing metal ions, or metal clusters linked by organic ligands[7], as shown in Figure 1.1. The coordination of metal ions with organic ligands can form zero-dimensional (0D) molecular complexes, or infinite one-dimensional (1D), two-dimensional (2D), or three-dimensional (3D) frameworks. Generally, these metal-organic compounds are termed coordination polymers[8]. MOFs form a specific class of coordination polymers (CPs), by being crystalline and porous[9]. Therefore, MOFs are also known as porous coordination polymers (PCPs). According to this classification, the first MOF material was reported in 1959[10]. However, the MOFs received little attention until

the 1990s. At that time, Zaworotko, Yaghi, Kitagawa, and Férey, amongst other scientists, uncovered the huge opportunities offered by MOF materials and made pioneering contributions to the field. Notably, the term MOFs was first introduced by Yaghi in 1995 for the synthesis of the extended crystalline network, $[Cu(4,4'\text{-bipyridyl})_{1.5}\cdot NO_3(H_2O)_{1.25}]$[11]. Soon afterwards, research efforts on MOF materials grew rapidly and led to extensive exploration of applications in gas storage[12, 13], separation[14], catalysis[15] and magnetism[16].

1.1.1 Design of MOFs

The design of MOFs structure firstly focuses on the primary building blocks. The choice of metal ions and ligands is critical in targeting defined topological networks. A widespread strategy to guide in building the MOF structure relies on a "node and spacer" approach. The concept was firstly introduced by Wells in 1977,[17] to simplify deal with complex structures. In the early 1990s, Robson applied this approach to produce coordination polymers[18]. With this method, the building blocks of the structure are simply modeled by nodes for the metal and by spacers for the organic linker. The appropriate interconnections represent nets. The sequential connection of the node by spacer forms a path and then a circuit can be built when the path starts and ends with the same node. A net can be viewed as the shortest connected circuit of node. The topology of a net depends on the number of nodes, which can be, for example, square, tetrahedral, octahedral. Additionally, a net represents the fundamental unit for the MOF structure and the connection of the nets forms the resulting MOF structure with a considerable degree of predictability. Furthermore, the geometric configuration also depends on the coordinative numbers of metal-based nodes and organic linker-based spacers.

Another concept that is commonly used for the design and the construction of MOFs is the secondary building units (SBUs). SBUs are geometric configurations of metal connecter in the MOF structure, which clearly depicts the possible coordinative sites for the organic ligands. Therefore, the knowledge of the probable SBUs structure of metal sources is of great help for the construction and synthesis of the target MOF configuration. Yaghi et al have contributed a review on SBUs, where the geometries of 131 SBUs are introduced[19].

1.1.2 Preparation of MOFs

Numerous methods or techniques for the synthesis of MOF materials have been developed , such as hydro- and solvothermal method[20], microwave synthesis[21], ionothermal synthesis[22], sonochemical synthesis[23], electrochemical synthesis[24], mechanochemical synthesis[25]. Among them, the hydro- and solvothermal synthesis is the most commonly used, as the self-assembly of the metal ions and the organic ligands is easily triggered in a liquid phase subjected to heating. Following this method, metal ions or metal clusters and organic ligands are mixed together with

solvents and subjected to heating process to yield MOF material. However, the production of a monocrystal, the control of the crystal size, or the obtention of a high yield usually present challenges in practice. This is because numerous empirical parameters, such as solvent, temperature, concentration of reactants, pH value, heating time, heating and cooling rates need to be carefully adjusted to optimize the crystallization reaction. The efforts from the MOF focused community has yielded in the past two decades a lot of now typical structures like the IRMOFs (isoreticular MOFs)[26-28], HKUST-1 (HKUST: Hong Kong University of Science and Technology)[29], MIL-series (MIL: Matériaux de l'Institut Lavoisier)[30-33], ZIF-series (ZIF: Zeolitic Imidazolate Framework)[20], DMOF [1,4-diazabicyclo[2.2.2]octane (Dabco) MOF, for example $Zn_2(bdc)_2(dabco)$, bdc: benzene-1,4-dicarboxylic acid][34] amongst others (Figure 1.2).

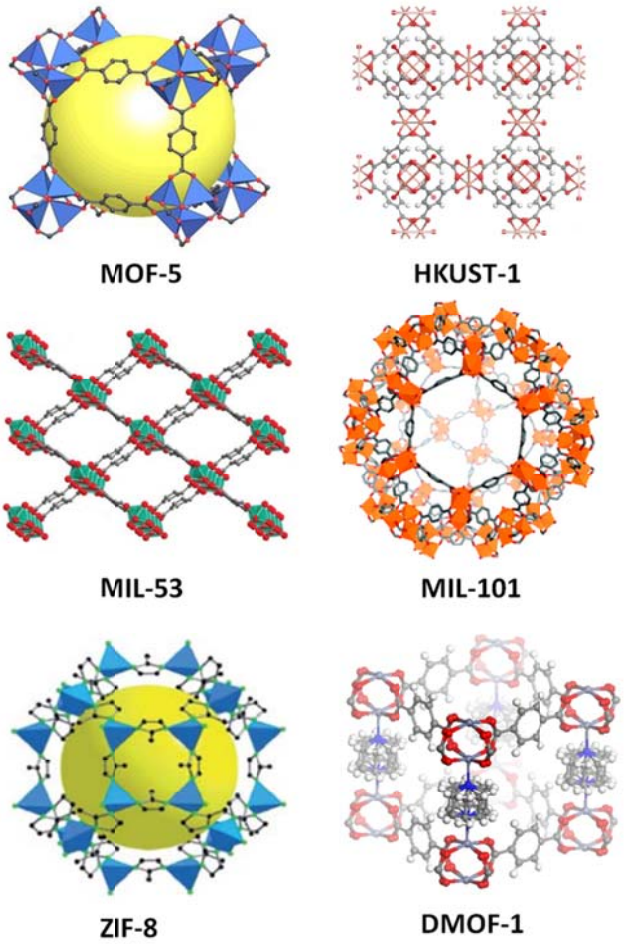

Figure 1.2: The structure of MOF-5(taken from Ref.[26]), HKUST-1, MIL-101(taken from Ref.[35]), MIL-53 (taken from Ref.[36]), ZIF-8(taken from Ref.[37]), DMOF-1 $[Zn_2(bdc)_2(dabco)]_n$.

1.1.3 Properties and application of MOFs

Compared to the properties of other porous materials, the beauties of MOFs reside in their

excellent high porosity, versatile chemistry, elastic and flexible structure[38-40]. In general, the specificity of a material leads to the development of corresponding applications. In the following, some of the MOF properties and corresponding applications are presented.

Porosity, one of the main properties of MOFs, is quantified standardly by a surface area density measure. Among all the MOF materials developed up to now, NU-110E (NU: Northwestern University), reported by Hupp and co-workers in 2012[41], exhibits the highest BET (Brunauer-Emmett-Teller) surface area with 7140 $m^2 g^{-1}$. This is slightly higher than the value of 6240 $m^2 g^{-1}$ reported by Yaghi and co-workers in 2010 for MOF-210[42]. Noteworthily, the highest BET surface area of the disordered and ordered structure are 3200 $m^2 g^{-1}$ for carbon aerogels[43] and 904 $m^2 g^{-1}$ for zeolite Y[44] respectively. Obviously, MOF structure stands out over all the other porous materials. Such a high porosity allows many applications, also because the pores can be designed to host different guest molecules. Numerous studies have demonstrated that MOFs exhibits outstanding capacity for gas storage. Regarding the energy and environment sectors, MOFs attracts more and more interest considering the storage of gas molecule, such as H_2[45], CH_4[46], CO_2[47], or CO[48]. Beside gas storage, MOF materials can also be used for the catalytic applications by incorporating metal nanoparticles into the pore or the channel [49]. Furthermore, when loaded with drugs, peptides or proteins, MOFs can be used for medical applications[50, 51].

Another advantage of MOFs is the versatile chemistry to fabricate them which results from the flexibility and simplicity in choosing and assembling various metal connectors and countless number of organic linkers[38]. The targeted framework can be designed and prepared by choosing adequate metal ions and organic ligands; the pore size and shape of MOFs can also be controlled by adjusting the length of ligands[52, 53], geometry of the ligands or metal sources as well as the functionality of MOFs can be controlled not only by using linkers with different functional groups[54] during fabrication (Figure 1.3), but also by applying postsynthetic modifications (PSM)[55]. MOFs can be also tuned using the corresponding metal or linker connecters such that chiral ligands yield chiral MOFs for chiral catalysis, adsorption, and separation[56-59]; the ligands with special function groups can be incorporated in the MOF structure to improve the interaction with guest molecule for a high loading capacity[54].

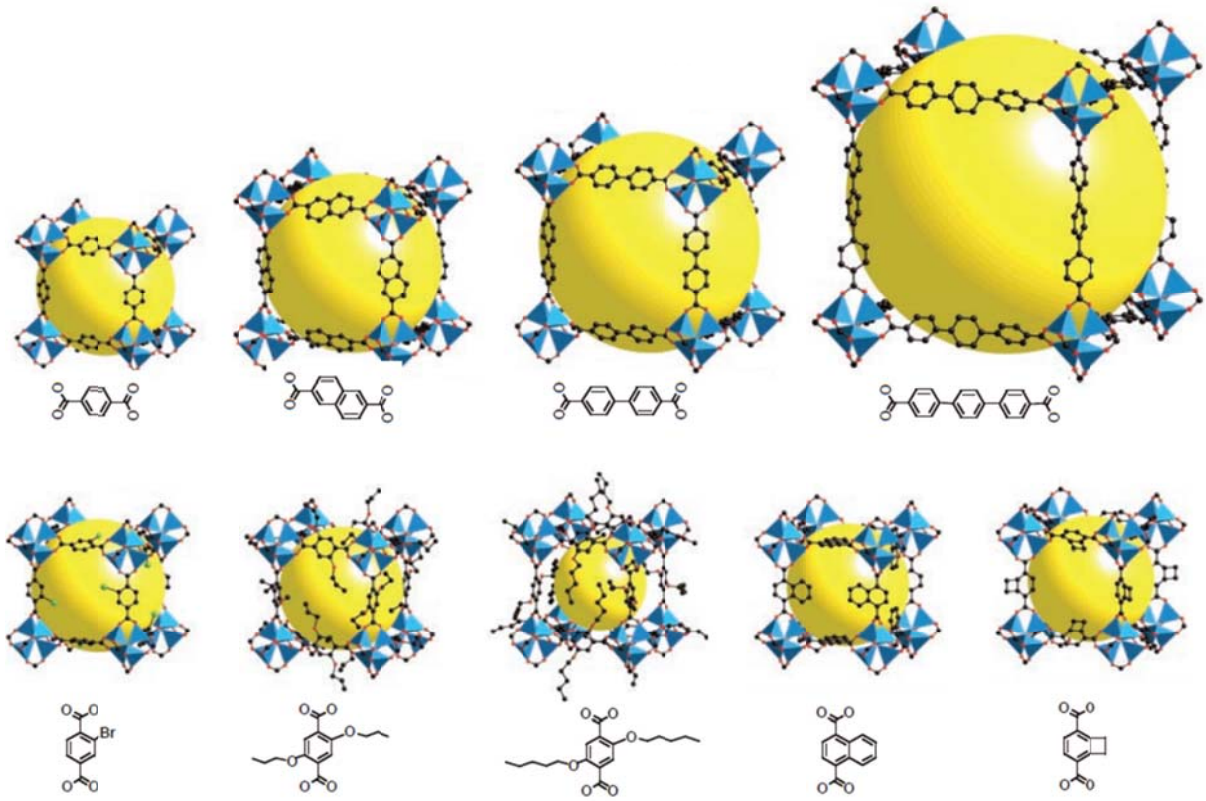

Figure 1.3: Structures of IRMOFs and their ligands. The pore size and functionality of MOFs can be tuned by using different types of organic ligands (taken from Ref.[26]).

Furthermore, the versatility of MOF chemistry provides huge opportunity for other applications, including fluorescence[60], luminescence[61], conductivity[62-64] and magnetism[16].

Mechanical compliance is also an important feature of some MOFs. Flexible MOFs are also called soft porous crystals[40, 65]. These materials can respond to the external stimuli, such as temperature, pressure, light, and chemical medium, by changing from one crystalline phase to another phase without breaking of connections. In some cases, this change is reversible. One important example is MIL-53 (Matériaux Institut Lavoisier) reported by Férey and co-workers in 2002[30], in which the unit cell volume can be changed around 30% by a reversible hydration and dehydration process (Figure 1.4). This phenomenon is also called breathing effect. This flexibility allows possible applications in gas separation[66, 67], sensing[68-70] and biomedicine[71, 72].

Noticeably, another recent and fast-tracked application is using MOF as a template to prepare porous carbon materials by a carbonization process under high temperature and inert atmosphere

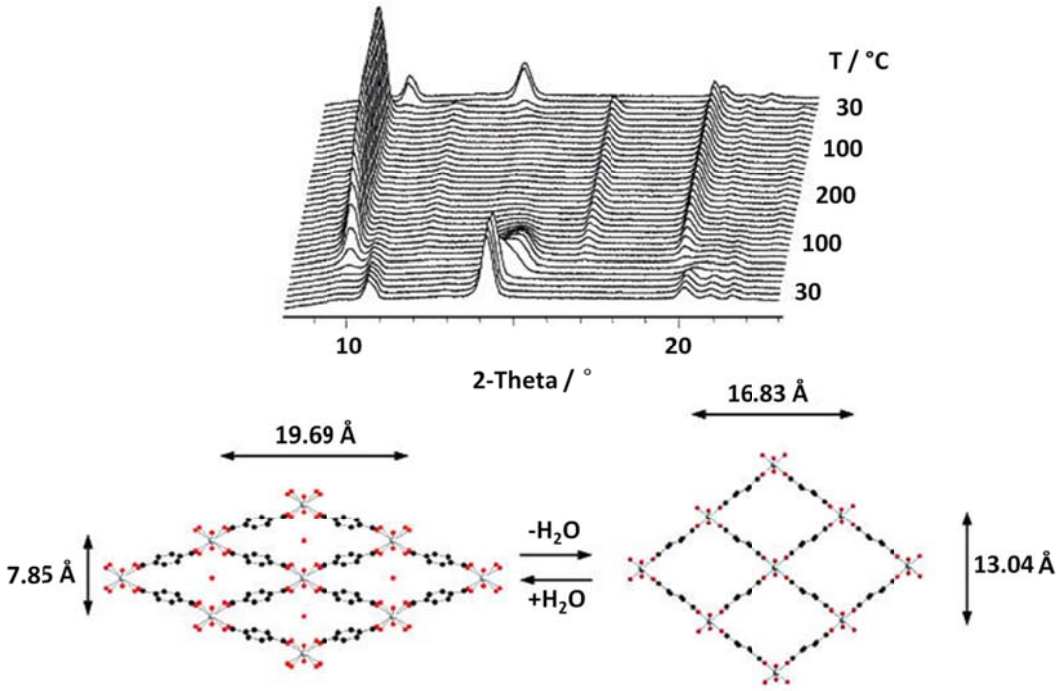

Figure 1.4: (top) X-ray thermodiffractogram of MIL-53 at different temperature under air; for a clearer view, a 2θ offset is applied for each pattern. (bottom) Schematic representation of the reversible hydration-dehydration of MIL-53 with the low-temperature form on the left hand side and the high-temperature form on the right hand side). (taken from Ref.[30])

[73]. Such MOF derived porous carbon materials exhibit great potential in the energy sector[74-83].

1.2 Surface-mounted metal-organic frameworks (SURMOFs)

Though MOFs have many possible applications (vide supra), the ability to grow or deposit MOF materials on a given solid substrate is still of great importance in other fields, especially for the fabrication MOF-based devices[84]. For the past two decades, a number of experimental methods have been developed for the deposition of MOF films[85], including mother solution[86], seeded growth[87], direct deposition of MOF crystals[88, 89], spin coating[90], electrochemical deposition[91], gel-layer deposition[92], Langmuir-Blodgett[93, 94], and direct generation from the appropriate metal precursor films[95-98]. However, most of MOF films grown with these methods have been too thick and/or inhomogeneous to be used in the considered device applications. The more recent liquid phase epitaxial (LPE) method, also called layer-by-layer procedure[99], have showed great potential to grow crystalline, uniform and highly oriented MOFs thin films on modified solid substrate. The film thickness can also be controlled by adjusting the number of growth cycles[100]. The resulting MOF thin films have been named surface mounted metal-organic frameworks (SURMOFs). In the following, the preparation and application of these SURMOFs are

introduced.

1.2.1 Preparation of SURMOFs

In comparison to the bulk MOFs, which are grown commonly by conventional hydrothermal or solvothermal methods through homogeneous mixing of all of the reactants (typically two to three primary building blocks) at elevated temperature, the layer-by-layer fabrication of SURMOFs proceeds with the repetition of a two-step cycle comprising the sequential immersion into the two solutions of the individual reactants[101] (Figure 1.5). To support the growth of SURMOFs, the substrate needs first to be functionalized by organic molecules with a specific terminal group, such as –COOH, -OH or pyridyl. The preparation of SURMOFs usually follows three steps: (1) Choice of the substrate; (2) Surface functionalization of the substrate to allow anchoring and seeding of the MOFs; (3) Layer-by-Layer growth of SURMOFs on the modified substrate.

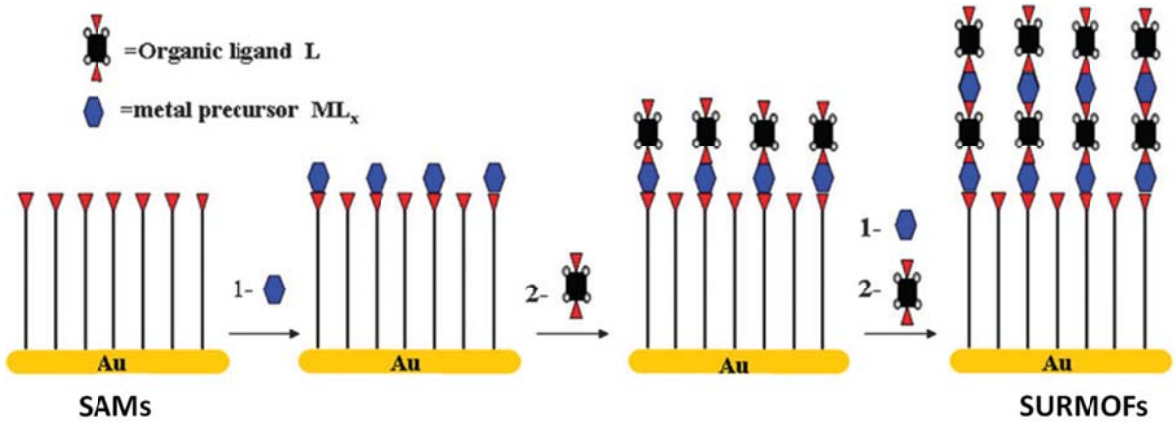

Figure 1.5: A schematic diagram for the step-by-step growth of MOFs on SAMs by repeating growth cycles separated by washing: 1- immersion in a solution of metal precursor and 2- subsequent immersion in the solution of organic ligands. (Reproduced from ref.[101]).

1.2.1.1 Substrates

The possibility to grow MOFs on different substrate kinds receives more and more attention. Originally only a limited number of solid materials have been used as substrates for the growth of SURMOFs[85], such as gold, silver, silicon, silicon oxide, standard glass, quartz, alumina, titanium, titanium oxide, calcium fluoride, indium tin oxide, and fluorine doped tin oxide amongst others. Very recently, a study has reported that HKUST-1 SURMOFs can also be grown on flexible and soft materials like plastics, papers, and textiles[102]. Following LPE-based methods, the substrate must provide a seeding and binding layer sufficient to anchor the deposited metal ions or linkers in the first growth step. Any solid material can be considered as

substrate as long as its surface is appropriately coated with extrinsic or intrinsic MOF coordinating functional groups.

1.2.1.2 Surface functionalization of substrates

The functionalization of substrate can be a chemical or physical process depending on which substrates are used and which functional groups are needed. For a metal substrate like gold, thiol based chemistry is the proven choice. The gold surface is soaked into an ethanol solution of thiol-terminated molecules such as 16-mercaptohexadecanoic acid (MHDA)[103], (4-(4-pyridyl)phenyl)-methanethiol (PP1)[104] or 11-mercapto-1-undecanol (MUD). The thiol groups react covalently with gold to form a self-assembled monolayer (SAM) (RSH + Au → RS-Au + $1/2H_2$). For some other nonmetallic materials, plasma treatment can be used to clean the surface as well as increase the density of surface hydroxyl groups. This can also be achieved by a chemical process (e.g. cleaning with piranha solution). To obtain carboxyl groups, the hydroxyl layer can be reacted with 11-(triethoxysilyl)undecanal. The now aldehyde groups presenting surface can be oxidized by potassium hypermanganate to form the carboxyl groups surface.

1.2.1.3 Layer-by-layer growth of SURMOFs

The layer-by-layer method allows growing multilayered thin film with a control over the thickness as well as the morphology of the film. This technique was firstly presented by Langmuir and Blodgett in 1937 for the fabrication of multilayer organic Langmuir and Blodgett (LB) films[105]. However, it had not received much attention until its reintroduction by Decher and co-workers in 1991 for the deposition of charged polymers[106]. It has since become one of the most preferred method for the deposition of a wide range of materials, including nanoparticles[107], ionic polymers[108], proteins[109], DNA[110] amongst others. It is based on a self-assembly process. Over the past seventy years, significant developments have been made to this technique and three categories can be distinguished: Langmuir-Blodgett (LB)[105], electrostatic layer-by-layer assembly[106] and covalent layer-by-layer assembly[111].

In 2007, Wöll and co-workers have implemented the layer-by-layer assembly method to prepare MOF thin films on SAMs modified substrates [101]. The schematic diagram for this MOF thin film growth is displayed in Figure 1.5. The first MOF example employed for the study was HKUST-1. Copper(II) acetate [$Cu(Ac)_2$] and 1,3,5-benzenetricarboxylic acid (BTC), are separately dissolved in ethanol, and the gold substrate is coated with MHDA-SAMs. The modified substrate is immersed into each solution alternatively. Each immersion is followed by a rinsing with pure ethanol to remove the uncoordinated metal or organic connectors. The repetition of these steps leads to the fabrication of MOF thin films. The synthesis of MOF materials in solution is a self-assembly process. The coordinative bonding of a multivalent metal ion with a polydentate

organic ligand, forms a connection; the multiplication and addition of this event results in periodic interconnected structures, i.e. metal-organic frameworks. However, the layer-by-layer method for the growth of SURMOFs directs this process by limiting only one reactant at a time to a confined coordinating surface (Figure 1.5). As a result, the SURMOF fabrication technique offers a huge advantage in controlling the thickness and morphology of the MOF thin films. For the past ten years, numerous types of MOF thin films have been grown with this method and the resulting studies have also been reviewed[85, 112-114].

1.2.2 Techniques and method for the growth of SURMOFs

In order to optimize the synthesis condition, to reach better morphology and high-throughput fabrication, or to allow specific in-situ experiments, a number of techniques and methods have been developed. These include the dipping[101], the spray[100], and the pump methods[115], and quartz crystal microbalance (QCM) system-based method[116].

1.2.2.1 Dipping method

Originally, the first SURMOF (HKUST-1) sample was prepared using hand-dipping method by, then PhD student, Hui Wang in 2007[101]. Hand-dipping is a simple and easy method to grow SURMOFs. Only four containers and three solutions are needed (two containers for the metal source and the organic ligands, and two others of solvent for rinsing). The growth of SURMOFs is carried out using the following steps (here the synthesis of HKUST-1 SURMOFs on MHDA SAMs is taken for an example):

- Four containers are filled with ethanol solution of copper acetate (1 mM), ethanol solution of 1,3,5-benzenetricarboxylic acid (BTC, 0.1mM) and twice with pure ethanol respectively.
- The MHDA SAMs modified gold substrate is firstly dipped in the copper acetate solution for 30 min.
- The sample was taken out and immersed in pure ethanol to remove the uncoordinated copper acetate.
- Then the sample was immersed into the BTC solution for 60 min.
- The sample was taken out and immersed in pure ethanol to remove the uncoordinated BTC. Note, there are two containers for pure ethanol, one work for cleaning copper acetate and another for cleaning BTC.
- By subsequently repeating the upper steps using the same modified gold substrate to receive a thicker HKUST-1 MOF thin film.

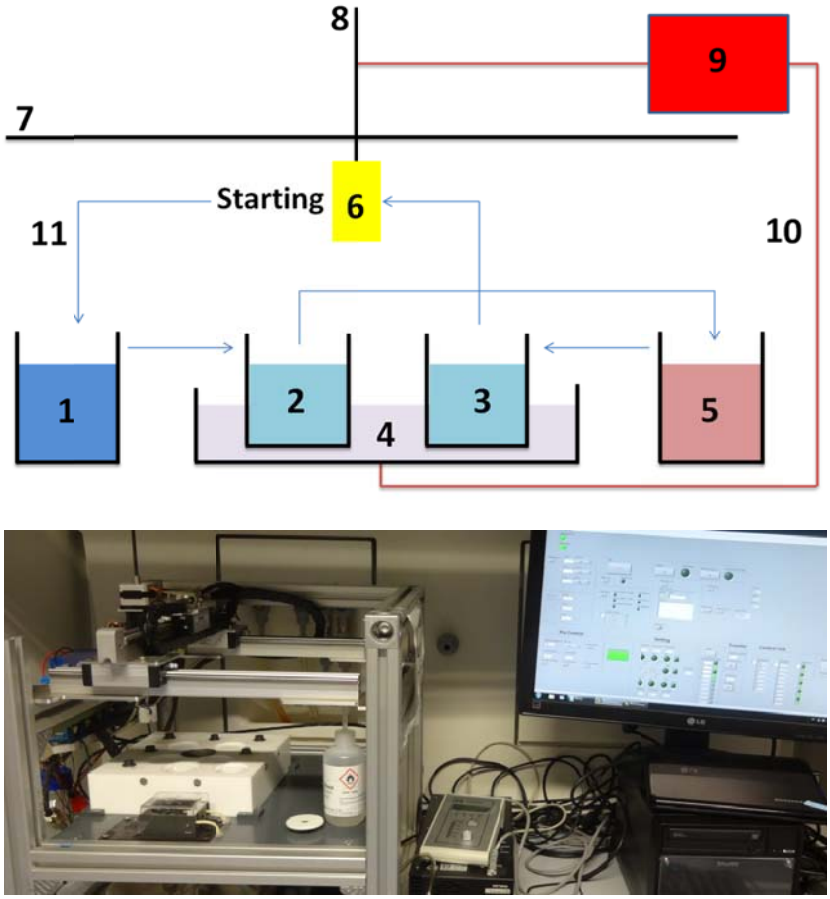

Figure 1.6: (top) A schematic diagram for the step-by-step growth of MOFs on SAMs using robot-dipping method: : (1) Metal solution, (2) pure ethanol, (3) pure ethanol, (4) ultrasonic bath, (5) linker solution, (6) substrate, (7) supporter, (8) substrate holder, (9) PC controller, (10) control electronic line, (11) dipping sequence. (bottom) The setup of robot dipping technique.

The studies have already verified that this process yields highly crystalline, orientated SURMOFs. However, hand-dipping is costly in term of manual labor. Thus, robot automation has been implemented as displayed in Figure 1.6. The presented system contains 8 PTFE containers. Normally, four containers are used for a standard synthesis. The residual containers allow for more elaborate fabrication, such as the growth of MOF-on-MOF, or the loading of molecules or nanoparticles during the synthesis process. Each container position on the robot operating table is preregistered with three dimensional coordinates. A robotic electromagnetic hand operates above the containers and is responsible for fetching the ferromagnetic lids. The substrate is hung below the lid of a central container. Commanded by the computer program, the hand opens and shuts the different containers, as well as dips the lid attached substrate into the corresponding reactant solutions. The synthesis route is equivalent to the hand-dipping method. In order to optimize the rinsing, the corresponding containers are placed in an ultrasonic bath,

also computer controlled. Compared to the hand-dipping method, this process allows an easy and accurate control of the dipping and rinsing times, and advantageously enhances the reproducibility of SURMOF syntheses.

1.2.2.2 Spray method

The automated spray method is a high-throughput technique, which can grow thick MOF films in a short time[100]. The schematic is displayed in Figure 1.7. It is also based on the layer-by-layer

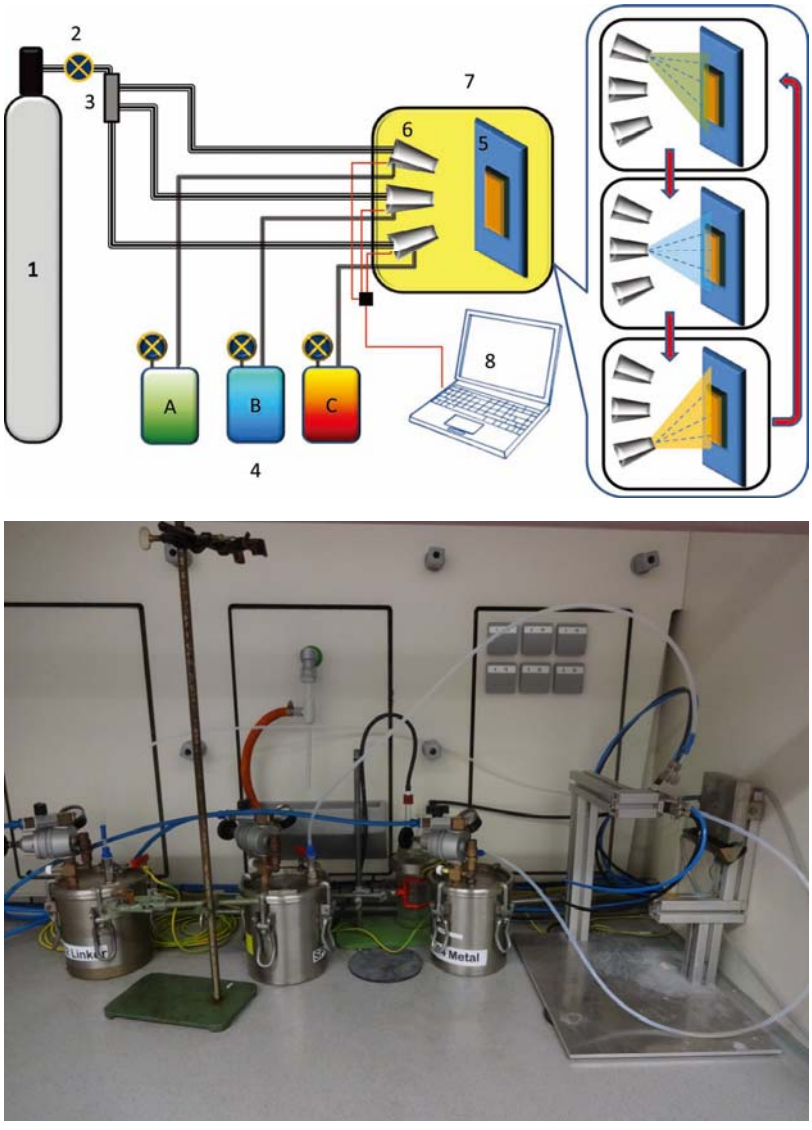

Figure 1.7: (top) A schematic diagram for the step-by-step growth of MOFs on SAMs using spray method: : (1) Gas supply, (2) gas flow controller, (3) three-way valve gas distributor, (4) (A, B, C) solutions storage containers, (5) sample holder, (6) dosing valves, (7) spray chamber, (8) PC, (Figure is taken from[100]). (bottom) The setup of spray technique.

process. Three separate solutions of metal ions and organic ligands are sprayed alternatively and repeatedly on the surface of a modified substrate with the pure solvent being used after each reactant spraying to rinse of the excess of metal ions or organic ligands.

Compared to the dipping method that requires long immersion time (metal: 30 min and organic linker: 60 min), much shorter times (metal: 1 min and organic linker: 2 min) of spraying yield highly crystalline and orientated SURMOFs. A film thickness of 1 μm is achieved in only a few hours by using the spray method, whereas several days would be needed with the dipping method. Thick SURMOFs could be easily obtained using spray method. However, only a limited number of SURMOFs have been obtained successfully (e.g. HKUST-1 and SURMOF-2 series[53]) and further works are needed to optimize the synthesis condition. In more detail, the procedure for the growth of SURMOFs (e.g. HKUST-1) with the spray method can follow these steps:

- The ethanol solution of copper acetate, ethanol solution of BTC and pure ethanol were filled into three distinct containers and then the containers were shut with lids.
- The program parameters (growth cycles, pressure, spray time, idle time, *etc*) were appropriately set up, and then place the modified substrate on the target.
- The modified substrate is first sprayed with the ethanol solution of copper acetate for 15 seconds, then left 30 seconds.
- The substrate is rinsed with pure solvent for 5 seconds to remove the excess of metal ions.
- The substrate is sprayed with the ethanol solution of BTC for 30 seconds, then left 30 seconds.
- The substrate is again rinsed with pure ethanol for 5 seconds to remove the excess amounts of BTC.
- By subsequently repeating these steps on the same gold substrate a thicker SURMOFs (HKUST-1) thin film is obtained.

1.2.2.3 Pump method

To control the temperature during the growth of SURMOFs, the pump method has been developed[115]. Similarly to the other methods, it is based on the layer-by-layer fabrication concept.

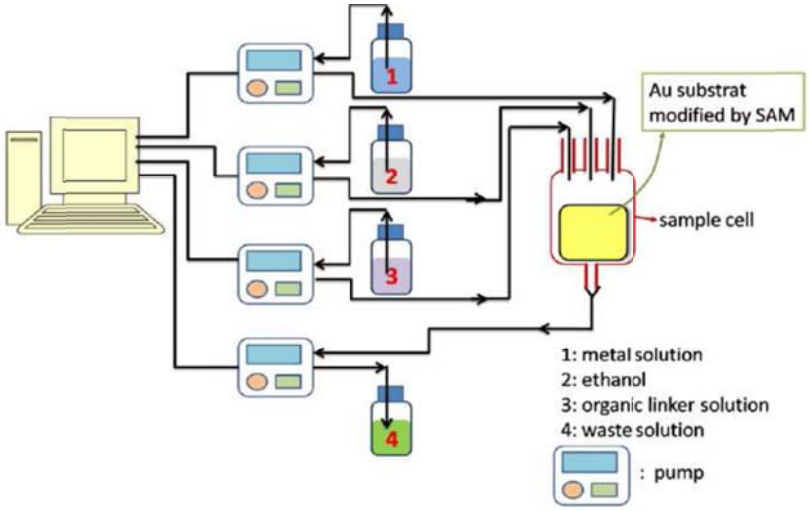

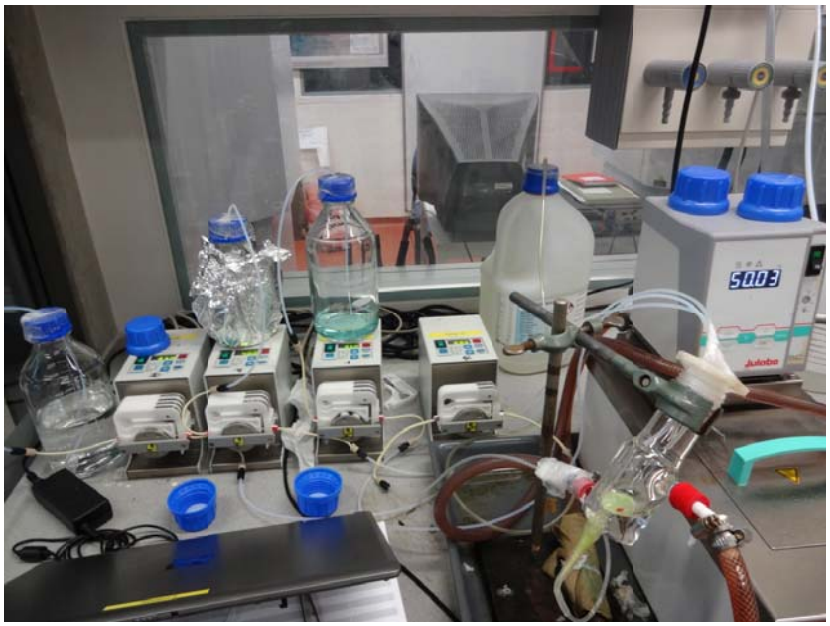

Figure 1.8: (top) A schematic diagram for the step-by-step growth of MOFs on SAMs using pump method. (Figure is taken from the supporting information of Ref.[115]). (bottom) The setup of pump technique.

The schematic diagram is displayed in 1.8. The solutions of metal source and organic ligands are alternatively pumped into the sample cell. After each reactant exposure, pure ethanol is flowed through the cell to remove the uncoordinated excess. Three pumps are used to deliver the metal solution, organic solution and the pure ethanol to the sample, while a forth one is to empty the cell. The temperature of the cell can be controlled by a heating/cooling circulation system (Figure 1.8 bottom right side, which displays 50.03 °C). The pump method is well suited for the synthesis of SURMOFs which require a defined temperature reaction. A temperature control

range of -20–100 °C is easily realized. The pump method also requires long coordination times to grow thick SURMOFs. In detail, the procedure to fabricate SURMOFs (e.g. HKUST-1) can follow these steps:

- The ethanol solution of copper acetate, ethanol solution of BTC and pure ethanol were filled into three distinct containers and the Teflon tubes were separately inserted to the container though the cover of containers. In this case, the solution in the container can be pumped out along the tubes.
- Set up the computer programs with appropriate parameters (growth cycles, pumping press, rinsing time, waiting time, *etc*), and then place the modified substrate on into the sample cell.
- Running the programs.
- The ethanol solution of copper acetate was firstly pumped into the sample cell and then 15 min was left for the coordination of copper acetate with the functional group on the substrate.
- Then the copper acetate solution was completely pumped out and immediately, pure ethanol is pumped into the sample cell for 4 min and then was completely pumped out to remove the excessive amounts of metal ions.
- In the following, the ethanolic solution of BTC was pumped into the sample cell, and then 30 min was left for the coordination of organic ligands to the metal source.
- Then the BTC solution was completely pumped out and immediately, pure ethanol is pumped into the sample cell for 4 min and then was completely pumped out to remove the excessive amounts of BTC.
- By subsequently repeating the upper steps using the same modified gold substrate to receive a thicker HKUST-1 MOF thin film.

1.2.2.4 Quartz crystal microbalance (QCM)

Quartz crystal microbalance (QCM) is a piezoelectricity based instrument that allows monitoring small mass changes. A mechanical stress results in a measurable electric modification on some materials, generally a quartz crystal as originally discovered by the Curie brothers in 1880[117]. QCM has been used for microgravimetry since 1959, when Sauerbray reported a linear relationship between the oscillation frequency of the piezoelectric crystal and the mass of a bound film[118]. When a molecule adsorbs on the electrodes, the inertial mass of the system is increased, and as a consequence, the harmonics of the piezoelectricity driven oscillator are

lowered. So, besides other sensing applications, QCM gravimetry is more than suited for the investigation of the MOF layer-by-layer fabrication process in real time.

A systematic investigation of the stepwise deposition of HKUST-1 MOFs on a QCM has been reported by Allendorf in 2012[116]. In fact, the QCM coupled growth method is an extension of the pump method with the QCM providing an in situ tracking of the layer-by-layer growth. An electrode coated with gold and modified with MHDA SAMs is fitted into the QCM cell. Firstly a pure ethanol is pumped through the QCM cell to record the baseline. The ethanol solution of copper acetate is pumped into the cell. In this case, a frequency decrease, corresponding to a mass increase, is recorded (Figure 1.9). This demonstrates that the copper ions bonds with the modified electrode. After a few minutes, an equilibrium is reached. This suggests that all the –COOH group on the SAMs have reacted with copper ions. Then, pure ethanol is pumped into the cell to clean it. The derived mass only shows a minor decrease due to a small amount of physically sorbed material being removed. Then the ethanol solution of BTC linkers is pumped

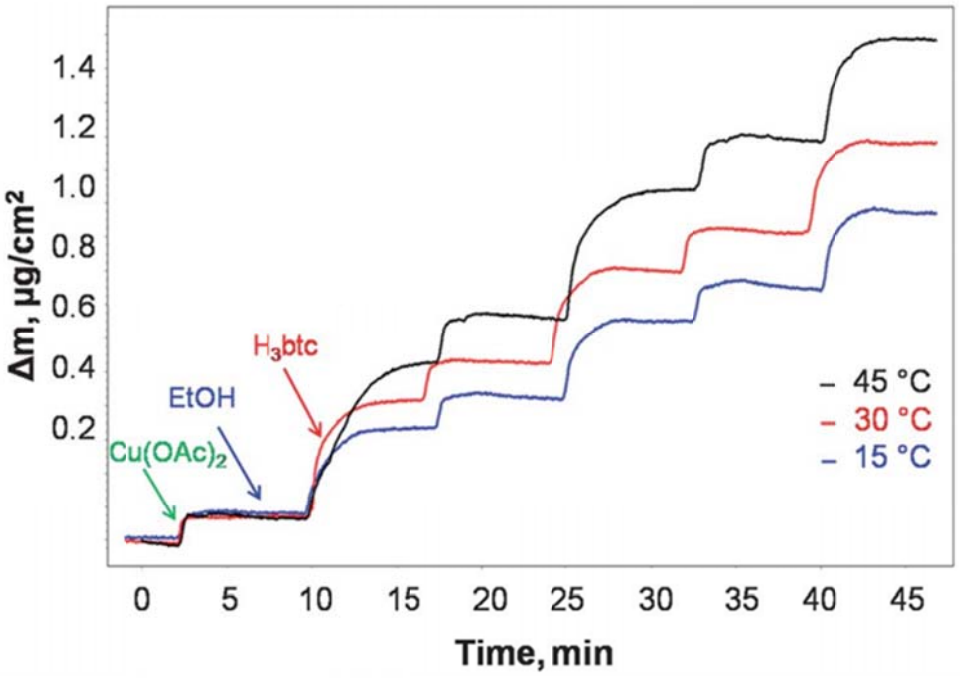

Figure 1.9: Sauerbrey mass change after three $Cu(OAc)_2$–BTC deposition cycles on SiO_2-coated electrodes at 15, 30 and 45 °C revealed by QCM. The inset shows the corresponding Eyring–Polanyi plots for each of the individual deposition steps. (Taken from Ref.[116])

into the QCM cell. Again a mass increase is monitored, and reveals a reaction of the linkers with the copper ions bonded on the electrode surface. An equilibrium is reached after a few minutes. The cell is then cleaned with pure ethanol. This forms a reaction cycle which is repeated to grow thicker MOF films. This QCM technique not only provides a method to grow the MOF with layer by layer, but also helps understand the growth mechanism of the MOF films. In the present work, a Q-sense E4 Auto was used, as shown in Figure 1.10. It is an automated real-time analytical instrument for the studies of molecular events occurring on the electrode surface.

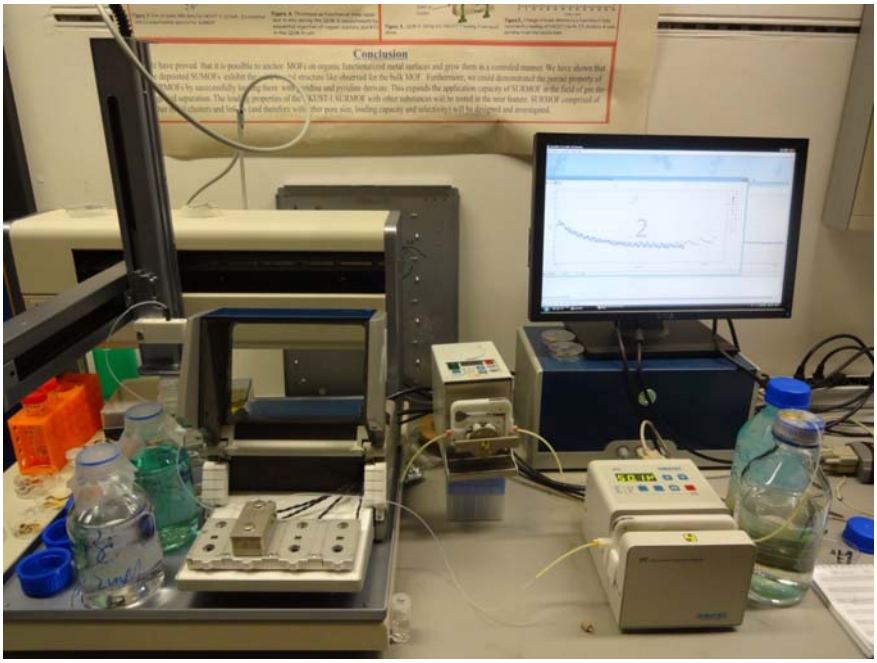

Figure 1.10: The setup of quartz crystal microbalance (QCM) technique.

1.2.3 Advantages and applications of SURMOFs

1.2.3.1 Control over the growth orientation

SURMOFs represent a kind of highly crystalline and oriented thin film MOF. More precisely, the growth orientation of SURMOFs can be controlled by the SAMs coating the substrate. For this, the first deposition cycle is of great importance since the orientation of the metal ions will initiate and guide further the growth. For an example, copper paddle wheel structure (Figure 1.11 a) is one of the most popular metal source employed to fabricate MOFs. The copper paddle wheel structure comprises a Cu(II) dimer bonded to four carboxylate groups. The two sites at the dimer axial positions are unoccupied and can be coordinated by H_2O, –OH and pyridyl groups. The –COOH groups exposed by the substrate surface can coordinate with two Cu(II), and lead to a stand-up orientation (Figure 1.11 b), whereas –OH groups favor bonding on the axial sites, and

thus direct a lie-down orientation (Figure 1.11 c). Studies have shown HKUST-1 can be grown along a [001] orientation on –COOH-terminated SAMs and along a [111] orientation on –OH or pyridyl terminated SAMs[119]. Therefore, SURMOF technique is quite suited to realize different orientation of paddle-wheel based MOFs, such as HKUST-1 and layer-pillar MOF $[Cu_2(BDC)_2(Dabco)]$.

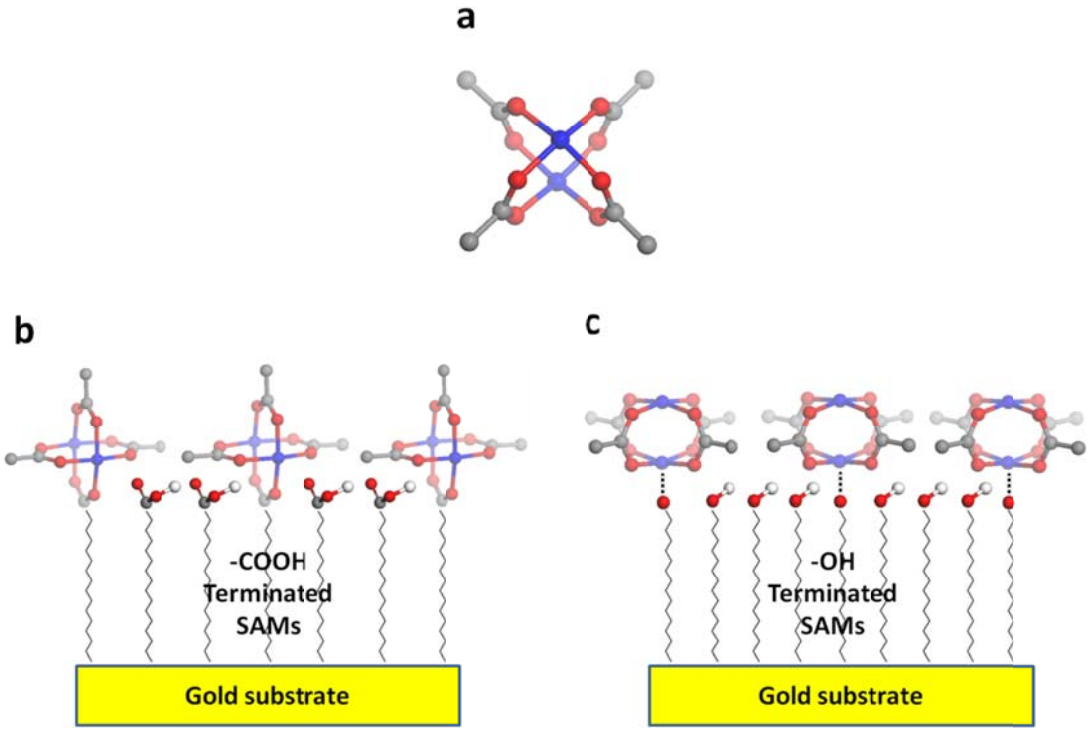

Figure 1.11: a) Cu-paddle-wheel unit; b) A model of Cu-paddle-wheel unit on MHDA SAMs; c) A model of Cu-paddle-wheel unit on MUD SAMs (carbon: dark grey ball, oxygen: red ball, copper: blue ball and hydrogen: grey ball).

The realization and control of an orientated growth of MOF thin film allow diverse applications. For example, the study reported by Liu et al have demonstrated that the adsorption behavior of volatile organic compounds strongly depends on the orientation of the MOF films[120]. Furthermore, the MOF film organized along one orientation can probably provide an ordered diffusion, or conductivity, of guest species, such as protons or electrons, and result in much better properties compared to the disordered MOF thin films.

1.2.3.2 Control over the thin film thickness

SURMOF fabrication technique is based on the step-by-step or layer-by-layer fabrication process. Normally, the deposition of materials on the surface by a layer-by-layer fashion results in a controllable thickness. In the SURMOF case, this is achieved by adjusting the number of growth

cycles. The study reported by Arslan et al have demonstrated that the thickness of HKUST-1 SURMOFs, fabricated using spray method, increased linearly with the number of growth cycles[100]. SURMOFs with well-defined thickness allow for better quantitative analysis of guest molecule events. For example, the SURMOFs can be used to determine the diffusion coefficients[121]. Additionally, MOF films with well-defined thickness are suited for MOF based device applications[84].

1.2.3.3 Versatile chemistry

As mentioned before, the versatility of the fabrication chemistry is one of the most important properties of MOFs, and is based on the possibility to realize the framework from numerous metal and countless organic connectors. Compared to the powder MOFs, the layer-by-layer assembly techniques used for SURMOFs allow even more combinations, because the organic ligands or the metal ions can be changed during the synthesis (the building blocks are successively and repeatedly deposited on the substrate). A study have shown that the epitaxial growth of $[Zn_2(NDC)_2(Dabco)]$ on $[Cu_2(NDC)_2(Dabco)]$ (NDC: naphthalene-2,6-dicarboxylic acid) can be realized by changing the copper source with zinc source during the synthesis process[122]. In another example, layer-selective incorporation of functional groups can also be achieved by changing the ligand during the synthesis process[123]. This versatile chemistry with SURMOFs opens new doors for smart and advanced applications. Recently, Heinke et al[124] reported the optically triggered release of guest molecules. This is realized by extending a MOF $[Cu_2(BPDC)_2(BiPy)$, (BPDC: 4,4'-biphenyldicarboxylic acid)] core with a MOFs $[Cu_2(AB\text{-}BPDC)_2(BiPy)$, (AB-BPDC: 2-azobenzene-4,4'-biphenyldicarboxylic acid, BiPy: 4,4'-bipyridine)] layer, where the azobenzene functioned as a UV switched lock.

Some other SURMOF applications such as in sensing[125], gas separation[126], photonic[127], electrochemistry[128], and conductivity[129] have also been investigated since recently.

1.3 Post-synthetic modification (PSM)

Post-synthetic modification (PSM) is the modification or the functionalization of a material that does not alter its main structure and is applied after the material has been synthesized completely. PSM allows developing materials with a variety of functionalities. This strategy can be used with various types of materials, including zeolite, and of course, MOFs.

1.3.1 PSM of MOFs

For the past decade, PSM has proven to be a very elegant method to modify finished MOFs. It offers vast possibilities to functionalize by covalently reacting molecules into the framework by

as shown in Figure 1.12. The PSM of MOFs results in the tuning of the size, shape or the functionality of the pores without changing the crystalline framework otherwise unobtainable through a direct fabrication. The concept of PSM of MOFs can be traced back to 1990[18], when Hoskins and Robson speculated that "relatively unimpeded migration of species throughout the lattice may allow chemical functionalization of the rods subsequent to construction of the framework". However, a study on PSM of MOFs has been published first in 2000 by Kimoon Kim et al and presents the chemical modification of cluster components[130]. Since, PSM has attracted more and more attention and numerous studies have been published. Cohen has contributed original and classical works in this field and published the first review article on PSM of MOFs in 2009[131].

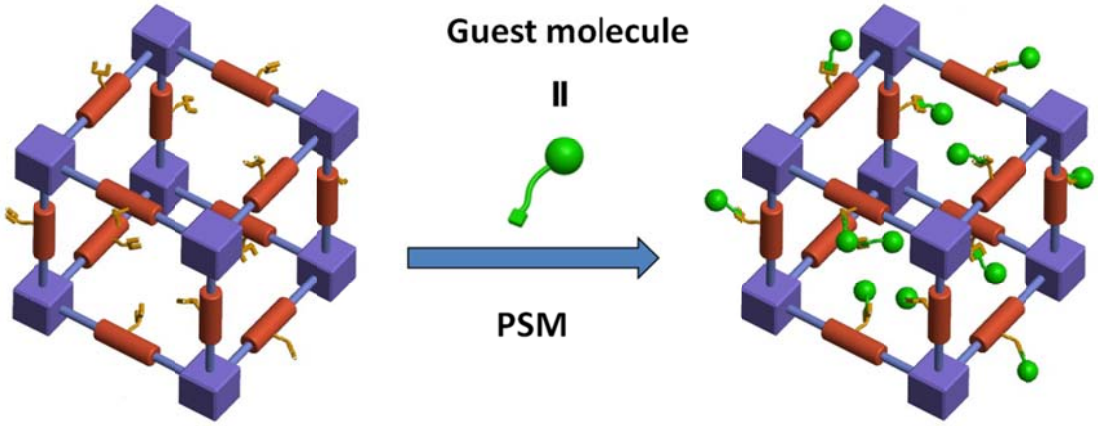

Figure 1.12: A general scheme illustrating the concept of post-synthetic modification (PSM) of MOFs based on the functional group on the organic linkers with covalent bonding of gust target molecules .

In general, the PSM of MOFs can be divided into two categories depending on whether they act on organic linkers or metal connectors. Most of the studies so far have focused on the PSM of the organic moieties since the functional groups on the linkers are more easily reacted with guest molecules. A few examples are presented in the following.

Obviously, the PSM is based on the functional groups available on the MOF incorporated linkers. Considering the number of relating studies, having an additional amino group on the linker reactant appears to be a practical choice, and many MOFs including NH_2-MIL-53[132], NH_2-UIO-66 (UIO: University of Oslo)[133], NH_2-HKUST-1[134], $Zn(NH_2BDC)_2$(Dabco) (also called DMOF-1-NH_2, DMOF: Dabco-MOF)[135] and IRMOF-3[26] have been successfully synthesized. Cohen and co-workers have contributed an initial study with the PSM of IRMOF-3, where the amino groups are acetylated with acetic anhydrides[136] (Figure 1.13). Farrusseng and co-workers[137] have

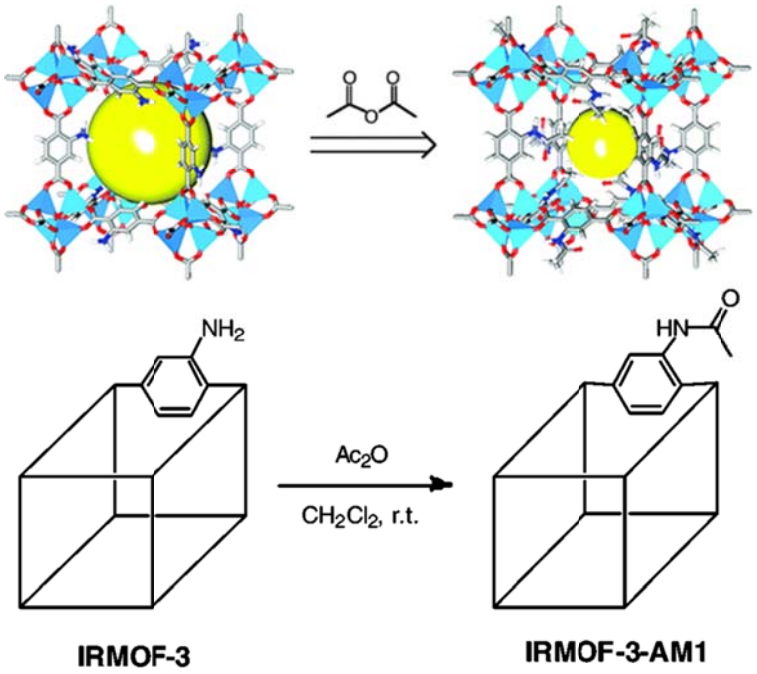

Figure 1.13: The general scheme illustrating the PSM of IRMOF-3 based on the acetylation of the amino groups in IRMOF-3. (Top) the pore size was decreased after PSM. (Figure is taken from Ref.[136]*).*

also demonstrated that the amino groups in DMOF-1-NH_2 can be transformed into azides using tBuONO and $TMSN_3$. The azide groups can further undergo a 1,3-dipolar (Huisgen) cycloaddition click reaction with phenylacetylene and catalyzed by Cu(I) to generate the triazole on the modified DMOF structure. Yield can reach around 90%. The click reaction has been firstly developed by Sharpless and co-workers 2001[138]. The PSM of MOFs on the view of the SBUs has also been carried out. One recent example is from Fischer and co-workers[139] and reports the uses of 1, 10-ferrocenediyldimethylsilane to treat MIL-53 (Al). The ferrocene can bridge to the hydroxide group through a ring-opening reaction.

A lot of studies have been reporting on PSM of MOF and numerous reviews have been published in the past few years[55, 131, 140, 141].

1.3.2 PSM of SURMOFs

The PSM of SURMOFs has been firstly reported by Liu et al[123], with the linker amino groups are selectively located either in the core layers, or the surface layers , and are reacted with fluoresceinisothiocyanate (FITC). The results confirm the efficiency of the synthesis methodology by revealing the selective incorporation of the amino group containing layer with fluorescence microscopy (Figure 1.14). Soon after, Shekhah et al[142] have reported the PSM of DMOF-1-NH_2 using an amino-based coupling strategy and the results have shown that the

ferrocene reagents are covalently bonded into the SURMOFs. Recently, Kitagawa et al[143] have contributed a study on the PSM of SURMOFs for sensing devices with tunable analyte affinity. They have prepared MOF on MOF structure with DMOF-1-NH_2 on DMOF-1 and the PSM of this heterogeneous structure has been carried out by condensation of the amino groups with succinic acid anhydride.

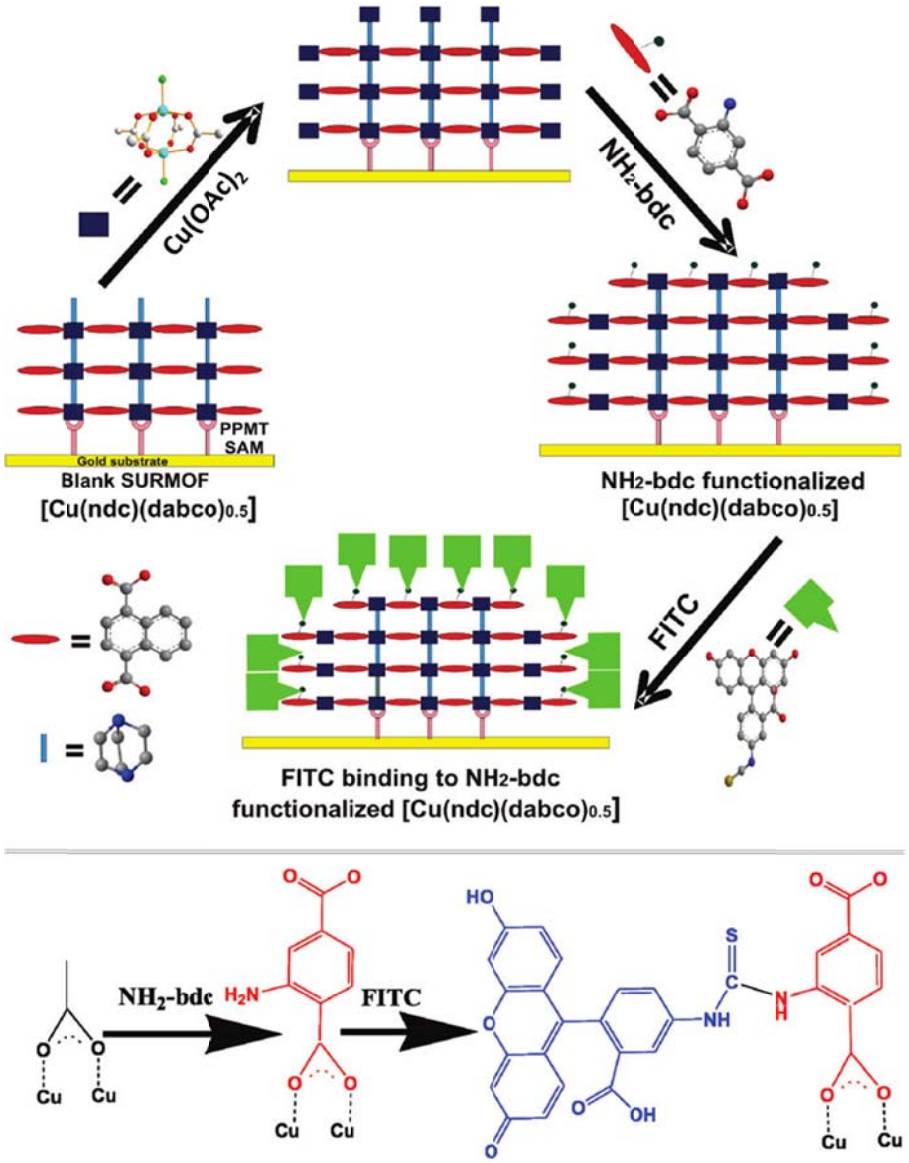

Figure 1.14: (Top) Stepwise Approach for External Surface Functionalization of the Pre-formed [001]-Oriented SURMOF [Cu(NDC)(Dabco)$_{0.5}$] at Pyridine-Terminated SAMs and (Bottom) Ligand Exchange between Acetate and NH_2-bdc and Reaction of NH_2-BDC with FITC.(Taken from Ref.[123])

1.4 Objectives of this thesis

For the past two decades, MOFs have been extended studied for potential uses in gas storage, gas separation, heterogeneous catalysis and magnetism. Recently, MOFs have also been found smart properties, such as proton and ion conductivity, photonic and electronic properties, photoluminescence and non-linear optical properties, static dielectric and super-capacitance properties. This has open new doors to more advanced applications, in which MOFs could be used as key materials for fuel cell, photonic and electronic, display, laser, memory switching and supercapacitor devices. To this end, MOFs, bulkily synthesized, do not satisfy the requirements, and thin film fabrication alternatives have become highly important.

A number of experimental methods have been developed for the direct deposition of MOF thin films on solid substrate. Though almost all of them produce uniform thin films, the SURMOF technique have showed greater potential by growing highly crystalline and oriented thin films ever since the first report of SURMOFs 2007 by Wöll and co-workers. After the introduction of SURMOFs, more studies have had the emphasis of developing new types of SURMOFs, as well as the understanding of their growth mechanism. In addition, a number of techniques and methods have been derived, and optimize the produced MOF quality and morphology. Since more recently, the MOF scientists have started to switch their focus on the versatile chemistry of SURMOFs to allow further applications.

Principally, the aim of this work was to construct functional SURMOFs, as well as, to tune their reactivity. It relied on the fact that the versatile chemistry of the SURMOFs not only encompasses the one from bulk MOFs, but also have the advantages brought by the fabrication control of the LPE layer-by-layer assembly.

Heteroepitaxial growth of MOF-on-MOF structures has been realized for bulk MOFs, and has great potential to produce filters or sieves for molecular absorption and separation. However, it is mostly relying on the crystals lattice parameters being similar between the different MOFs. The first objective of the presented study was then to build a multiheteroepitaxial MOF system with a lattice constant gradient since MOFs are flexible structures, and the SURMOF technique controls the assembly process layer-by-layer. These MOF systems could then be used for the size-selective loading of the metal-nanoparticles or proteins, with the large pore MOF layers serving as containers, and the small pore layers as sieves.

Functionalization of MOFs can be realized by using linkers with extra functionalization, and also by PSM. Another focus of this study was to obtain functional SURMOFs using post-synthetic modification based on azide-alkyne click reaction, as well as to monitor such reaction using infrared reflection absorption spectroscopy (IRRAS) and surface X-ray diffraction (out-of-plane and in-plane XRD). The reaction dynamics of two types of azide-alkyne click reaction, Cu(I)-

catalyzed and strain-promoted, were compared for the same MOF structure.

If a PSM of a whole SURMOFs sample is practically feasible, a spatially and temporally controlled modification of it is yet to be realized. Therefore, another goal was the study of functional patterning of SURMOFs by PSM. This combined photolithography techniques, which allowed the functional groups to be bonded locally to the MOF structure. In this project, two types of click reaction were used: azide-alkyne click reaction and thiol-yne click chemistry. Both reactions could be photo-controlled. In the azide-alkyne case, photoinitiated Cu(II) reduction to Cu(I) can be used to catalyze the reaction, whereas the thiol-yne click chemistry could be induced directly by UV light.

Though the presence of the coordinative defective sites in MOF crystals shows a structure is not perfect, it increases the material activity and functionality, for an example its catalytic activity. In this work, another aim was the tuning of Cu-paddle-wheel based MOFs with such coordinative defects knowing that post-synthetic thermal treatment can trigger the reduction of perfect Cu(II) to the defective Cu(I) sites. For this study, the defect-free UHM-3 SURMOFs was used as an investigation model, since other MOFs, such as HKUST-1, synthetically contain around 5% of defective Cu(I). The combined analyses of UHV-IRRAS, XPS, and XRD measurements allowed identifying a relationship between the defect content and the annealing temperature of the post synthetic treatment. The defect containing MOFs adsorbed guest molecule (CO and CO_2) differently. Additionally, a collaboration with the theoretical chemistry group can be initiated for a better understanding regarding the bonding energy of these two gases.

2 Characterization methods

Various, well established, characterization methods are available for the investigation of bulk material properties. With regards to surface science, analysis techniques are of great importance for the researchers.

To face these challenges a numbers of characterization techniques, including X-ray diffraction (XRD), infrared spectroscopy (IR), X-ray photoelectron spectroscopy (XPS), ultraviolet–visible spectroscopy (UV-Vis), optical microscope, fluorescence microscope, scanning electron microscope (SEM), atomic force microscopy (AFM), water contact angle measurement, quartz crystal microbalance (QCM), spectroscopic ellipsometry (SE) have been applied to character the produced SURMOFs in this PhD study.

This chapter introduces the theoretical background and relevant instrument of the above-mentioned characterization techniques, as well as specifies testing process relevant for SURMOFs

2.1 X-ray diffraction

X-ray diffraction (XRD) is perhaps the most widely used method to probe the structure, including atomic ordering and spacing of crystalline materials[144]. It is sometimes named X-ray powder diffraction as the samples used were originally in a powdery form. However, this technique can be also used to study crystalline thin film materials[21], and in this thesis, XRD was applied to determine the crystalline structure of the produced SURMOFs.

2.1.1 Theoretical background

XRD is based on the constructive interference of monochromatic X-rays within a crystalline sample. A crystalline material possesses an ordered and periodic arrangement of elements in the three-dimensional space. The distances between the nearest neighboring atoms or ions are typically a few angstroms and are comparable with the magnitude of X-ray wavelengths. Therefore, when the monochromatic X-rays hit into the crystalline sample, the interaction of the incident X-rays with the crystalline sample will exhibit constructive interference in some scattering direction. This phenomenon is called as “X-ray diffraction”, and was first discovered by Laue in 1912. Soon after, 1913, Braggs successfully determined the crystalline structure of sodium chloride (NaCl) and potassium chloride (KCl) by using the X-ray diffraction in the crystals and obtained the famous Bragg's law, which shows the relation of X-ray diffraction and crystalline structure. According to the Bragg’s law, the diffracted X-rays exhibit constructive interference and diffraction patterns are visible when the path difference between the X-rays

diffracted on the parallel and adjacent lattice planes is a multiple of the X-ray wavelength. As shown in Figure 2.1, the incident X-rays are scattered by the atoms or ions in the neighboring lattice plane, the intensity of X-ray diffractions will reinforce each other if the additional path difference (BC+BD) is dependent upon the inter-planar spacing (d) and the angle of incident X-rays. Therefore, the Bragg's law is expressed as the following equation:

$$n\lambda = 2d\sin\theta \quad (2.1)$$

Where n (a positive integer) denotes the order of reflection, and λ is the wavelength of the incident X-rays.

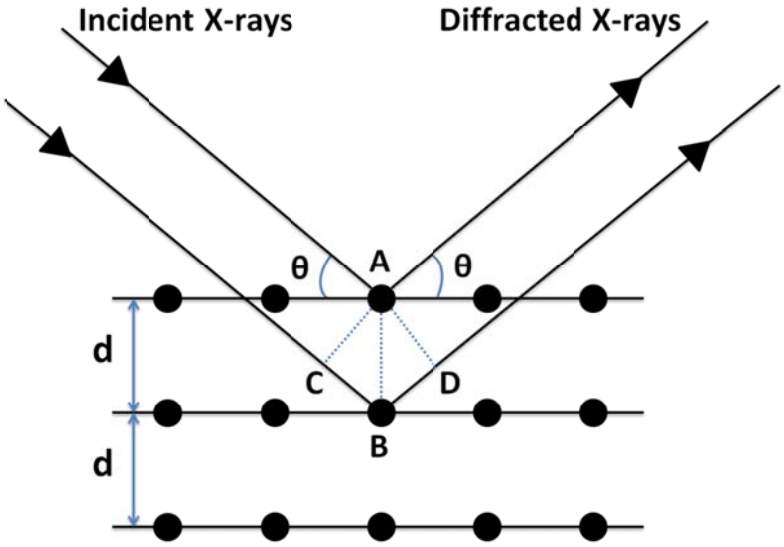

Figure 2.1: A schematic showing the Bragg's law. (d) The inter-planar spacing; (θ) The angle of incident X-rays with the lattice plane; (BC+BD) The additional path difference, BC=BD=d sinθ.

By recording the diffracted X-rays in a range of 2θ angles, all possible diffraction directions of the lattice are obtained because of the random orientation distribution of crystals in powder samples. Then the crystalline structure can be extracted by comparing the obtained diffraction patterns with entries in the database or with simulated results.

2.1.2 X-ray diffractometer

The X-ray diffractometer measures the X-ray diffraction of a given crystalline sample, and can provide the structure and atoms spacing within this sample. Generally, an X-ray diffractometer consists of three essential components: an X-ray source, an X-ray detector and a goniometer. Figure 2.2 displays the schematic diagram and basic geometry of the apparatus.

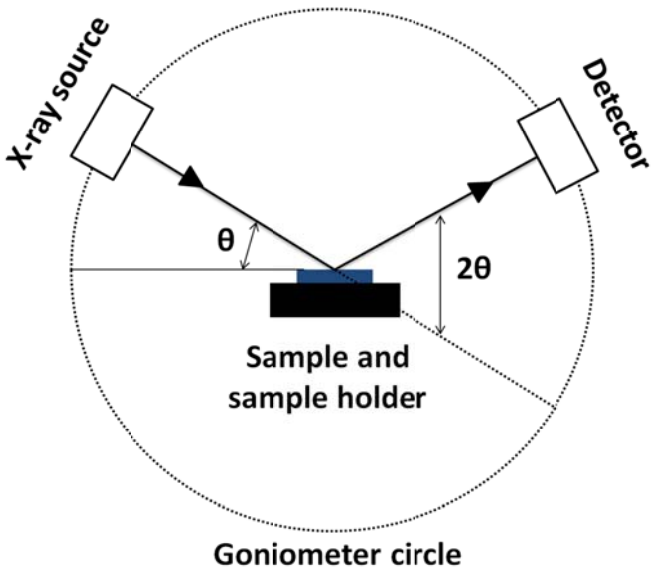

Figure 2.2: Schematic diagram showing the X-ray diffraction measurement.

The X-ray sources are generally vacuum tube diodes, typically under −40 kV. The diode provides a thermionic emission of electrons, i.e. electrons are thermally released from the cathode filament, and accelerated towards the metal plate anode (Cu or Mo), onto which they collide. The collisions induce the emission of X-ray photons. Those are filtered to obtain a monochromatic radiation, concentrated through a collimator, and directed toward the sample.

The X-ray detector records the X-rays that are diffracted by the sample. When the detector absorbs an X-ray, it generates a pulse of current, which can be interpreted computationally to the diffraction patterns of the test samples.

At the same time, the goniometer allows for providing the precise angles of the mechanical motions of the tube, test sample, and detector.

2.1.3 Out-of-plane and in-plane XRD

Unlike powdery samples which have a random orientation distribution of crystals, the thin film samples like SURMOFs mainly possess one orientation to the supporting surface normal. To determine the crystalline structure and orientation of such thin films, the combination of in-plane and out-of-plane XRD techniques is needed. As shown in Figure 2.3, these two techniques provide orientation information in the directions perpendicular and parallel, respectively, to the sample surface.

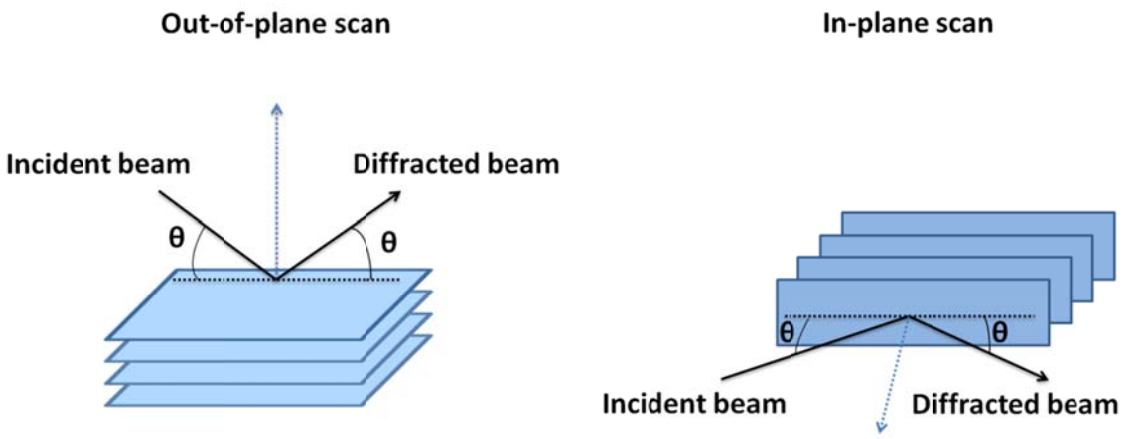

Figure 2.3: Geometries showing the out-of-plane and in-plane XRD measurements.

The out-of-plane diffraction technique records the X-rays scattered from the lattice planes parallel to the surface, and provides the crystallographic information along the direction perpendicular to the surface (see Figure 2.3 right side). This means only the crystallographic information along one direction of the crystal are obtained. In contrast, the in-plane diffraction technique monitor the X-rays scattered from the lattice planes perpendicular to the surface, and can provide the information for any direction tangential to the surface, though the geometry in Figure 2.3 (right side) displays only one example of lattice plane orientation.

For the characterization of SURMOFs in this thesis, the out-of-plane XRD measurements were carried out using a Bruker D8-Advance diffractometer in θ-θ geometry equipped with a PSD Lynxeye®. The in-plane XRD measurements were carried out using Bruker D8 Discover equipped with a quarter Eulerian cradle, tilt-stage and 2.3° Soller-slits installed in both sides. A Göbel-mirror, and a PSD Lynxeye® in θ-2θ geometry were applied. For both machines, Cu-anodes (Cu Kα1, 2-radiation with λ= 0.15418 nm) were used. The out-of-plane and in-plane measurement were usually carried out in the range of 2θ = 5 °- 20 ° at a scan step of 0.02 ° at 40 kV and 40 mA with various counting times in this PhD study.

To monitor the thermal dynamic response, the in-situ heating out-of-plane XRD measurements were performed with a PAAR HTK 1200 heating stage which was installed into the Bruker D8-Advance diffractometer. The heating rate was set to 1 °C per minute and the temperature range was set between room temperature and 180 °C. The stage temperature was calibrated using Boron Nitride.[145] The in-situ heating in-plane XRD measurement were carried out with a special adapted heating stage made by Mesicon (Dr. Ecker scientific consulting, Germany).

2.2 Infrared spectroscopy

Infrared spectroscopy is a powerful analytical method to identify chemical structures within a

material especially when having organic moieties[146]. IR spectroscopy is based on the specific vibrational modes of the chemical bonds in the materials. A chemical bond between two atoms, being similar to a harmonic oscillator, only absorbs infrared radiation of certain frequencies. Typically, each molecule is a different combination of atoms and chemical bonds, and can give a unique IR 'fingerprint'. Therefore, IR spectroscopy is used to identify different kinds of materials by matching database references. More particularly, IR spectroscopy is applied to detect the presence of functional groups, since each group also has a characteristic IR absorption spectrum. Additionally, changes in the size of resolved vibration peaks can be used to analyze quantitatively the proportion of the corresponding material or functional group. Furthermore, IR spectroscopy is also used to characterize the linkage environment of metal complexes. For an example, carbon monoxide (CO) bound to Cu(II), and to Cu(I) present different adsorption frequencies at 2179 cm^{-1}, and 2121 cm^{-1}, respectively[147]. Therefore, IR spectroscopy is an important and handy technique used by many chemists for the study of gas, liquid, and solid samples. Different IR techniques including transmission infrared spectroscopy, infrared reflection-absorption spectroscopy (IRRAS), attenuated total reflection (ATR) and ultra high vacuum infrared reflection-absorption spectroscopy (UHV-IRRAS) have been developed for different investigation conditions, and are now introduced.

2.2.1 Transmission infrared spectroscopy

Transmission infrared spectroscopy is the most common technique for the qualitative analysis of materials and the identification of their chemical composition thanks to the availability of a large number of spectral libraries. The samples can be solid, liquid or gaseous, but the preparations differ accordingly. For solid materials, thin films and thin polymer membranes that can be directly placed into the sample holder are readily analyzed. The powder samples can be mixed and pelleted (5% in weight) with another powder that is IR transparent, for an example potassium bromide (KBr). The pellet is placed into the sample holder for the IR acquisition. The liquid samples are prepared by squeezing liquid between two IR transparent windows. Additionally, some solid samples can be dissolved and also prepared in this way. The gas samples require a gas cell with suitable path length to enable detection.

2.2.2 Infrared reflection-absorption spectroscopy

Infrared reflection-absorption spectroscopy (IRRAS) is a powerful analytical technique for the characterization of adsorbed materials or thin molecular layers on metal surfaces[148]. An incident IR beam irradiates the sample layer, and is reflected toward the detector by the underneath metallic layer as metal substrates present a good IR reflectivity. Part of the spectrum is then absorbed by the sample layer while passing through it. The chemical composition of the

materials can be extracted by Fourier transforming the detected signal. However due to the metal surface reflection the theory differ from the standard transmission technique.

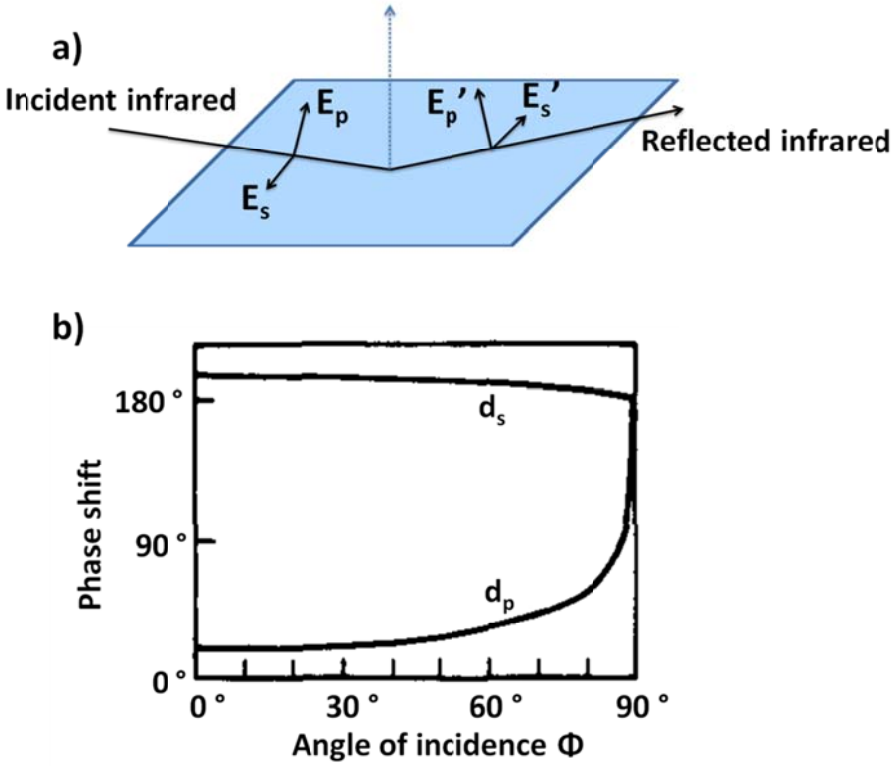

Figure 2.4: a) Schematic illustration of the p and s components of polarizated infrared radiation. The incident IR beam is reflected by the metallic surface (blue colored plane). The incidence plane is defined by the incident and the reflected light path. p is coplanar with this plane, whereas s is normal to it. b) Phase change of p-component and s-component radiations after reflected by the metal surface as a function of incident angel of infrared light (redraw from Ref.[149]).

In general, the IR vibrational excitation of molecules is based on the interaction of the dipole moment of the molecule with the electric field of the incident IR light, but the absorption of IR light by a molecule adsorbed on a metal surface is dominated by the dielectric behavior of the metal surface, since the electric field of the incident light as well as that of the dipole moment of the molecular vibration will interact with the metal electrons. The electric field of a linearly polarized, incident and reflected, infrared light can be decomposed into two vectors E_p and E_s, where E_p and E_s refer respectively to the component parallel to the incident plane and to the component perpendicular to E_s as show in Figure 2.4 a. The s component of radiation exhibits a phase shift of nearly 180° for all incident angles (Figure 2.4 b), therefore the sum amplitude of IR radiation parallel to the substrate surface is nearly zero at the reflection point. There is no

essential electric field parallel to the surface to interact with the dipole moment of the probed sample parallel to the surface. In contrast, the phase shift of the p component strongly depends on the incident angle and a phase shift of 90° can be obtained at an incident angle of 88° (grazing incidence), which maximized the p component. This leads to a dipole selection rule where only the p polarized component can excite the vibrational modes of the probed molecule on the metal surface. In addition, only molecules with dipole moments along the normal of the metal surface can be excited by the p component. This phenomenon is called "surface selection rule". As shown in Figure 2.5, the electric field of the dipole moment of the molecule induces the mirror charges in the metallic substrate. The dipole moment parallel to the surface will be screened by the mirror charges and only the dipole moment of the molecule perpendicular to the surface can be exited.

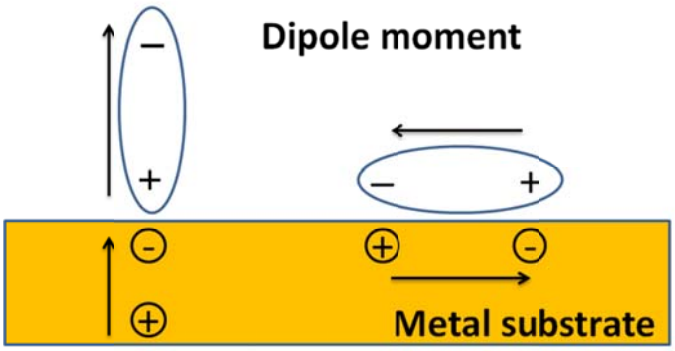

Figure 2.5: Schematic illustration of IR surface selection rule on metallic surface.

In this PhD study, IRRAS results of SURMOF samples were recorded using a FTIR spectrometer (Bruker VERTEX 80). An incident angle of 80° (near to the grazing incidence 88°) and a resolution of 2 cm^{-1} were applied in the measurement. Liquid nitrogen (N_2) was used to cool the detector (mercury cadmium telluride (MCT) narrow band or middle band). Perdeuterated hexadecanethiol SAMs on gold substrate was used as reference for the SURMOFs and SAMs samples. Dry air was purged continuously through the spectrometer and the sample compartment, to prevent atmospheric water and CO_2 contamination of the spectra and samples. Measurements were stopped if absorption bands for ambient humidity appeared.

2.2.3 Attenuated total reflection

Attenuated total reflection (ATR) is a useful technique to record the infrared characteristic of solid or liquid material without extensive sample preparation. IR ATR technique monitors the change in evanescent waves produced by the internal reflectance of an infrared beam on the surface of an optically dense crystal as depicted in Figure 2.6. Such evanescent waves can extend a few microns (0.5 - 5μ) (parameter d_p in Figure 2.6) beyond the crystal-sample interface and

into the sample. The sample absorbs part of the energy corresponding to the vibration of the present chemical bond. The evanescent waves are then attenuated or altered. This is passed onto the reflected light and monitored by the IR detector. The infrared absorption spectrum of the sample can be then recorded. However, two requirements must be met for the measurement: (1) The sample must be in direct contact with the ATR crystal; (2) The refractive index of the sample must be significantly smaller than that of the ATR crystal.

In this PhD study, ATR results were recorded from a Bruker Optics Tensor 27 spectrometer with a Bruker Optics Platinum® ATR (Attenuated total reflectance) accessory and a deuterated tri glycine sulfate (RT–DTGS) detector. The FTIR ATR spectra were recorded at room temperature (ca. 22 °C) with a resolution of 4 cm^{-1} using air as background.

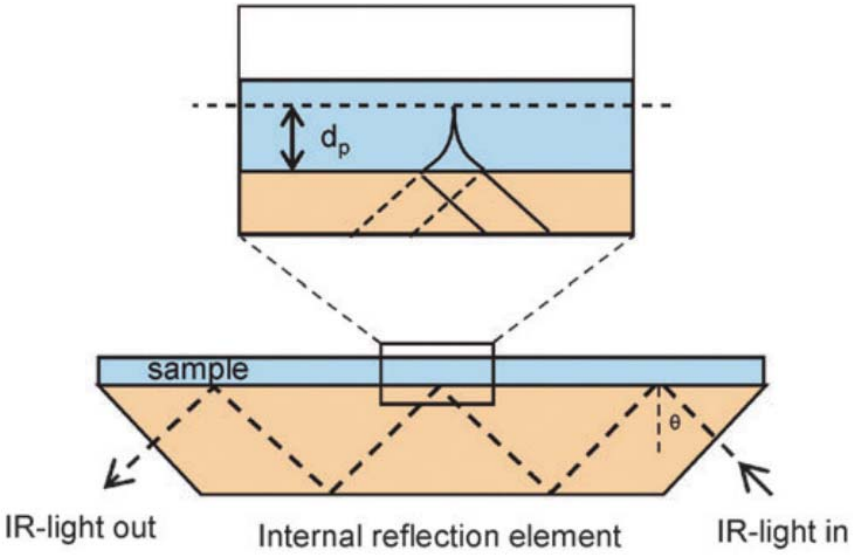

Figure 2.6: Schematic illustration of ATR setup (Figure taken from Ref.[150])

2.2.4 Ultra high vacuum infrared reflection-absorption spectroscopy

Ultra high vacuum infrared reflection-absorption spectroscopy (UHV-IRRAS) is a technique that the IRRAS measurement is carried out under UHV condition, in which the whole IR chamber with the pathway of infrared light is under UHV condition as shown in Figure 2.7 a and b[151]. In this condition, the IRRAS measurement provides a few advantages: (1) Avoid the contamination of the samples by ambient humidity or atmospheric gases. (2) Provide a long mean free path (MFP) for the IR light beam. (3) Allow dosing specific guest molecules for the investigation of adsorption and reaction phenomena. (2) Produce high quality infrared spectrum.

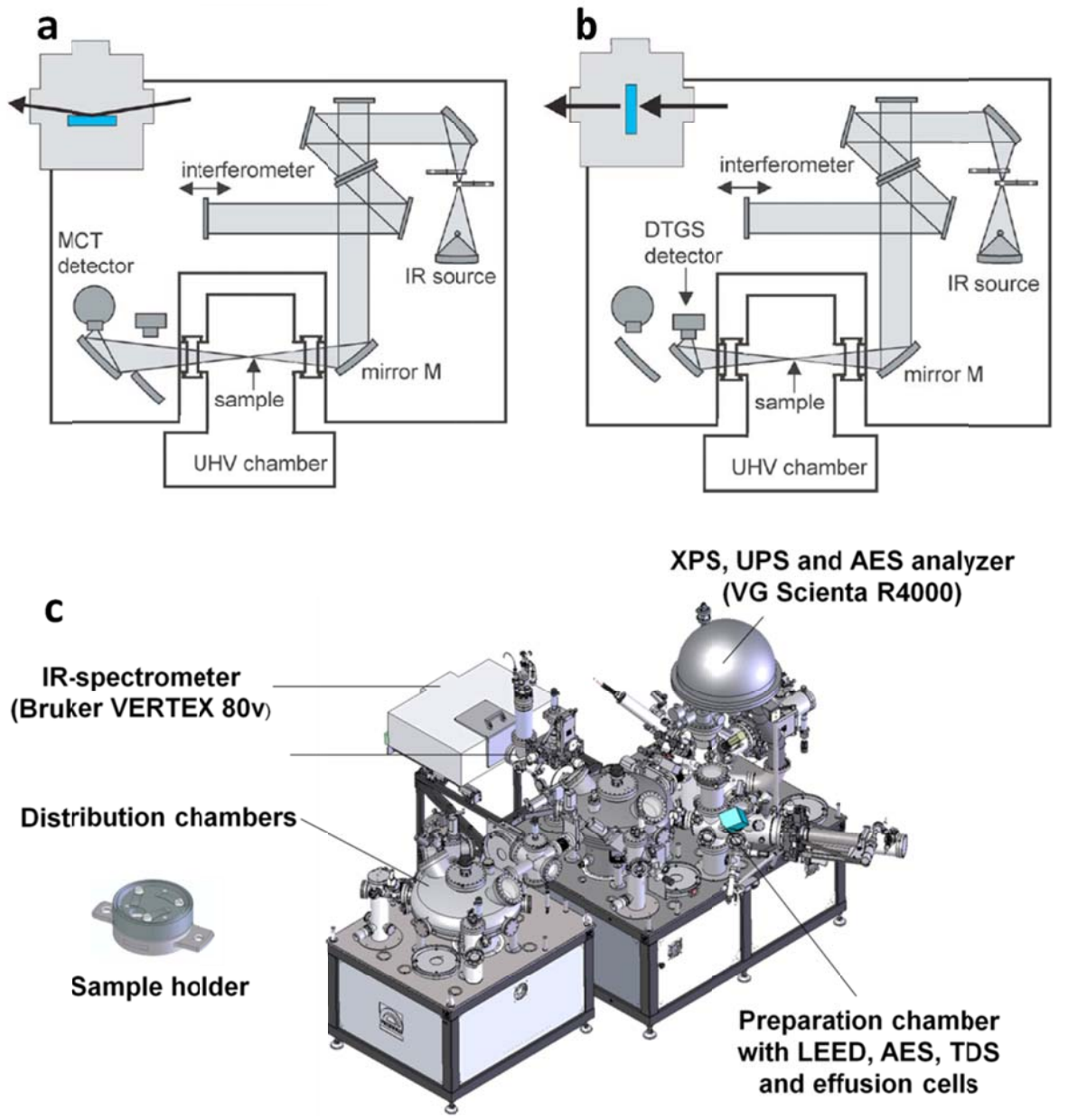

Figure 2.7: Schematic representation of reflection-absorption at grazing incidence IR measurement (a) and transmission absorption of IR measurement (b). (c) A specifically designed UHV apparatus. (Taken from Ref.[151])

In the presented work, the UHV-IRRAS Fourier transform results were recorded using a specifically designed apparatus (Prevac, Rogów, Poland) as shown in Figure 2.6 c, where a FTIR spectrometer (Bruker Vertex 80v, Bruker Optics, Ettlingen, Germany) is directly coupled to a UHV chamber.

2.3 X-ray photoelectron spectroscopy

X-ray photoelectron spectroscopy (XPS) is one of the most widely used techniques for the surface chemical analysis[152]. XPS technique was developed by Kai Siegbahn, who was awarded with the Nobel Prize in 1981for his significant contributions.

XPS is based on the photoelectric effect, in which the bound electron in the core (inner) levels of the atom absorbs the energy ($E=h\nu$, where h is Plank's constant and ν is the frequency) of an incident photon and overcomes the work function (Φ) and then is emitted from the material surface as depicted in Figure 2.8. Note that the value of the work function of the material and the material in the spectrometer are denoted differently, as Φ_1 and Φ_2 in Figure 2.8. The kinetic energy of the emitted photoelectron is measured by the electron energy analyzer and the bonding energy of the photoelectron is calculated using the following equation:

$$E_{kin} = h\nu - E_B - \Phi \qquad (2.2)$$

Where E_{kin} is the kinetic energy of the photoelectron (relative to the vacuum level E_V), E_B is the bonding energy (relative to the Fermi level E_F).

In general, XPS apparatus consists of five essential components: an X-ray source, a sample holder, a UHV chamber, an electron energy analyzer, and a detector. The X-ray source produces X-ray photons which can be focused toward the sample on the sample holder. UHV condition is needed to increase the mean free path of photoelectron. The electron energy analyzer allows measuring the kinetic energy of the photoemitted electrons, as well as filtering them and letting pass a define energy distribution. The detector counts the number of the energetically selected photoelectrons passing through the exit slit of the hemispherical electron energy analyzer for a given time

XPS allows a number of applications including the identification of chemical composition and chemical state, and their quantitative analyses. However, XPS is a highly surface specific technique which can only yield information up to 10 nm or less below the sample surface due to the limitation of the electron mean free path. In comparison, X-ray can penetrate micrometers below the surface. The sensitivity of the XPS measurement is mainly dependent on the spectra background level and the element specific photoelectron cross sections. In general, a high sensitivity (concentration down to 0.1 atomic%) can be achieved in XPS measurement[153].

Here, the XPS measurements were carried out with a specifically designed ultrahigh vacuum apparatus with a hemispherical electron energy analyzer (VG-Scienta R4000) and a non-monochromatic Al Kα X-ray source, as shown in Figure 2.7c.

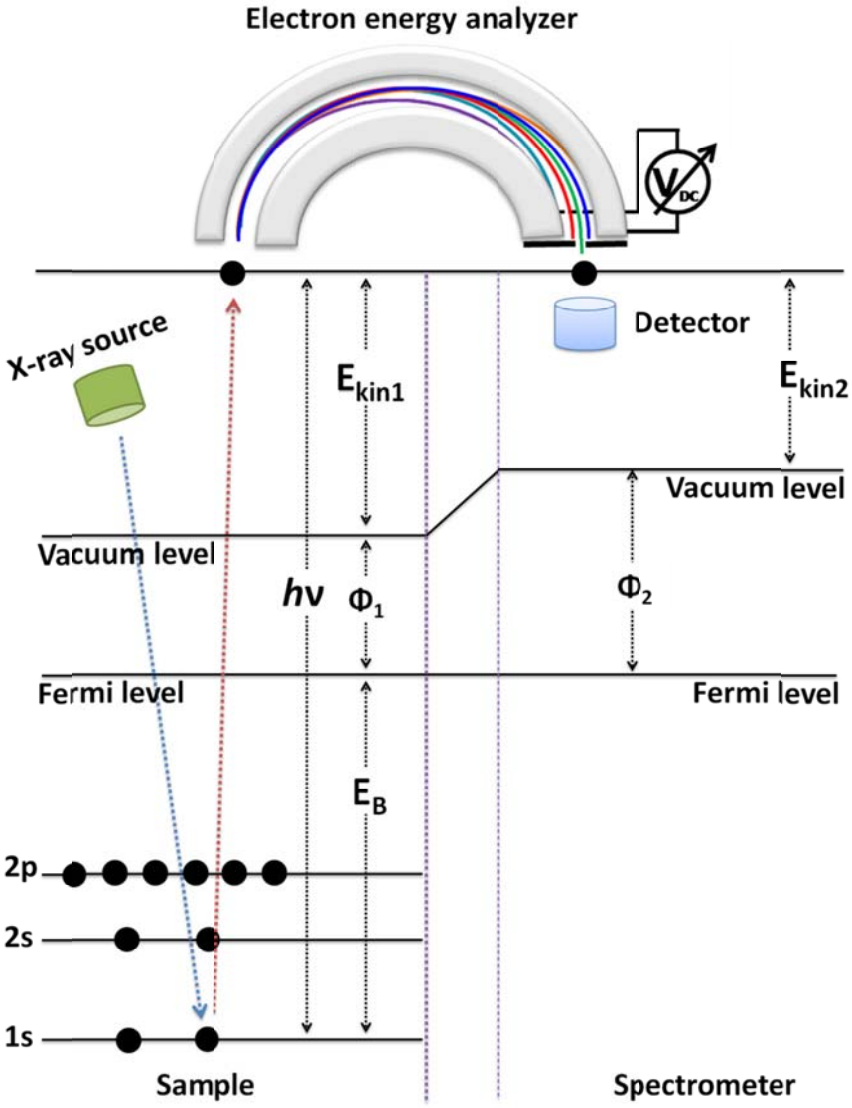

Figure 2.8: Schematic illustration of the photoemission.

2.4 Ultraviolet-visible spectroscopy

Ultraviolet-visible spectroscopy (UV-vis) is a useful technique for monitoring electronic transitions in materials absorbing in the 200-400 nm (UV) and 400-700 nm (visible) ranges. The electrons of the materials absorb the photons energy and are promoted from their ground state to an excited state[154]. The transition usually occurs for one of the following three electronic orbitals: (1) σ bonding orbital. (2) π bonding orbital. (3) non-bonding orbitals (lone pair electrons), as shown in Figure 2.9. When the energy of incident photons matches with the energy for the electron transitions, the energy is absorbed and the electrons jump from the bonding orbital to their anti-bonding orbital (see Figure 2.9). The absorption spectra can then be recorded.

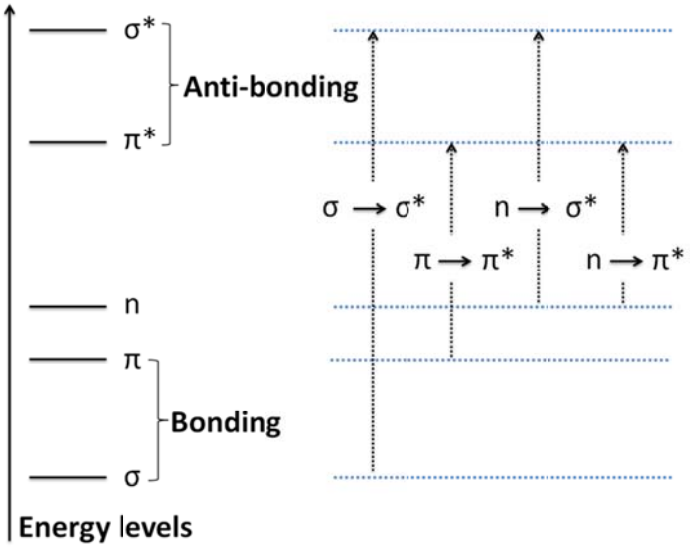

Figure 2.9: Possible electronic transitions of σ, π, and n electrons.

In my PhD study, the UV-vis spectra were recorded by means of a Cary5000 spectrometer with a UMA unit from Agilent. The linker molecules were studied in an ethanol solution in transmission mode. The UV-vis spectra of the SURMOFs on the gold substrate were measured in reflection mode with an incident angle of 30° to the surface normal.

2.5 Optical microscope

An optical microscope is an instrument that observes the visible light from a sample by combining a system of lenses to produce magnified images and bypass the limitations of the naked eye[155]. In general, it consists of two lenses systems: the objective lens and the ocular, as show in Figure 2.10. The lights emitted from the object firstly go through the objective lens and produce a real intermediate image of the object inside the microscope. That image is then magnified by the ocular lens, which produces enlarged inverted virtual image of the object. Therefore, the final magnification *M* of the image for the sample is obtained by the following equation:

$$M_{final} = M_{obj} \times M_{oc} \tag{2.3}$$

The principle of an optical microscope is rather simple. However, the design of this instrument and the accurate assembly of all the components are much more complicated, as both the objective and ocular contain multiple optical, aligned but mobile, elements performing close to their theoretical limits. The resolution d of an optical microscope is limited by observing light wavelength λ according to Ernst Karl Abbe law:

$$d = \frac{\lambda}{2\mathrm{NA}} \tag{2.4}$$

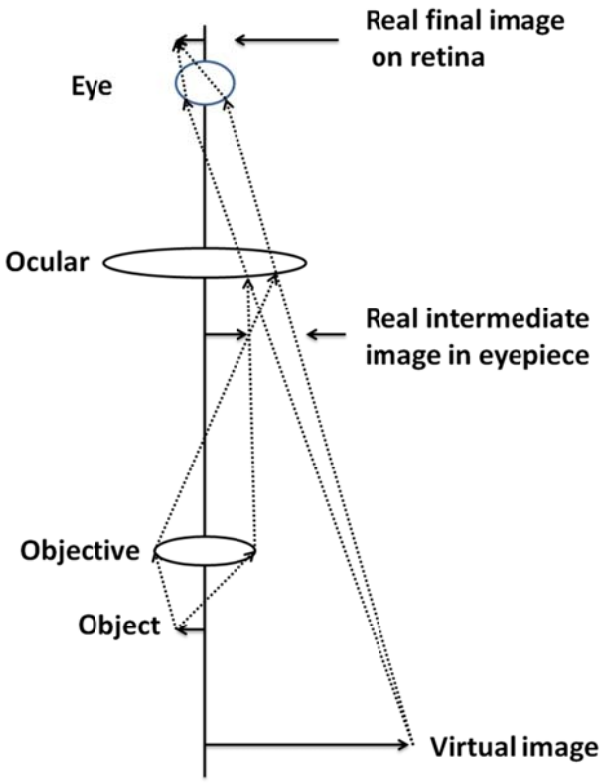

Figure 2.10: Schematic diagram showing the principle of the optical microscope.

Where NA is the numerical aperture. If using air as the medium between the sample and the objective, the highest practical NA is 0.95, whereas NA can reach 1.5 when using oil. It means the resolution of optical microscope is around 200 nm. When using UV light, the resolution can be increased with two times, but the use of fused quartz glass for the UV transmission is very expansive.

In this PhD study, optical images were recorded from a Leica DM2500 M optical microscope.

2.6 Fluorescence microscope

Fluorescence microscope is a special case of optical microscope, which allows the visualization of specific molecules that fluoresce when expose to a specific light spectrum[156]. Fluorescent molecule absorb energy in this range with electron being exited from the ground state to higher state before almost immediately collapsing back to its initial ground state. During the collapse process, the molecule can emit light. Since some energy is lost in course, the emitted light exhibits a lower frequency (longer wavelength) than that of the exciting light. Compared to a traditional optical microscope, fluorescence microscopes contain specific wavelength filters, as well as a unique lighting method, as show in Figure 2.11. A monochromatic filter reduces the excitation spectrum of the light source. Whereas other monochromatic filters prevent the passing

through of this light to observe only the response in the expected fluorescence range. Though optical microscopy presents a resolution limitation due to diffraction limitation, several super-resolved fluorescence microscopy including 4Pi (laser scanning fluorescence microscope with an improved axial resolution) microscope, near-field scanning optical microscope (NSOM), near-field optical random mapping (NORM) microscopy and structured illumination microscopy (SIM) have been developed, and brought optical microscopy into the nanoscopic dimension. The 2014 Nobel Prize in Chemistry was awarded to Eric Betzig, William Moerner and Stefan Hell for their contribution to this super-resolved fluorescence microscopy.

In this PhD study, the fluorescence images of the SURMOFs were measured with a Fluorescence Microscope equipped with a mercury short arc reflector lamp (Type HXP-R 120W/45C VIS), Supplier: OSRMA; the band pass filter (BP) with BP 546/12 and long pass (LP) filter LP 590 were separately used as excitation and emission filters.

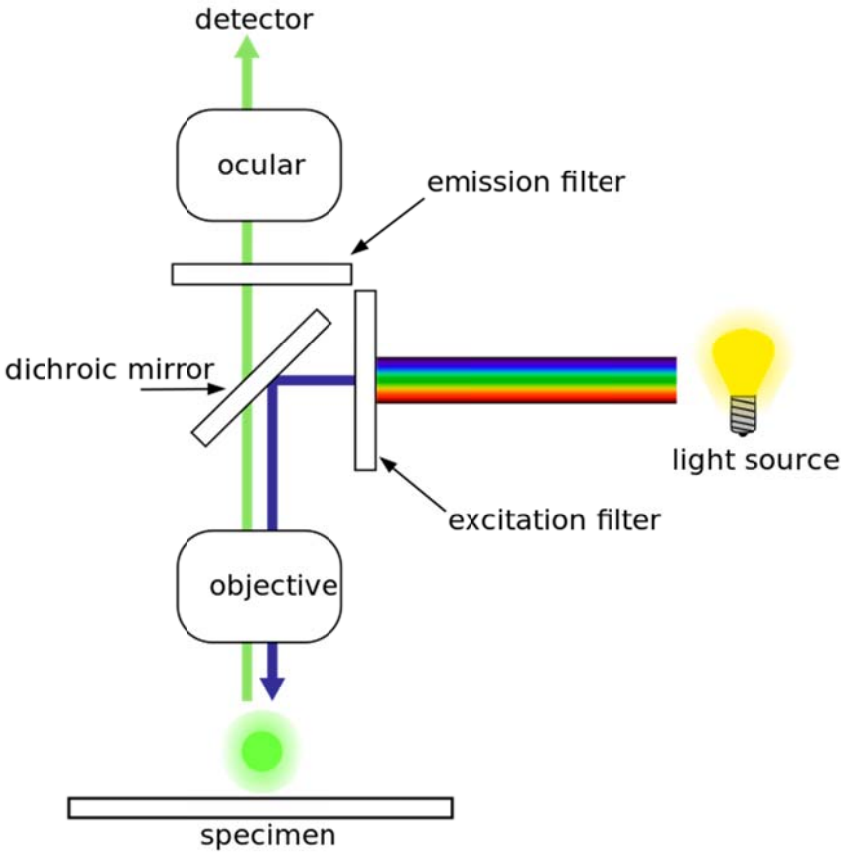

Figure 2.11: Schematic diagram showing the principle of the fluorescence microscopy (Picture Taken from Ref.[157]) .

2.7 Scanning electron microscope and energy dispersive X-ray analysis

Scanning electron microscopy (SEM) is a microscopy technique where the images are obtained by scanning the sample with a high energy focused electron beam. In a typical SEM apparatus, the high energy electron beam is generated by an electron gun and focused on the sample surface by an electromagnetic lens system, as shown in Figure 2.12. The focused electron beam scans over an area of the sample in a raster. The electrons interact with the atoms of the sample and are scattered by the sample surface. The signals produced by a SEM include secondary electrons (SEs) and back-scattered electrons (BSE). Inelastic scattering produces SEs with low energy (<50 eV). Note, only the SEs produced from the sample surface (a few nanometer below the sample surface) can contribute to the observable signals, while the others are absorbed by the sample due to their low energy. Elastic scattering produces the backscattered electrons (BSEs) with high energies (>50 eV), and can be generated at various sample depths.

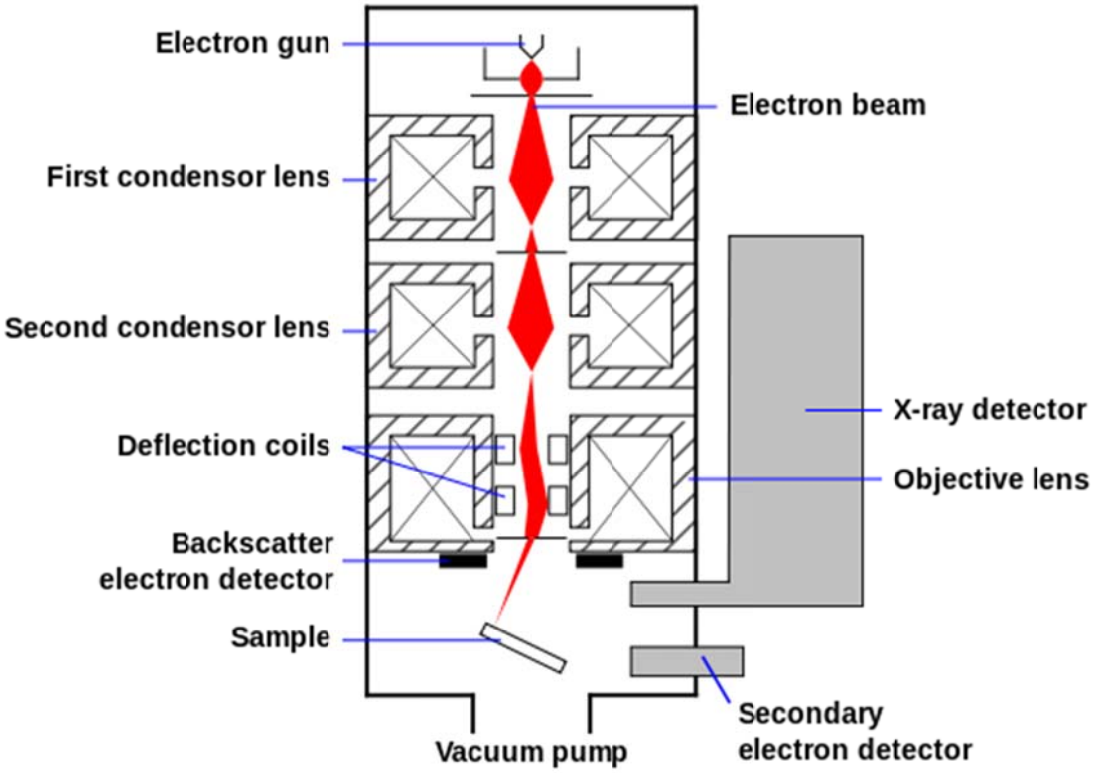

Figure 2.12: Schematic diagram showing the main components of a scanning electron microscope (Figure taken from Ref.[158]).

Additionally, the scattered electrons from the sample as well as the beam current absorbed by the sample are recorded, and can be used to produce an image with a current distribution over the scanned area. Finally, the obtained signals are amplified and rendered as contrast variations. The recorded image is indeed a distribution map of the intensity scattering from the sample.

SEs and BSEs, both can be used for the imaging of a sample. However BSEs can also provide additional information about the elemental density of a sample as heavy elements (high atomic number) backscatter electrons more strongly than lighter elements (low atomic number) Therefore BSEs are commonly used to contrast between areas with different chemical compositions and to identify of the elemental distribution within a sample.

The preparation of a sample, especially to deal with its insulation, is important to produce high quality images. In general, the high energy electron beam, leads to charge accumulation onto the sample surface, and especially due to insulation. This may cause displacement resulting in an unfocused and indistinct image. To avoid the issue, the sample surface is usually pretreated by coating with a few nanometers of gold or carbon. Noteworthy, carbon coating is more appropriate to BSEs measurement because gold, having a high atomic number, strongly backscatter electrons.

In general, an energy dispersive X-ray (EDX) analysis system is attached to the SEM instrument to identify the elemental composition of the sample. The data recorded by the EDX analysis consist of spectra showing the peaks corresponding to the elements in the samples. This technique can be qualitative, semi-quantitative, quantitative and also provide spatial distribution of elements through mapping. Therefore by means of this technique an elemental mapping of a sample also becomes possible.

In this study, SEM images were recorded using a Philips XL30 (FEI Co., Eindhoven, NL), a field emission gun environmental scanning electron microscope (FEG-ESEM), operated between 15 keV and 30 keV, and 0.7 to 1.0 Torr chamber pressure. Elemental analyses was performed using an energy dispersive X-ray fluorescence spectroscopic unit (EDX) from EDAX (EDAX Inc., Mahwah, NJ, USA) with a liquid nitrogen cooled sapphire Si(Li) detector. For the spectra collection, the microscope was operated at 15 kV and a 100 mm aperture was used. Measurement times were five minutes for the collection of the spectra.

2.8 Atomic force microscope

Atomic force microscopy (AFM) is a high resolution type of scanning probe microscopy, which is applied to image the morphology of a sample surface with a three-dimensional (3D) detail[159]. The resolution can be down to the nanometer scale. The technique accept a wide range of the sample types including biological structures, such as cells and biomolecules[160]. Acquisition can be run in air, liquid, or vacuum condition. Generally, it is a non-destructive method. Therefore, AFM is one of the most widely used techniques for the topological investigation of nanomaterials and biological materials.

The AFM technique consists of a thin, flexible microscopic cantilever beam with a sharp tip at the end that probes the sample surface as shown in Figure 2.13. The interaction of the tip with the vicinal probed surface usually leads to an observable displacement of the beam. The surface scanning is then achieved by moving the sample in a plane, while recording the movement changes of the cantilever along the plane normal. The interaction can be attractive or repulsive forces, or their combinations. A laser beam is pointed on the back of the cantilever, and reflected signal altered by the deflection of the cantilever is monitored by feeding back the laser onto a four-quadrant photodiode detector. The recorded signals control the piezoelectric element to maintain a constant force between the tip and the sample. Finally, the scanner records all the movements in the x, y and z direction, and transform all the information to a topographical image of the sample surface.

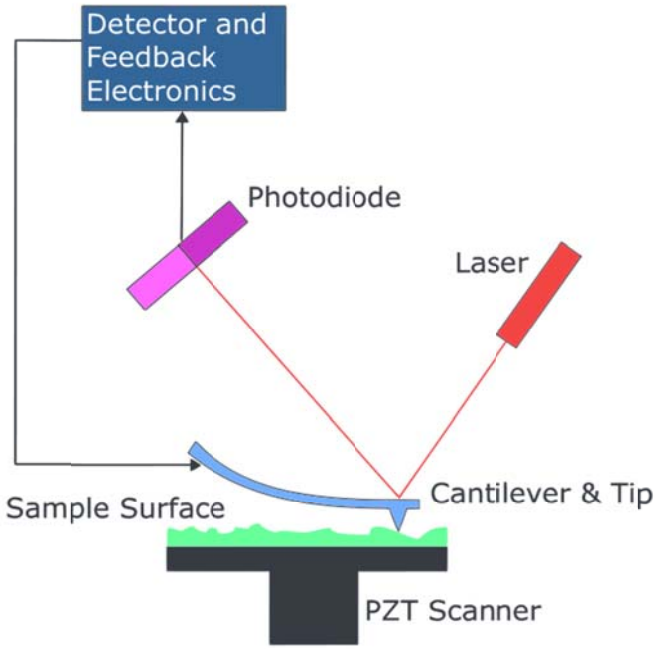

Figure 2.13: Schematic diagram showing the main components of an atomic force microscopy. (Figure is taken from Ref.[161])

Two operational modes are usually used for the morphological characterization of the surface. One is the contact mode. In the contact mode, also known as repulsive mode, the tip has a continuous light physical contact with the sample surface during the scanning. The resulting contact force is between 0.01 and 1.0 N/m in air and induces the deflection of the cantilever according to the changes of the surface topography. This mode is commonly used to image hard material, since the shear force produced by the movement of tip on the surface may not cause damage to the sample surface and alter the result of the measurement. Another mode is the intermittent-contact mode, also called alternate current mode (AC-mode). In this mode, the

cantilever oscillates and the contact of the tip with the surface is only intermittent. The energy transfer from the oscillating probe to the sample surface is much lower than in the contact mode, and makes the method especially suitable for the analysis of delicate soft or brittle matter. Additionally, as regions with different hardness, elasticity, adhesion, or charge characteristics are encountered by the tip, the oscillation phase is changed. Therefore the AC-mode is commonly applied to distinguish different types of materials on a sample surface.

In this PhD study, the AFM image was obtained by using an Asylum Research Atomic Force Microscope, MFP-3D BIO. The substrates were measured in air as received. The AFM was operated at 25°C in an isolated chamber in alternating current mode (AC mode). AFM cantilevers were purchased from Nano&more. NSC-18 AFM-HQ cantilevers with the following properties were used: nominal resonance frequency: 75 kHz; nominal spring constant: 3.5 N/m.

2.9 Water contact angle measurement

Water contact angle measurements are applied to determine the wettability of a solid surface. Wettability is the ability of a solid surface to interact with a liquid. Different liquids will wet a given surface to different extents depending on the interactions between them. This extent of the interactions can be quantified by the contact angle (θ), which is the angle at the interface of liquid, vapor and solid, between the surface tangential of the liquid the solid as shown in Figure 2.14. Water is often used. The surface is usually termed as "hydrophilic" when $\theta < 90°$, or "hydrophobic" when $\theta > 90°$. When the water completely wets the solid surface, it results in a zero degree contact angle. This case is called superhydrophilicity. In contrast, when the water contact angle is greater than 150° as well as the roll-off angle or contact angle hysteresis is less than 10° is called superhydrophobicity. The contact angle hysteresis is described as the difference between the maximum advancing angle and the minimum receding angle. Note that superhydrophobicity has attached considerable attention from a wider interdisciplinary scientific

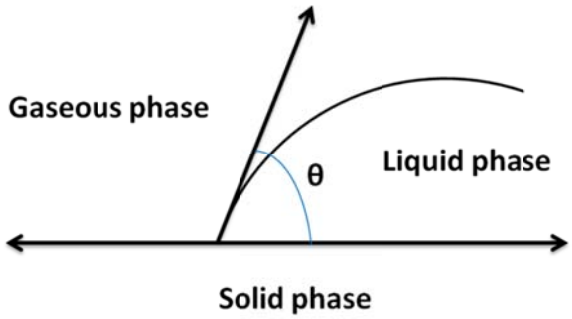

Figure 2.14: Schematic of the contact angle formed between a liquid and a solid surrounding gaseous phase.

community because of its many applications including the study of non-sticky coating, self-cleaning and biofouling preventing surfaces.

In this PhD study, static water contact angles were measured using the sessile drop method with a home-built water contact angle measurement device. Typically, 3 μL of deionized water was used for the static water contact angle measurement. Pictures of the water droplets on the surface were taken with a UK 1115 digital camera (EHD imaging, Germany). Image J software with the Dropsnake plug-in was used to analyze the images. The reported water contact angle values were the average of at least three WCA values from repeated experiments.

2.10 Quartz crystal microbalance for gas molecule loading

The background and principle of quartz crystal microbalance has been introduced briefly in the previous chapter (1.2.3.4). Here the focus is directed on the measurement of gaseous molecule loading.

As a guest molecules are adsorbed directly on the QCM electrode, or indirectly on the sample materials coating the electrode, the resonance frequency decreases due to the inertial mass increase. This allows a dynamic monitoring of an adsorption process[116]. In this thesis, SURMOFs were pre-grown on gold-coated QCM electrode. The gaseous molecule loading of the SURMOFs were carried out with a dissipation monitoring (QCM-D) instrument combined with a home-built gas phase controller as depicted in Figure 2.15. The gas phase controller control a flow of pure (6.0) argon gas (1) directly into the QCM cell (8) along the gas tube (7) or first into the liquid guest molecule container (5) and to evaporate and carry the guest molecules into the QCM cell. To perform the loading experiment, the SURMOFs were activated at 60 °C under pure argon flow overnight. Thereafter the temperature of the QCM cell was decreased to 30 °C to run the experiment, also under pure argon flow. When the baseline is obtained (stable oscillation frequency), the gas flow was adjusted to carry the guest molecules into the QCM-cell (Figure 2.16 ‘start to load’ point). The loading of the guest molecule in the SURMOFs resulted in the decrease of the observed frequency until it reached an equilibrium after a certain time (Figure 2.16 a). The maximum change of the frequency allowed computing the maximum mass loading (see Figure 2.16 b). The unloading experiment was carried out by switching the three-way valve to flow pure argon into the QCM-cell (Figure 2.16 ‘start to unload’ point). When the physically adsorbed molecules were desorbed, the frequency changes went back to equilibrium. The difference of the frequencies (ΔF), or masses (ΔM), between the loading equilibrium and the unloading equilibrium were attributed to chemical or coordinated adsorption on the SURMOFs (Figure 2.16).

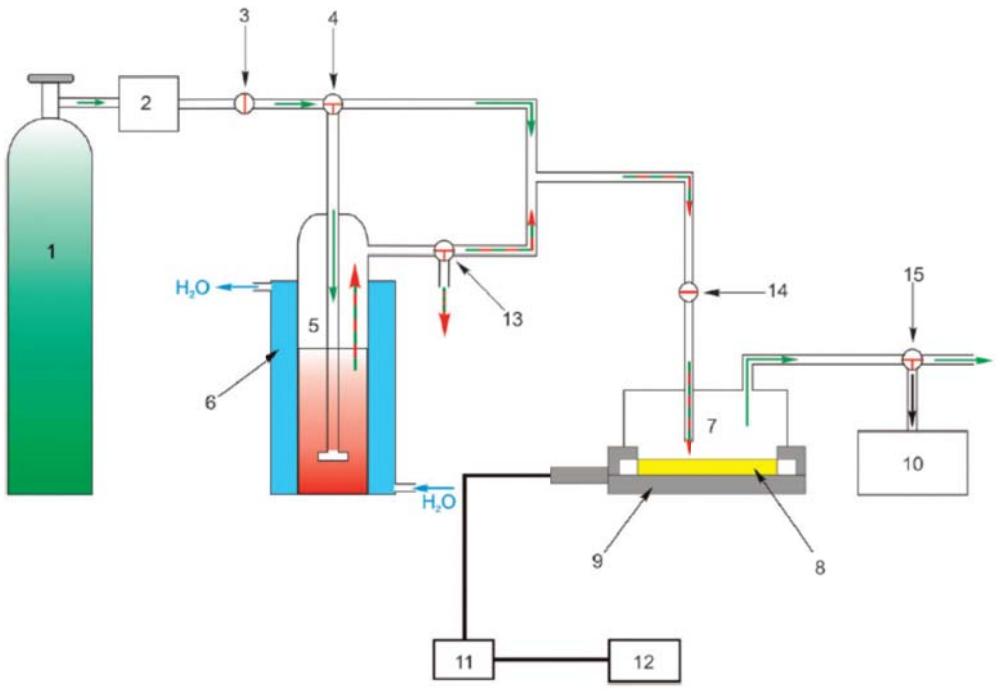

Figure 2.15: Setup employed for the sorption measurements: (1) argon supply, (2) gas flow controller (FMD PR4000), (3) main valve, (4) three-way valve, (5) storage container with the loading substance, (6) thermostat, (7) glass tube, (8) QCM sensor with gold electrodes, (9) sample holder with electric feed through, (10) membrane pump, (11) impedance analyzer, (12) PC, (13, 15) outlet valves, (14) inlet valve. (Figure adapted from Ref. [121])

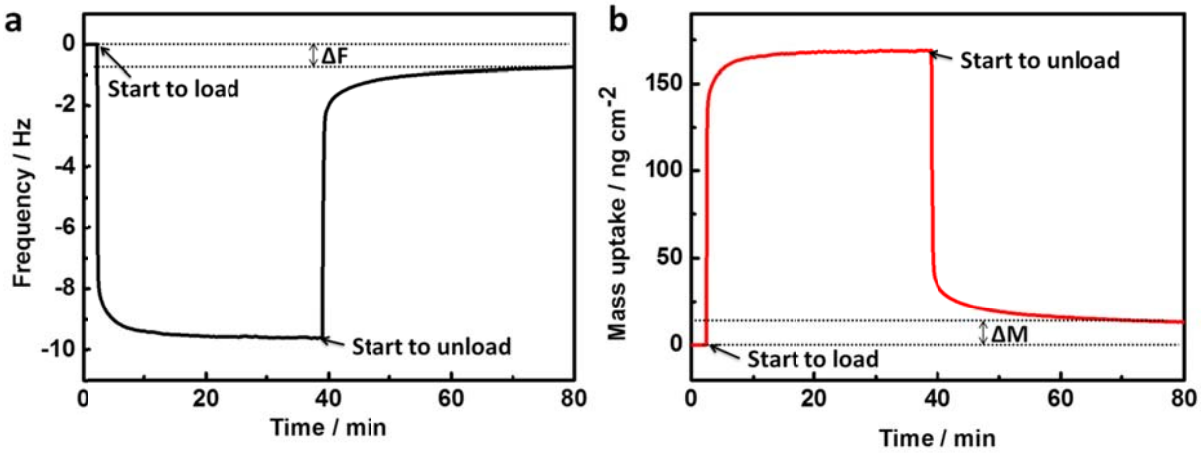

Figure 2.16: The loading of gas phase ethanol in HKUST-1 SURMOFs using QCM: (a) Frequency changes. (b) Calculated mass changes.

2.11 Spectroscopic ellipsometry

Spectroscopic ellipsometry (SE) is an optical analysis technique used to determine the thickness, refractive index and relative permittivitiy of the thin films[162]. Typically, the SE technique relies on measuring the change of the polarization state of a light train passing through and interacting with the thin film sample. The polychromatic light is linearly polarized by a polarizer and is described by two orthogonal components in reference to the incidence plane: the s-polarized and p-polarized states (see Figure 2.17 a). The electric field of the s-polarized is perpendicular to the incidence plane while that of the p-polarized is coplanar. As the incident polarized light is reflected from materials, the polarization and intensity of the light are changed due to the interaction with the thin film. These changes depend on the thickness and the optical properties of the thin films. These changes are monitored with a rotating analyzer placed on the pathway of the reflected light as shown in Figure 2.16 c. After the reflected light passes though the rotating analyzer, the detector records the intensity change and phase shift between s- and p-polarized light. Compared to the incident and linearly polarized light, the reflected light is not linearly but elliptically polarized due to the distinct interaction of the p and s components with the thin film as show in Figure 2.16 a and b. The complex reflectance ratio (ρ) can be directly calculated from the amplitude ratio (Ψ) and the phase difference (Δ) according to the following equation:

$$\rho = \tan(\Psi) \times e^{i\Delta} \qquad (2.5)$$

Though the amplitude ratio (Ψ) and the phase difference (Δ) are experimentally measured, the optical constant of the thin film cannot be directly determined. Therefore, a modeling analysis using an iterative procedure (least-squares minimization) is performed. The unknown optical constants and/or thickness based on the applied model are varied and all ellipsometry parameters are calculated using the Fresnel equation. The experimental data are tested with match function against the model to provide the desired parameters. In the case of multilayer samples the model considers the optical constants and thickness parameters of all distinct layers, thus each layer has to be modeled individually. Although ellipsometry is suited for of thin surfaces in ranges from sub-nanometers to a few microns, some surfaces are still difficult to investigate. As an example, with films deposited on glass substrates, the reflection from the backside of the glass strongly interferes with the reflection from the surface.

In this PhD study, the film thicknesses were measured using an M-44 multiple wavelength ellipsometer from J. A. Woollam Co., Inc. (Lincoln, NE, USA) which was aligned at a fixed incident angle of 70° to the sample surface. An arc lamp with a high pressure Xe discharge point source operating in a wavelength range of 200–1000 nm was used. The data analysis was carried out using the modeling software WVASE^{TM} from J. A. Woollam Co. The SAMs and conditioning layer were modeled as a single Cauchy layer model with an estimated refractive index of 1.45.

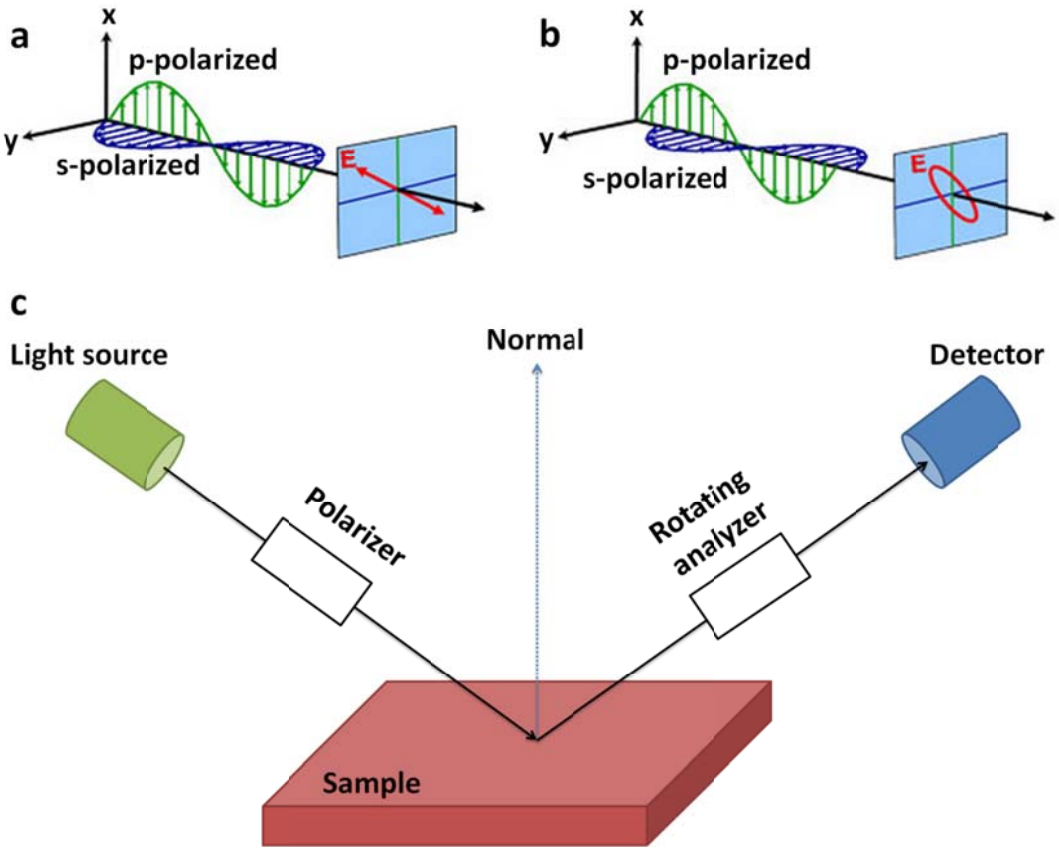

Figure 2.16. Working principle of spectroscopic ellipsometry. Decomposition of the electric field of a light wave into its two orthogonal components with the light wave being (a) linearly polarized and (b) elliptically polarized. (c) Schematic diagram showing a spectroscopic ellipsometry setup: A linearly polarized incident light (c) emitted from the light source and linearly polarized by a polarizer, is reflected by the sample and becomes elliptically polarized. This light is analyzed and detected to determine optical parameters and film thickness. (Figure a and b adapted from Ref.[163])

3 Materials and experiments

3.1 Materials

Gold substrates (100 nm Au/5 nm Ti evaporated on Si wafers) were purchased from Georg Albert–Physical Vapor Deposition (Silz, Germany).

16-mercaptohexadecanoic acid (MHDA, 99%), 11-mercapto-1-undecanol (MUD, 99%), copper (II) acetate hydrate (98%), copper(II) trifluoroacetate hydrate, zinc acetate dihydrate (≥98%), tetrakis(acetonitrile)copper(I) hexafluorophosphate ($Cu(I)(CH_3CN)_4PF_6$, 97%), copper(II) sulfate (≥99%), benzene-1,4-dicarboxylic acid (BDC, 98%), naphthalene-2,6-dicarboxylic acid (NDC, 99 %), Biphenyl-4,4′-dicarboxylic acid (BPDC, 97%), 2-aminoterephthalic acid (NH_2-BDC, 99%), 1,4-diazabicyclo[2.2.2]octane (Dabco,≥99%), phenylacetylene (98%), 2,2-Dimethoxy-2-phenylacetophenone (99%), α, α′-dibromo-o-xylene (97%), 1-ethynyl-4-pentylbenzene (97 %), Alkyne MegaStokes dye 673, Alkyne MegaStokes dye 608, ethanol (99.99%), methanol(≥ 99.9%), tetrahydrofuran (THF, ≥99.9%), *tert*-Butyl nitrite (90%), trimethylsilylazide (95%), ethyl acetate, acetic acid (100%), hydrochloride (37%, in water), hexane (≥95%), toluene (≥ 99.9%), dichloromethane (≥99.8) were obtained from Sigma-Aldrich and used without further purification.

3.2 Preparation of SAMs

Preparation of MHDA SAMs on gold substrate

The gold substrate was immersed for 48 h in a 20 μM MHDA solution (prepared by dissolution of MHDA in a 5% (v/v) acetic acid in ethanol solution), rinsed with pure ethanol, and then, gently dried under nitrogen flux to obtain the MHDA SAMs.

Preparation of MUD SAMs on gold substrate

The gold substrate was immersed for 24 h in a 1 mM MUD solution (prepared by dissolution of MUD in ethanol solution), rinsed with pure ethanol, and then, gently dried under nitrogen flux to obtain the MUD SAMs.

Preparation of patterned SAMs on gold substrate

Patterned SAMs were prepared using micro contact printing (μCp) technique. To obtain the SAMs on gold surface with different patterns, such as square, triangular, roundness and strip-type, an elastomeric polydimethylsiloxane (PDMS) stamp with corresponding pattern is need. To perform the preparation, the SAMs solution (MHDA or MUD) was dropped on the patterned PDMS stamp until

it fully covered the whole pattern on the stamp. And waiting 2 min allow the absorption of SAM molecule on the stamp surface. Then stamp was dried with nitrogen, gently pressed on the clean gold substrate for 2 min to obtain the patterned SAM on gold surface. Usually, this patterned SAMs modified substrate can be immersed into 1 mM 1-decanethiol ethanol solution for 5 min to block the non-patterned area with 1-decanethiol for receiving inert terminated groups around the patterned functional terminated groups (-OH or -COOH).

3.3 Compounds or molecules loading in SURMOFs

Loading Eu(bzac)$_3$bipy into trilayer SURMOF systems

The trilayer SURMOF systems (Cu-BDC+Cu-NDC+Cu-BPDC or Cu-BPDC+Cu-NDC+Cu-BDC) were first activated at 80 °C for 4 h. Then the sample was broken into two parts and the pieces were immediately immersed into a 0.1 mM hexane solution of Eu(bzac)$_3$bipy (bzac=1-benzoylacetone, bipy=2,2'-bipyridine) at 60 °C for 72 h. Finally, the pieces were removed from the solution, rinsed with pure hexane and then dried in a flow of N_2 before recording the SEM micrographs.

Loading methanol into SURMOFs

The loading of methanol was determined by gas-phase QCM using $Zn_2(N_3\text{-bdc})_2(dabco)$] SURMOFs grown on QCM gold substrates modified with a MUD SAM. The detail technique for the gas-phase loading experiment using QCM was introduced in the second chapter. Prior to the QCM measurements the SURMOF sample was activated at 60 °C for 4 h under a flow of pure nitrogen to remove any residual solvent hosted in MOFs. Before switching to the vessel containing methanol, pure nitrogen gas (carrier gas) was passed over the SURMOF sample to obtain a stable baseline. The adsorption curve was recorded at 25°C using a flow rate of 100 sccm.

Gas absorption and tuning defect sites in SURMOFs

The adsorption of CO or CO_2 gases in the UHM-3 MOF thin films were monitored using a specifically designed ultrahigh vacuum Fourier transform infrared (UHV-FTIR) apparatus (Prevac, Rogów, Poland), where a FTIR spectrometer (Bruker Vertex 80v, Bruker Optics, Ettlingen, Germany) is directly coupled to a UHV chamber. The X-ray photoelectron spectroscopy (XPS) measurements were carried out from the same UHV chamber by fitting it with a hemispherical electron energy analyzer (VG-Scienta R4000) and a non-monochromatic Al Kα X-ray source. Leaking valves allowed the dosing of CO and CO_2 gases into the chamber. The dosed amount was expressed in langmuirs (1 L is equivalent to an exposure of 10^{-6} mbar of a gas during 1 second). The temperature of the SURMOFs sample was controlled by type K thermocouple bound to the edge of sample support. Once a sample was placed in and the UHV

was set, annealing could be carried out in-situ by simply increasing the temperature to 320 K, 370 K, 420 K, 470 K, or 520 K, and heating continuously for 30 min. Thereafter, the sample was cooled down to a temperature of interest, if needed, gases were dosed in, and further measurements (XPS or IRRAS) were run. UHV was maintained at all times during these processes.

3.4 PSM of SURMOFs

PSM of $Zn_2(N_3\text{-bdc})_2(dabco)$] MOF thin films in volume and N_3-bdc surface-modified [$Zn_2(bdc)_2(dabco)$] MOF thin films on the surface with Cu(I)-catalyzed click chemistry.

The reaction solution was prepared by mixing 0.2 mL of phenylacetylene [0.1 mg of 1-ethynyl-4-pentylbenzene or 0.1 mg of Alkyne MegaStokes dye 673 for surface modification] and 5 mg of $Cu(I)(CH_3CN)_4PF_6$) into 4 mL of THF solvent under a nitrogen atmosphere. The bottles were sealed with covers to avoid contact with oxygen. The THF solvent was bubbled with nitrogen to remove residual oxygen in the solvent before adding the reactants. The solutions were then mixed in an ultrasonic bath for 5 min, and then the activated SURMOF sample was placed into the reaction solution under a nitrogen atmosphere. Finally, the bottles were sealed with covers again, and the reaction was carried out under continuous stirring at room temperature. After reaction, the sample was rinsed with pure THF and dichloromethane to remove residual reactants or catalyst and then dried in nitrogen gas. To monitor the reaction, the sample was taken out from the solution for the infrared reflection absorption spectroscopy (IRRAS) and X-ray diffraction (XRD) measurements at time intervals of 1 h. The reaction was continued afterward with the same sample.

PSM of $Zn_2(N_3\text{-bdc})_2(dabco)$] MOF thin films with Cu-free click chemistry.

The activated SURMOF samples were first immersed into THF, and then the surface functionalization was initiated by adding 1 mg of cyclooctyne derivative (either compound 1 or 2) under continuous stirring. The reaction was carried out at room temperature. After the reaction, the sample was rinsed with pure THF and dichloromethane to remove residual reactants and finally dried using nitrogen gas. To monitor the reaction, the sample was taken out for IRRAS and XRD measurements every 30 min.

PSM of patterned $Zn_2(N_3\text{-BPDC})_2(dabco)$] SURMOFs with dye molecule using Cu-free click chemistry.

The new-synthesized patterned SURMOF [$Zn(N_3\text{-BPDC})_2(Dabco)$] was firstly activated at 80 °C for 4 h to remove the solvent remove residual solvent from the SURMOF pores. And then the activated sample was soaking in a toluene solution of Alkyne MegaStokes dye 608 (0.01 mM)

for 30 min at 60 °C. After the reaction, the sample was rinsed with pure toluene and dichloromethane to remove residual reactants and finally dried under a nitrogen stream.

Cu(I) catalyzed alkyne–azide cycloaddition controlled by photoinitiated Cu(II) reduction.

The new-synthesized SURMOF [$Zn_2(N_3\text{-BPDC})_2$(Dabco)] was firstly activated at 80 °C for 4 h to remove residual solvent. Then the sample was placed on the UV-light irradiation table. A THF solution of copper(II) sulfate, photoinitiator (2,2-Dimethoxy-2-phenylacetophenone), and alkyne terminated molecules (Alkyne MegaStokes dye 673) was deposited drop-wise on the surface of the activated SURMOF sample and covered with a quartz glass lid to avoid oxygen. A photomask on the lid allowed controlling the area exposed to light. Thereafter, the sample was exposed to UV irradiation, then rinsed with THF and dichloromethane to remove residual reactants, and finally dried under a nitrogen stream.

Patterned decomposition of azide groups using photo-lithography and their PSM.

The freshly synthesized SURMOF [Cu(N_3-BPDC)] were activated at 80 °C for 4 h to remove the residual solvent from the SURMOF pores. A photomask was directly position on the top of the MOF surface and then were exposed to UV light irradiation at room temperature under atmospheric conditions. With regard to the PSM, the patterned irradiated SURMOFs were soaked in a toluene or THF solution of Alkyne MegaStokes dye 608 (0.01 mM) for 30 min at 60 °C. After the reaction, the sample was rinsed with pure toluene and dichloromethane to remove residual reactants and finally dried under a nitrogen stream.

Photo-induced thiol-yne click chemistry.

Likewise, the new-synthesized SURMOF [Zn_2(alkyne-BPDC)$_2$(Dabco)] was firstly activated at 80 °C for 4 h and placed on the irradiation table. A ethanol solution of photoinitiator (2,2-dimethoxy-2-phenylacetophenone) and thiol terminated molecules (anthracene-2-thiol) was deposited drop wise on its surface , and covered with a quartz glass lid. After irradiation, ethanol and dichloromethane were also used to rinse the sample of residual reactants. Finally, the samples were dried under a nitrogen stream.

Layers-selected PSM of six-layers SURMOF systems.

The freshly synthesized six-layers SURMOF systems (Cu-N_3BPDC+Cu-BPDC+Cu-N_3BPDC+Cu-BPDC+ Cu-N_3BPDC+Cu-BPDC) were firstly activated at 80 °C for 4 h. Then the sample was broken into two pieces which were immediately immersed into solution of iodine reactant (methyl 2-((2-(1-fluorocyclooct-2-yn-1-yl)-2-oxoethyl)amino)-3-(4-hydroxy-3-iodophenyl)propanoate) in toluene for 24 h at 60 °C. Thereafter, the pieces were recovered, rinsed with pure toluene, and then dried under a nitrogen stream before the SEM micrographs were recorded.

3.5 Theoretical calculation

Theoretical model of the Cu-BDC and Cu-NDC interface.

These theoretical calculations were contributed by, Prof. Thomas Heine and Dr. Binit Lukose from Jacobs University Bremen.

The Cu-BDC and Cu-NDC interface has been modeled by investigating a supercell incorporating 5 times NDC and 6 BDC linkers along the interface, accounting to an interface length of 6.7 nm. Two layers are on top and below the interface, where the outer atoms are fully saturated using carboxylate group. Only one SURMOF layer (perpendicular to the growth layer) has been modeled. All geometries have been fully optimized using the density-functional based tight-binding method (DFTB)[164-166]. The strain energy has been evaluated using the same method, by taking the structural units separately, saturating and relaxing them. The total strain energy of the Cu-NDC strip accounts to 0.22 eV/nm, the Cu-BDC strip is slightly stronger strained with 0.29 eV/nm, and finally the bridging linkers contribute with 0.17 eV/nm, thus adding up to a total strain of 0.68 eV/nm.

DFT calculations of perfect and defective UHM-3 with CO and CO_2.

These theoretical calculations were contributed by Prof. Thomas Heine, Dr. Andreas Mavrantonakis and Dr. Barbara Supronowicz from Jacobs University Bremen.

Density Functional Theory (DFT) calculations were performed on two molecular clusters resembling the pristine and defect structure. In order to reduce the complexity of the system, instead of the fairly large dmsdip linkers the smaller BTC units were used. The cluster contained a dicopper moiety along with four ($Cu(BTC)_4$) or three ($Cu_2(BTC)_3$) benzene tricarboxylate linkers for the pristine or defect case, respectively. The distant (i.e. not bound to the dicopper unit) carboxylate groups were saturated with lithium cations instead of protons. In this way, the two oxygen atoms of a distant carboxylate group are equivalent, whereas in the case of a proton saturation, two nonequivalent oxygen atoms would be generated. The pristine dicopper paddlewheel was always modeled in the high spin triplet spin state, with an unpaired electron per copper atom, whereas the defect paddlewheel was in the doublet spin state. This treatment have also been used in our previous work on CO adsorption on defect sites of HKUST-1 [147]. The models used in the present study are displayed in Figure 3.1. The B3LYP [167, 168] hybrid functional was applied in combination with the 6-311G(d) basis set for the non-metal atoms and the LANL2TZ(f) for the copper along with the appropriate effective core potentials. London dispersion interactions were treated classically by Grimme's approach (denoted as DFT-D3) [169]. The geometry optimizations were carried out using tight convergence criteria to obtain the minimum energy structures for the empty and CO/CO_2 loaded pristine and defect paddlewheels. Subsequently, the loaded structures were all verified to be minima on the potential energy surface by performing a harmonic analysis. Due to the large size of the systems, only partial frequencies of the

guest molecules were computed. The binding energies were determined using the following expression: BE = E(MOF…guest) – E(MOF) – E(guest). Zero Point Energies (ZPEs) were always included. The interaction energies were always corrected for the Basis Set Superposition Error (BSSE) by applying the Counterpoise (CP) method [170]. For the bonding analysis, we used the method of Weinhold [171] to calculate the natural bond orbitals (NBO) and the charges based on the natural population analysis (NPA). All calculations were performed with the Gaussian 09 program suite (Gaussian 09, Revision D.01, Gaussian Inc., Wallingford CT, 2009).

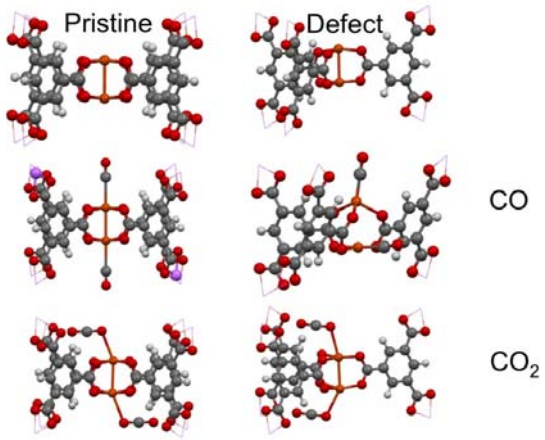

Figure 3.1: Cluster models of perfect and defective UHM-3 and their complexes with CO and CO_2.

4 Results

4.1 Multi-heteroepitaxial growth of SURMOF-2 series

4.1.1 Background

The countless number of different MOF types resulting from the combination of metal or metal-oxo connectors with organic linkers can be extended further by employing heteroepitaxy. Growing different types of MOFs in a sequential fashion[172-175] allows entering the next level of complexity. Of particular interest here is the stacking of MOFs with different lattice constants for some smart applications. For example in sensorics, it may be required to have a first layer of MOFs with pore sizes sufficiently large to accommodate nanoobjects such as proteins[52] or metal-nanoparticles. An additional topping layer with smaller pore size could then serve as a filter to reduce cross-talk in MOF-based sensors.[176] However, a combination of MOF materials with different lattice constants is a major challenge, because the heteroepitaxy of conventional materials requires lattice constant matching, that is, the lattice constant of the material to be grown must match that of the templating substrate. Particularly important is the case of metal-on-semiconductor epitaxy, where sophisticated strategies are used to overcome the restrictions imposed by the fact that the second material must match the lattice constant of the first material by better than 2 %.[177]

Here, we show the epitaxial growth of different MOF types with lattice constant mismatches as large as 20 %. The experiments were carried out by using the structure platform provided by SURMOF-2, an isoreticular class of metal organic frameworks described in previous work.[53] SURMOF-2 is synthesized from Cu-acetate and dicarboxylic acids using LPE method,[53] and the crystal structures of the compounds used in this study are shown in Figure 4.1. For better understanding of this heteroepitaxial growth, a collaboration with the theoretical chemistry group of Prof. Thomas Heine and Dr. Binit Lukose was initiated and the quantum chemical calculations were used to determine the related interface energy penalty and the theoretical results demonstrated that the intrinsic elasticity of MOFs helps to yield epitaxial growth also in case of strongly different lattice constants.

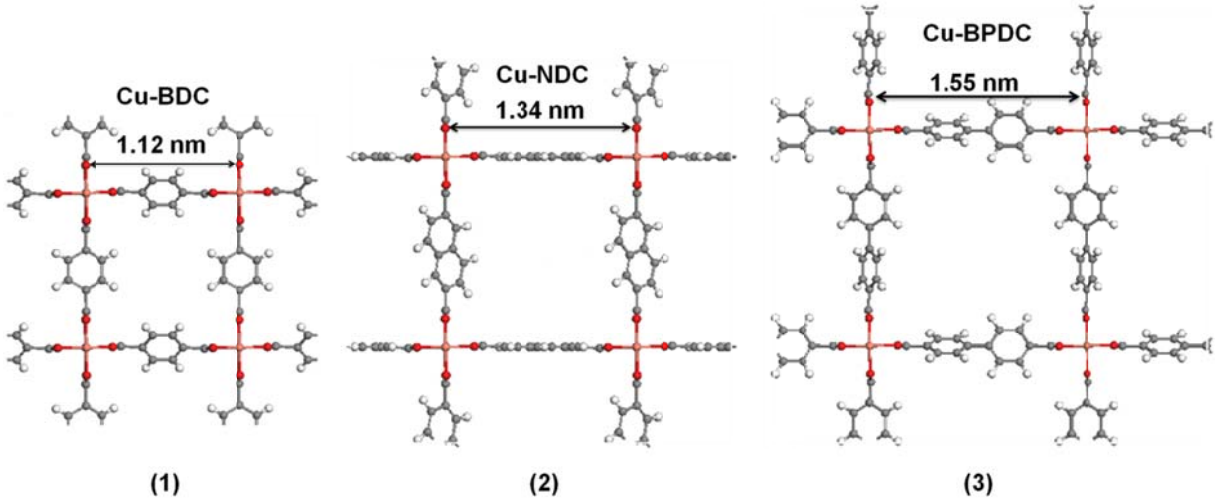

Figure 4.1: Structure of the SURMOF-2 used in the present study: (1) Cu-BDC (BDC: benzene-1,4-dicarboxylic acid) with a lattice-constant of 1.12 nm. (2) Cu-NDC (NDC: naphthalene-2,6-dicarboxylic acid) with a lattice-constant of 1.34 nm. (3) Cu-BPDC (BPDC: biphenyl-4,4'-dicarboxylic acid) with a lattice-constant of 1.55 nm.

4.1.2 Heteroepitaxial growth of SURMOFs

The heteroepitaxial growth of SURMOF-2 series was carried out by using spray method as shown in the first chapter (1.2.2.2). The gold substrates with MHDA SAMs prepared according to the process in the third chapter (3.2) were placed on the sample holder and subsequently sprayed with a 1mM of metal sources ethanol solution for 10 seconds and then with a 0.2 mM of organic ligand ethanol solution for 20 seconds at room temperature. Between each step the substrates were rinsed with ethanol to remove the under-coordination ligands or metal connectors and repeated the steps above in order to grow thicker MOF layers. In order to investigate the importance of lattice mismatch in MOF-on-MOF heteroepitaxy, here we keep the same metal connector (Cu-paddle wheel) but used different organic linkers, resulting in changing the lattice constant of the MOF thin films for yielding hierarchically organized MOF multilayer systems. In a first set of experiments, an initial MOF-layer has been grown from BPDC ligand and Cu-acetate. As evidenced by the out-of-plane [Figure 4.2 (1), green curve] and in-plane [Figure 4.2 (3), green curve] X-ray diffractograms, this process yields a crystalline, highly oriented SURMOF-2 with a lattice-constant of 1.55 nm. The out-of-plane XRD data reveals the crystallinity perpendicular to the substrate surface. The fact that only the $(001)_C$ and $(002)_C$ diffraction peaks are seen, demonstrates the orientated nature of the SURMOFs. After 10 deposition cycles, the long BPDC linker was replaced by the shorter NDC linker. No change was made to the metal connector. As evidenced by the X-ray diffractograms (peaks labeled $(001)_B$ and $(002)_B$) shown in Figure 4.2, after another 10 deposition cycles with the shorter NDC ligand,

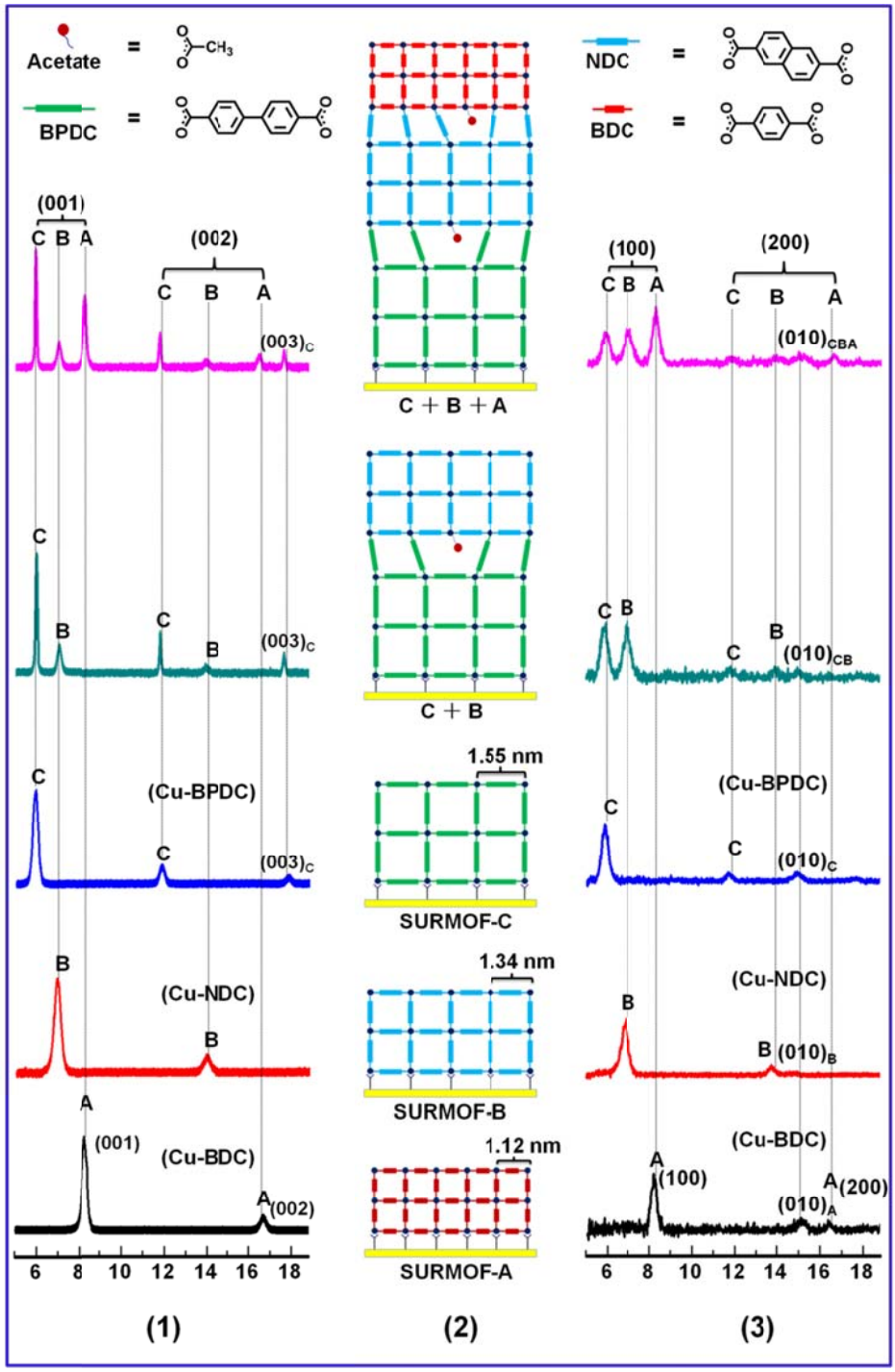

Figure 4.2: (2) Schematic illustration of the construction of hierarchically porous MOF crystal films (Cu-BPDC + Cu-NDC + Cu-BDC) with large lattice mismatches grown on self-assembled monolayer (SAM) modified Au-substrates by using layer-by-layer LPE method (Dark blue circles represent metal connectors). (1) Out-of-plane XRD data recorded for the SURMOFs depicted on (2). (3) In-plane XRD data recorded for the SURMOFs depicted (2).

a second MOF layer with a smaller lattice constant of 1.34 nm was formed on the first one. A comparison to the XRD-data recorded for the corresponding SURMOFs made directly using Cu-acetate and NDC reveals that the structures are identical. Note, the XRD peaks located at 5.9° demonstrate that the initial SURMOF layer is still present. In the next step, an even shorter ligand, BDC (benzene-1,4-dicarboxylic acid), was used. Again, the XRD data (peaks labeled $(001)_A$ and $(002)_A$) shown in Figure 4.2 (black curve, out-of-plane) and Figure 4.2 (black curve, in-plane) demonstrate that a third type of MOFs with the same orientation but with a lattice-constant decrease to 1.12 nm has been grown on the supporting substrate (Cu-NDC).

In order to demonstrate that the constraint of lattice matching is virtually nonexistent for this reticular class of MOFs, we have instead of stepwise decreasing the lattice constant as in the example presented above also realized the opposite scenario of increasing lattice constants. To perform the experiment, we started here first with an initial layer of Cu-BDC (with a pore-size of 1.12 nm) and then continued to deposit Cu-NDC and finally Cu-BPDC, thus increasing the pore-sizes to 1.34 nm (NDC) and finally 1.55 nm (BPDC). The resulting scenario is shown in the schematic illustration displayed in Figure 4.3 (2). As confirmed by the out-of-plane [Figure 4.3 (1)] and in-plane [Figure 4.3 (3)] X-ray diffractograms, also for this case of increasing lattice constants the heteroepitaxial growth proceeds without difficulties despite the rather pronounced lattice mismatch.

Additionally, an analysis of the peaks-widths in the out-plane XRD-data (Figure 4.2 (1) and 4.3 (1)) using the Debye-Scherrer equation yields average domain sizes of 35 nm for MOF-A, 31 nm for MOF-B and 52 nm for MOF-C in the case of A+B+C systems and 37 nm for MOF-A, 36 nm for MOF-B and 96 nm for MOF-C in the case of C+B+A systems. For the in-plane XRD-data (Figure 4.2 (3) and 4.3 (3)), it yields average domain sizes of 60 nm for MOF-A, 40 nm for MOF-B and 25 nm for MOF-C in the case of A+B+C systems and 36 nm for MOF-A, 33 nm for MOF-B and 52 nm for MOF-C in the case of C+B+A systems.

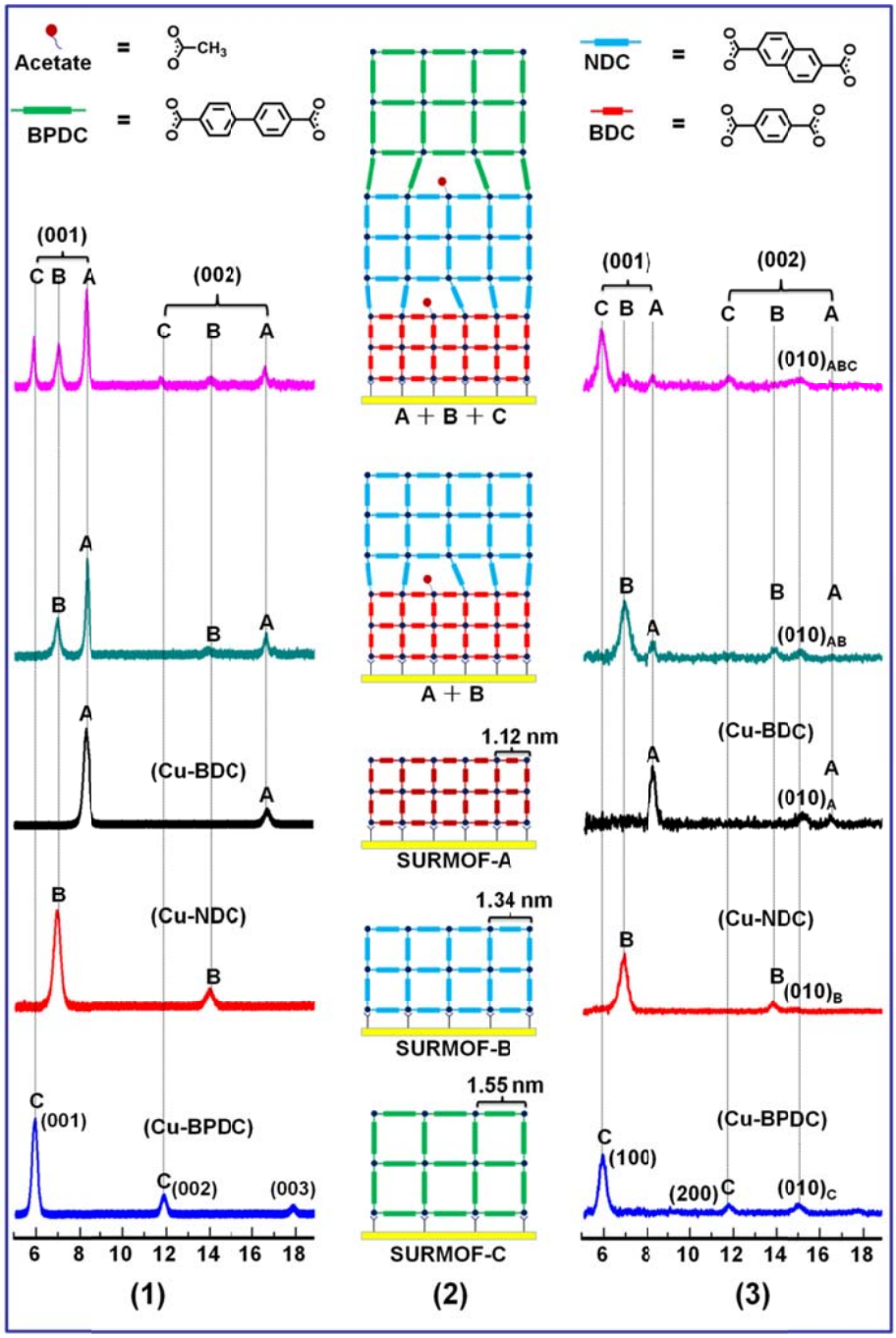

Figure 4.3: (2) Schematic illustration of the construction of hierarchically porous MOF crystal films (Cu-BDC + Cu-NDC + Cu-BPDC) with large lattice mismatches grown on self-assembled monolayer (SAM) modified Au-substrates by using layer-by-layer LPE method (Dark blue circles represent metal connectors). (1) Out-of-plane XRD data recorded for the SURMOFs depicted on (2). (3) In-plane XRD data recorded for the SURMOFs depicted (2).

4.1.3 Size-selected loading of nano-particles in SURMOFs

The well-defined multilayer structure of the trilayer synthesized above is directly demonstrated by the SEM micrographs shown in Figure 4.4 A (Cu-BPDC + Cu-NDC + Cu-BDC) and Figure 4.5 A (Cu-BDC + Cu-NDC + Cu-BPDC). Whereas the cross sections of the hierarchically porous MOF crystal films in the both cases reveal only little contrast, selective staining[178, 179] can

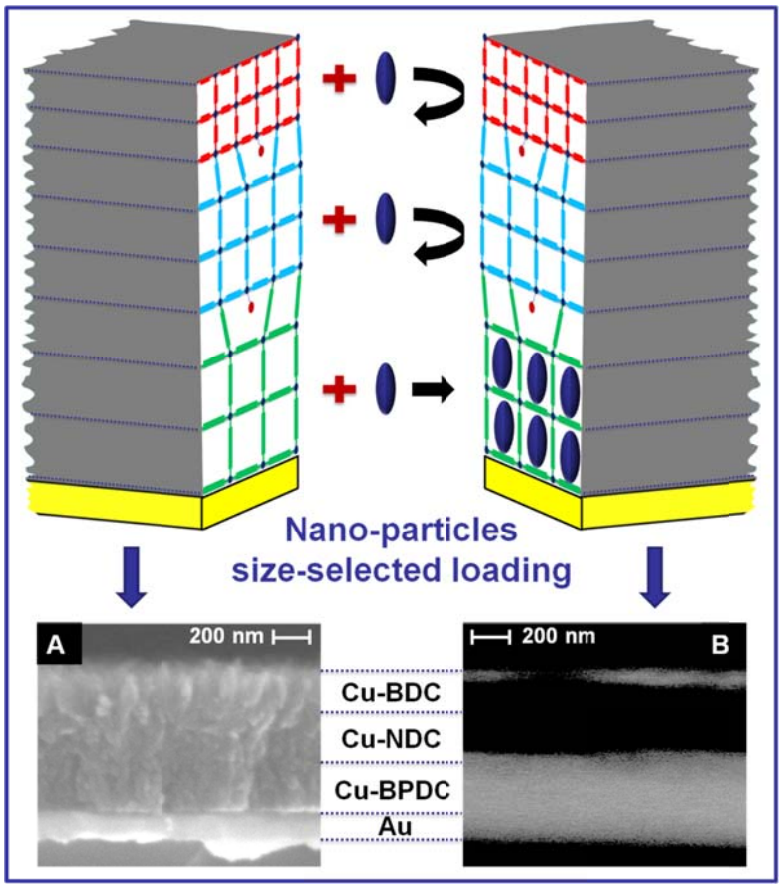

Figure 4.4: (Top) Schematic of nano-particles size-selected loading in hierarchically porous SURMOFs; (Down) (A) SEM image recorded for a hierarchically porous SURMOF (Cu-BPDC + Cu-NDC + Cu-BDC) with coating 5 nm gold films on the surface; (B) SEM image recorded for a hierarchically porous SURMOF (Cu-BPDC + Cu-NDC + Cu-BDC) after loading $Eu(bzac)_3bipy$ (bzac=1-benzoylacetone, bipy=2,2'-bipyridine) compound without coating gold films on the surface.

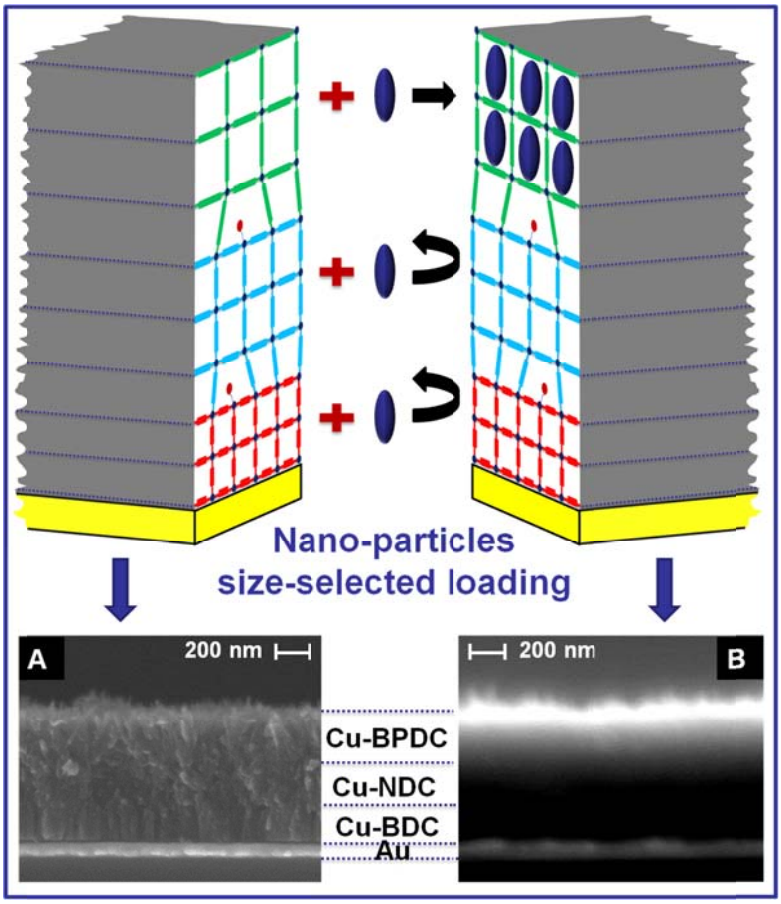

Figure 4.5: (Top) Schematic of nano-particles size-selected loading in hierarchically porous SURMOFs; (Down) (A) SEM image recorded for a hierarchically porous SURMOF (Cu-BDC + Cu-NDC + Cu-BPDC) with coating 5 nm gold films on the surface; (B) SEM image recorded for a hierarchically porous SURMOF (Cu-BDC + Cu-NDC + Cu-BPDC) after loading Eu(bzac)$_3$bipy (bzac=1-benzoylacetone, bipy=2,2'-bipyridine) compound without coating gold films on the surface.

be designed to make the different porosities of the adlayers visible by loading the heavy metal-nanopartcile into the big pore of the trilayer, as shown in the schematic in Figure 4.4 and 4.5, since the heavy metal backscatter electron more strongly and then present bright in the image when using SEM with detection of backscattered electrons. Here, a metal-organic compound, Eu(bzac)$_3$bipy (bzac = 1-benzoylacetone, bipy = 2,2′-bipyridine), was chose for the staining or loading experiment, since it can only fit into the layer of Cu-BPDC when comparing the particle size to the pore sizes of the trilayer (see Figure 4.6 top). To perform this experiment, both of the

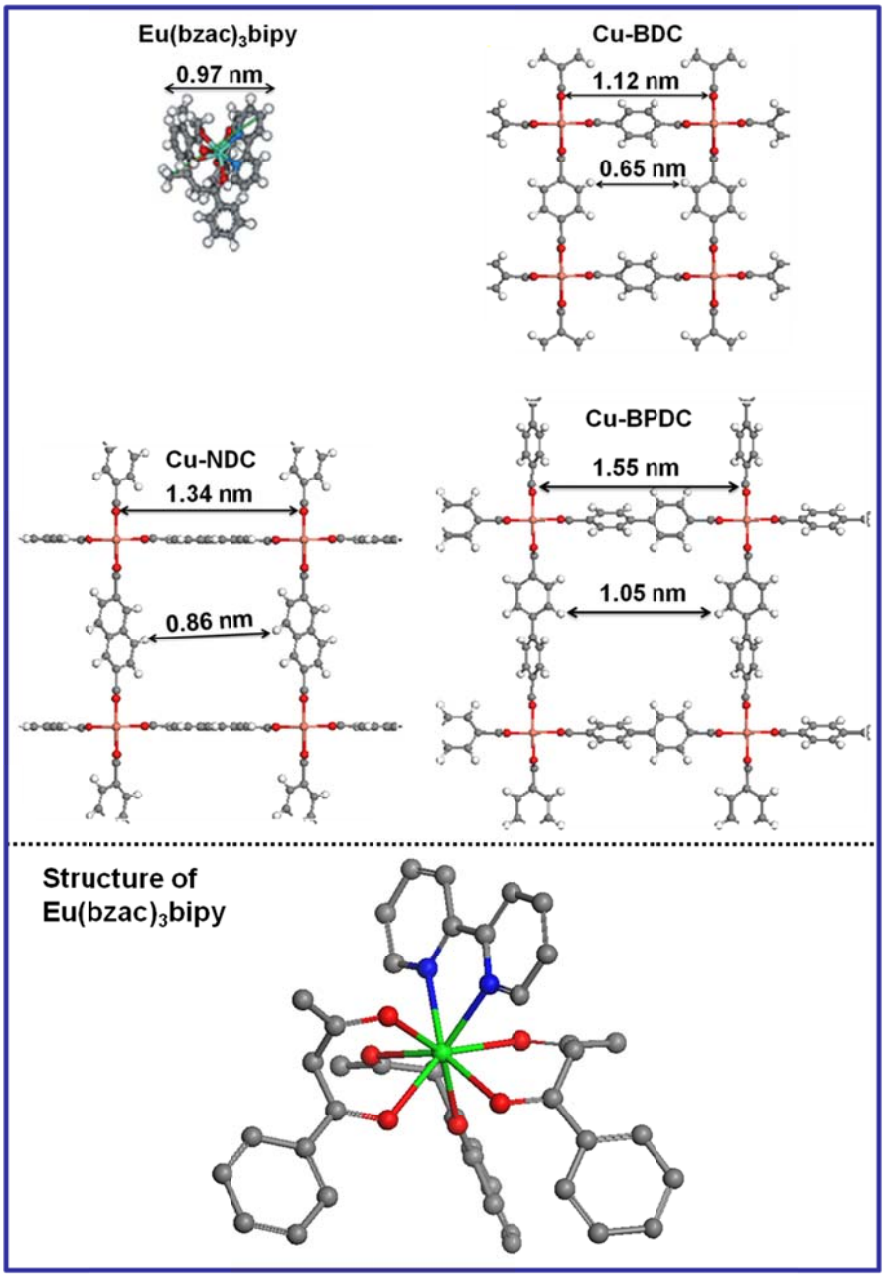

Figure 4.6: (Top) A comparison of the size of Eu(bzac)$_3$bipy with the size of the channels in Cu-BDC, Cu-NDC and Cu-BPDC. (Down) The structure of Eu(bzac)$_3$bipy.

samples shown in Figure 4.4A and 4.5A were firstly activated at 80 ^{o}C for 4 hours to remove the ethanol solvent or water absorbed in the pore. Then the sample was broken into two parts and the pieces were immediately immersed into a 0.1 mM hexane solution of Eu(bzac)$_3$bipy at 60 °C for 72 h. Finally the samples were taken out from the solution and rinsing with pure hexane to remove the week-absorbed Eu(bzac)$_3$bipy on the sample surface. The SEM images with detection of backscattered electrons for both cases of the samples were recorded on Figure 4.4 B

and 4.5 B. As expected, the Cu-BPDC-layer (thickness ~250 nm) in both cases can be clearly identified. Noteworthily, the very effective spray-process[100] used here yields a thickness of ~250 nm with only 10 cycles.

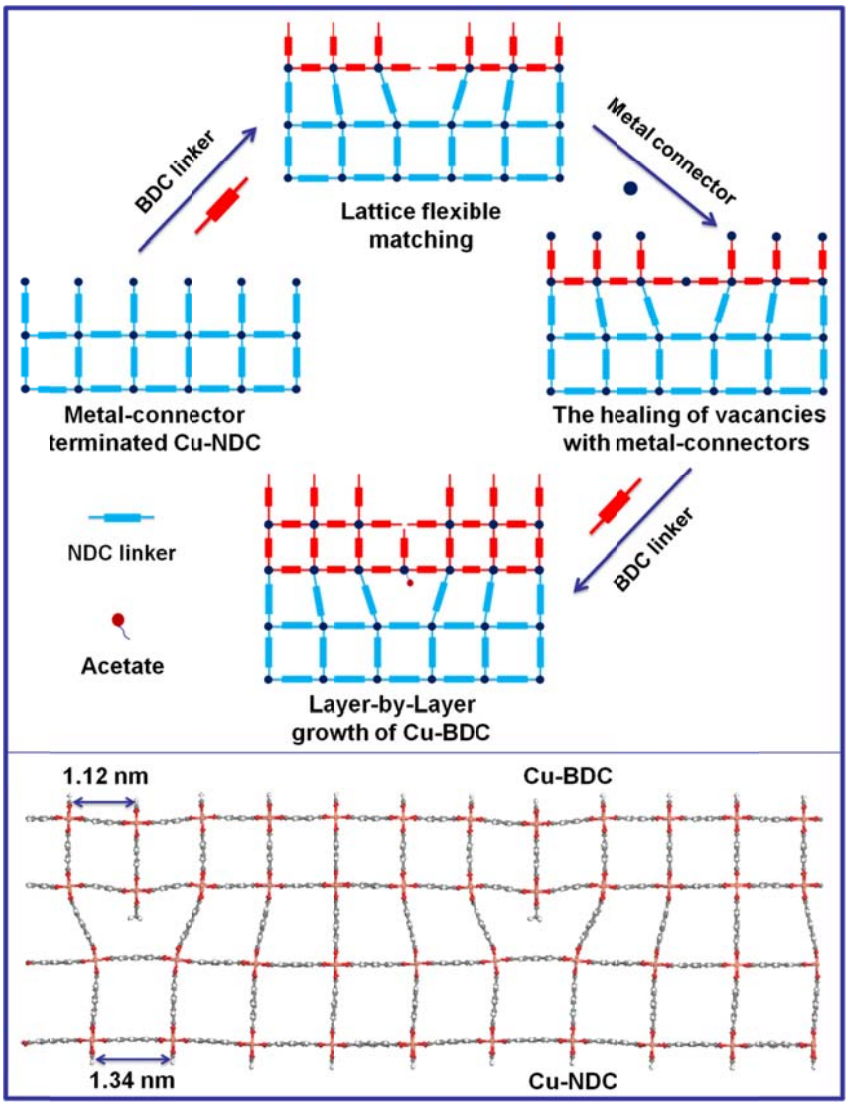

Figure 4.7: (top) Schematic illustration of the formation of flexible lattice matching junction in MOF-on-MOF epitaxy. (bottom) Molecular arrangement as obtained from the quantum chemical calculations (see text) for the heterojunction between Cu-BDC and Cu-NDC.

4.1.4 Theoretical model

To better understand why for the MOF-on-MOF heteroepitaxy the lattice matching requirement appears to be less stringent than for other cases of heteroepitaxy, an extensive set of quantum chemical calculations (Contributed by Prof. Thomas Heine and Dr. Binit Lukose) were carried

out for the hetero-junction between Cu-BDC and Cu-NDC. The method used here is an approximate variant of density functional theory (DFT), London dispersion-corrected self-consistent charge density-functional based tight-binding (DFTB)[164-166]. The extra energy needed

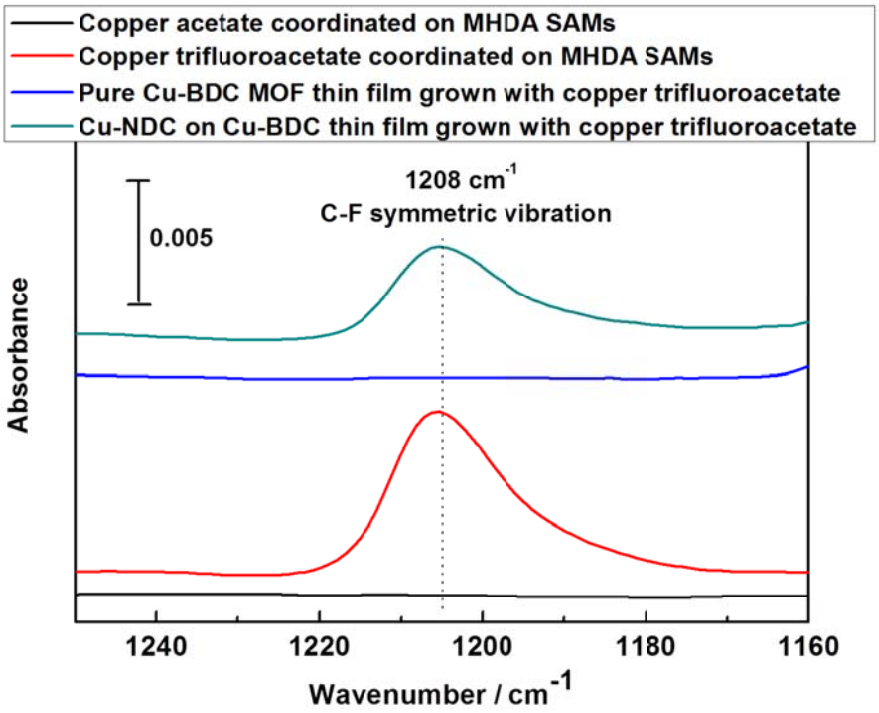

Figure 4.8: IRRAS data demonstrating of the presence of acetate groups at hetero-junctions in SURMOFs.

for creating a heterojunction between Cu-BDC and Cu-NDC lattices was obtained by placing six unit cells of Cu-BDC on top of five unit cells of Cu-NDC (see Figure 4.7). The lattice constants of Cu-NDC and Cu-BDC amount to 1.34 and 1.12 nm, respectively. The corresponding ratio, 1.20 (1.34/1.12), is sufficiently close to 5/6 = 0.997 [(1.34*5)/(1.12*6)]. To warrant the applicability of the 5-on-6 model for the heterojunction, the 5-on-6 matching leaves one undercoordinated (only three instead of four linkers attached) paddle wheel on the Cu-BDC/Cu-NDC interface (see Figure 4.7 top, dotted blue circle). This vacancy was annihilated by attaching an acetate group. This is a rather plausible way to saturate this unsatisfied valence since the $(Cu^{++})_2$ dimers are provided in the form of Cu-acetate during the growth process. To support this hypothesis, an additional experiment was designed by using the copper trifluoroacetate instead of copper acetate during the synthesis, the IRRAS results was displayed in Figure 4.8, the adsorption band at 1208 cm^{-1} is assigned to the CF_3 symmetric vibration. The obtained results clearly demonstrate the presence of a substantial amount of PAc in the hetero-SURMOFs, as expected from the model for the heterojunction described in the text, since the absorption peak of

CF_3 vibration can be observed from the hetero-SURMOFs (Cu-BDC+Cu-NDC), but not from a homogenous Cu-BDC SURMOFs. Therefore, using the geometry indicated in the upper part of Figure 4.7 as starting point, a geometry optimization was carried out for a model with a thickness of one layer on each side of the heterojunction. The resulting geometry is shown in Figure 4.7 (bottom), which demonstrates that the lattice distortion imposed by this rather large lattice mismatch is confined to the immediate vicinity of the junction.

There is a significant difference between the interface of the heterojunction between two MOF phases, exemplified for the Cu-BDC-on-Cu-NDC MOFs, and typical interfaces between covalently bound materials, as for example semiconductors. In the latter case, unsatisfied valences result in the formation of dangling bonds, leading to a severe energy penalty and also a chemical instability resulting from the pronounced chemical reactivity of dangling bonds. In case of metal−organic frameworks, because of the large pore size enough space is available to annihilate such vacancies by attaching a smaller chemical functionality in this case an acetate group instead of the large organic linkers (BDC, NDC, or BPDC) used to build the MOF framework. As a result, all valences at the MOF/MOF heterointerface can be fully satisfied, and the only contributions to the energy penalty resulting from the lattice mismatch come from excess strain. The strain energy, that is, the summation of the deformation energy of all connectors and linkers compared to the pristine MOF lattice, accounts to a total of 0.68 eV per nm interface length, normalized for one layer. This is significantly less than the energy of a typical covalent bond, which amounts to 3 eV or more. Moreover, the strain is delocalized over a rather large area, allowing for little local stress.

The relatively low lattice deformation energy that is necessary to form the heteroepitactic interface can be understood in terms of the very small elastic constants that are present in MOFs. For SURMOF-2 we obtain, within DFTB values for the bulk modulus of B = 37.4 GPa for SURMOF-2 (BDC) and of B = 22.1 GPa for MOF-2 (NDC). These values are similar to those of other MOFs (B = 34.7, 15.34, 10.10, and 10.73 GPa for HKUST-1, MOF-5, −177, and DUT-6 (MOF-205) within DFTB.[165] This elastic constant is about one order of magnitude lower than those of normal inorganic solids such as silicon or III−V semiconductors.[180]

4.1.5 Summary

we have demonstrated in this study that the idealized, highly crystalline, oriented hierarchically porous MOF crystal structure, Cu-BPDC/Cu-NDC/Cu-BDC and Cu-BDC/Cu-NDC/Cu-BPDC, with large lattice mismatches of 19.6 and 15.7% for which a synthesis using the conventional route is either difficult or impossible, can be readily prepared by using a liquid phase epitaxy scheme involving a layer-by-layer deposition on a templating organic surface. Such unusually strong lattice mismatches are possible as no chemical bond defect is introduced to the structure,

and the associated stress is distributed over a large volume. The availability of MOF coatings with vertical pore size gradients opens up the possibility to use them in multilevel filtering systems or in MOF-based sensors.[181]

This chapter is based on a publication in Nano Letters in February 2014[182] and the quantum chemical calculations were contributed by Dr. Binit Lukose and Prof. Thomas Heine from Jacobs University Bremen.

4.2 Liquid-phase epitaxial growth of azido-based SURMOFs and their post-synthetic modification

4.2.1 Background

An enormous number of topologically equivalent MOFs with very similar unit cells but differently functionalized linkers have been realized in the past. Although, in most cases, the linker functionalization does not affect MOF growth, there are exceptions where the new function interferes with the MOF forming process and a direct growth cannot be observed.[55, 131, 141, 183] For these cases, the so-called post-synthetic modification (PSM) offers an alternative, because the addition of the target function is carried out after the MOF lattice is formed. In the past few years, numerous studies have shown that bulk MOFs built from organic linkers exhibiting functional groups, such as $-NH_2$, $-OH$, $-NO_2$, and $-N_3$, are well-suited for the PSM process.[55, 131, 141, 183] In a number of works, it has been demonstrated that PSM is particularly attractive in the context of providing a platform material that can then be functionalized to optimize certain properties, e.g., in the context of sensors,[184] semiconductors,[185] and molecular sieves.[186]

Among the different approaches to PSM, a coupling via click chemistry, the copper(I)-catalyzed azide-alkyne Huisgen 1,3-dipolar cycloaddition (CuAAC),[187] is particularly appealing because the reaction can be carried out with high yields under mild conditions.[137, 188-191] Although the method has been very successful for the PSM of MOFs, it does exhibit a few disadvantages. In particular with regard to biological applications,[192-195] the necessity to use a Cu(I) catalyst is a drawback, because some of the Cu(I) metal ions will remain in the converted MOF and a thorough cleaning is necessary for the applications where the cytotoxic metal ions are unwanted. In addition, typically, the total conversion yield in click-chemistry based PSM of MOFs is substantially lower than 100%. The remaining azide groups may hinder more advanced applications of surface-anchored MOF (SURMOF) thin films, e.g., in the context of proton transport pathways in fuel cells.[196] Recently, a strain-promoted metal-free click reaction, azide-alkyne cycloaddition (SPAAC), has been developed to solve these problems.[197-199] However,

only very few applications have been found in the context of bulk (powder) MOF PSM[199] and the application of SPAAC to MOF thin films has not yet been reported.

In this study, an azido-based layer-pillar SURMOF [$Zn_2(N_3\text{-bdc})_2$(dabco)] (N_3-bdc: 2-azidoterephthalic acid; dabco: 1,4-diazabicyclo[2.2.2]octane) was used as a platform for the investigation of PSM employing both CuAAC and SPAAC click chemistry. The MOF structure is shown in Figure 4.9a. Both reactions were monitored using infrared reflection absorption spectroscopy (IRRAS) and surface X-ray diffraction (out-of-plane and in-plane XRD). The reaction dynamics of these two types of azide-alkyne click reactions were also demonstrated.

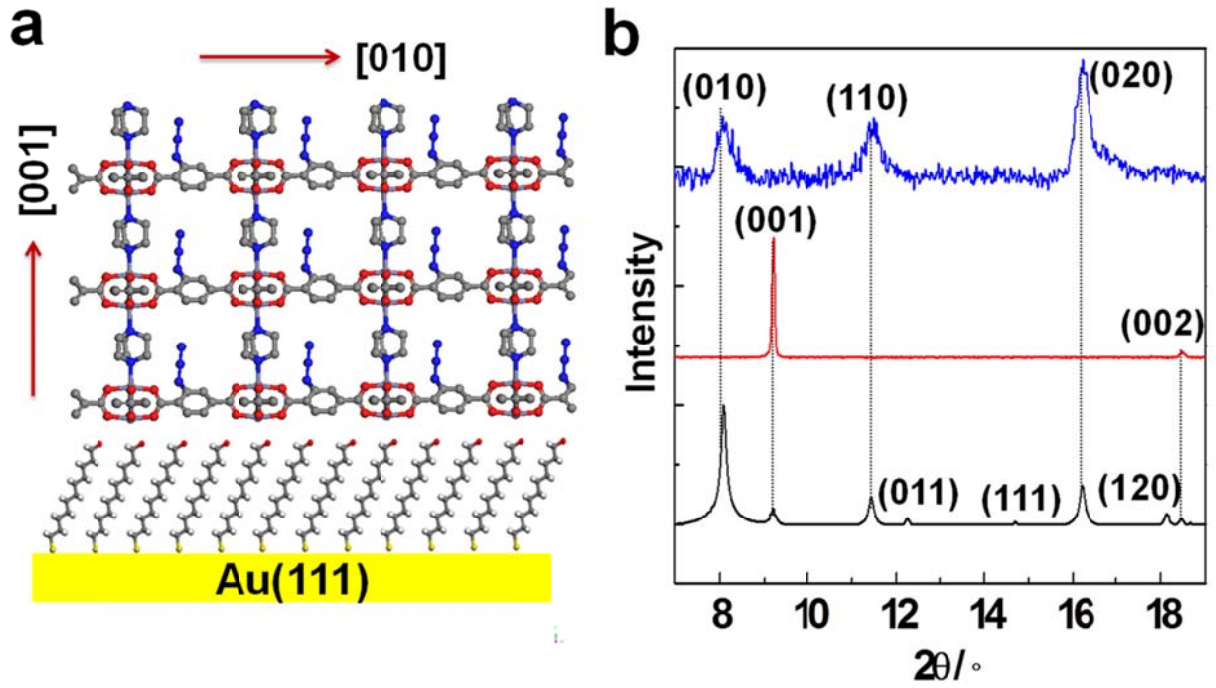

Figure 4.9: a) Schematic structure of a $Zn_2(N_3\text{-bdc})_2$dabco SURMOFs grown on a MUD-SAM; b) X-ray diffraction patterns recorded for $Zn_2(N_3\text{-bdc})_2$dabco SURMOFs on MUD-SAM: calculated XRD pattern for $Zn_2(N_3\text{-bdc})_2$dabco with bulk structure (black), experimental XRD data recorded in out-of-plane (red) and in-plane (blue) scattering geometry.

4.2.2 Characterization of SURMOF [$Zn_2(N_3\text{-bdc})_2$(dabco)]

SURMOF [$Zn_2(N_3\text{-bdc})_2$(dabco)] were deposited on a MUD-SAM modified gold substrate using pump method as shown in the first chapter (1.2.2.3). The modified substrate was sequentially exposed in zinc acetate solution for 15 min and then in N_3-bdc/dabco solution for 30 min. Each immersion step was followed by a rinsing step (4 min) with pure ethanol to remove residual reactants. The repetition of these steps allowed growing thicker MOF films. In this study, 40 growth cycles were used and XRD was carried out to character the structure of synthesized MOF

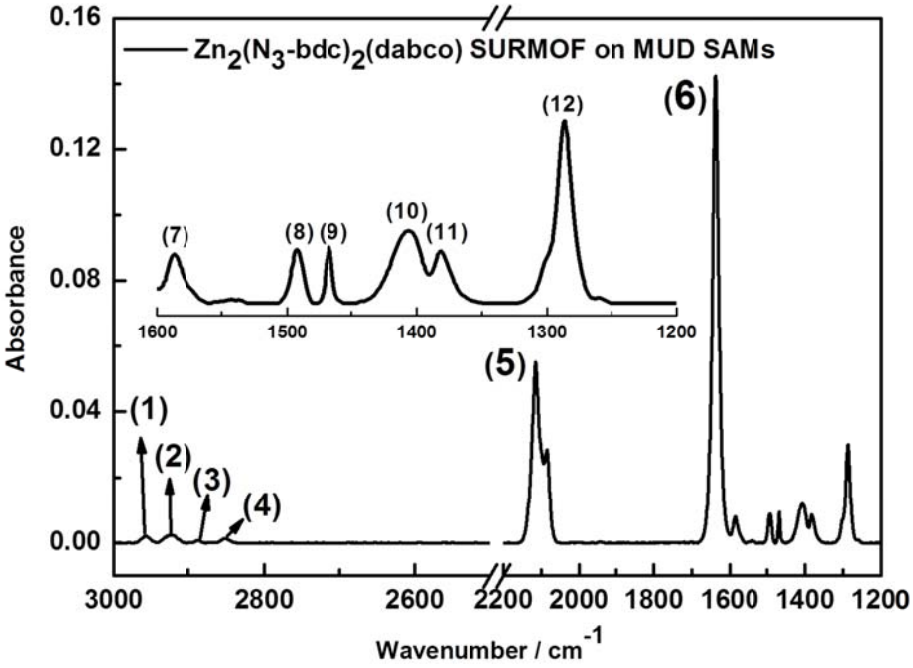

Figure 4.10: IRR spectra recorded for a 40 cycles [$Zn_2(N_3\text{-}bdc)_2(dabco)$] MOF thin film grown on a MUD-SAM modified gold substrate.

Table 4.1: Peak assignment for IR spectra (Figure 4.10)

NO.	Band position / cm^{-1}	Assignments
(1)	2958	CH_3 asym.
(2)	2925	CH_2 asym.
(3)	2885	CH_2 sym.
(4)	2850	CH_2 sym.
(5)	2114	azide (N_3) stretching vibration
(6)	1640	COO asym
(7)	1586	Benzene ring, ip
(8)	1492	C-N vibration from dabco
(9)	1467	…..
(10)	1406	COO sym.
(11)	1381	COO sym.
(12)	1286	…..

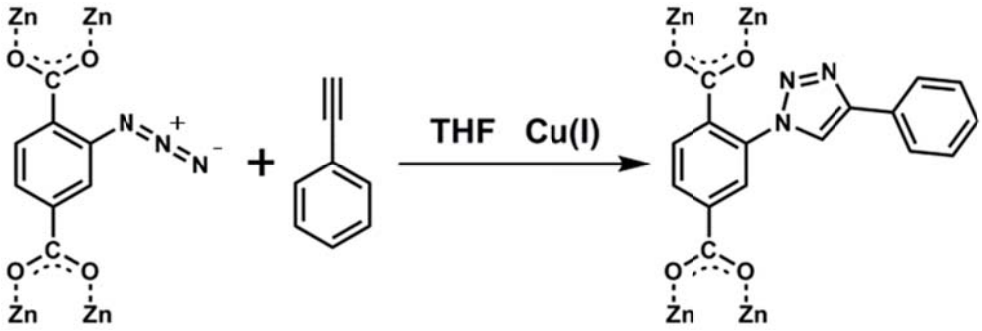

Scheme 4.1: "Click" reaction of N_3-bdc ligands in the $[Zn_2(N_3\text{-bdc})_2(dabco)]$ SURMOFs using Cu(I)-catalyzed Huisgen cycloaddition.

thin films. The out-of-plane and in-plane XRD patterns displayed in Figure 4.9b reveal that the positions and relative intensities of the diffraction peaks are fully consistent with the XRD patterns of the bulk material. Furthermore, the out-of-plane XRD also confirms that, on MUD SAMs, $[Zn_2(N_3\text{-bdc})_2(dabco)]$ grows along the [001] direction and yields highly oriented films (see Figure 4.9a). Additional characterization of the SURMOFs was carried out using IRRAS (see Figure 4.10) and the corresponding assignments of the IR bands are provided in Table 4.1. Noteworthily, the adsorption band at 2114 cm^{-1} is assigned to azide (N_3) stretching vibration in the SURMOFs.

4.2.3 PSM of $[Zn_2(N_3\text{-bdc})_2(dabco)]$ SURMOFs using CuAAC

In a first set of PSM experiments, we studied the CuAAC reaction of the $[Zn_2(N_3\text{-bdc})_2(dabco)]$ SURMOFs with phenylacetylene. As shown in Scheme 4.1, the triple bond reacts with the N_3 group of the ligand to yield a new SURMOF with the phenyl-modified pore surface. The reaction was carried out by the addition of excess phenylacetylene in the presence of $[Cu(I)(CH_3CN)_4]PF_6$, followed by continuous stirring for 8 h. The progress of the reaction was monitored using IRRAS. Figure 4.11 shows the corresponding IRRAS data recorded after 1, 2, 4, 6, and 8 h. The peak intensity of the $\nu(N_3)$ stretching vibration at 2114 cm^{-1} clearly decreases with increasing time. Using the intensity of this IR peak as a measure of the reacted N_3 groups, conversion yields were determined (see the inset of Figure 4.11). At the beginning, a linear increase of the conversion over time is observed. After 4 h, the increase in conversion slows and eventually saturates at a value of 91.7%, reached after a reaction time of 8 h. Long reaction times did not lead to a further increase in the conversion yield.

The crystallinity of the pristine N_3-SURMOFs and the PSM modified N_3-SURMOFs has been investigated by XRD. The results depicted in Figure 4.12 show the out-of-plane and in-plane XRD patterns of the pristine N_3-SURMOFs and the N_3-SURMOFs after subsequent (3 + 2) click

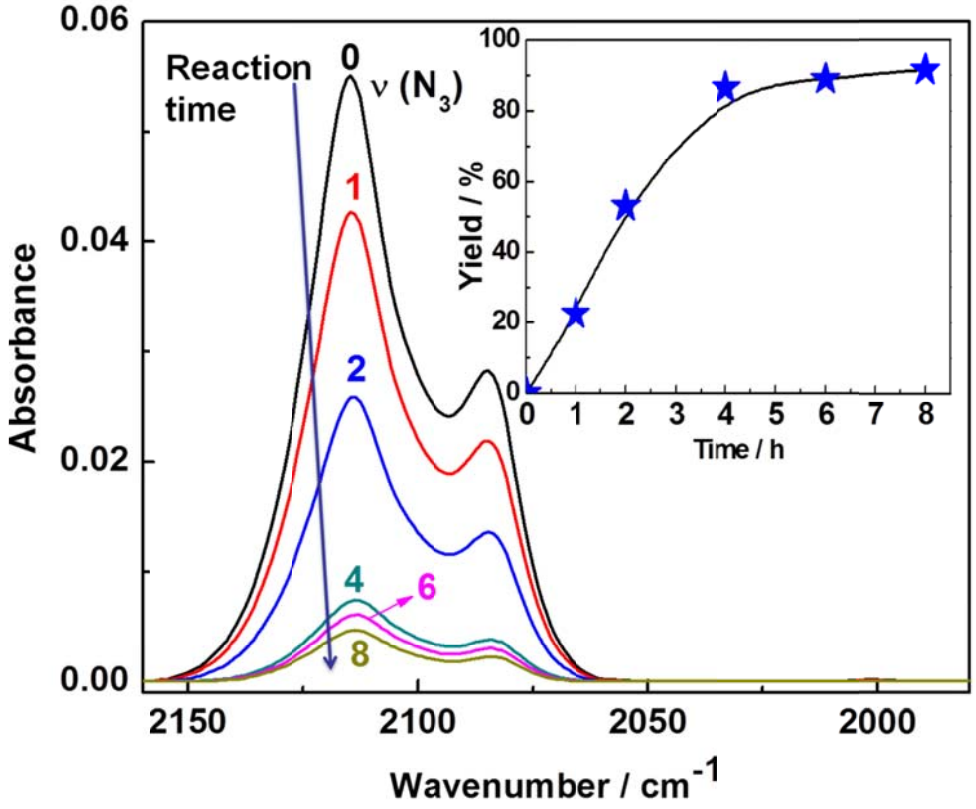

Figure 4.11: Post-modification of the highly oriented [$Zn_2(N_3$-bdc$)_2$(dabco)] MOFs thin film monitored by IRRAS at different reaction times. (Inset) Yield calculated from the maximum absorbance of the N_3 stretching vibration (2114 cm^{-1}) at different reaction times.

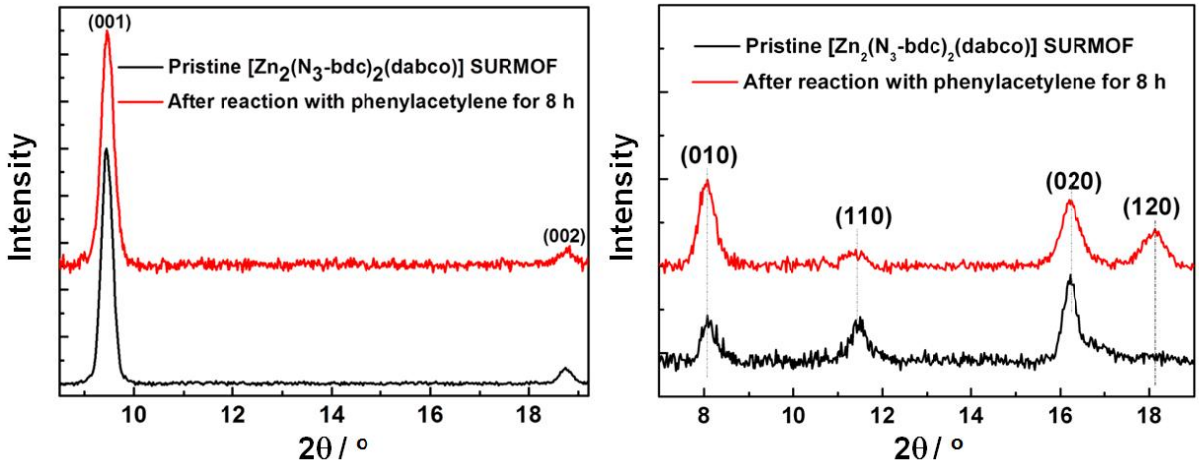

Figure 4.12: Comparison of out-of-plane (left) and in-plane (right) XRD patterns from as-synthesized [$Zn_2(N_3$-bdc$)_2$(dabco)] (black), prepared by the LPE method, and after reaction with phenylacetylene (red).

cycloaddition reaction for 8 h. The reaction leaves the XRD peak positions unchanged. Furthermore, the widths of the peaks show no or very small changes, providing strong evidence that the thickness of the SURMOF layers has remained unaffected.[200] We thus conclude that the PSM reaction does not change the periodicity, crystallinity, and orientation of the SURMOFs and the backbone of the frameworks is not affected by the click reaction. Control experiments where SURMOFs were immersed into solutions containing only Cu(I) catalyst or only phenylacetylene did not lead to any changes of the SURMOF structure (see the Supporting Information of Ref. [201]).

In the case of PSM with phenylacetylene, the maximum number of reacted N_3 groups was found to be slightly more than 90% (a total of six samples were investigated). The fact that not all N_3 groups could be converted is attributed to steric effects, which affect the diffusion of the catalyst into the MOF. Also, the subsequent removal of the Cu(I) catalyst from the SURMOFs after click

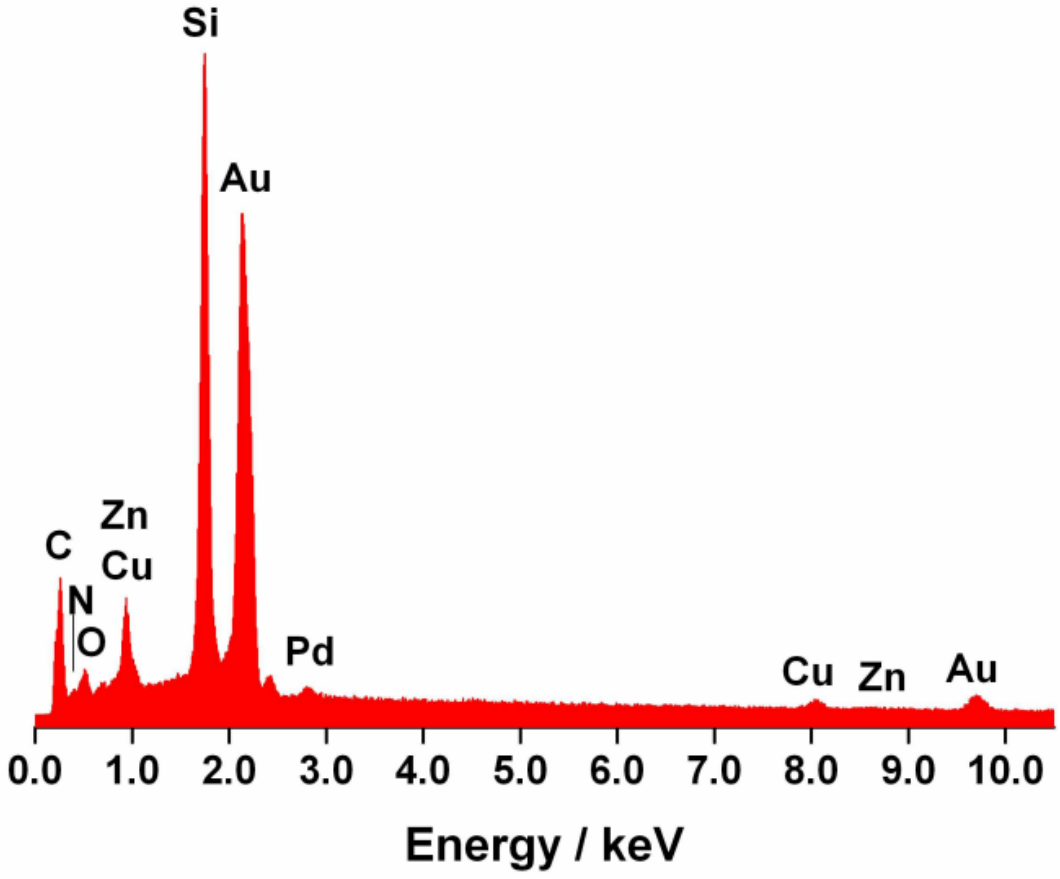

Figure 4.13 EDX data of [$Zn_2(N_3$-bdc$)_2$(dabco)] MOF thin films after Cu-catalyst click reaction, followed by soaking in ethanol under ultrasonic for 4 h.

reaction was very slow. Even after soaking the sample in ethanol under ultrasound for 4 h, a Cu signal could still be observed in energy-dispersive X-ray (EDX) (see Figure 4.13). To test the hypothesis that steric constraints are responsible for the conversion yields not reaching a full 100%, we carried out experiments with SURMOFs where only the top layer of ligands was functionalized with the azide groups, as shown in Figure 4.15. It is a particular advantage of the LPE method used to grow the SURMOFs in a way that such vertical composition gradients can be created in a straightforward fashion. As shown by the IR data presented in Figure 4.14, for the azide groups within the top layer of the SURMOFs, a yield of almost 100% is reached. The characteristic $\nu(N_3)$ stretch vibration at 2114 cm^{-1} disappears completely after immersing the N_3-bdc-functionalized $[Zn_2(bdc)_2(dabco)]$ SURMOFs in a THF solution of phenylacetylene in the presence of $[Cu(I)(CH_3CN)_4]PF_6$, followed by continuous stirring for 1 h (Figure 4.14c). This observation provides strong support for the hypothesis presented above, namely, that steric constraints are the major limiting factor for the Cu(I)-catalyzed coupling reaction in the inner pores of the SURMOFs.

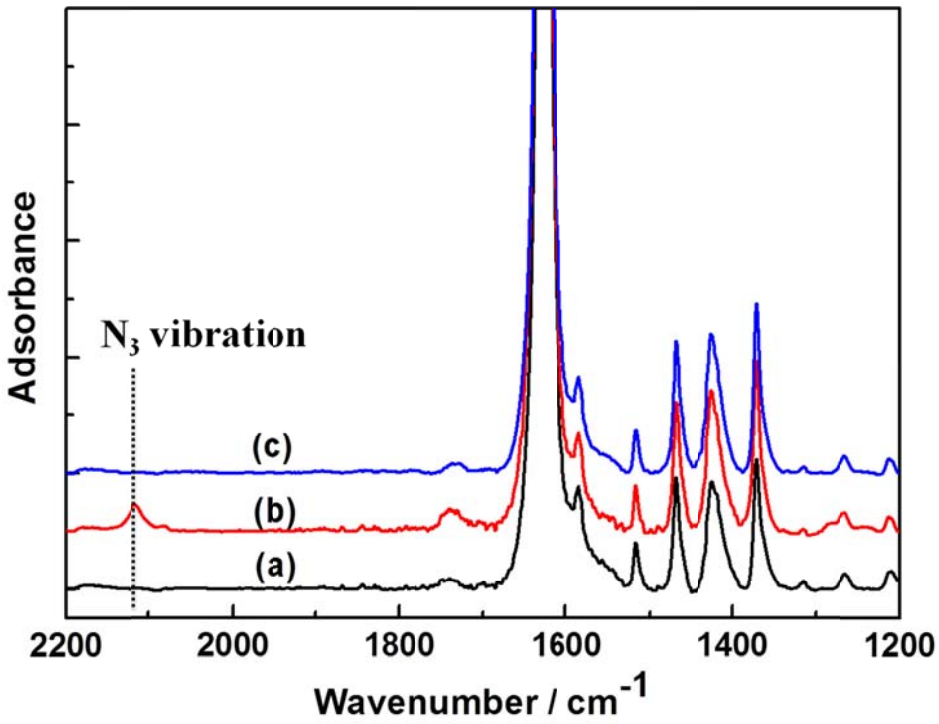

Figure 4.14: IR spectroscopy of: (a) 40 cycles of $[Zn_2(bdc)_2(dabco)]$ SURMOFs; (b) N_3-bdc functionalized $[Zn_2(bdc)_2(dabco)]$ SURMOFs; (c) N_3-bdc functionalized $[Zn_2(bdc)_2(dabco)]$ SURMOFs after carried out Cu-catalyst click reaction with phenylacetylene for 1 h.

4.2.4 Surface modification of SURMOFs

The successful modification of the N_3-SURMOFs using Cu(I) catalyzed azide−alkyne cycloaddition allows for anchoring different types of functional groups onto the outer surface of the SURMOF for a rational modification of surface properties, e.g., hydrophilicity/ hydrophobicity, the selective attachement of target analytes,[172] and optical response (e.g., fluorescence[123, 202]). Here, hydrophobic functionalities (1-ethynyl-4-pentylbenzene) and fluorescent labels (Alkyne MegaStokes dye 673) were employed to modify SURMOF surfaces using CuAAC (see Figure 4.15). The hydrophobic property of SURMOFs before and after the modification was characterized with contact angle measurement, as shown in panels a and b of Figure 4.16. The surface-functionalized SURMOFs obtained by the click reaction exhibited a substantial higher hydrophobicity than the pristine SURMOF. The water contact angle increased from 19° for N_3-bdc functionalized [$Zn_2(bdc)_2(dabco)$] SURMOFs (Figure 4.16a) to 62° for the SURMOFs after modification with long alkane molecules (Figure 4.16b). An intense and homogeneous red fluorescence is observed after grafting the Alkyne MegaStokes dye 673 to the SURMOF surface using the click reaction (see Figure 4.16d). The IRRAS results in Figures 4.17 (1) and 4.17(2) also demonstrate that a quantitative yield can be achieved with the click reaction on the SURMOF surface.

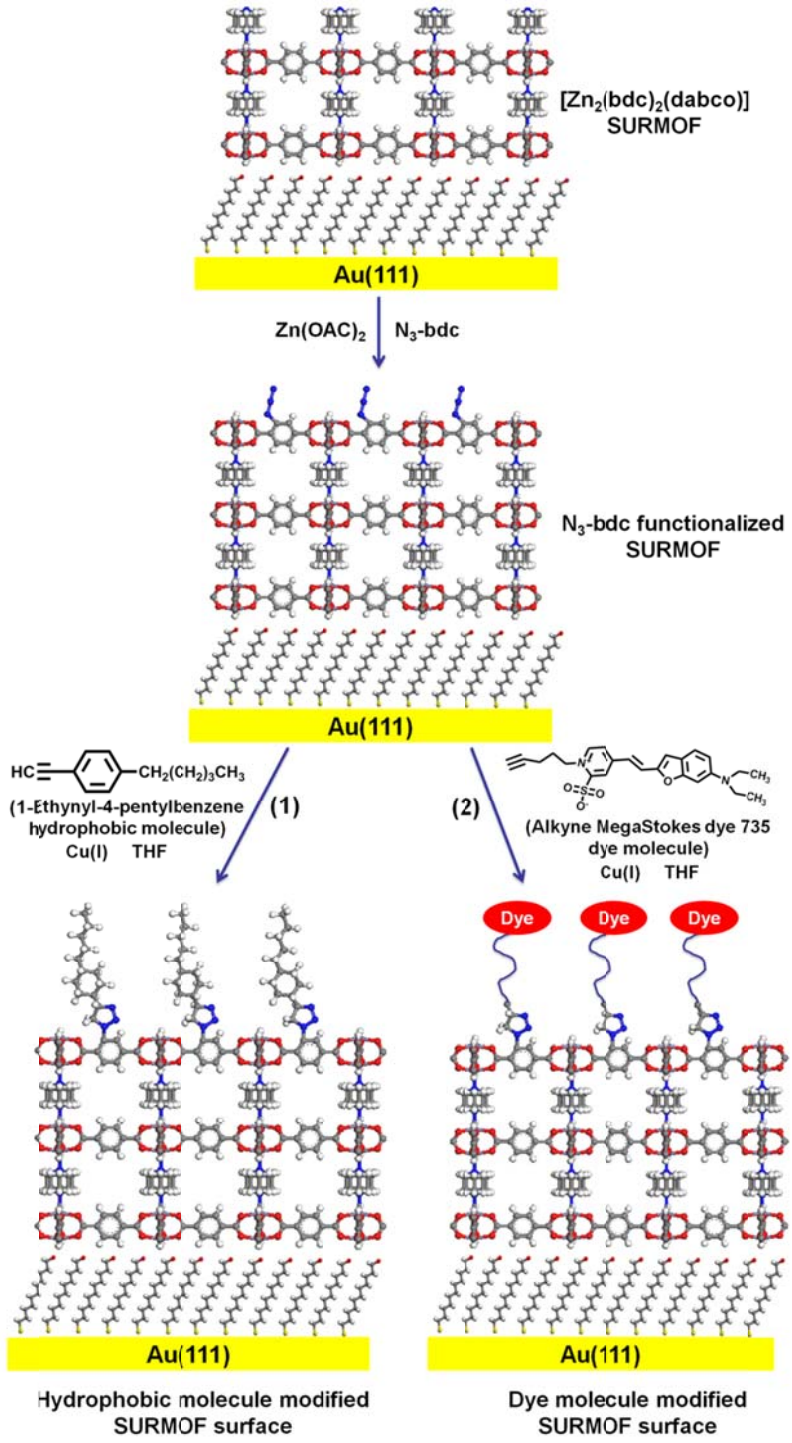

Figure 4.15: Schematic illustration of Cu-catalyst click reaction carried out on the surface of the MOFs.

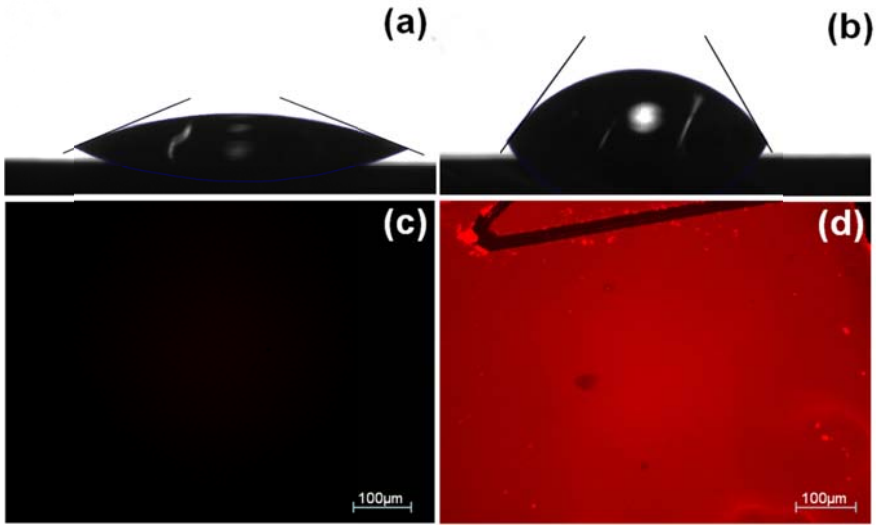

Figure 4.16: Water contact angle of the N_3-bdc functionalized $[Zn_2(bdc)_2(dabco)]$ MOF thin film (one layer $[Zn_2(N_3\text{-}bdc)_2(dabco)]$ on 40 layers $[Zn_2(bdc)_2(dabco)]$ SURMOFs) before reaction (a) and after surface modification with alkyne-bearing hydrophobic molecule (1-Ethynyl-4-pentylbenzene) (b); fluorescence of the N_3-bdc functionalized $[Zn_2(bdc)_2(dabco)]$ MOFs thin film before reaction (c) and after surface modification with alkyne-functionalized fluorescent dye (Alkyne MegaStokes dye 673) (b).

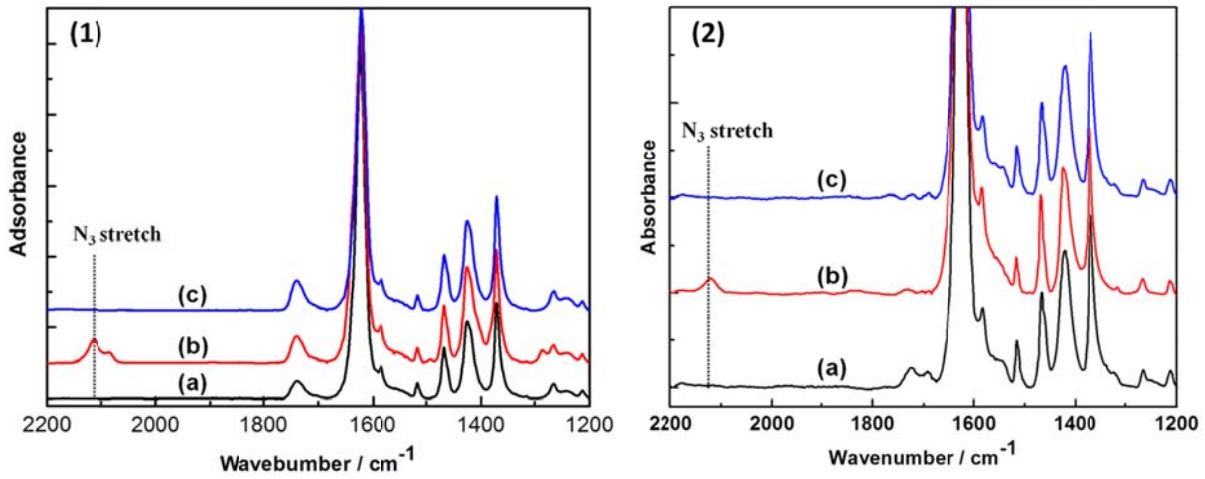

Figure 4.17: IR spectroscopy of: (a) 40 cycle $[Zn_2(bdc)_2(dabco)]$ SURMOF; (b) N_3-BDC functionalized $[Zn_2(bdc)_2(dabco)]$ SURMOF; (c) N_3-BDC functionalized $[Zn_2(bdc)_2(dabco)]$ SURMOFs after carrying out the Cu-catalyst click reaction with an hydrophobic molecule (1-ethynyl-4-pentylbenzene) for 1 h (1) and with a fluorescence molecule (Alkyne MegaStokes dye 673) for 1 h (2).

4.2.5 PSM of $[Zn_2(N_3\text{-bdc})_2(dabco)]$ SURMOFs using SPAAC

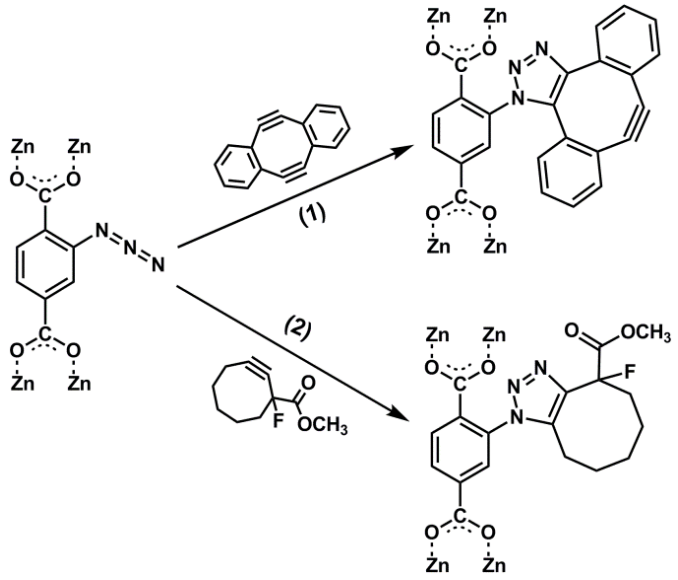

Scheme 4.2: Click reaction of N_3-bdc ligands in the $[Zn_2(N_3\text{-bdc})_2(dabco)]$ SURMOFs using strain-promoted azide-alkyne cycloaddition

In comparison to the Cu(I) catalyzed azide-alkyne cycloaddition, the advantage of the metal-free azide-alkyne cycloadditions is that they proceed in the absence of metal catalyst and the potential toxicity or contamination of metal catalysts for the products can be avoided.[197, 198, 203-206] In the case of the Cu(I)-induced catalysis, three species have to be in close proximity (azide, Cu(I) catalyst, and alkyne) to trigger the reaction, while in the case of the SPAAC reaction, only two species are required (alkyne and azide). Accordingly, one would expect that reaction times are faster and that reaction yields are higher compared for the SPAAC reaction than for the Cu-catalyzed reaction. However, the azides do not react easily with alkynes in the absence of a metal catalyst. In the earlier studies, different approaches have been developed to increase the reactivity of alkyne groups to allow for metal-free azide-alkyne cycloadditions under mild conditions. One elegant approach was reported by Wittig and Krebs,[207] who achieved alkyne activation by incorporating the alkyne group into an eight-membered ring. This strategy has been elaborated lately on various types of cyclooctynes, in particular in cellular systems.[197] The scheme of SPAAC is illustrated in Scheme 4.2 for compounds 1 and 2. The detail modification process was displayed in chapter 3 (3.4). As shown in panels A and B of Figure 4.18, the peak intensity of the characteristic $\nu(N_3)$ stretching vibration at 2114 cm^{-1} gradually decreases with increasing the time. Overall, the reaction proceeds much faster than the Cu(I)-catalyzed reactions

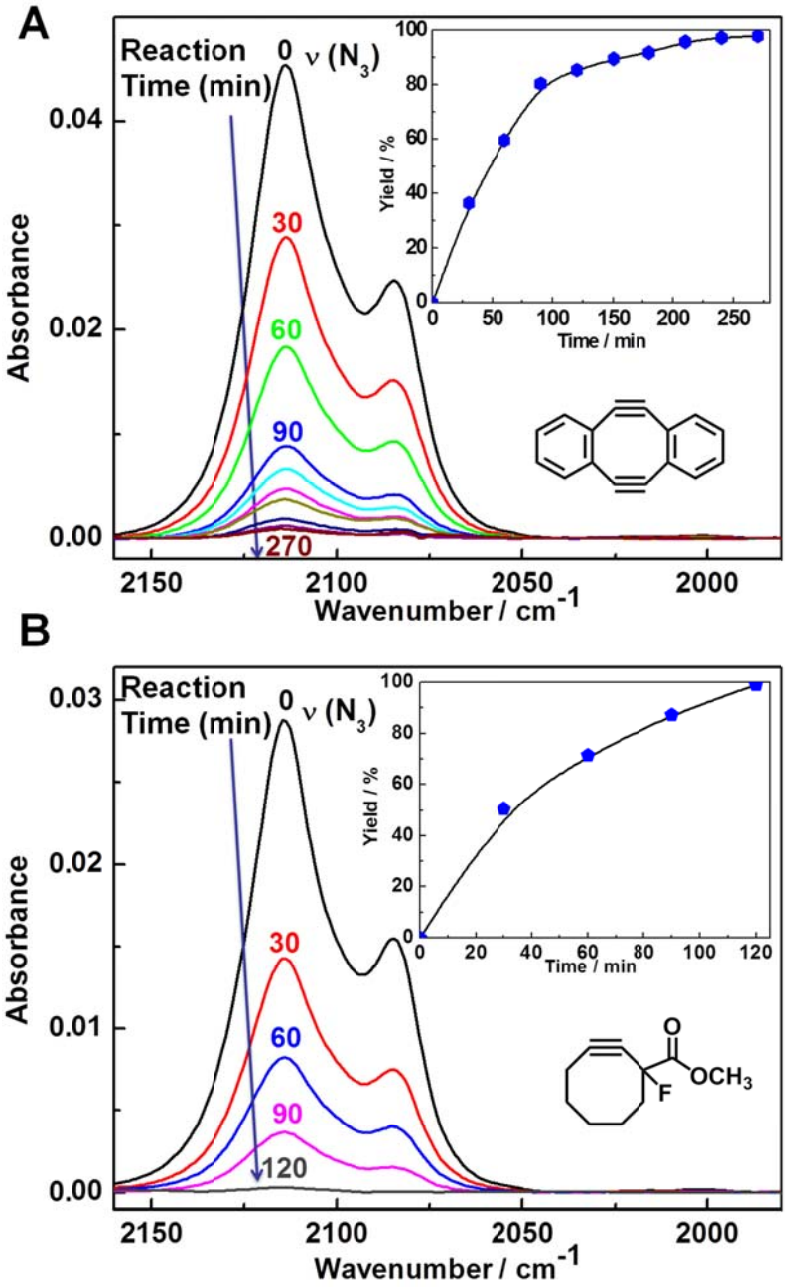

Figure 4.18: The post-modification of the highly oriented [$Zn_2(N_3$-bdc$)_2$(dabco)] MOFs thin film monitored by IRRAS with increasing the reaction time (increased every 30 min): (A) Reaction with compound 1; (B) Reaction with compound 2. (Inset) Yield calculated from the maximum absorbance of the N_3 stretching vibration (2114 cm^{-1}) at different reaction times.

above. For compound 1, a fast reaction rate is observed after 90 min and the saturation was reached after 240 min, with a total conversion yield of 98.1%. In the case of compound 2, as shown in Figure 4.18B, the $\nu(N_3)$ stretching vibration around 2114 cm^{-1} almost disappeared after 120 min, giving a total conversion yield of nearly 100%. As already observed for the Cu(I)-

catalyzed click reaction and in accordance with expectation, the PSM did not lead to any changes in the XRD diffraction pattern (See Figure 19). Note, that in both cases, the total conversion yields are substantially higher than the Cu(I)-catalyzed click reaction with phenylacetylene (91.7%), even though the two synthons used are substantially larger than the phenylacetylene used in the Cu(I)-catalyzed click reaction.

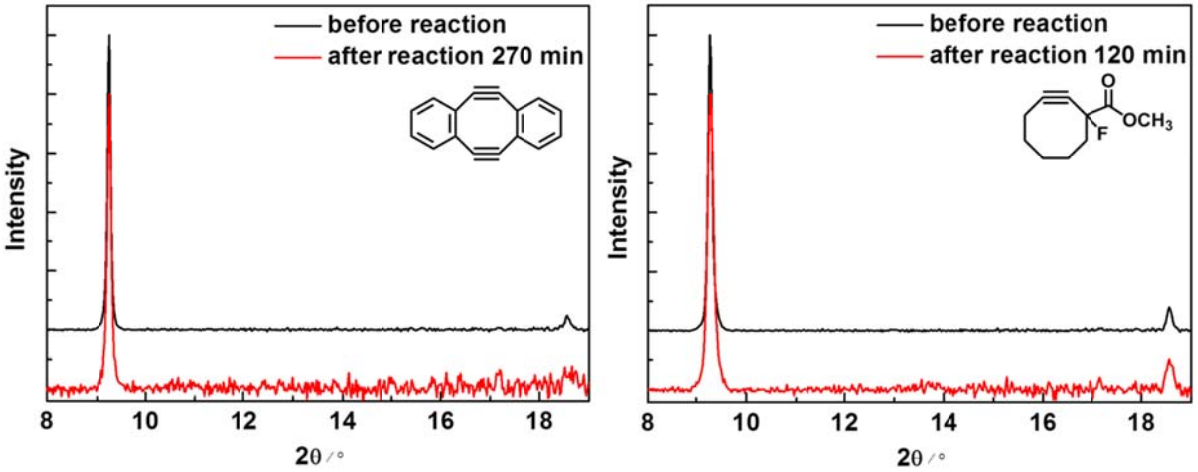

Figure 19: The post-modification of the highly oriented [$Zn_2(N_3$-bdc$)_2$(dabco)] MOFs thin film monitored by XRD with increasing the reaction time.

4.2.6 Summary

In this study, the functionalization of surface-attached MOF thin films can be readily achieved by PSM via click chemistry. The present experiments reveal that layer-pillar-based SURMOFs containing an azido-modified dicarboxybenzene ligand offer a robust platform for attaching various types of functional units. SPAAC shows substantial advantages over the conventional Cu(I)-catalyzed azide−alkyne cycloaddition. Not only the contamination by residual Cu ions with potential toxicity can be avoided, but the reaction rate is also strongly enhanced. Most importantly, the total conversion yield reaches values of close to 100%. When only the SURMOF top layer contains the azide functionality, the surface properties of the SURMOFs can be modified in a straightforward fashion, e.g., by labeling with hydrophobic or fluorescent molecules. In future work, we will investigate the possibility of a two-step PSM using linkers with orthogonal coupling units, e.g., an azido function coupled in the bottom of a SURMOFs and an amino function coupled at the top. Such SURMOF PSM offers a number of advantages. In the case of optimizing the response of SURMOF-based sensors (see the review by Kreno et al.[184]), often the linkers used to grow the SURMOFs have to be modified to improve the response of the sensor or to reduce cross-talk. Instead of finding and optimizing reaction conditions for the SURMOF growth with the new ligands (results from this laboratory show that adding a

functionality like an amino group to a linker severely affects SURMOF growth and frequently renders the synthesis impossible), the azido-based SURMOFs used in this study provide an excellent platform to add the desired functionalities without affecting the SURMOF growth process. The tedious optimization of growth conditions for each new type of ligand can now be replaced by a rational, straightforward subsequent reaction with high (almost 100%) yield. In addition to sensor, this finding is expected to have a pronounced impact on biological and biomedical applications of SURMOFs.[195, 208] As an example, the covalent grafting of small peptides will provide the possibility to render antimicrobial properties to SURMOFs.

This chapter is based on the publication in Langmuir in November 2013[201] and Dr. Sylvain Grosjean, Dr. Tobias Hagendorn and Prof. Stefan Bräse synthesized the organic compound (2-azidoterephthalic acid and cyclooctyne derivative) used in this study and the detail processes are displayed in chapter 6 (6.1).

4.3 Patterning of MOF thin films using post-synthetic modification

4.3.1 Background

The ability to pattern the MOFs on the surfaces is essential for the development of MOF-based device. For the past decade, a lot of the research effort has been directed toward patterning MOF thin films on a given substrate[84, 112]. However, most of the patterning technologies whether bottom-up or top-down approaches only offer a way to control the shapes of MOF films in the mounting surface plane dimensions (x and y dimensions)[112] and it is limited by the initial patterning. As such, it does not enable a full three-dimentional (3D) control. The LPE approach used relies on a stepwise, layer by layer, building block deposition[101], which allows producing hybrid and multiheteroepitaxial SURMOF systems[122, 182]. Therefore, controlling the patterned functionalization of MOF thin film along growth direction (z dimension) would become possible. Additionally, the x and y dimension control could also arise from its quality of having a high porosity. There are enough space that the organic linkers, as well as the metal connector, are effectively accessible for further chemical reaction after the MOF fabrication, in a process named post synthetic modification (PSM)[209]. In this work focus was on azide-alkyne click chemistry as it offers appealing PSM schemes[188, 201, 210]. Click chemistry has already proven to be a reliable tool to graft modifications, as described in the last chapter (4.2), but more importantly, the derived reactions can be influenced by UV exposure[211-215]. They can be either started using photo-initiators[211, 212], or in the contrary, prevented through azide photodecomposition[215]. This major feature enables the use of available photolithography techniques to modify the SURMOFs.

Considering the above mentioned chemistries, we present preliminary results and lay the foundations for a methodology combining a top-down (UV lithography) and bottom up (LPE

spraying) approaches and using MOFs as pseudo 3D multifunctional resist material. In this work, our study is divided into five parts. In the first part, the growth of patterned azido-SURMOFs on patterned SAMs using a recent developed robot dipping method and the PSM of such patterned azido-SURMOFs by strain-promoted azide-alkyne click chemistry were demonstrated. The second part showed that the PSM of SURMOFs could be controlled in a spatial and temporal fashion for the patterned modification of azido-SURMOFs by using a photolithography technique, which directed photo reduction of Cu(II) to Cu(I) and enabled the catalysis of azide-alkyne click action of alkyne molecules on azido-SURMOFs. In the third part, the patterned decomposition of azide functional group in azido-SURMOFs by UV irradiation combined with a photo mask was achieved and revealed by PSM with alkyne molecules grafted on the rudimental azide area by strain-promoted click chemistry. In a fourth part, another photoreaction for patterning was probed by photo-induced thiol-yne click chemistry. In the last part, the design of 3D-patterned multifunctional SURMOFs was sought. A multilayer MOF system was grown by alternatively stacking two structure, MOF-A and MOF-B. A layer-selective staining process then revealed the quality of hetero-layer deposition. This multilayer could be used for the patterned modification by UV lithography to reach the 3D-patterned multifunctional SURMOFs.

4.3.2 Deposition of MOFs on patterned SAMs modified Au-substrate and their post-synthetic modification.

As mentioned in the first chapter (1.2.1.2), to grow MOF thin film on the solid surface by LPE, the substrate usually needs to be coated with SAMs or treated by plasma to yield a surface of dentate group such as -COOH, -OH, $-NH_2$ and pyridyl that provide the location of MOF materials[99, 216]. The LPE SURMOF technique is well suited to obtain a patterning of MOF thin film through the controlled deposition of the MOF building blocks since a huge numbers of methods have been extent studied to obtain patterned SAMs with dentate and non-dentate terminal groups on solid-substrate[217-219]. Our previous works has demonstrated successful in growing patterned SURMOFs from patterned SAMs by an auto-pump LPE system[220]. However, the morphology and roughness have not been satisfying enough to meet advanced application requirement. The most possible reason is the suboptimal removal of the uncoordinated metal connectors or organic linkers excess from the reaction surface, which affects the following step

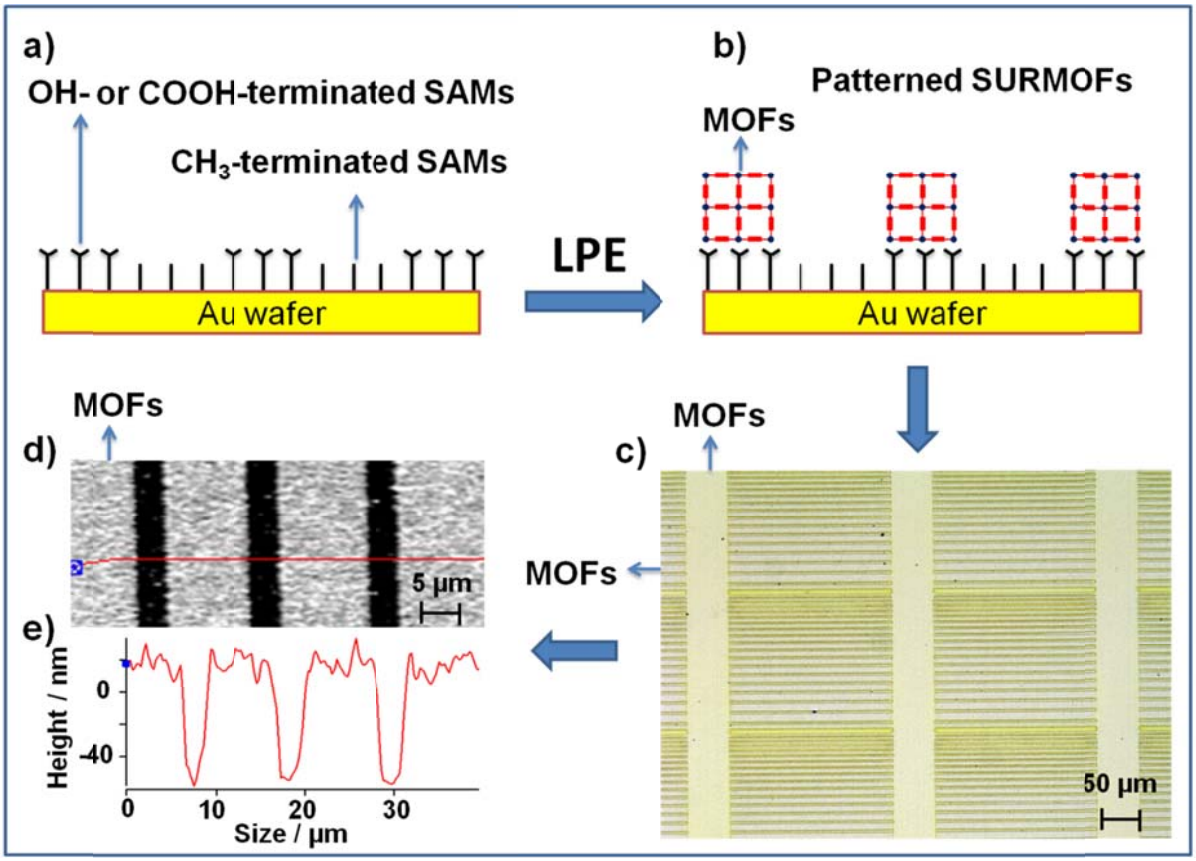

Figure 4.20: a) Schematic diagram of the growth of MOF on patterned SAMs. c) Optical image of SURMOFs [Zn(N_3-BPDC)$_2$(Dabco)] on patterned OH-terminated SAMs. d) AFM image of SURMOFs [Zn(N_3-BPDC)$_2$(Dabco)] on patterned OH-terminated SAMs. e) Height profile along the line depicted in the AFM image.

of the layer-by-layer deposition. Additionally, it is challenging to obtain a well-selective growth of patterned SURMOFs since uncoordinated connectors materials on the inert surface could not be removed entirely with a simple rinsing step. Here, a new synthetic technique combined the robot dipping method with an ultrasonic bath which was implemented to improve the rinsing step, as shown in Figure 1.6. A gold substrate was modified with a patterned SAMs of mixed OH- and CH_3-terminatal groups, which was obtained by micro-contact printing (Figure 4.20 a). The substrate was sequentially dipped into the metal solution (1 mM of zinc acetate hydrate ethanol solution) and into the linker solution (an equimolar (0.2 M) of 2-azido-4,4'-biphenyl-dicarboxylic acid (N_3-BPDC)/1,4-diazabicyclo[2.2.2]octane (Dabco) ethanol solution), with interleaved rinsing step under ultra-sonication. After 40 cycles repeated, the SURMOFs [Zn(N_3-BPDC)$_2$(Dabco)] thin film was obtained, as depicted in figure 4.20 c. From the optical image, the

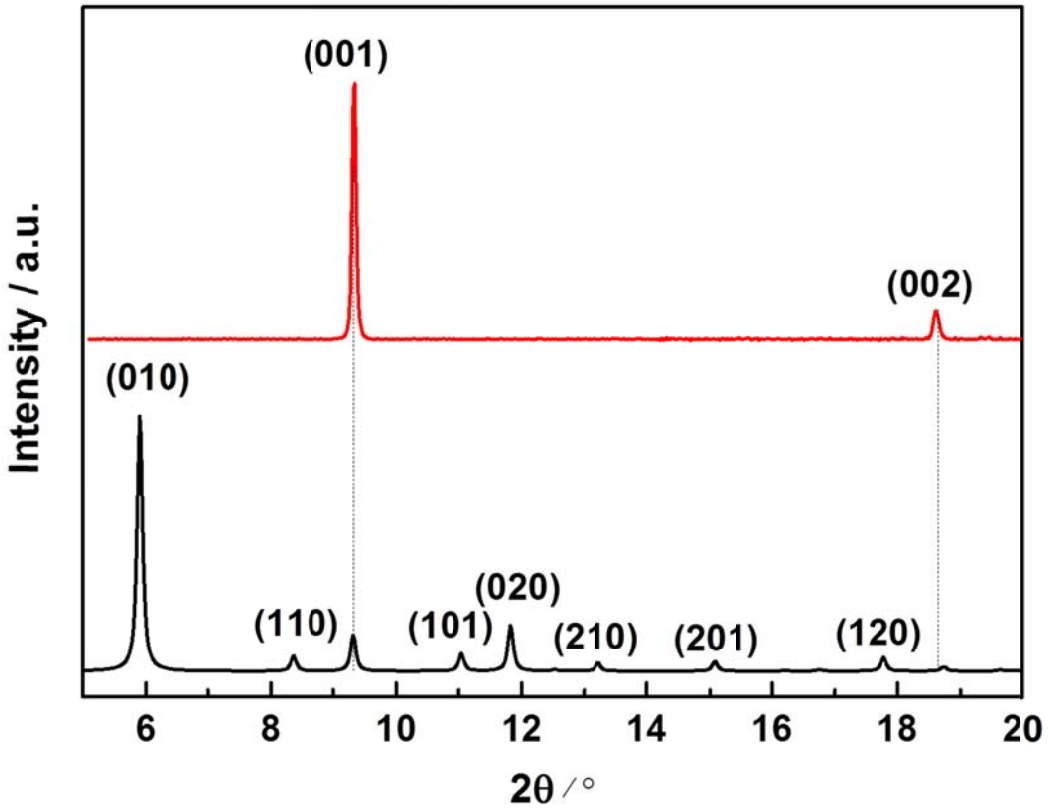

Figure 4.21: (Black curve) simulated XRD result of bulk [Zn(N_3-BPDC)$_2$(Dabco)] and (red curve) experimental XRD result of patterning SURMOF [Zn(N_3-BPDC)$_2$(Dabco)] grown using robot dipping method.

thin film patterning was easily observable and showed a full match to the patterning of the seeding SAMs. The AFM image in Figure 4.20 d demonstrated the close-packing of MOF crystallites on OH-terminated SAM and the absence of materials on the CH_3-terminated SAM area, which further proved the selective-growth of MOF materials according to the terminal functional group. From the AFM height profile (Figure 4.20 e) along the line depicted in the AFM image, a film thickness of 80 nm and a roughness below 10 nm were clearly obtained. Notably 80 nm arose from 40 deposition cycles. This means one full cycle deposits a layer about two crystal unit cell thick and implies that there are still some uncoordinated metal or linkers present on the surface or stored in proximal pores of MOF, which lead to the further growth building block even the surface was cleaned by ethanol under ultra-sonication. Additional characterization of the patterned SURMOFs was carried out using X-raw diffraction (XRD). The XRD patterns displayed in Figure 4.21 shows the film is highly crystalline with [001] orientation and the peak positions matched with the simulation of bulk MOF [Zn(N_3-BPDC)$_2$(Dabco)].

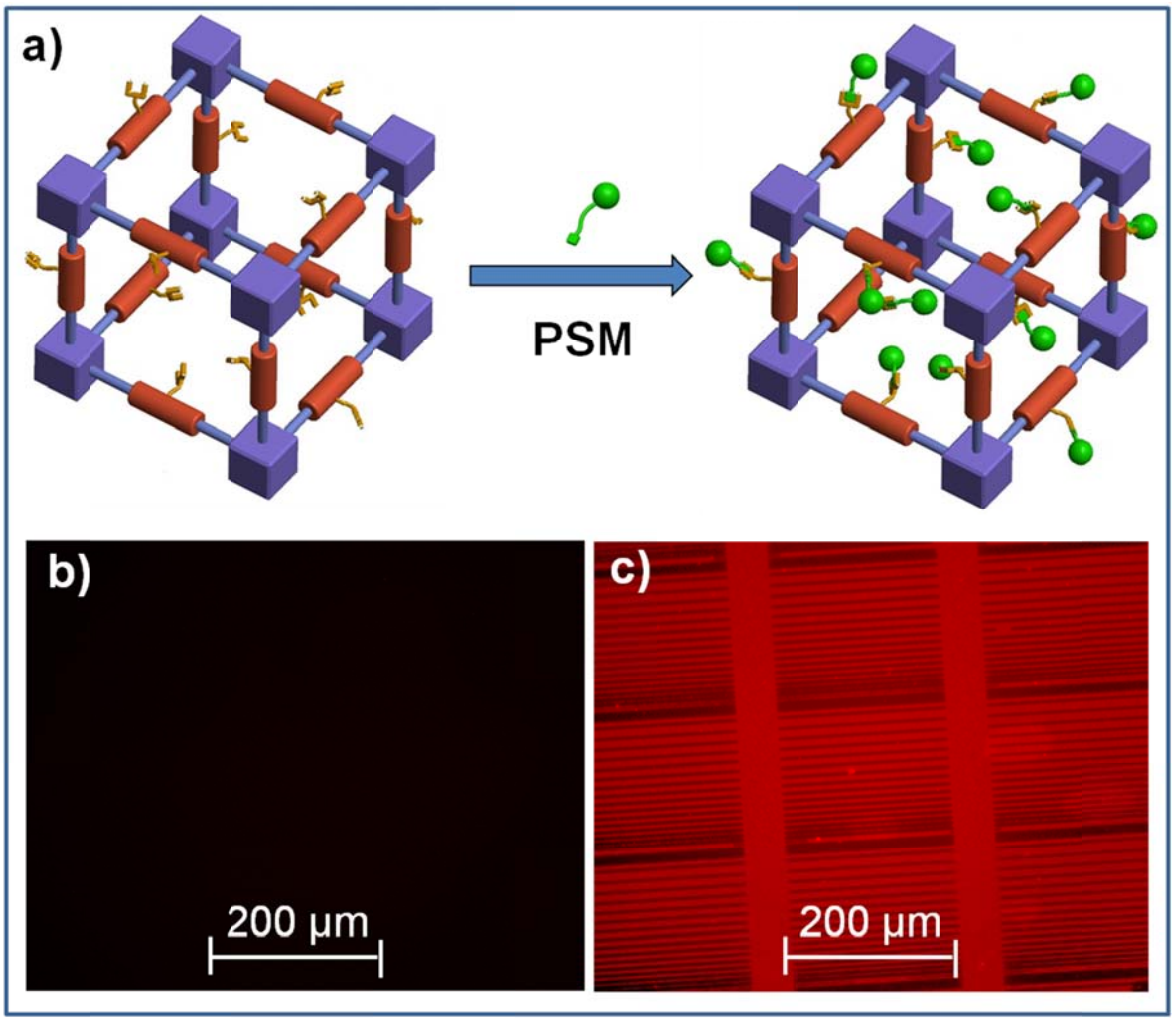

Figure 4.22: a) Schematic diagram of post-synthetic modification (PSM) of MOFs. b) Before reaction and c) after modification with alkyne-functionalized fluorescent dye molecules (Alkyne MegaStokes dye 608) of SURMOFs [Zn(N_3-BPDC)$_2$(Dabco)] on patterned OH-terminated SAMs.

In the last chapter (4.2), we demonstrated that PSM provide a elegant tool to tune the functionality of the pore surface by latching functional molecules onto the linkers[201], as depicted in figure 4.22a. The functionalization of SURMOFs was based here on an azide−alkyne cycloaddition click reaction using N_3-BPDC linkers in MOF [Zn(N_3-BPDC)$_2$(Dabco)] following our previous studies, see chapter 3 (3.4). A dye molecule (Alkyne MegaStokes dye 608, sigma) was used as a probe to bond covalently to MOF structure in a copper-free azide−alkyne cycloaddition reaction. As shown in Figure 4.22 b and c, the samples before and after functionalization were characterized by fluorescence microscopy. A patterned fluorescence signal was observed from the sample after reaction (Figure 4.22 c) and clearly replicated the patterning shape from the [Zn(N_3-BPDC)$_2$(Dabco)] SURMOFs (Figure 4.21 c). As a negative control, no fluorescence was monitored in non-modified SURMOF samples (Figure 4.22 b). This indicated

that the dye molecules anchored only in the MOF area and that the structure patterning was not destroyed by the PSM. The functionalization of patterned SURMOFs was then successfully demonstrated. The IRRA spectrum (Figure 4.23A) allowed estimating the fluorescent marking yield at around 33%, as calculated from the maximum intensity decrease of the N_3 vibration peak after a 30 min reaction time. Furthermore, the XRD results in Figure 4.23B confirmed no change in the crystalline structure of the SURMOFs occurred after the PSM.

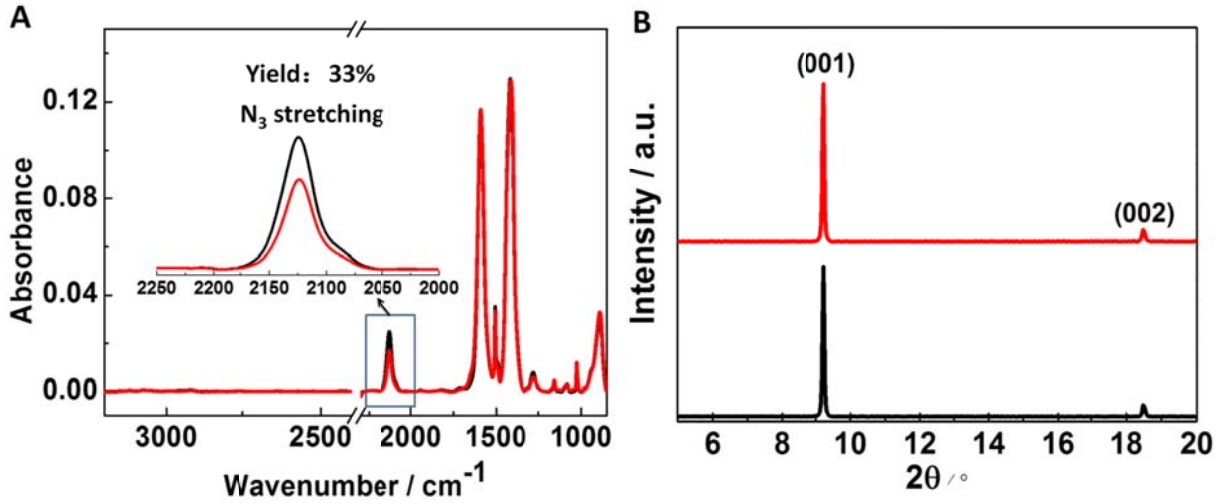

Figure 4.23: IRRA spectrum (A) and XRD patterns (B) of patterning SURMOF [Zn(N_3-BPDC)$_2$(Dabco)] before (back curve) and after (red curve) reaction with dye molecule (Alkyne MegaStokes dye 608) in toluene for 30 min using Cu(I)-free azide-alkyne cyclooddition click chemistry.

4.3.3 Cu(I) catalyzed alkyne–azide cycloaddition controlled by photoinitiated Cu(II) reduction

The copper(I)-catalyzed alkyne–azide cycloaddition (CuAAC) has been extensively applied in the functionalization of MOF materials in the past decade[55, 131, 137, 141, 183, 188, 191, 197-199, 202, 206]. Recently, the study reported that Cu(I) had been obtained by photo induced reduction of Cu(II) [211], which could be used to catalyze a alkyne–azide reaction in a spatial and temporal controllable fashion. However, obtaining a functional patterning of MOF thin film by controlling the location of this reaction has not been done so far to our knowledge. Here, the zinc based SURMOF [Zn(N_3-BPDC)$_2$(Dabco)] was prepared on a modified gold surface [Figure 4.24 (1)]. Here the pump method as displayed in chapter 1 (1.2.2.3) was employed to synthesize the SURMOFs with using 1 mM of zinc acetate hydrate ethanol solution) and an equimolar (0.2 M) of 2-azido-4,4'-biphenyl-dicarboxylic acid (N_3-BPDC)/1,4-diazabicyclo[2.2.2]octane (Dabco) ethanol solution.

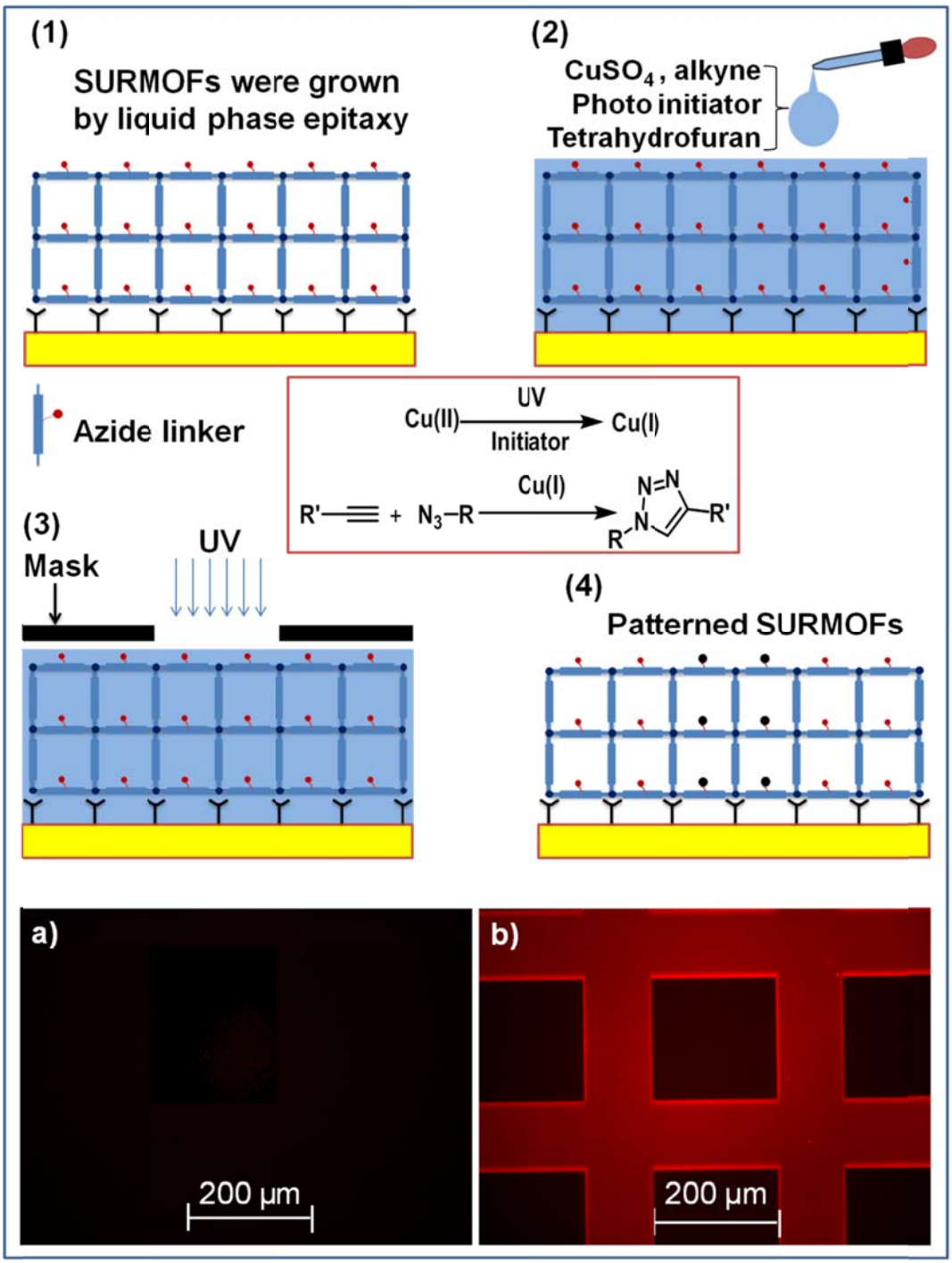

Figure 4.24: (1), (2), (3) and (4) Schematic diagram of the preparation of patterned SURMOFs by photo-controlled post-synthetic modification. (a) Before reaction and (b) after patterned modification of SURMOFs [Zn(N_3-BPDC)$_2$(Dabco)] with alkyne-terminated fluorescent dye molecules.

The SURMOF was soaked with a solution of Copper(II) sulfate, photoinitiator, and alkyne terminated molecules. A photo-mask was used to achieve a patterned UV exposure (Figure 4.24 (2)- (4)). In the irradiated area, the Cu(II) were reduced to Cu(I) and could catalyze the alkyne–azide cycloaddition reaction with fluorescent alkyne molecules. As a result, the patterned functionalization of the SURMOF thin film was obtained and revealed by the patterned fluorescence signal (Figure 4.24 b). The images show that a patterned feature of 100 µm can be realized with an irradiation time of 5 min. Additional characterizations of the SURMOFs before and after irradiation were carried out using XRD and IRR spectroscopy (Figure 4.25 A and 4.25 B). The XRD results (Figure 4.25 A) showed that the crystallinity was conserved after the reaction and the IRRAS data (Figure 4.25 B) revealed a decrease (15 %) of the azide vibration peak after the patterning functionalization of SURMOFs, This further confirmed the induction of the alkyne-azide cycloaddition by the photo-reduction of Cu(II) to Cu(I). The low yield may originate from the diffusion limitation of the large reactants within the MOFs pore.

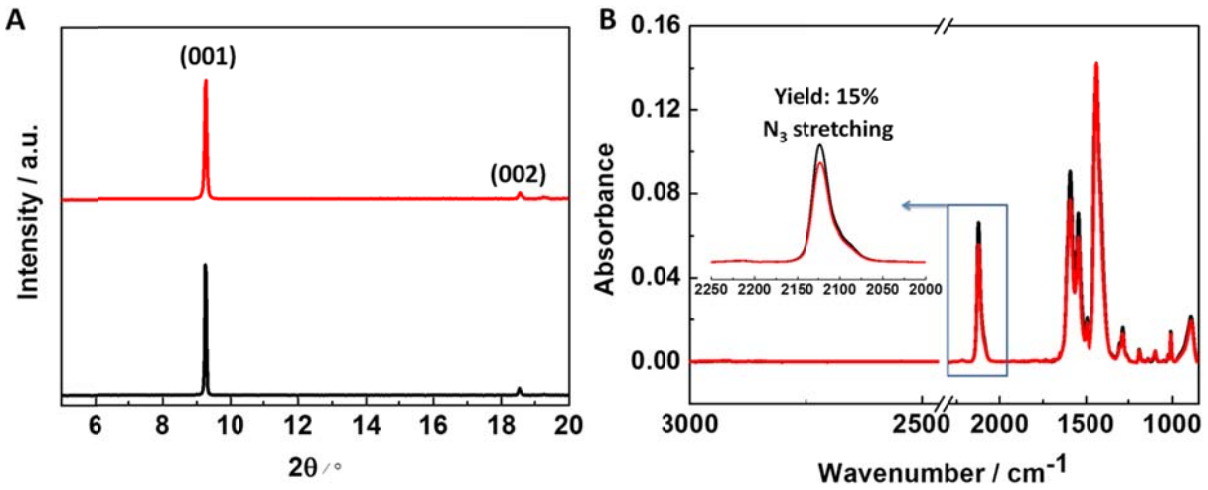

Figure 4.25: XRD (A) and IRRAS (B) results of SURMOF [Zn(N_3-BPDC)$_2$(Dabco)] before (black curve) and after (red curve) patterned modification of SURMOFs [Zn(N_3-BPDC)$_2$(Dabco)] with alkyne-functionalized fluorescent dye molecules controlled by photo-induced reduction of Cu(II).

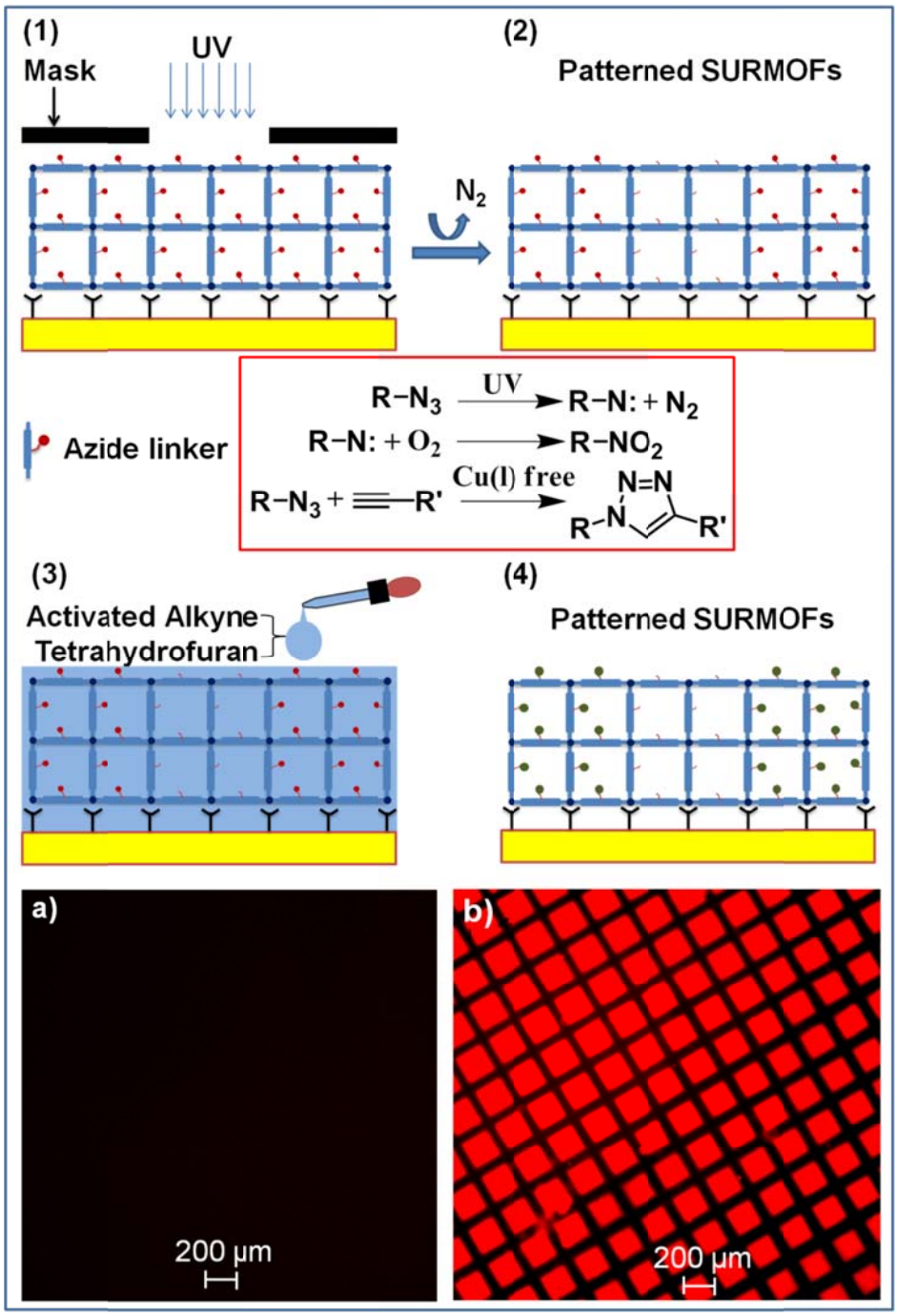

Figure 4.26: (1), (2), (3) and (4) Schematic diagram of the preparation of patterned SURMOFs by photo-controlled post-synthetic modification. (a) Before reaction and (b) after patterned modification of SURMOFs [Cu(N_3-BPDC)$_2$] with activated-alkyne-terminated fluorescent dye molecules.

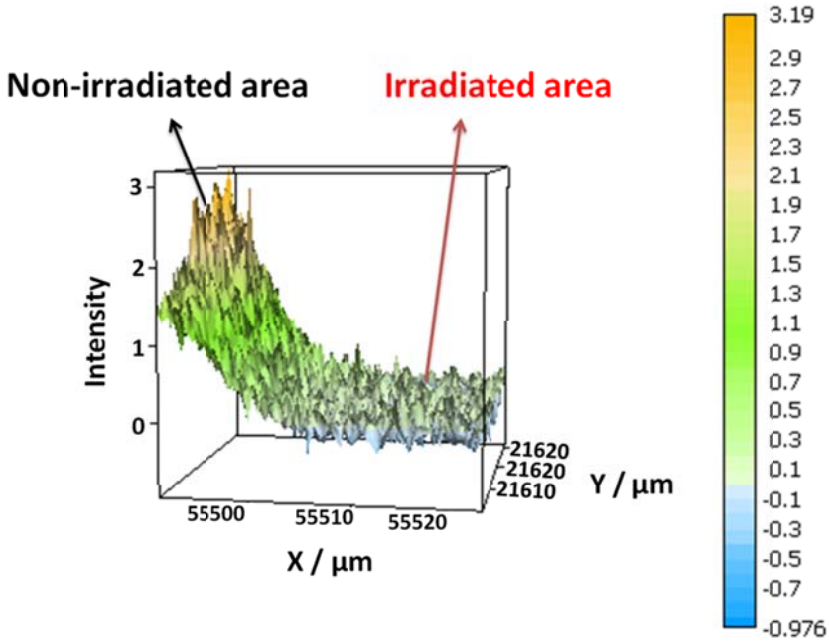

Figure 4.27: FT-IR imaging of azide vibration in the patterning UV-irradiated SURMOF Cu(N_3-BPDC)$_2$].

4.3.4 Patterned decomposition of azide group

Though the photo-initiated processes provide a spatial and temporal control for the alkyne–azide cycloaddition click reaction, the studies have shown that the azide group could undergo explosive decomposition when exposed to UV irradiation for an extended period of time[215, 221]. This was used advantageously to pattern the functionalization by photo-controlled decomposition of the azide groups. A SURMOF-2 structure [Cu(N_3-BPDC)$_2$] was used as a template for this study and the SURMOFs were prepared using spray method as shown in chapter 1. The sample was first irradiated under UV light for 1h with a photomask (Figure 4.26 (1) and (2)). To quantify the content of azide group in the differently exposed area (irradiated and photomask protected) the FTIR imaging over a region of interest was carried out with an attenuated total reflectance (ATR) microscope. Figure 4.27 shows the intensity of the azide band between 2000 cm^{-1} and 2200 cm^{-1}, illustrates boundary between a UV-irradiated and non-irradiated areas, by confirming the presence of azide groups or absence of it following the photo-decomposition. Post-synthetic modification of the UV treated SURMOFs was also carried out using Cu-free alkyne–azide cycloaddition click reaction with a dye tagged alkyne molecule. As shown in Figure 4.26, a fluorescence signals could be clearly observed from the non-irradiated areas. Control experiments where the whole SURMOF [Cu(N_3-BPDC)$_2$] was irradiated by UV light for 1h in air were also done and the samples before and after irradiation were monitored by IRRAS

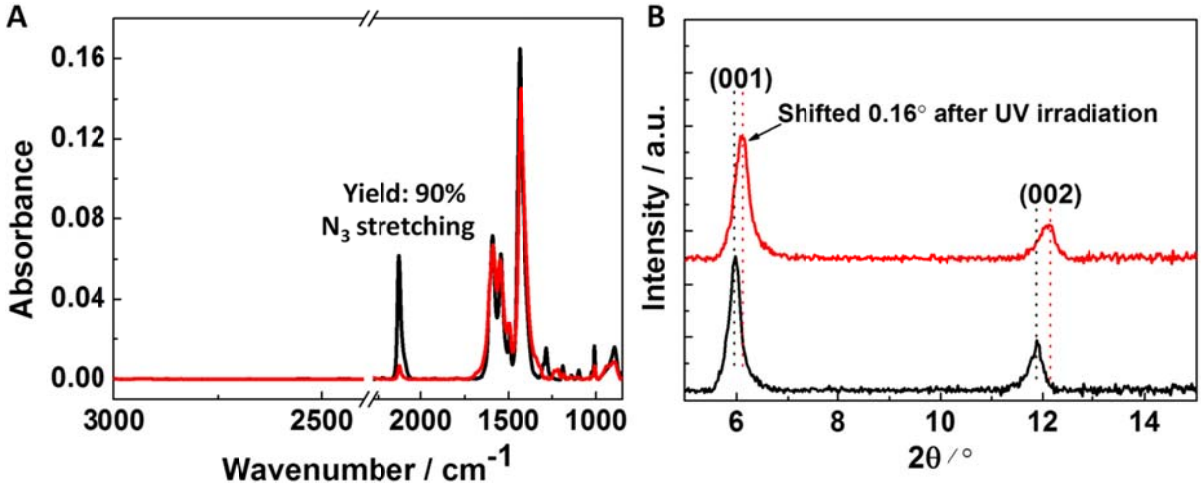

Figure 4.28: IRRA spectrum (A) and XRD (B) of SURMOF Cu(N_3-BPDC)$_2$] before (black curve) and after (red curve) irradiated by UV for 1h.

and XRD. The IRRA spectrum showed a decrease (90%) of the azide vibration peaks (Figure 4.28 A) was due to the decomposition of the groups. Furthermore, the XRD result (Figure 4.28 B) demonstrated that the intensity of XRD peak were mostly not affected as only a small peak shift attributed to the steric effects of NO or NO_2 in the pores was observed, which were produced by the decomposition of the azide groups and the further reaction with O_2.

4.3.5 Photo-induced thiol-yne click chemistry

Despite the increasing interest in Cu(I) catalyzed azide-alkyne cycloadditon reaction for the functional pattering of surface, the present of toxic Cu(I) catalyst still remain a challenge. Thiol-yne click reaction may be another choice since it has been commonly used for the synthesis of functional materials and the functionalization of surfaces[222]. The need of photogenerated radicals for mediating this reaction allow realizing a controlled patterned functionalization of the surface[223]. The application of thiol-yne click reaction for the modification of MOFs has only been reported occasionally[224]. Here, we contributed further hindsight by studying the PSM of SURMOFs using thiol-yne click reaction. For this, an alkyne-functionalized 4,4'-biphenyl-dicarboxylic acid (alkyne-BPDC) was synthesized as a linker (Prof. Stefan Bräse and Dr. Sylvain Grosjean synthesized the organic ligands, see chapter 6 6.1) and allowed producing the SURMOF [Zn(alkyne-BPDC)$_2$(Dabco)] (Figure 4.29). The XRD results displayed in Figure 4.30 show that the alkyne-SURMOFs are highly crystalline and grows along the [001] direction on MUD SAMs. To carry out the thiol-yne click reaction, an ethanol solution of photoinitiator and alkyne terminated fluorescence molecule was added drop wise on the surface of the alkyne-SURMOFs. A quartz glass covered the top of wetted area to avoid the oxygen exposure. Then a photomask was applied to control the UV area exposure. After 5 min irradiation, the sample was

probed by fluorescence microscopy. As shown in Figure 4.29, a clear patterned fluorescence signal was observed, and confirmed the successfully patterned functionalization of the thin films using thiol-yne click reaction. Additionally, the XRD and IRR spectrum characterized the material before and after the PSM (Figure 4.31 A and B). The results demonstrated that a yield of 41% was obtained, and this without destroying the MOF structure.

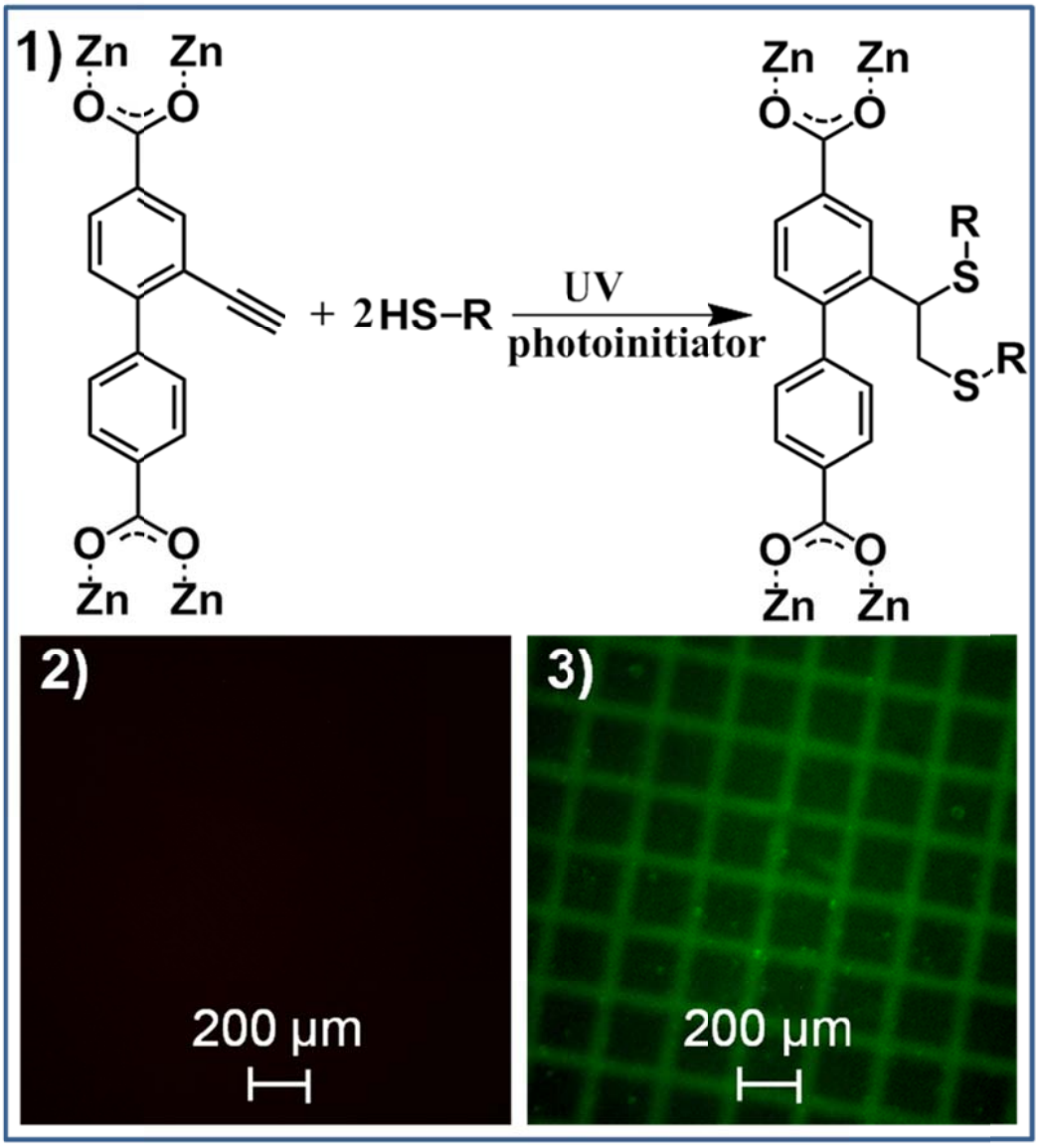

Figure 4.29: 1) Scheme of the photo-controlled thiol-yne Click Reaction of alkyne-BPDC Ligands in the [Zn_2(alkyne-BPDC)$_2$(Dabco)] SURMOF. (a) Before reaction and (b) after photo-controlled thiol-yne Click Reaction with thiol-functionalized fluorescent molecules of SURMOFs [Zn_2(alkyne-BPDC)$_2$(Dabco)].

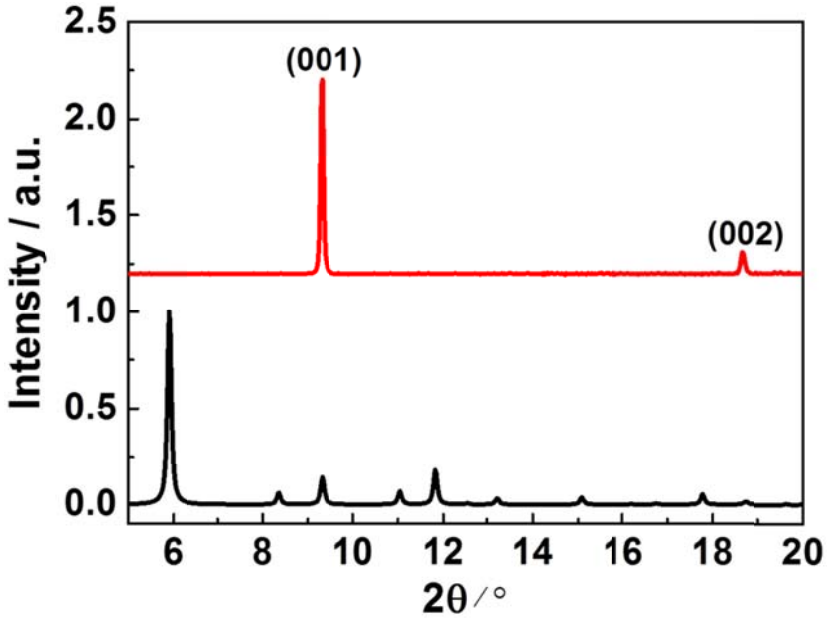

Figure 4.30: (Black curve) simulated XRD result of bulk [Zn(alkyne-BPDC)$_2$(Dabco)] and (red curve) experimental XRD result of SURMOF [Zn(N_3-BPDC)$_2$(Dabco)].

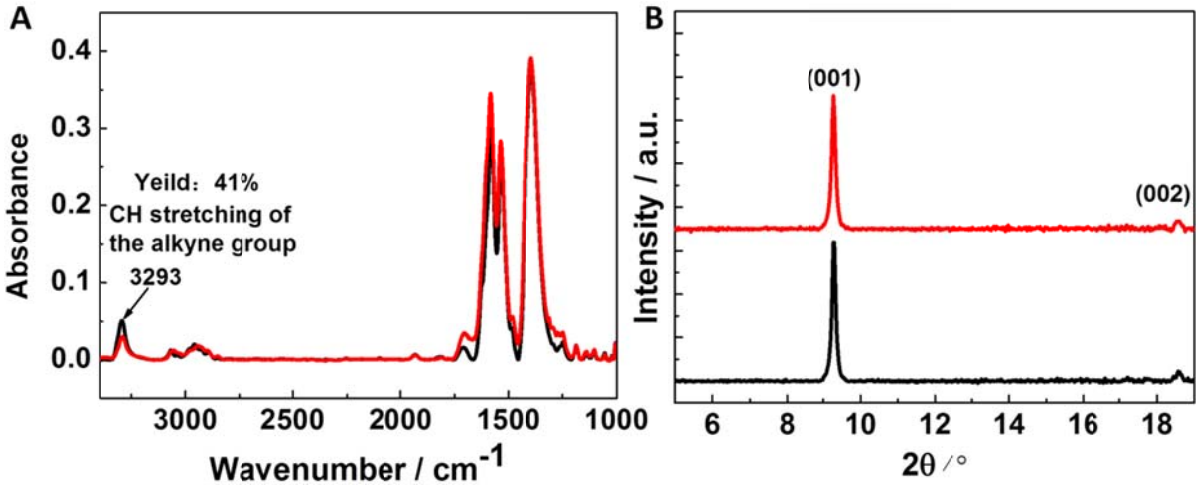

Figure 4.31: IRRA spectrum (A) and XRD patterns (B) of SURMOF [Zn_2(alkyne-BPDC)$_2$(Dabco)] before (black curve) and after (red curve) patterned modification of SURMOFs [Zn_2(alkyne-BPDC)$_2$(Dabco)] with thiol-functionalized fluorescent dye molecules controlled by photo irradiation.

4.3.6 Multiheteroepitaxy growth of layers-patterned SURMOFs and their post-synthetic modification.

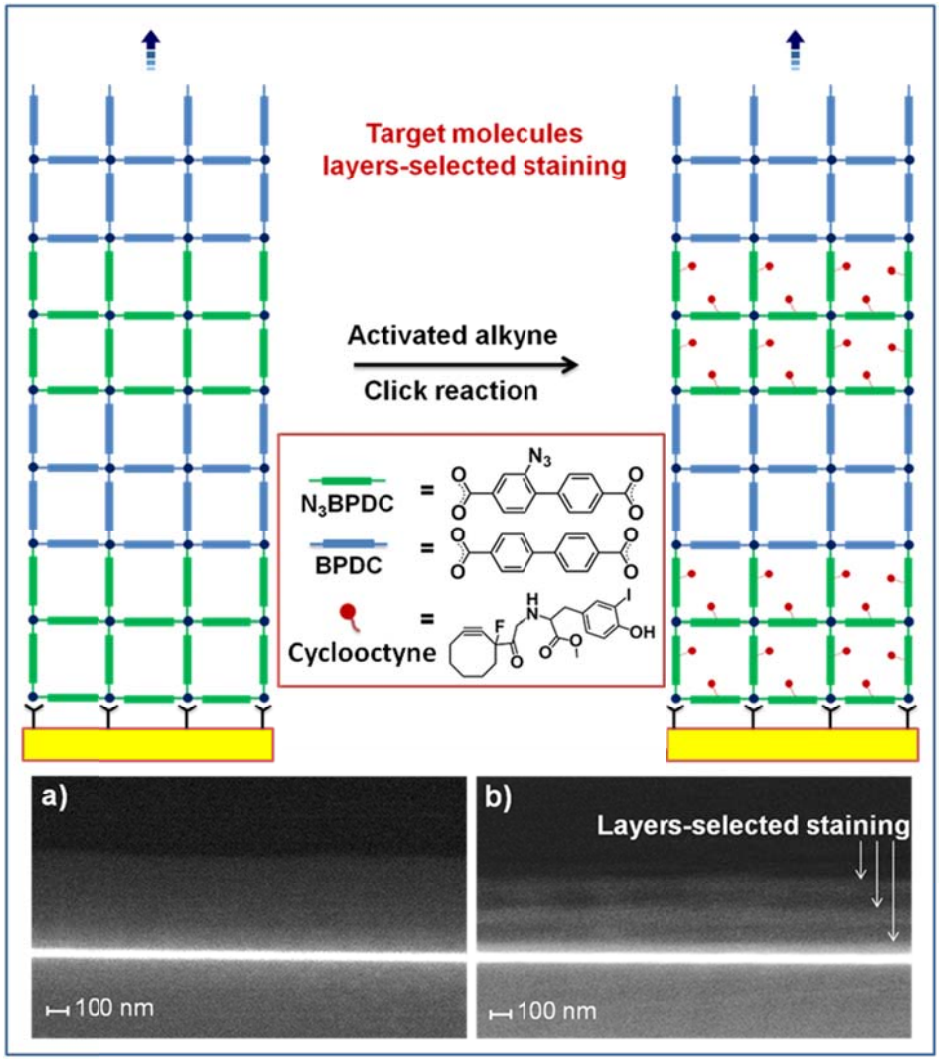

Figure 4.32: (Top) Schematic diagram of the selective staining of MOF layers in a multiheteroepitaxy Metal−Organic Frameworks system. Backscattered electrons of the multiheteroepitaxy Metal−Organic Frameworks system [Cu(BPDC)-on-Cu(N_3BPDC)-on-Cu(BPDC)-on-Cu(N_3BPDC)-on-Cu(BPDC) on-Cu(N_3BPDC)] before (a) and after (b) click reaction.

In contrast to the typical hydrothermal method for the synthesis of powder MOFs, the techniques for SURMOF fabrication deposit metal connectors and organic linkers on the modified substrate in a sequential fashion. This provides the opportunity to change the building blocks during the synthesis. This advantage was already demonstrated in the chapter 4.1 for the multiheteroepitaxy growth of MOFs with huge lattice constant gradients. The surface-functionalization of

SURMOFs and the MOF-on-MOF hetero-epitaxy growth of SURMOFs have been realized and the studies have suggested that such heterogeneous porous materials have great potentials for separation, selective adsorption or loading applications[182]. However, a definitive evidence confirming the clear stacking of distinct MOFs phases is lacking. The ability to obtain a multilayers-patterned functionalization of MOF films is also needed. Here a multilayers MOF system was realized with an automatic spray LPE system. As schematized in Figure 4.32 up, 40 cycles of Cu(N_3BPDC) were firstly grown on a MHDA modified gold substrate; thereafter, another 40 cycles of Cu(BPDC) were deposited on top of it. This was repeated to grow the multilayer MOFs system. XRD patterns and IRR spectra acquisitions confirmed the crystallinity

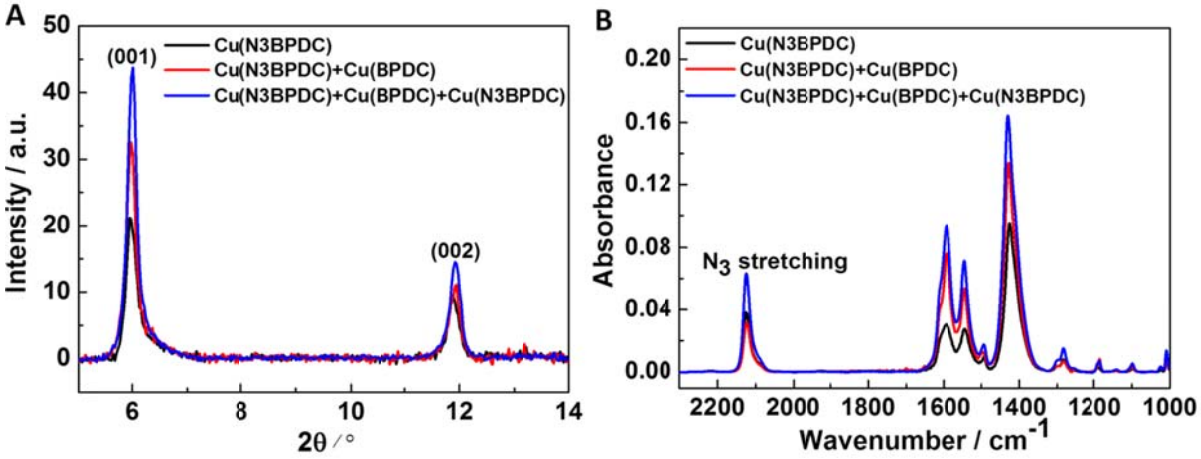

Figure 4.33: Step-wise monitor the multi-layer growth of SURMOF [Cu(N_3BPDC)+ Cu(BPDC)+Cu(N_3BPDC)] by XRD patterned (A) and IRRA spectrum (B).

and the azide functionalization (Figure 4.33). The azide groups allowed the click chemistry base PSM. The six layers system of [Cu(BPDC)-on-Cu(N_3BPDC)-on-Cu(BPDC)-on-Cu(N_3BPDC)-on-Cu(BPDC)-on-Cu(N_3BPDC)] was marked with a iodine compounds having activated-alkyne moieties, and selectively stained the MOF layers in a copper-free azide-alkyne cycloaddition click reaction. Since heavy elements, like iodine, backscatter electrons more strongly and appear brighter in the SEM images, backscattered electrons (BSE) were used to contrast between the MOF layers. The azide functionalized MOF layers were distinctively observed as appearing brighter through the PSM. The pictures (Figure 4.32 a and b) showed that a continuous, homogeneous and multilayers-patterned functional SURMOFs is formed.

In further development, a patterned modification will be achieved in the three spatial dimension, as schematized in Figure 4.34.

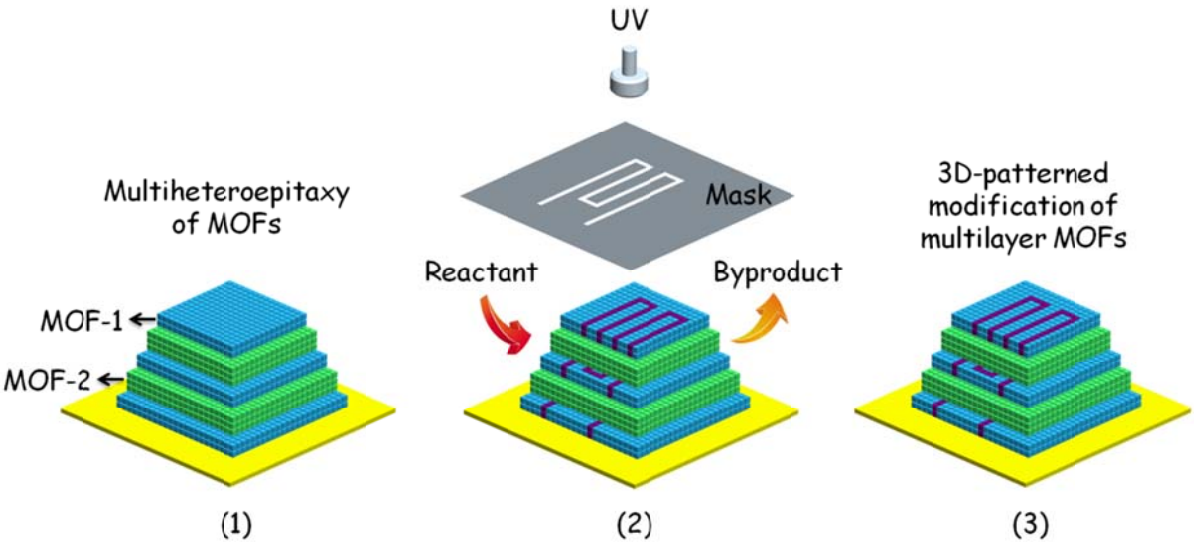

Figure 4.34: (1) Multiheteroepitaxy of MOFs with a stack of alternating MOF thin layers (MOF-1 and MOF-2). (2)photo-induced grafting reaction happened only in MOF-1.(3) a 3D-patterned functionalzation of multilayer MOF can be produced after the layer-selective modification.

4.3.7 Summary

In this study, patterned modifications of SURMOFs based on a photo-induced post-synthetic modification were presented, and showed that SURMOFs could be considered as excellent patterning and photoresist materials. The obtained results demonstrated that a combined top-down (UV lithography) and a bottom up (LPE spraying) approaches would allow reaching a 3D-patterned multi-functionalization of SURMOF films. This would allow for the development of great MOF-based devices. For an example, a photo-voltage cell, where the electron donor and electron accepter can be separately grafted on the different layers or different area of the SURMOFs could be possible. PSM have also been used to cross-link the linkers in bulk MOFs and SURMOFs, and this allows the metal nodes to be removed without dissolving the frameworks. As a consequence, 3D printed gel could be effectively realized using this elegant approach,

This chapter will be submitted as an article for publication and Prof. Stefan Bräse and Dr. Sylvain Grosjean synthesized the organic ligands (N_3-BPDC and Alkyne-BPDC) used in this study and detail information was displayed in chapter 6 (6.1).

4.4 Tunable coordinative defects in UHM-3 SURMOFs by post-synthetic thermal treatment and their application for gas adsorption

4.4.1 Background

MOFs that exhibit accessible coordinative unsaturated metal sites are particularly interesting for sensing and catalytic applications[225-227]. Such active sites not only improve the adsorption properties with regard to hydrogen (H_2)[228-230], methane (CH_4)[46], carbon dioxide (CO_2)[227], or carbon monoxide (CO) gases [226, 231], but also function as Lewis acid sites in catalytic applications[232, 233]. Only certain types of MOFs possess such active metal sites in their regular lattice. For example HKUST-1 displays open metal sites at the axial positions of the Cu(II) dimer[234]. However, studies reported that such active sites can also be generated via the introduction of defects, e.g. missing linkers. Wu and coworkers [235] have reported direct structural evidence in UiO-66 (University of Oslo-66) materials of such active defect sites due to the absence of linkers. Such defects strongly affect the CO_2 adsorption behavior of UiO-66, as shown by a striking CO_2 uptake enhancement with increased defect concentration. More recently, Fischer and coworkers have reported a series of defect-engineered MOFs (DEMOFs) made by adding small concentrations of linkers with a reduced number of carboxylate groups to the reactant solution[236, 237]. They have also demonstrated that the reduction of carboxylate groups coordinated to the Ru_2 paddle-wheel centers enhances CO adsorption and can catalyze dissociative CO_2 chemisorption as well as olefin hydrogenation reactions [237].

Another strategy to introduce or increase the number of defective (or undercoordinated) metal sites in MOFs is to apply a postsynthetic treatment. Vermoortele and coworkers have used postsynthetic treatment of MIL-100 with inorganic acids to increase the number of Lewis and Brønsted sites, resulting in higher activity and selectivity in Diels−Alder reactions[238]. Szanyi and co-workers have found that Cu(II) dimers in HKUST-1 can be reduced and oxidized to Cu(I) by postsynthetic thermal treatments. These reactions produce defects, where Cu(I) and Cu(II) entities coexist inside the hybrid structure, and increased the active site population[239]. Our previous studies have also confirmed that the Cu(I) defects in HKUST-1 SURMOFs can be induced by annealing treatment[99, 147]. Noticeably, Nijem and co-workers have reported that those Cu(I) defects in HKUST-1 exhibit a preferential adsorption of NO compared to H_2O [240]. A more thorough study on the induction of defect sites in these materials is however hampered to some extent by the fact that the nominally ideal material contains a synthetically inherent and relevant proportion of defective sites[147].

To tackle this issue, we focus on the fabrication of a different MOF, UHM-3, which also contains Cu-paddle wheel units. UHM-3[229], also referred to as PCN-12-Si (isoreticular to PCN-12 [228]), is constructed by the coordination of di-copper and 5,5'-(dimethylsilanediyl)diisophthalate

(dmsdip), a non-linear linker, the structure was displayed in Figure 4.35. It possesses a similar structure to HKUST-1, but has larger pores (1.3 nm diameter compared to 0.9 nm for HKUST-1). In this structure, the paddle-wheel units fit the 12 vertices of a cuboctahedron and connect each other through dmsdip linkers. As for PCN-12, these open metal sites result in a remarkably high hydrogen storage capacity (volumetric low pressure hydrogen physisorption isotherms at 77 K reveal an uptake of 2.6% (w/w) H_2 at 1 bar)[229].

In this chapter, we firstly report on the production of virtually defect-free UHM-3 SURMOF thin films. Subsequently, defects were induced in a quantitative fashion by postsynthetic thermal treatment. The liquid phase epitaxy (LPE) spraying method[241] was used to produce the surface mounted UHM-3 MOF thin films. X-ray diffraction (XRD) and IR characterization data were acquired to confirm the structure of the thin films, and the morphology of SURMOFs was checked by scanning electron microscope (SEM). Additionally, using X-ray photoelectron spectroscopy (XPS) and IR spectroscopy at low temperature (110 K) and under ultrahigh vacuum (UHV) conditions, we monitored the content of Cu(I) defects within the UHM-3 MOF thin film, as well as the possible controlled induction of such defects by postsynthetic annealing treatment. The XRD, XPS and IRRAS data were acquired for the samples annealed at the different temperature to confirm how the amount of Cu(I) defect would affect the order in UHM-3 structure. The obtained UHM-3 thin films with active defects showed, as revealed by subsequent IRRAS data, selective adsorption characteristics between CO and CO_2 gases within a 140 K to 200 K temperature range. This behavior was also confirmed by density-functional theory calculations (Contributed by Prof. Thomas Heine, Dr. Andreas Mavrantonakis and Dr. Barbara Supronowic).

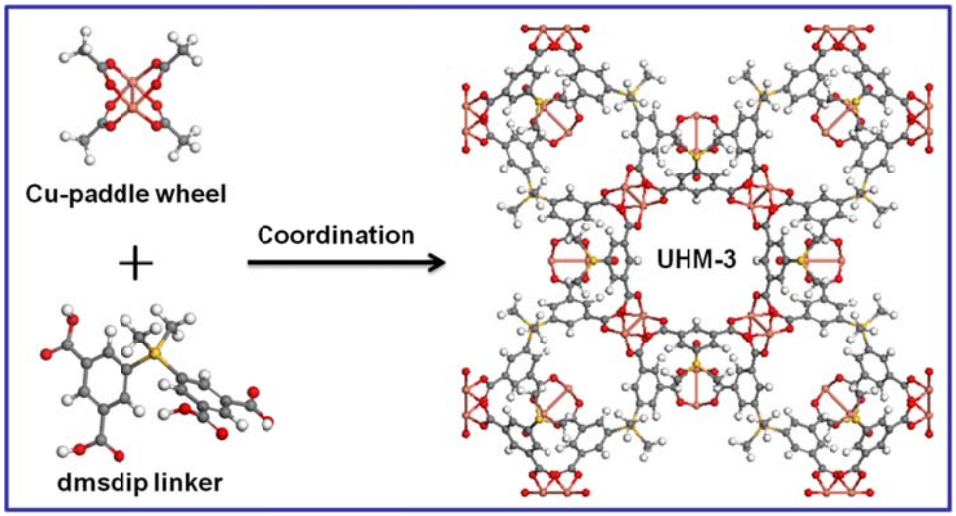

Fiure 4.35: Ball and stick representation of the building blocks of UHM-3: oxygen (red), hydrogen (grey), carbon (dark grey), copper (magenta) and silicon (yellow).

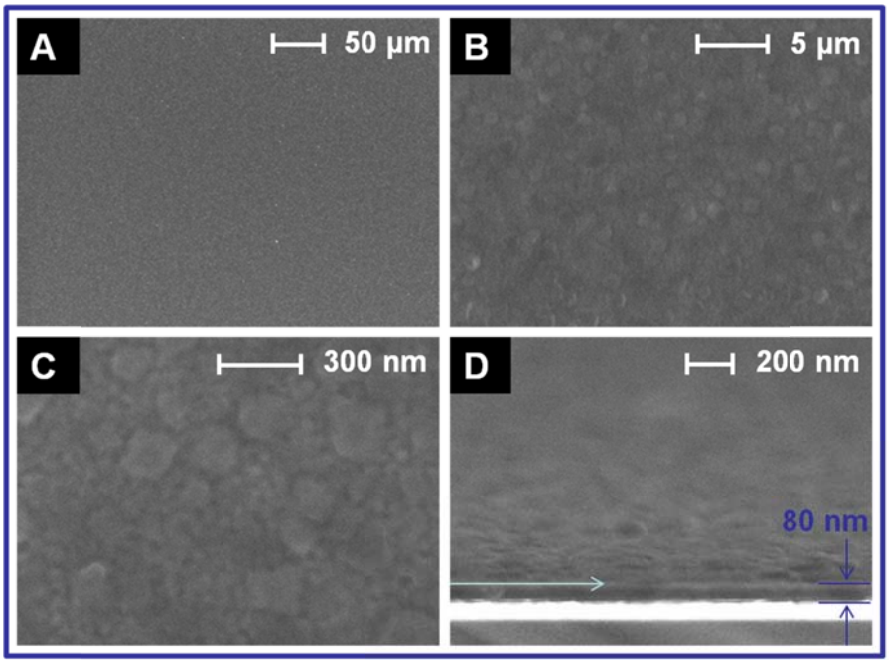

Figure 4.36: SEM top (a–c) and cross-sectional (d) micrograph views of UHM-3 SURMOFs at different magnifications: the fine grit observable in frame (a) originates from the crystal packing, as better seen in frames (b) and (c). The arrow in frame (d) indicates the top layer of the SURMOFs while the white strip directly underneath the SURMOFs thin film is the 100 nm thick gold layer.

4.4.2 Characterization of pristine UHM-3 SURMOFs

UHM-3 SURMOFs were grown on MHDA SAMs modified gold substrate by spray method displayed in chapter 1 (1.2.2.2)[100]. Here, the metal sources (1 mM copper acetate ethanol solution) and organic ligands (0.2 mM dmsdip ethanol solution) were used. Thereafter, the SEM images of the samples surface were acquired (Figure 4.36 a–c) at different magnifications and confirmed the fabrication of continuous and homogeneous thin films, having no visible cracks under all magnifications. Images of thin film cross-sections were also collected (Figure 4.36 d). The images showed that the thin films tightly adhered to the gold substrate and had a constant thickness of approximately 80 nm.

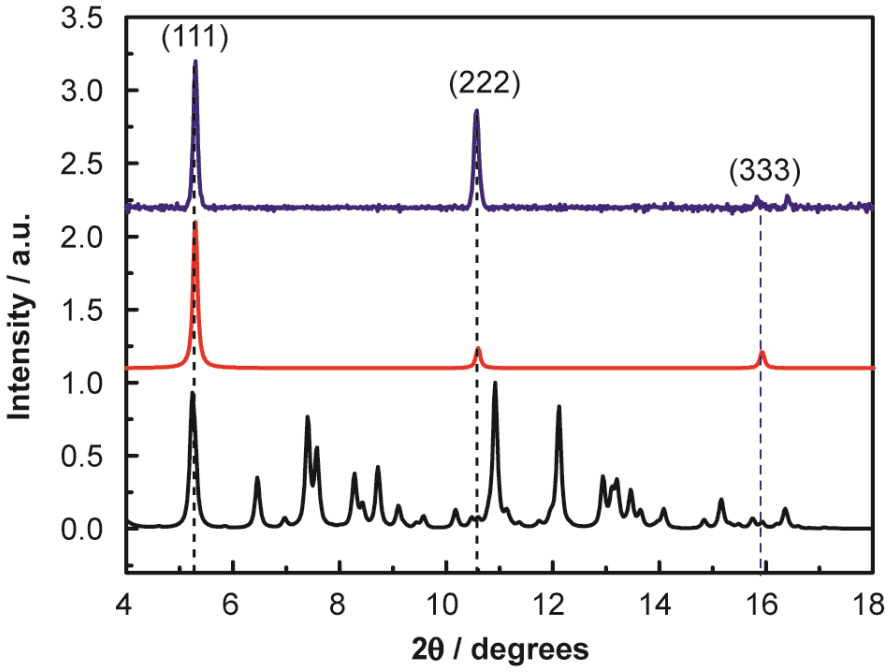

Figure 4.37: Out-of-plane XRD patterns: SURMOFs UHM-3 sample grown on a MHDA SAM surface (top curve), simulated diffraction pattern for a bulk MOF UHM-3 (bottom curve) and simulated diffraction pattern for a surface oriented MOF layer of UHM-3 (middle curve).

The structure of the LPE grown thin film was examined using XRD. A typical experimental pattern is displayed in Figure 4.37 (top curve). Compared to the diffraction patterns of the bulk UHM-3 material (Figure 4.37, bottom curve), only the peaks at the 2θ positions of 5.3°, 10.6°, and 15.9° appeared for the thin film sample. This is consistent with the XRD patterns of the bulk UHM-3 where the reflexes at 5.3°, 10.6° and 15.9° are assigned to the (111), (222) and (333) diffraction planes [229]. To aid the interpretation of these XRD-data, a diffraction pattern for a (111) oriented UHM-3 SURMOF layer was simulated (Figure 4.37, middle curve). The good agreement of the peak positions and the relative intensities between the experimental and the simulated patterns confirmed the presence of a well-ordered MOF thin film exhibiting a (111) orientation.

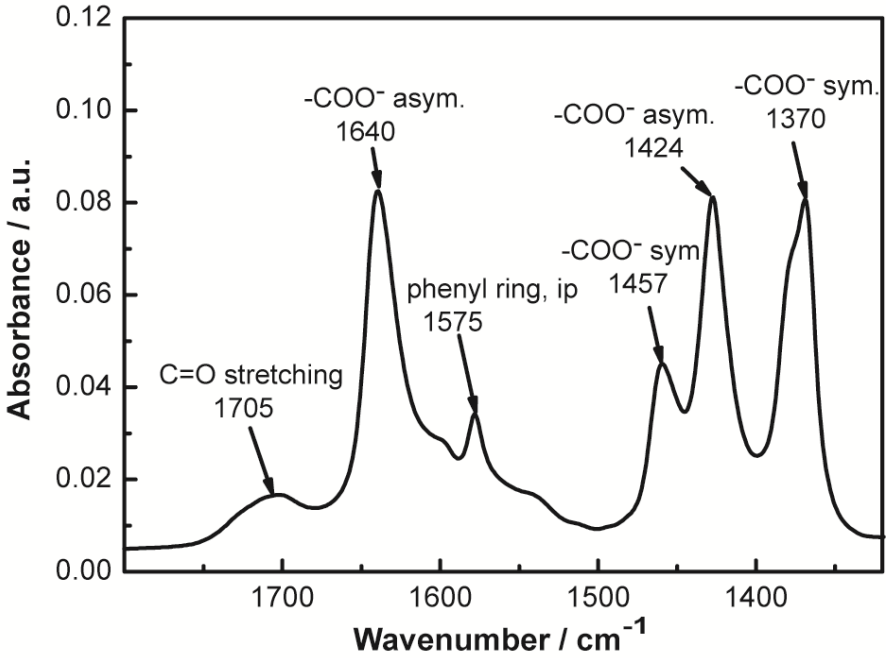

Figure 4.38: IRRA spectrum of UHM-3 SURMOF sample grown on a MHDA SAMs.

Chemical structure characterization of the pristine MOF thin film was also carried out using infrared spectroscopy. The corresponding IRRAS data displayed in Figure 4.38 shows characteristic asymmetric vibration peaks of carboxylate groups at 1640 cm^{-1} and 1424 cm^{-1}. The bands at 1457 cm^{-1} and 1370 cm^{-1} are assigned to the symmetric vibration of carboxylate moieties and indicated that such groups from dmsdip linkers had coordinated with copper ions to form the paddle wheel units. Additionally, we observed a very weak vibration band at 1705 cm^{-1} which is assigned to a C=O stretching vibration.

4.4.3 Coordinatively unsaturated dicopper units in UHM-3 SURMOFs

To identify the co-existence of Cu(II) and Cu(I) in UHM-3 SURMOFs, CO was used as a probe molecule since the stretching frequency of CO adsorbed to the metal centers within the porous MOF structure can be easily measured by IR spectroscopy and used to draw a conclusion on the charge state of Cu-ions[147]. The highly oriented and crystalline pristine UHM-3 MOF thin films were first characterized by IRRAS at low temperature (110 K) under UHV conditions. For the empty MOF, no vibrational bands were observed in the range of 2300–2000 cm^{-1} (Figure 4.39 a, black-colored dashed curve). After dosing CO (by backfilling the UHV chamber), a strong vibrational band at 2175 cm^{-1} was detected (Figure 4.39a black-colored continuous curve). This band is blue shifted by 32 cm^{-1} with respect to the gas phase CO frequency of 2143 cm^{-1} and is assigned to CO bound to Cu(II) sites[147]. Subsequently, the sample was heated to different temperatures, cooled back to low temperature and then again exposed to CO. The IR spectra

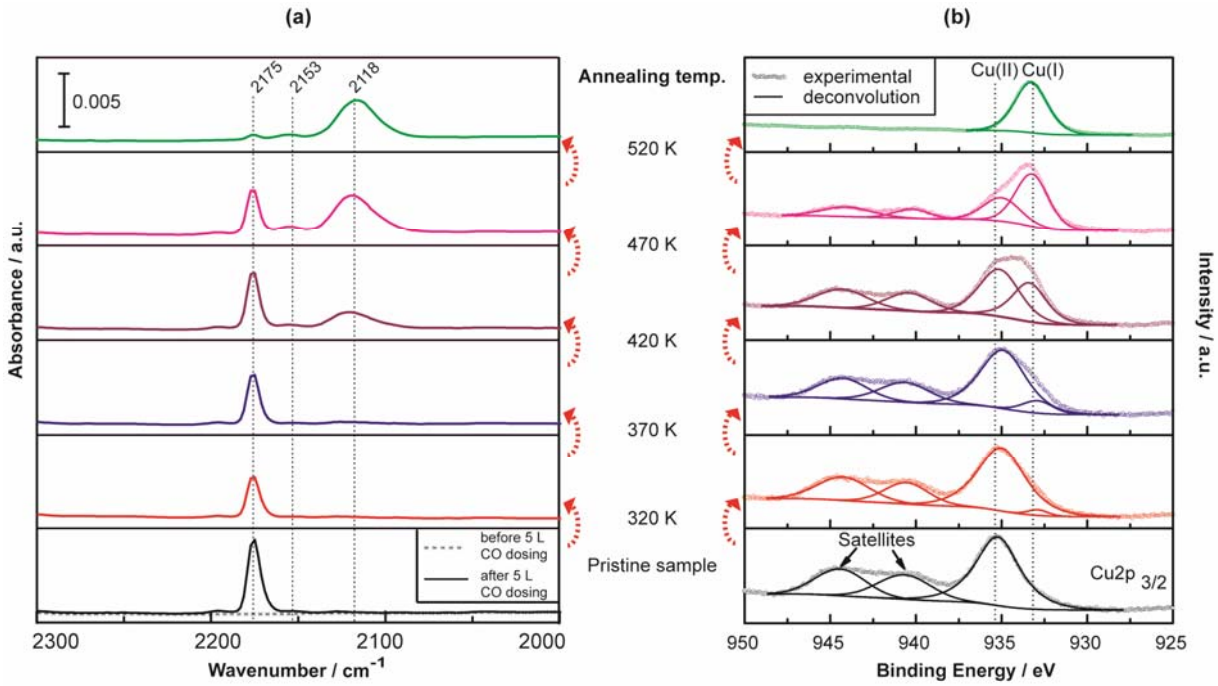

Figure 4.39: UHV-IRRA spectra (a) and XPS curves (b) of a UHM-3 SURMOF sample in a pristine state, and after successive annealing at 320 K, 370 K, 420 K, 470 K, and 520 K. At first and after each annealing, the sample was cooled down to 110 K before the measurements were carried out. XPS data for the copper 2p3/2 region are shown. XPS experimental curves are depicted with circles and the deconvoluted curves according to the Cu(I) and the Cu(II) populations with plain lines. IRRAS spectra were acquired before (dashed line) and after (plain line) a 5 L CO dosing.

depicted in Figure 4.39(a) upper panels show that for annealing to temperatures below 320 K no new vibration bands are detected. After annealing to 370 K a new, strong band at 2118 cm^{-1} as well as a weak feature at 2153 cm^{-1} were observed. Whereas the vibrations at 2118 cm^{-1} can be assigned to CO bound to Cu(I) sites [147], the origin of the weak band is unclear. Note the fact that the width of the band at 2118 cm^{-1} is clearly larger than the band at 2175 cm^{-1}.

The Cu(II/I) ratio in the UHM-3 SURMOFs was also determined using XPS (Figure 4.39b). XPS can be easily applied to SURMOFs supported on a metal but not to the powder material where electrical charging greatly complicates the data interpretation. The analysis of the XPS data (Table 4.2) shows that the Cu(I) defect density was below 1% in pristine samples, and that the amount of Cu(I) defects clearly increased when higher annealing temperatures were used, until all Cu(II) atoms were reduced to Cu(I) after annealing to 520 K.

Table 4.2 Results from XPS data fitting.

Temperature / K	Binding Energy / eV		Ratio / %
	Cu(I)	Cu(II)	Cu(I)/ [Cu(I)+Cu(II)]
300	-	935.2	<1
320	932.9	935.0	2
370	932.9	934.9	7
420	933.1	934.9	27
470	933.2	935.0	51
520	933.3	-	>99

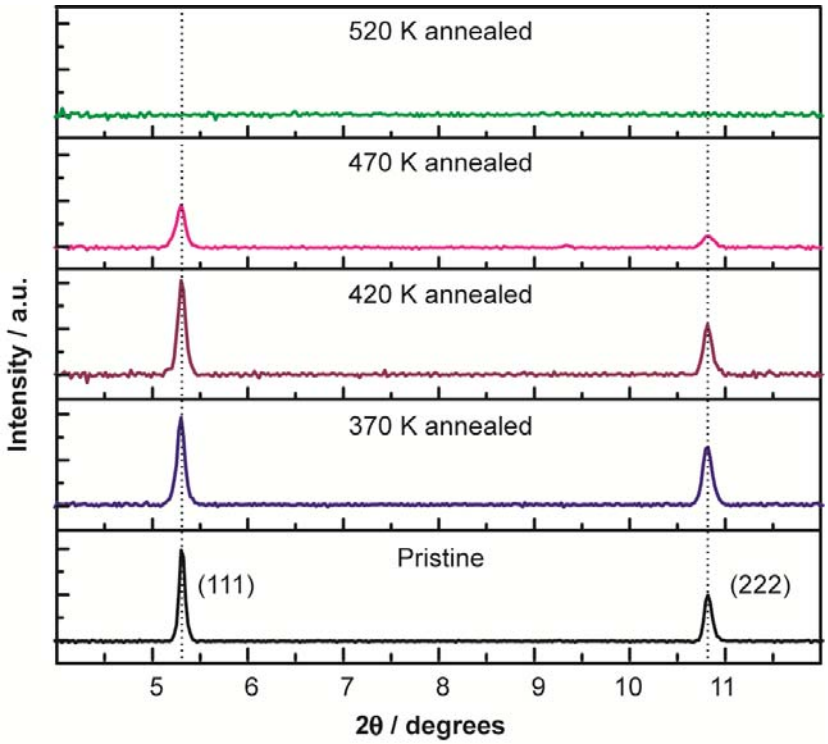

Figure 4.40: XRD patterns for UHM-3 SURMOF sample that were annealed at different temperatures.

The crystallinity of UHM-3 MOF thin films after annealing to different temperatures was analyzed by XRD. The XRD patterns shown in Figure 4.40 reveal no changes in the position and intensity of the reflexes up to an annealing temperature of 420 K, where the Cu(I) concentration amounts to 27%.

For higher annealing temperatures the intensity of the diffraction peaks decreased. The thin film lost its crystallinity (i.e. all diffraction peaks disappeared) after annealing to 520 K.

4.4.4 Adsorption of CO_2 and coadsorption of CO and CO_2 in UHM-3 SURMOFs with defects

Firstly, we monitored the adsorption of CO_2 at the metal atoms within the UHM-3 structure for different amounts of Cu(I) defects (see Table 4.2). Figure 4.41 shows the UHV-IRRAS results for pristine UHM-3 SURMOFs with different CO_2 amounts dosed. Already for small exposures (5L), a distinct peak at a position of 2336 cm^{-1}, assigned to CO_2 adsorbed at Cu(II) sites, was clearly observed. When increasing the CO_2 dosing, (Figure 4.41), the peak intensity increased, accompanied

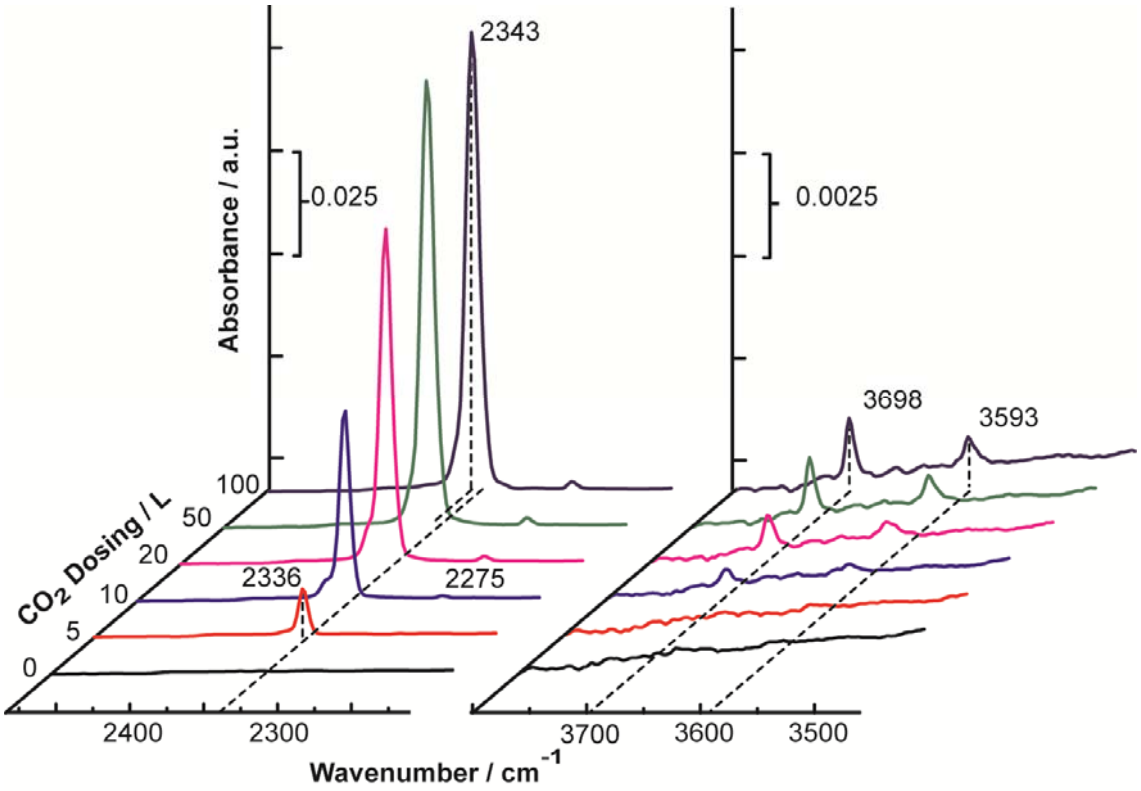

Figure 4.41: UHV-IRRA spectra from a pristine UHM-3 SURMOF sample with dosing different CO_2 amounts. All spectra were recorded at 110K.

by a slight blue shift to 2343 cm^{-1}. A weak feature at 2275 cm^{-1} was attributed to the minor natural occurrence of ^{13}C isotopes in CO_2. In the high frequency range (3800– 3500 cm^{-1}), two other vibration peaks were observed at 3593 cm^{-1} and 3698 cm^{-1} after increasing the dosages to 10 L.

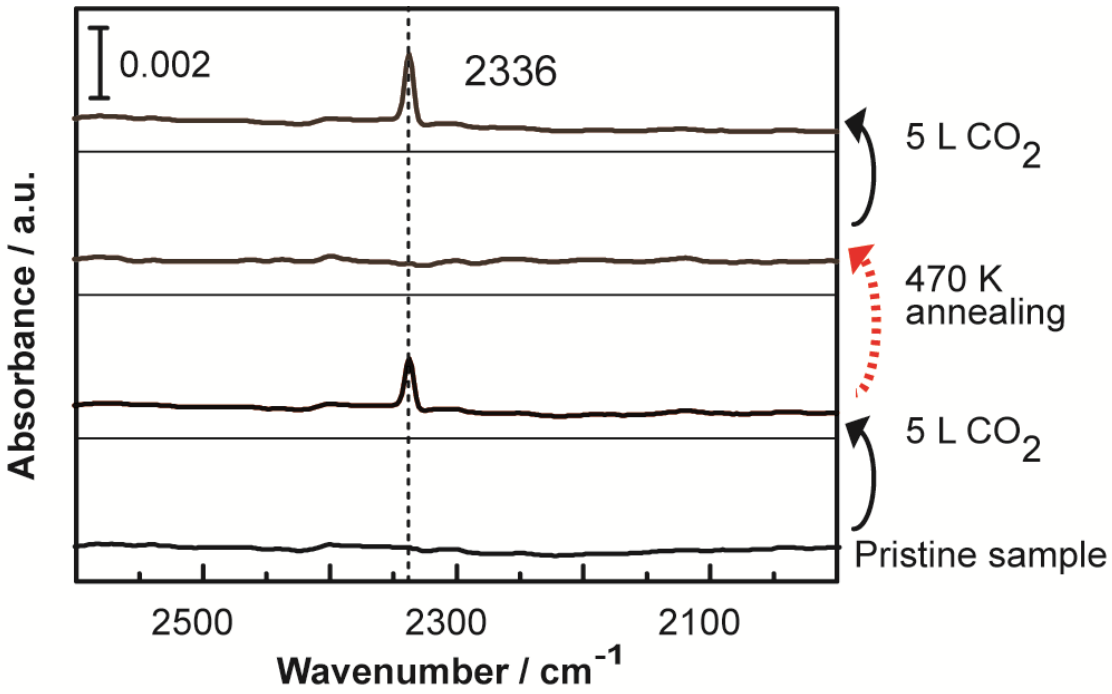

Figure 4.42: UHV-IRRA spectra of a pristine and then 470 K annealed UHM-3 SURMOF sample with dosing 5 L CO_2. All spectra were recorded at 110 K.

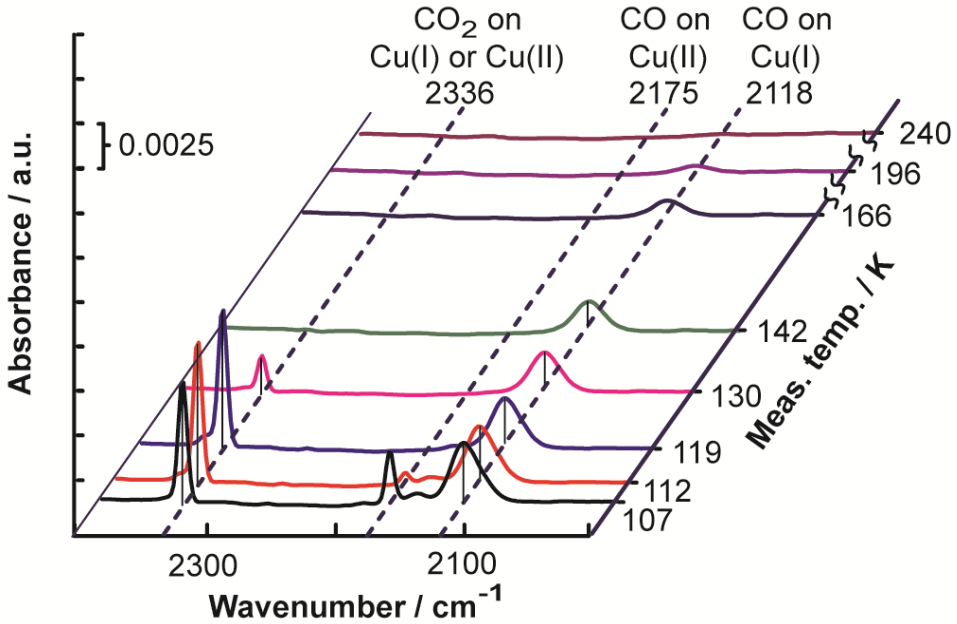

Figure 4.43: UHV-IRRA spectra of a 470K-annealed UHM-3 SURMOF sample with dosing CO and CO_2 mixture (1:1) at different temperature and showing a preferential desorption of CO.

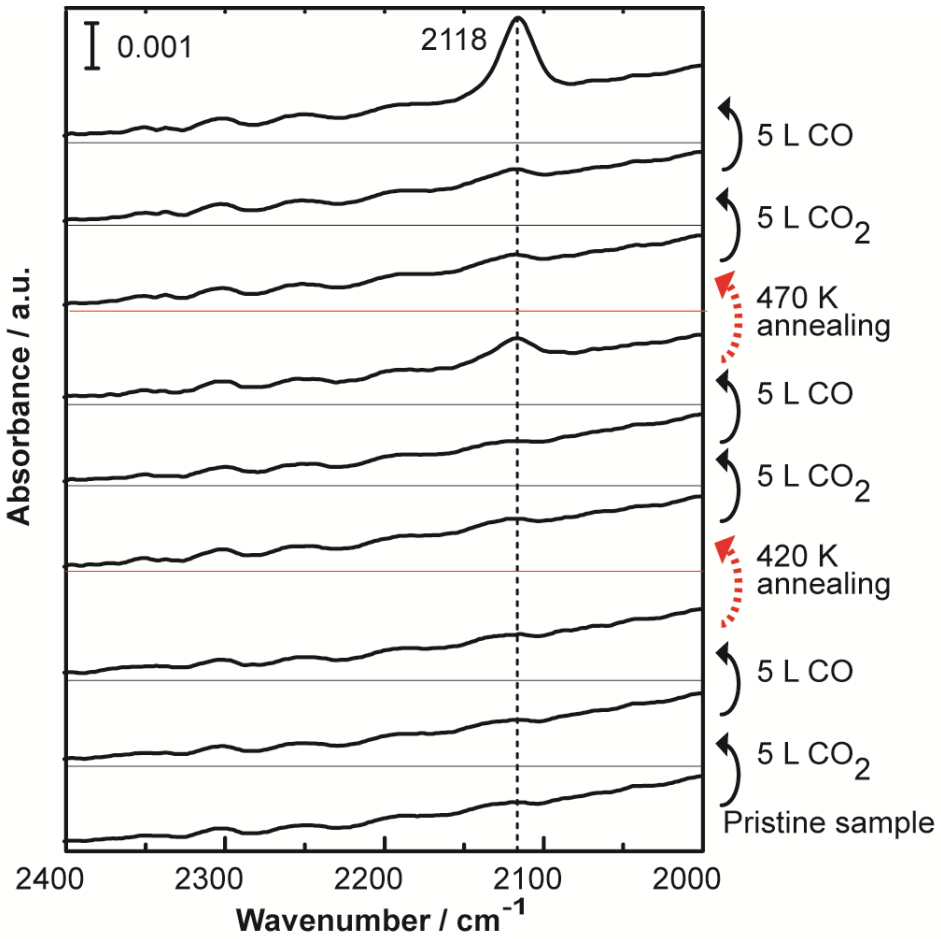

Figure 4.44: UHV-IRRA spectra of pristine UHM-3 SURMOF samples in a pristine state, after an annealing at 420 K and another at 470 K before and after dosing 5 L of CO_2 and 5 L of CO. All spectra were recorded at 160K.

Subsequently, the UHM-3 SURMOFs were heated to 470K (to generate Cu(I) sites) and then exposed again to CO_2. Surprisingly, no new bands were observed (Figure 4.42), revealing that CO_2 bound to Cu(I) has the same vibrational frequency as CO_2 bound to Cu(II). With another set of experiments, we examined the co-adsorption of CO and CO_2 on a SURMOF sample heated to 470 K. In such a sample, half of the Cu(II) ions were reduced to Cu(I) (Table 4.2). The sample was cooled down to 107 K and 5 L of a CO/CO_2 (1:1) mixture were dosed into the UHV chamber. The adsorption of both, CO and CO_2, species was clearly detected (Figure 4.43). Then, the temperature of the sample was increased stepwise and up to 240 K. After each step of increasing, an IR spectrum was recorded. We found that CO was completely desorbed from the Cu(II) sites at 119K. When increasing the temperature to 142 K, the CO_2 vibrations disappeared, whereas the vibration characteristic for CO bound to Cu(I) sites was still visible and disappeared only after heating to 200 K. The dosing and desorption experiment was repeated on the same sample and showed no

noticeable changes in the selective adsorption properties of the SURMOFs.

For a sample temperature of 160 K no adsorption of CO or CO_2 could be detected (see Figure 4.44). Only after creating Cu(I) species through annealing to 470 K (Figure 4.44) the IR spectra revealed the adsorption of CO within the MOF.

Table 4.3 Calculated B3LYP-D3 binding energies (kJ/mol), vibrational frequencies of CO (stretching mode) and CO_2 (asymmetric mode) on the Cu(I) and Cu(II) sites and their corresponding shifting with respect to the free gas molecules. The experimental vibrational shifts are also reported. The charge Forward- and Back-donation as calculated from the NBO analysis is also given.

Guest	Site (Modela)	BE (kJ/mol)[b]	$\Delta\nu_{calc}$ (cm^{-1})[c]	$\Delta\nu_{exper}$ (cm^{-1})[d]	Charge Forward-donation (guest → M)	Charge Back-donation (M→ guest)
CO	CuI (Defect)	-60.2	-42	-25	0.30	0.18
	CuII (Defect)	-20.4	+35	+32	0.27	0.05
	CuII (Pristine)	-23.2	+28	+32	0.22	NO
CO_2	CuI (Defect)	-23.8	-13	-13	0.04	NO
	CuII (Defect)	-23.9	-10	-13	0.04	NO
	CuII (Pristine)	-26.5	-10	-13	0.05	NO

[a]Defect corresponds to the $Cu_2(BTC)_3$ molecular model and Pristine to the $Cu_2(BTC)_4$.

[b]The binding energies include the Zero Point Energies and have been corrected for the BSSE.

[c]The calculated stretching frequency for free gaseous CO is 2220 cm^{-1} and the calculated asymmetric mode for free CO_2 is 2435 cm^{-1}.

[d]The experimentally observed frequencies for CO on the SURMOF are 2118 & 2175 cm^{-1} and for CO_2 is 2336 cm^{-1}.

4.4.5 DFT calculations

DFT calculations were contributed by Prof. Thomas Heine, Dr. Andreas Mavrantonakis and Dr. Barbara Supronowic from Jacobs University Bremen.

Results of the DFT calculations are summarized in Table 4.3 and the structures are shown in Figure 3.1 in the third chapter. At the B3LYP-D3 level, the binding energy of adsorbed CO_2 on both sites, that is, at Cu(I) and Cu(II) models, is -23.8 kJ/mol. The asymmetric stretching frequency of the adsorbed CO_2 molecule was reduced by 13 and 10 cm^{-1} for the Cu(I) and Cu(II) sites, with respect to

the free gaseous molecule. Results of the NBO and NPA calculations are summarized in Table 4.3 and the most important NBOs are shown in Figures 4.45 and 4.46. For adsorbed CO, the calculations reveal a significant charge transfer of 0.2 |e| from CO to the Cu(II), whereas for the Cu(I) the charge transfer is substantially smaller with0.1 |e| . In the case of CO_2, the charge transfer is negligible (0.04 |e|) for both the Cu(I) and Cu(II) centers.

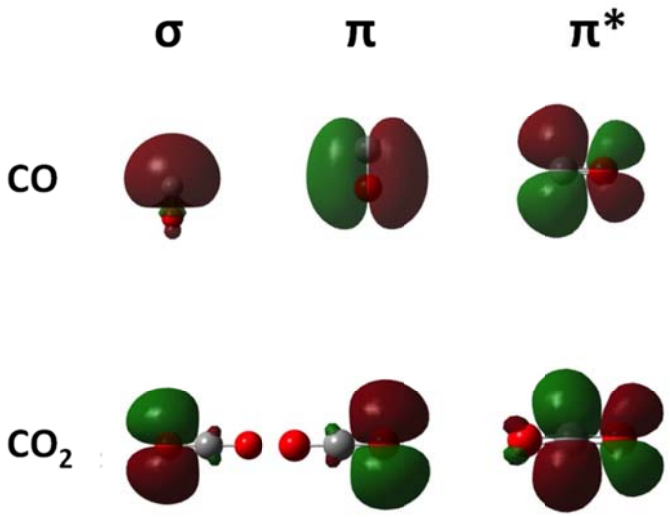

Figure 4.45: The most important NBOs of CO and CO_2.

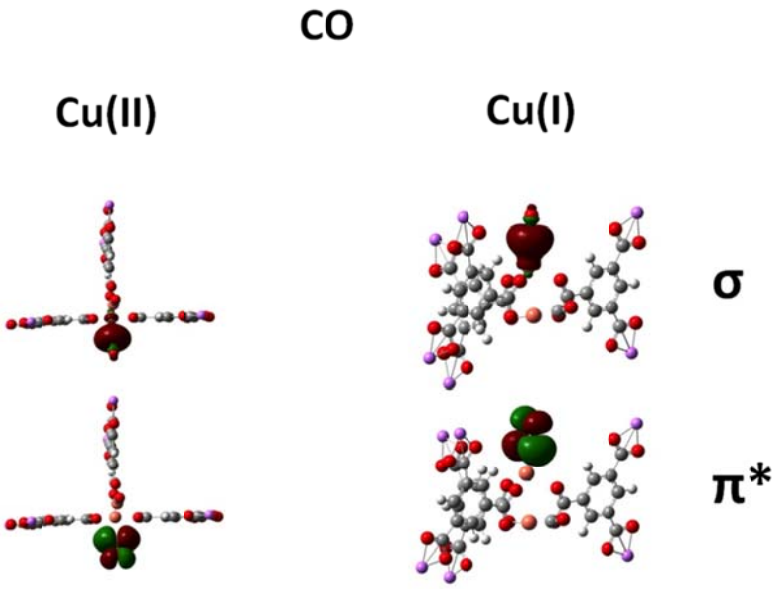

Figure 4.46: σ and π antibonding NBOs of CO that contribute to Forward- and Back-donation of charge respectively.*

4.4.6 Experimental results and discussion

The XRD, IR, SEM and XPS data demonstrated that with the LPE fabrication process, well-defined, homogeneous, and highly oriented MOF thin films with the same structure as bulk UHM-3 were grown. The XRD results also confirmed that these UHM-3 films were highly crystalline, and that the obtained crystals grew along the [111] direction only (Figure 4.37). In the pristine films the density of Cu(I) defects was below 1%, an amount clearly lower than the 4% observed in the related HKUST-I material that has been fabricated with the same deposition method [147].

In the ideal UHM-3 structure, the coordination of a Cu(II) dimer with four carboxyl groups of the linkers yields a fully coordinated paddle wheel unit (Figure 4.35). The XPS data, as well as the CO-adsorption results, demonstrated that the applied annealing treatment induced a partial reduction of Cu(II) to Cu(I). In the absence of any other possible reductive species than the linkers (heating was carried out under UHV-conditions), we propose that either a Cu(II)-catalyzed oxidative decarboxylation or a Cu(II)-catalyzed cross coupling of the linkers occurred. Such reactions have been known for a long time [242], but have not yet been studied under the present conditions (part of a porous solid, vacuum). Further investigations will be required to identify the details of this reaction in more detail. In any case, the reduction of the Cu(II) to Cu(I) will lead to a loss of carboxylate moieties that coordinate to the Cu dimers. The XRD and XPS results demonstrated that a small amount of missing carboxylate groups did not affect the crystalline structure of the UHM-3. Even at a relative Cu(I) concentration of 27%, the UHM-3 structure was still essentially intact (Table 4.2 and Figure 4.40). However, at a defect concentration of 50.9 %, the XRD data revealed that the structure had collapsed, with the intensity of the diffraction peaks decreasing drastically. After a 520 K annealing, the XPS data showed the total reduction of Cu(II) to Cu(I), and no XRD peak was observed. These results demonstrated that it was possible to induce a fairly high density of defects without losing the ordered packing of the paddle wheel units in the UHM-3 structure when annealing temperatures between 420 K and 470 K were used. This is in agreement with the results of Wenzel and coworkers who have found their powder UHM-3 MOF samples to be still highly crystalline after a 24 h post-synthetic thermal treatment in vacuum at around 420 K (150 °C)[229].

The vibration at 2175 cm^{-1} can be clearly assigned to CO bound to Cu(II) species in structurally flawless parts of the UHM-3 SURMOFs. An investigation of the temperature dependence of this peak (see Figure 4.43) revealed a continuous decrease until heating up to 119 K, above which temperature the peak completely disappeared. A quantitative analysis results in a binding energy of 0.34 eV, a value identical to the one reported previously for HKUST-I[147]. The vibrations at 2118 cm^{-1} arising from CO bound to Cu(I) sites showed a similar temperature dependence. In this case, however, the peaks were visible for temperatures up to 200 K. This corresponds to a binding energy of 0.46 eV which is again similar to the value reported for HKUST-I[147].

The experimental data suggest that CO_2 binds weakly to the Cu(II) species in pristine UHM-3 with an asymmetric stretch frequency of 2336 cm^{-1} for a low loading, which shifts to 2343 cm^{-1} for higher CO_2 loading. We attributed this small blue shift to inter-molecular couplings that occur when multiple CO_2 bind to the same Cu(II) site. The two vibrational peaks observed after dosing 10 L at 3593 and 3698 cm^{-1} are tentatively assigned to ν_1 (symmetric stretching) and ν_3 (asymmetric stretching) mode combination overtones.

Surprisingly, the vibrations for CO_2 bound to Cu(II) and Cu(I) appeared at the same position in the IRRA spectra. This unexpected insensitivity to the charge state of the Cu ions can be understood on the basis of the DFT calculations. They reveal a rather weak interaction of the molecules with both, Cu(I) and Cu(II), and – in contrast to CO – only a very small charge transfer. The theoretical results for the CO_2 ν_1-shift relative to the gas phase, -10 cm^{-1}, are in excellent agreement with the experimental value of -13 cm^{-1}.

The computed binding energies are presented in Table 4.3. According to the B3LYP-D3 calculations, CO on Cu(I) has the largest binding energy with around -60 kJ/mol, and CO_2 on Cu(I)/Cu(II) has an energy around -24 kJ/mol, relatively close to the approximately -20 kJ/mol obtained for CO on Cu(II). The CO/Cu(I) and CO/Cu(II) binding energies are fully consistent with previous experimental and theoretical work. The theoretical CO_2/Cu(I) and CO_2/Cu(II) binding energies are slightly lower than the value (36 kJ/mol) calculated from the temperature dependent disappearance of the IR vibration peak upon heating (Figure 4.43).

The NBO analysis shows that the binding to the differently charged Cu-ions, Cu(I) and Cu(II), is rather different for CO, but essentially identical in case of CO_2 (Table 4.3). In the case of CO, there is a constant donation of ~0.30 |e| from the C atom to the metal through the σ bond to both, Cu(I) and Cu(II). For the Cu(II) binding, the calculations reveal a negligible back-donation of ~0.05 |e| from the metal to the CO π* antibonding orbitals. For adsorption at Cu(I), this back-donation is much stronger with 0.18 |e|. This explains the higher binding energy for Cu(I). The relevant NBOs of CO that are participating in the interaction with the metal sites are shown in Figure 4.46. The overall charge transfer is 0.20 |e| for Cu(II) and only 0.1 |e| for Cu(I).. In the case of CO_2, an identical behavior with the Cu(I) and Cu(II) centers is calculated with a negligible charge transfer of 0.04 |e| from the CO_2 molecule to the MOF. Upon interaction with the metal site, a redistribution of the electron density is occurring from the carbon and distant oxygen atoms towards the oxygen atom closest to the metal. The proximal oxygen atom receives an excess of electron density in comparison to a free unperturbed molecule, whereas the carbon and the distant oxygen atoms loose electron density (Figure 4.47). This explains why the CO_2 molecule interacts in the same manner with Cu(I) and Cu(II), whereas CO shows different behaviors.

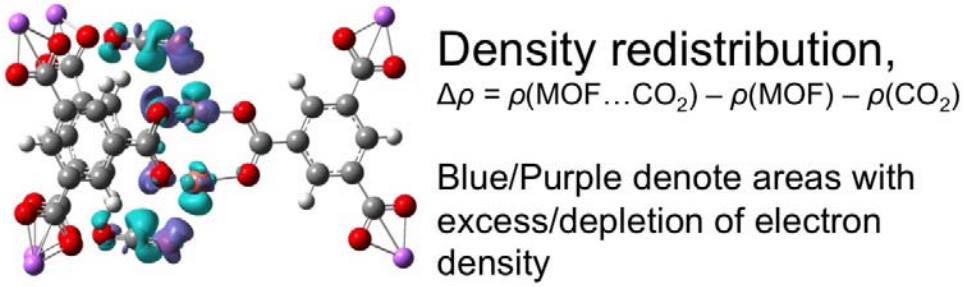

Figure 4.47: Plot of the electron redistribution upon interaction of CO_2 with the Cu(I) and Cu(II) sites. Densities plotted with a contour value of 0.001 e•A^3.

To investigate the gas separation properties of the material, an annealed sample with a Cu(I) concentration of 51% was exposed to a mixture of CO and CO_2. The IRRA spectra showed that only CO bound the UHM-3 in the temperature range of 140-200K.

4.4.7 Summary

In this work, UHM-3 MOF thin films were grown using a LPE based method at room temperature on a gold substrate coated with a COOH terminated SAM. The XRD results demonstrated that the produced SURMOFs were highly crystalline and oriented. CO adsorption experiments, as well as XPS measurements, revealed a very low Cu(I) defect density quantified below 1%. Defects were induced in a controlled fashion by an annealing treatment that caused a reduction of Cu(II) to Cu(I). Up to a Cu(I) concentration of 27%, no major degradation of the crystalline order was observed. Whereas the binding energy of CO to Cu(I) is substantially stronger than to Cu(II), the binding of CO_2 is very similar with both Cu species. DFT calculations were fully consistent with the experimental findings and confirmed that the chemical interaction of CO_2 with Cu(I) and Cu(II) is rather weak, as, in contrast to the binding of CO to Cu(I) and Cu(II), no charge transfer seems to occur. Also, the calculated vibrational modes were in excellent agreement with the experimental observations. Our results demonstrated that post-synthetic annealing offers an interesting alternative to produce MOFs containing different concentration of defects.

This chapter will be submitted as an article for publication and Prof. Michael Fröba, Dr. Stephanie E. Roggenbuck and Dr. Katharina Peikert synthesized the organic ligands (5,5'-(dimethylsilanediyl)diisophthalate) used in this study.

5 Conclusions

This PhD thesis showed the preparation, characterization and application of new-type surface mounted metal-organic frameworks (SURMOFs). Liquid phase epitaxy (LPE) process was used for growing the thin films on functionalized substrates, as this layer-by-layer procedure yields highly oriented and crystalline MOF thin films. The growth orientation was controlled through having a substrate SAMs coating with specific functional group terminations. Additionally, the layer-by-layer procedure allowed controlling the film thickness by adjusting the number of growth cycles. The crystal structure and chemical composition of the produced SURMOFs were determined by X-ray diffraction (XRD) and infrared reflection-adsorption spectroscopy (IRRAS). The resulting data showed the quality of the samples and confirmed the reliability of the method. The objective of this thesis was focused on constructing functional SURMOFs, as well as, tuning their reactivity for challenging applications.

Since the layer-by-layer approach allows us to separately control the deposition of metal and organic linker on the substrate, it advantageously enables changing the composition of the SURMOFs along the growth direction during the fabrication. This was put into practice, and a hierarchically organized MOF multilayer system with pronounced differences in the size of the nanoscale pores was successfully realized at first. The huge lattice constant variability was obtained by depositing integratively the components of SURMOF-2 structures namely Cu-BDC, Cu-NDC and Cu-BPDC, with lattice constants of 1.12, 1.34, and 1.55 nm respectively. The out-of-plane and in-plane XRD results confirmed the crystallinity and orientation of this tri-layer (or ternary phase) system, and demonstrated that lattice constant increase (Cu-BDC+Cu-NDC+Cu-BPDC) and decrease (Cu-BPDC+Cu-NDC+Cu-BDC) were both possible despite the rather pronounced lattice mismatch (19.6% and 15.7%, respectively). A collaboration with the theoretical chemistry group of Prof. Thomas Heine and Dr. Binit Lukose was initiated to understand this remarkable mismatch tolerance that a thorough theoretical analysis of the MOF-on-MOF heterojunction structure and energetics was carried out. The vacancies left by the huge lattice mismatch can be healed with acetate groups that originate from the applied metal source reactant, since MOFs present available pore space that acetate groups can easy diffuse into for annihilating the vacancies. This theoretical hypothesis was confirmed experimentally: since fluor-labeled acetate has a specific IR absorption, it was used as a marker to reveal the presence of acetate ligands at the heterojunctions by IRRAS. The theoretical analysis also demonstrated that the low elastic constant of MOF materials can help them overcome the excess strain induced from the huge lattice mismatch. In all, the results indicated that the epitaxial growth of integral hetero MOF thin film with huge lattice mismatch was possible. This extends the possibilities for the fabrication of functional and complex MOF systems fabrication for the realization of more advanced application, such as multilevel filtering systems and MOF-based sensors.

The focus in the second part was on the fabrication of MOFs with defined functional group distribution within the material or over its surface, and on the subsequent (i.e. post fabrication) chemical modification of these active groups. Post-synthetic modification (PSM) provides additional pathway to obtain MOFs materials otherwise not realizable with a direct synthesis process. A strategy based on azide-functionalized MOF was established and layer-pillar MOFs [$Zn_2(N_3\text{-bdc})_2$(dabco)] were synthesized. The out-of-plane and in-plane XRD results demonstrated that SURMOF [$Zn_2(N_3\text{-bdc})_2$(dabco)] were grown on MUD-SAMs modified substrate with [001] orientation. PSM was carried out based on the linker azide group reactivity. Two different reaction pathways were used namely Cu(I)-catalyzed azide-alkyne click reaction (CuAAC) and strain-promoted azide-alkyne click reaction (SPAAC). The IRRAS and XRD results demonstrated that both reaction pathways succeeded in the PSM of [$Zn_2(N_3\text{-bdc})_2$(dabco)]. Advantages and disadvantages of both methods were revealed by comparing each other. In the case of CuAAC, cytotoxic Cu(I) ions, that cannot be removed completely after the reaction, would be a drawback for the biological applications. Additionally, three species (azide, Cu(I) catalyst, and alkyne) have to meet in close proximity to initiate the reaction. This is a challenging condition given the limited diffusion of reactants through the nanopores, and resulted in low reaction yield. Both problems could be overcome by SPAAC, where a metal catalyst is not needed. After optimization of the reaction conditions, conversion yields of nearly 100% were achieved. Though the synthesis of active alkyne derivatives required more complicated procedures compared to the common alkyne derivatives, SPAAC-based PSM of MOF materials should attract considerable attention for application in the fields of biomedicine, or proton and electron transport.

The ability to obtain patterned SURMOFs is also essential for the development of MOF-based devices. Here patterned SURMOFs could be grown on a patterned SAMs, since the terminal groups such as –COOH or –OH on the SAMs provide the primal and only ligation of metal connectors. Micro contact printing (μCp) technique was used to produce these –OH terminated patterned SAMs. Patterned SURMOF [$Zn_2(N_3\text{-bpdc})_2$(dabco)] were grown on such SAMs with [001] orientation using a robot dipping apparatus comprising a ultrasonic cleaning process. This yielded uniformly patterned MOF thin films with high quality and high selectivity. The morphology and roughness was determined using optical microscopy and atomic force microscopy. Additionally, fluorescence dye markers were used to label the patterned SURMOFs based on a SPAAC reaction scheme. The fluorescence images confirmed the labeling was successful and the patterned SURMOFs were formed. Since the azide-alkyne reaction used for the PSM can be influenced by the UV-induced reduction of Cu(II) to Cu(I), the functional patterning of monolithic SURMOFs was achieved and the functional groups were specifically localized in the MOF structure. Such experiments were performed using a photo mask and only irradiated parts reacted as evidenced by the fluorescent images when using alkyne terminated

dye molecules as reactants. However, the azide group could also be destroyed by UV irradiation, which at first appeared as a drawback with this reaction scheme. This was used as a strategy for functional patterning. In a first step, a SURMOF-2 namely [Cu(N_3BPDC)] was synthesized and the azide groups in the SURMOFs were locally destroyed by UV exposure through a photo mask. As a result, the subsequent SPAAC reaction could only occurred in the non-irradiated areas. This was also confirmed by the fluorescent images when active alkyne terminated dye were used as reactant. In addition, photo-induced thiol-yne click chemistry was also used for the functional patterning of SURMOF [Zn_2(alkyne-bpdc)$_2$(dabco)]. To realize a 3D functional patterning of SURMOFs, a six-layers MOF system (Cu-N_3BPDC+Cu-BPDC+ Cu-N_3BPDC+Cu-BPDC+Cu-N_3BPDC+Cu-BPDC) was synthesized and the azide groups allowed the later staining with iodo-labelled reactant using SPAAC reaction. This multilayer system was imaged by SEM with the detection of backscattered electrons since material with heavy elements like iodine should scatter electron more strongly. This revealed the successful growth of such multilayer system that should bring the control into the three spatial dimensions for the modification of SURMOFs.

In the fourth part, the defect engineering of SURMOFs and its application for adsorption of gas molecule such as CO and CO_2 were investigated. The presence of Cu(I) defects in Cu(II)-based MOFs usually makes the material more reactive. Here, UHM-3, a Cu(II) paddle wheel composed MOF, was investigated. The SURMOFs were grown on MHDA-SAMs along the [111] orientation. The SEM images demonstrated the resulting UHM-3 MOF films being continuous and homogenous with no evidence of cracks. Exposure of the UHM-3 SURMOF to carbon monoxide (CO) adsorption experiments, as well as XPS measurements, revealed a very low density of Cu(I) defects (<1%) in pristine film (i.e. before annealing). The postsynthetic annealing under ultra-high vacuum allowed a controlled induction of Cu(I) defect sites, through the reduction of Cu(II). XRD results demonstrated that a small quantity of defects (up to a Cu(I) concentration of 27%) did not affect the crystalline order. Both theoretical (Contributed by the group of Prof. Thomas Heine, Dr. Andreas Mavrantonakis and Dr. Barbara Supronowic) and experimental results demonstrated the bonding energy of CO/Cu(I) being higher than that of CO/Cu(II) and CO_2/Cu(I)+Cu(II). The selective adsorption with CO–CO_2 mixture at temperatures ranging from 140 to 200 K, showed the potential of such a fabrication and modification strategy to produce materials for gas separation.

6 Appendix

6.1 Synthesis of chemical compounds

Synthesis of 2-azidoterephthalic acid (N_3-BDC).

The synthesis was done by Prof. Stefan Bräse and Dr. Sylvain Grosjean from Karlsruhe Institute of Technology.

2-Aminoterephthalic acid (2.000 g, 11.04 mmol, Aldrich) was dissolved in tetrahydrofuran (THF, 150 mL); *tert*-butylnitrite (3.972 mL, 33.12 mmol) was added at T = 0 °C. After 15 min of stirring, trimethylsilylazide (2.904 mL, 22.08 mmol) was added at T= 0 °C, and then the reaction mixture was allowed to proceed to room temperature and stirred for 48 h. The reaction mixture was concentrated under reduced pressure, and the crude product was purified by column chromatography on silica gel (90:9:1 ethyl acetate/ tetrahydrofuran/acetic acid). After chromatography, the solid obtained was washed with water and hexane and then air-dried to give 2-azidoterephthalic acid (N_3-BDC) as a pale yellow solid (2.018 g, 88%). ^{1}H NMR (500 MHz, DMSO-d_6, ppm) δ: 13.45 (b-s, 2H, CO_2***H***), 7.84 (d, 1H, J = 8.5 Hz, C***H***$_{Ar}$), 7.78−7.76 (m, 2H, C***H***$_{Ar}$). ^{13}C NMR (125 MHz, DMSO-d_6, ppm) δ: 166.2 (***C***O_2H), 166.0 (***C***O_2H), 138.8 (***C***$^{IV}_{Ar}$), 134.6 (***C***$^{IV}_{Ar}$), 131.2 (***C***H$_{Ar}$), 127.9 (***C***$^{IV}_{Ar}$), 125.4 (***C***H$_{Ar}$), 121.1 (***C***H$_{Ar}$). IR (ATR, cm^{-1}): 2121, 1682, 1564, 1495, 1397, 1245. HRMS (EI) *m*/*z*: calcd for $C_8H_5N_3O_4$ $[M]^+$, 207.0280; found $[M]^+$, 207.0282.

Synthesis of the Cyclooctyne Derivative.

The synthesis was done by Prof. Stefan Bräse and Dr. Tobias Hagendorn from Karlsruhe Institute of Technology.

Cyclooctyne derivative 1 (compound 1, Figure 6.1) was synthesized in five steps from α,α′-dibromo-o-xylene according to a literature procedure[243], and the synthesis of cyclooctyne derivative 2 (compound 2, Figure 6.1) was carried out in three steps according to a literature procedure.[244]

Compound 1 Compound 2

Figure 6.1 Molecule structure of the cyclooctyne derivative.

Synthesis of 2-azido-[1,1'-biphenyl]-4,4'-dicarboxylic acid (azido-BPDC) and 2-ethynyl-[1,1'-biphenyl]-4,4'-dicarboxylic acid (alkyne-BPDC).

The synthesis was done by Prof. Stefan Bräse and Dr. Sylvain Grosjean from Karlsruhe Institute of Technology.

The key intermediate dimethyl 2-amino-[1,1'-biphenyl]-4,4'-dicarboxylate (1) was prepared via a literature procedure [245]. The procedure was displayed in Scheme 6.1.

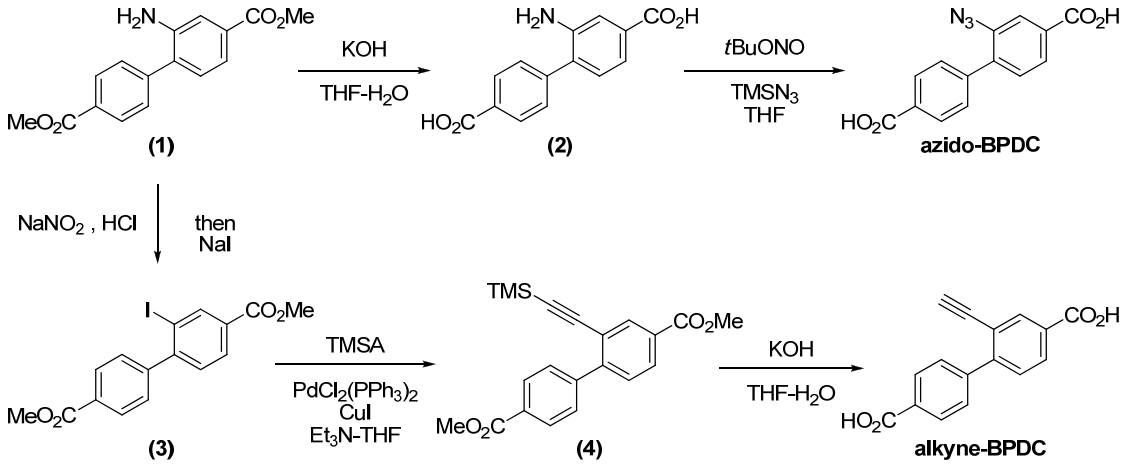

Scheme 6.1: Synthesis of 2-azido-[1,1'-biphenyl]-4,4'-dicarboxylic acid (azido-BPDC) and 2-ethynyl-[1,1'-biphenyl]-4,4'-dicarboxylic acid (alkyne-BPDC)

2-amino-[1,1'-biphenyl]-4,4'-dicarboxylic acid (2) [246]. Dimethyl 2-aminobiphenyl dicarboxylate (1) (1.00 g, 3.51 mmol, 1 eq) was suspended in tetrahydrofuran (30 mL). A solution of potassium hydroxide (1.18 g, 21.03 mmol, 6 eq) in water (20 mL) was added and the reaction mixture was refluxed for 20 h. Tetrahydrofuran was evaporated under reduced pressure then HCl 6M was added until pH = 1. The aqueous suspension was filtrated, the solid was washed with water and methanol, and dried in vacuo to give (2) as a pale yellow solid (0.86 g, 95%). ^{1}H-NMR (500 MHz, DMSO-d_6): δ = 13.04 (br-s, 2H, CO_2H), 8.03 (d, 2H, J = 7.5 Hz, C$\boldsymbol{H}_{Ar}$), 7.67 (s, 1H, C$\boldsymbol{H}_{Ar}$), 7.63 (d, 2H, J = 7.5 Hz, C$\boldsymbol{H}_{Ar}$), 7.49 (d, 1H, J = 8.0 Hz, C$\boldsymbol{H}_{Ar}$), 7.28 (d, 1H, J = 8.0 Hz, C$\boldsymbol{H}_{Ar}$) ppm. ^{13}C-NMR (125 MHz, DMSO-d_6): δ = 167.1 ($\boldsymbol{C}O_2H$), 167.0 ($\boldsymbol{C}O_2H$), 142.3 ($\boldsymbol{C}^{IV}_{Ar}$), 140.3 ($\boldsymbol{C}^{IV}_{Ar}$), 132.1 ($\boldsymbol{C}^{IV}_{Ar}$), 131.2 ($\boldsymbol{C}^{IV}_{Ar}$), 130.8 ($\boldsymbol{C}H_{Ar}$), 130.0 ($\boldsymbol{C}^{IV}_{Ar}$), 129.8 ($\boldsymbol{C}H_{Ar}$), 129.0 ($\boldsymbol{C}H_{Ar}$), 121.3 ($\boldsymbol{C}H_{Ar}$), 119.3 ($\boldsymbol{C}H_{Ar}$) ppm. IR (ATR): ν = 3349, 1678, 1606, 1430, 1392, 1234, 1114 cm^{-1}. MS (EI) *m/z* = 257 [M^{+}]. HRMS (EI) *m/z* $C_{14}H_{11}NO_4$, calcd.: 257.0688, found: 257.0681.

2-azido-[1,1'-biphenyl]-4,4'-dicarboxylic acid (azido-BPDC)[247]. 2-aminobiphenyl dicarboxylic acid (2) (0.40 g, 1.56 mmol, 1 eq) was dissolved in dry tetrahydrofuran (45 mL) and tert-butylnitrite (0.56 mL, 4.67 mmol, 3 eq) was added at T = 0°C. After 15 min. stirring

trimethylsilylazide (0.41 mL, 3.11 mmol, 2 eq) was added at T = 0°C and the reaction mixture was slowly allowed to room temperature and stirred for 48 h. The reaction mixture was evaporated under reduced pressure and the solid was treated with cold tetrahydrofuran and filtrated, then dried in vacuo to give (azido-BPDC) as a yellow-white solid (0.43 g, 97%). 1H-NMR (500 MHz, DMSO-d_6): δ = 13.22 (b-s, 2H, $CO_2\boldsymbol{H}$), 8.02 (d, 2H, J = 7.5 Hz, C$\boldsymbol{H}_{Ar}$), 7.85-7.81 (m, 2H, C$\boldsymbol{H}_{Ar}$), 7.64 (d, 2H, J = 7.5 Hz, C$\boldsymbol{H}_{Ar}$), 7.56 (d, 1H, J = 7.5 Hz, C$\boldsymbol{H}_{Ar}$) ppm. ^{13}C-NMR (125 MHz, DMSO-d_6): δ = 167.0 ($\boldsymbol{C}O_2H$), 166.3 ($\boldsymbol{C}O_2H$), 141.1 ($\boldsymbol{C}^{IV}{}_{Ar}$), 137.2 ($\boldsymbol{C}^{IV}{}_{Ar}$), 135.7 ($\boldsymbol{C}^{IV}{}_{Ar}$), 131.9 ($\boldsymbol{C}^{IV}{}_{Ar}$), 131.4 ($\boldsymbol{C}H_{Ar}$), 130.2 ($\boldsymbol{C}^{IV}{}_{Ar}$), 129.6 ($\boldsymbol{C}H_{Ar}$), 129.2 ($\boldsymbol{C}H_{Ar}$), 125.9 ($\boldsymbol{C}H_{Ar}$), 119.9 ($\boldsymbol{C}H_{Ar}$) ppm. IR (ATR): ν = 2119, 1684, 1556, 1493, 1394, 1279 cm^{-1}. MS (EI) *m/z* = 283 [M^+], 255 [M^+-N_2]. HRMS (EI) *m/z* $C_{14}H_9N_3O_4$, calcd.: 283.0593, found: 283.0586.

Dimethyl 2-iodo-[1,1'-biphenyl]-4,4'-dicarboxylate (3). Dimethyl 2-aminobiphenyl dicarboxylate (1) (1.43 g, 5.00 mmol, 1 eq) was suspended in 15% hydrochloric acid (10 mL), the suspension was cooled at 0°C and a solution of sodium nitrite (0.40 g, 5.75 mmol, 1.15 eq) in water (3 mL) was added dropwise. The mixture was stirred at 0°C for 10 min., then a solution of sodium iodide (0.90 g, 6.00 mmol, 1.2 eq) in water (3 mL) was added dropwise; the resulting solution was heated at 60°C for 20 min. The reaction mixture was poured into water (50 mL) and extracted with ethyl acetate (3 x 250 mL). The combined organic phases were washed with a 10% sodium sulfite solution and brine, dried over Na_2SO_4, filtered and concentrated under reduced pressure. The residue was purified with column chromatography (silica gel, toluene) to give (3) as a white solid (1.27 g, 64%). 1H-NMR (500 MHz, $CDCl_3$): δ = 8.62 (s, 1H, C$\boldsymbol{H}_{Ar}$), 8.12 (d, 2H, J = 8.5 Hz, C$\boldsymbol{H}_{Ar}$), 8.06 (d, 1H, J = 8.0 Hz, C$\boldsymbol{H}_{Ar}$), 7.42 (d, 2H, J = 8.5 Hz, C$\boldsymbol{H}_{Ar}$), 7.35 (d, 1H, J = 8.0 Hz, C$\boldsymbol{H}_{Ar}$), 3.95 (s, 6H, $CO_2C\boldsymbol{H}_3$) ppm. ^{13}C-NMR (125 MHz, $CDCl_3$): δ = 166.9 ($\boldsymbol{C}O_2CH_3$), 165.5 ($\boldsymbol{C}O_2CH_3$), 150.1 ($\boldsymbol{C}^{IV}{}_{Ar}$), 147.8 ($\boldsymbol{C}^{IV}{}_{Ar}$), 140.9 ($\boldsymbol{C}H_{Ar}$), 131.1 ($\boldsymbol{C}^{IV}{}_{Ar}$), 130.0 ($\boldsymbol{C}^{IV}{}_{Ar}$), 129.8 ($\boldsymbol{C}H_{Ar}$), 129.6 ($\boldsymbol{C}H_{Ar}$), 129.4 ($\boldsymbol{C}H_{Ar}$), 129.3 ($\boldsymbol{C}H_{Ar}$), 97.5 ($\boldsymbol{C}^{IV}{}_{Ar}$-I), 52.6 ($CO_2\boldsymbol{C}H_3$), 52.4 ($CO_2\boldsymbol{C}H_3$) ppm. IR (ATR): ν = 2950, 1717, 1592, 1435, 1372, 1273, 1195 cm^{-1}. MS (EI) *m/z* = 396 [M^+], 365 [M^+-OCH_3]. HRMS (EI) *m/z* $C_{16}H_{13}IO_4$, calcd.: 395.9859, found: 395.9855.

Dimethyl 2-((trimethylsilyl)ethynyl)-[1,1'-biphenyl]-4,4'-dicarboxylate (4)[245]. Dimethyl 2-iodobiphenyl dicarboxylate (3) (1.00 g, 2.52 mmol, 1 eq), copper iodide (24 mg, 0.13 mmol, 0.05 eq) and bis(triphenylphosphine)palladium(II) chloride (53 mg, 0.08 mmol, 0.03 eq) were dissolved in a mixture of tetrahydrofuran and triethylamine (1/1, 50 mL) under argon. Trimethylsilylacetylene (TMSA) (1.05 mL, 7.57 mmol, 3 eq) was added and the mixture was stirred at room temperature for 24 h under argon. The reaction mixture was diluted with water (100 mL) and extracted with dichloromethane (3 x 200 mL). The organic phase was washed with water and brine, then dried over Na_2SO_4, filtered and evaporated under reduced pressure. The residue was purified with column chromatography (silica gel, dichloromethane / n-hexane, $Rf_{(DCM/nHx:7/3)}$ = 0.27) to give (4) (0.84 g, 91%) as a yellow-white solid. 1H-NMR (500 MHz,

$CDCl_3$): δ = 8.26 (d, 1H, J = 1.5 Hz, C***H***$_{Ar}$), 8.09 (d, 2H, J = 8.0 Hz, C***H***$_{Ar}$), 8.03 (d, 1H, J = 8.0 Hz, J = 1.5 Hz, C***H***$_{Ar}$), 7.70 (d, 2H, J = 8.0 Hz, C***H***$_{Ar}$), 7.45 (d, 1H, J = 8.0 Hz, C***H***$_{Ar}$), 3.95 (s, 3H, $CO_2C\boldsymbol{H}_3$), 3.94 (s, 3H, $CO_2C\boldsymbol{H}_3$), 0.14 (s, 9H, $Si(C\boldsymbol{H}_3)_3$) ppm. ^{13}C-NMR (125 MHz, $CDCl_3$): δ = 167.0 ($\boldsymbol{C}O_2CH_3$), 166.3 ($\boldsymbol{C}O_2CH_3$), 147.1 (C^{IV}_{Ar}), 144.0 (C^{IV}_{Ar}), 134.9 (CH_{Ar}), 129.8 (C^{IV}_{Ar}), 129.7 (CH_{Ar}), 129.6 (CH_{Ar}), 129.6 (C^{IV}_{Ar}), 129.5 (CH_{Ar}), 129.3 (CH_{Ar}), 122.0 (CIV_{Ar}-C≡CTMS), 103.2 (Ar***C***≡CTMS), 99.5 (ArC≡***C***TMS), 52.5 ($CO_2\boldsymbol{C}H_3$), 52.4 ($CO_2\boldsymbol{C}H_3$), -0.3 ($Si(\boldsymbol{C}H_3)_3$) ppm. IR (ATR): ν = 2948, 2896, 2155, 1715, 1605, 1431, 1386, 1278, 1185 cm^{-1}. MS (EI) *m/z* = 366 [M^+], 351 [M^+-CH_3], 335 [M^+-OCH_3]. HRMS (EI) *m/z* $C_{21}H_{22}O_4Si$, calcd.: 366.1287, found: 366.1282.

2-ethynyl-[1,1'-biphenyl]-4,4'-dicarboxylic acid (alkyne-BPDC). Dimethyl 2-((trimethylsilyl)ethynyl)biphenyl dicarboxylate (0.50 g, 1.36 mmol, 1 eq) was dissolved in tetrahydrofuran (20 mL). A solution of potassium hydroxide (0.77 g, 13.64 mmol, 10 eq) in water (15 mL) was added and the reaction mixture was stirred at room temperature for 72 h. Tetrahydrofuran was evaporated under reduced pressure and HCl 6M was added until pH = 1. The brown-yellow milky suspension was extracted with ethyl acetate (3 x 150 mL), the combined organic phases were washed with a water and brine, dried over Na2SO4, filtered and concentrated under reduced pressure to give (alkyne-BPDC) as a yellow-white solid (0.33 g, 92%). 1H-NMR (500 MHz, DMSO-d_6): δ = 13.19 (b-s, 2H, $CO_2\boldsymbol{H}$), 8.10 (s, 1H, C***H***$_{Ar}$), 8.04-8.03 (m, 3H, C***H***$_{Ar}$), 7.72 (d, 2H, J = 8.0 Hz, C***H***$_{Ar}$), 7.61 (d, 1H, J = 8.0 Hz, C***H***$_{Ar}$), 4.29 (s, 1H, ArC≡C***H***) ppm. ^{13}C-NMR (125 MHz, DMSO-d_6): δ = 167.0 ($\boldsymbol{C}O_2H$), 166.2 ($\boldsymbol{C}O_2H$), 146.3 ($\boldsymbol{C}^{IV}_{Ar}$), 143.0 ($\boldsymbol{C}^{IV}_{Ar}$), 134.3 ($\boldsymbol{C}H_{Ar}$), 130.5 ($\boldsymbol{C}^{IV}_{Ar}$), 130.1 ($\boldsymbol{C}H_{Ar}$), 129.9 ($\boldsymbol{C}H_{Ar}$), 129.3 ($\boldsymbol{C}H_{Ar}$), 129.2 ($\boldsymbol{C}H_{Ar}$), 120.4 ($\boldsymbol{C}^{IV}_{Ar}$-C≡CH), 84.8 (Ar***C***≡CH), 81.6 (ArC≡***C***H) ppm. IR (ATR): ν = 3279, 1678, 1599, 1572, 1420, 1289, 1191 cm^{-1}. MS (EI) *m/z* = 266 [M^+], 249 [M^+-OH]. HRMS (EI) *m/z* $C_{16}H_{10}O_4$, calcd.: 266.0579, found: 266.0575.

Sythesis of 5,5'-(dimethylsilanediyl)diisophthalate.

The synthesis was done by Prof. Michael Fröba, Dr. Stephanie E. Roggenbuck and Dr. Katharina Peikert from University of Hamburg.

5,5'-(dimethylsilanediyl)diisophthalic acid (dmsdip) was prepared as previously reported[229].

6.2 Abbreviations

0D	zero-dimensional
1D	one-dimensional
2D	two-dimensional
3D	three-dimensional
μCp	micro contact printing
AB-BPDC	2-azobenzene-4,4’-biphenyldicarboxylic acid
AC-mode	alternate current mode
AFM	atomic force microscopy
alkyne-BPDC	2-alkyne-[1,1'-biphenyl]-4,4'-dicarboxylic acid
ATR	attenuated total reflection
BET	Brunauer-Emmett-Teller
BiPy	4,4’-bipyridine
BPDC	4,4’-biphenyldicarboxylic acid
BSE	back-scattered electrons
BSSE	basis set superposition error
BTC	1,3,5-benzenetricarboxylic acid
bzac	1-benzoylacetone
CP	counterpoise
CPs	coordination polymers
CuAAC	Cu(I) catalyzed azide alkyne click reaction
Dabco	1,4-diazabicyclo[2.2.2]octane
DEMOFs	defect-engineered MOFs
DFT	density-functional theory
DFTB	density-functional based tight-binding method
DMOF	Dabco MOF
dmsdip	5,5’-(dimethylsilanediyl)diisophthalic acid
DUT-6	Dresden University of Technology-6

EDX	energy-dispersive X-ray
FITC	fluoresceinisothiocyanate
FT-IR	Fourier Transform Infrared
HKUST-1	Hong Kong University of Science and Technology-1
IR	infrared spectroscopy
IRMOFs	isoreticular MOFs
IRRAS	infrared reflection absorption spectroscopy
LB	Langmuir and Blodgett
LPE	liquid phase epitaxy
MFP	mean free path
MHDA	16-mercaptohexadecanoic acid
MIL	Matériaux de l'Institut Lavoisier
MOFs	metal-organic frameworks
MUD	11-mercapto-1-undecanol
N_3-BDC	2-azidoterephthalic acid
N_3-BPDC	2-azido-[1,1'-biphenyl]-4,4'-dicarboxylic acid
NBO	natural bond orbitals
NDC	naphthalene-2,6-dicarboxylic acid
NH_2-BDC	2-aminoterephthalic acid
NORM	near-field optical random mapping
NPA	natural population analysis
NSOM	near-field scanning optical microscope
NU	Northwestern University
PC	personal Computer
PCPs	porous coordination polymers
PDMS	polydimethylsiloxane
PhD	doctor of philosophy
PP1	(4-(4-pyridyl)phenyl)-methanethiol

PSM	post-synthetic modification
PTFE	polytetrafluoroethylene
QCM	quartz crystal microbalance
SAM	self-assembled monolayer
SBUs	secondary building units
SE	spectroscopic ellipsometry
SEM	scanning electron microscope
SEs	secondary electrons
SIM	structured illumination microscopy
SPAAC	strain promoted azide alkyne click reaction
SURMOFs	surface-mounted metal-organic frameworks
THF	tetrahydrofuran
UHM-3	University of Hamburg-3
UHV	ultra high vacuum
UIO	University of Oslo
UV	ultraviolet
UV-Vis	ultraviolet–visible spectroscopy
XPS	X-ray photoelectron spectroscopy
XRD	X-ray diffraction
ZIF	zeolitic imidazolate framework
ZPEs	zero point energies

7 References

1. Anglin, E. J.; Cheng, L.; Freeman, W. R.; Sailor, M. J. Porous silicon in drug delivery devices and materials. *Advanced Drug Delivery Reviews* 2008, 60, 1266-1277.
2. Wolkin, M. V.; Jorne, J.; Fauchet, P. M.; Allan, G.; Delerue, C. Electronic states and luminescence in porous silicon quantum dots: The role of oxygen. *Physical Review Letters* 1999, 82, 197-200.
3. Torres-Costa, V.; Martín-Palma, R. J. Application of nanostructured porous silicon in the field of optics. A review. *Journal of Materials Science* 2010, 45, 2823-2838.
4. Priolo, F.; Gregorkiewicz, T.; Galli, M.; Krauss, T. F. Silicon nanostructures for photonics and photovoltaics. *Nature Nanotechnology* 2014, 9, 19-32.
5. Hoa, M. L. K.; Lu, M.; Zhang, Y. Preparation of porous materials with ordered hole structure. *Advances in Colloid and Interface Science* 2006, 121, 9-23.
6. Davis, M. E. Ordered porous materials for emerging applications. *Nature* 2002, 417, 813-821.
7. Zhou, H.-C.; Long, J. R.; Yaghi, O. M. Introduction to Metal–Organic Frameworks. *Chemical Reviews* 2012, 112, 673-674.
8. Kitagawa, S.; Kitaura, R.; Noro, S.-i. Functional Porous Coordination Polymers. *Angewandte Chemie International Edition* 2004, 43, 2334-2375.
9. James, S. L. Metal-organic frameworks. *Chemical Society Reviews* 2003, 32, 276-288.
10. Kinoshita, Y.; Matsubara, I.; Higuchi, T.; Saito, Y. The Crystal Structure of Bis(adiponitrilo)copper(I) Nitrate. *Bulletin of the Chemical Society of Japan* 1959, 32, 1221-1226.
11. Yaghi, O. M.; Li, H. Hydrothermal Synthesis of a Metal-Organic Framework Containing Large Rectangular Channels. *Journal of the American Chemical Society* 1995, 117, 10401-10402.
12. Sumida, K.; Rogow, D. L.; Mason, J. A.; McDonald, T. M.; Bloch, E. D.; Herm, Z. R.; Bae, T.-H.; Long, J. R. Carbon Dioxide Capture in Metal-Organic Frameworks. *Chemical Reviews* 2012, 112, 724-781.
13. Suh, M. P.; Park, H. J.; Prasad, T. K.; Lim, D.-W. Hydrogen Storage in Metal-Organic Frameworks. *Chemical Reviews* 2012, 112, 782-835.
14. Herm, Z. R.; Bloch, E. D.; Long, J. R. Hydrocarbon Separations in Metal-Organic Frameworks. *Chemistry of Materials* 2014, 26, 323-338.
15. Corma, A.; Garcia, H.; Llabres i Xamena, F. X. L. I. Engineering Metal Organic Frameworks for Heterogeneous Catalysis. *Chemical Reviews* 2010, 110, 4606-4655.
16. Kurmoo, M. Magnetic metal-organic frameworks. *Chemical Society Reviews* 2009, 38, 1353-1379.
17. Wells, A. F. *Three dimensional nets and polyhedra*. Wiley: 1977, Twin Cities.

18. Hoskins, B. F.; Robson, R. Design and construction of a new class of scaffolding-like materials comprising infinite polymeric frameworks of 3D-linked molecular rods. A reappraisal of the zinc cyanide and cadmium cyanide structures and the synthesis and structure of the diamond-related frameworks $[N(CH_3)_4][Cu^{I}Zn^{II}(CN)_4]$ and Cu^{I}[4,4',4",4'"-tetracyanotetraphenylmethane]$BF_4.xC_6H_5NO_2$. *Journal of the American Chemical Society* 1990, 112, 1546-1554.

19. Tranchemontagne, D. J.; Mendoza-Cortes, J. L.; O'Keeffe, M.; Yaghi, O. M. Secondary building units, nets and bonding in the chemistry of metal-organic frameworks. *Chemical Society Reviews* 2009, 38, 1257-1283.

20. Banerjee, R.; Phan, A.; Wang, B.; Knobler, C.; Furukawa, H.; O'Keeffe, M.; Yaghi, O. M. High-Throughput Synthesis of Zeolitic Imidazolate Frameworks and Application to CO_2 Capture. *Science* 2008, 319, 939-943.

21. Rafaja, D. X-Ray Diffraction and X-Ray Reflectivity Applied to Investigation of Thin Films. *Springer Berlin Heidelberg* 2001, Berlin.

22. Lin, Z.; Slawin, A. M. Z.; Morris, R. E. Chiral Induction in the Ionothermal Synthesis of a 3-D Coordination Polymer. *Journal of the American Chemical Society* 2007, 129, 4880-4881.

23. Son, W.-J.; Kim, J.; Kim, J.; Ahn, W.-S. Sonochemical synthesis of MOF-5. *Chemical Communications* 2008, 6336-6338.

24. Li, M.; Dincă, M. Reductive Electrosynthesis of Crystalline Metal–Organic Frameworks. *Journal of the American Chemical Society* 2011, 133, 12926-12929.

25. Yan, D.; Gao, R.; Wei, M.; Li, S.; Lu, J.; Evans, D. G.; Duan, X. Mechanochemical synthesis of a fluorenone-based metal organic framework with polarized fluorescence: an experimental and computational study. *Journal of Materials Chemistry C* 2013, 1, 997-1004.

26. Eddaoudi, M.; Kim, J.; Rosi, N.; Vodak, D.; Wachter, J.; O'Keeffe, M.; Yaghi, O. M. Systematic Design of Pore Size and Functionality in Isoreticular MOFs and Their Application in Methane Storage. *Science* 2002, 295, 469-472.

27. Li, H.; Eddaoudi, M.; O'Keeffe, M.; Yaghi, O. M. Design and synthesis of an exceptionally stable and highly porous metal-organic framework. *Nature* 1999, 402, 276-279.

28. Deng, H.; Grunder, S.; Cordova, K. E.; Valente, C.; Furukawa, H.; Hmadeh, M.; Gándara, F.; Whalley, A. C.; Liu, Z.; Asahina, S.; Kazumori, H.; O'Keeffe, M.; Terasaki, O.; Stoddart, J. F.; Yaghi, O. M. Large-Pore Apertures in a Series of Metal-Organic Frameworks. *Science* 2012, 336, 1018-1023.

29. Chui, S. S.-Y.; Lo, S. M.-F.; Charmant, J. P. H.; Orpen, A. G.; Williams, I. D. A Chemically Functionalizable Nanoporous Material $[Cu_3(TMA)_2(H_2O)_3]_n$. *Science* 1999, 283, 1148-1150.

30. Serre, C.; Millange, F.; Thouvenot, C.; Noguès, M.; Marsolier, G.; Louër, D.; Férey, G. Very Large Breathing Effect in the First Nanoporous Chromium(III)-Based Solids: MIL-53 or

$Cr^{III}(OH)\cdot\{O_2C-C_6H_4-CO_2\}\cdot\{HO_2C-C_6H_4-CO_2H\}_x\cdot H_2O_y$. *Journal of the American Chemical Society* 2002, 124, 13519-13526.

31. Serre, C.; Mellot-Draznieks, C.; Surblé, S.; Audebrand, N.; Filinchuk, Y.; Férey, G. Role of Solvent-Host Interactions That Lead to Very Large Swelling of Hybrid Frameworks. *Science* 2007, 315, 1828-1831.

32. Horcajada, P.; Surble, S.; Serre, C.; Hong, D.-Y.; Seo, Y.-K.; Chang, J.-S.; Greneche, J.-M.; Margiolaki, I.; Ferey, G. Synthesis and catalytic properties of MIL-100(Fe), an iron(iii) carboxylate with large pores. *Chemical Communications* 2007, 2820-2822.

33. Férey, G.; Mellot-Draznieks, C.; Serre, C.; Millange, F.; Dutour, J.; Surblé, S.; Margiolaki, I. A Chromium Terephthalate-Based Solid with Unusually Large Pore Volumes and Surface Area. *Science* 2005, 309, 2040-2042.

34. Dybtsev, D. N.; Chun, H.; Kim, K. Rigid and Flexible: A Highly Porous Metal–Organic Framework with Unusual Guest-Dependent Dynamic Behavior. *Angewandte Chemie International Edition* 2004, 43, 5033-5036.

35. Lee, J.; Farha, O. K.; Roberts, J.; Scheidt, K. A.; Nguyen, S. T.; Hupp, J. T. Metal-organic framework materials as catalysts. *Chemical Society Reviews* 2009, 38, 1450-1459.

36. Biswas, S.; Ahnfeldt, T.; Stock, N. New Functionalized Flexible Al-MIL-53-X (X = -Cl, -Br, $-CH_3$, $-NO_2$, $-(OH)_2$) Solids: Syntheses, Characterization, Sorption, and Breathing Behavior. *Inorganic Chemistry* 2011, 50, 9518-9526.

37. Isimjan, T. T.; Kazemian, H.; Rohani, S.; Ray, A. K. Photocatalytic activities of Pt/ZIF-8 loaded highly ordered TiO2 nanotubes. *Journal of Materials Chemistry* 2010, 20, 10241-10245.

38. Furukawa, H.; Cordova, K. E.; O'Keeffe, M.; Yaghi, O. M. The Chemistry and Applications of Metal-Organic Frameworks. *Science* 2013, 341, 974.

39. Long, J. R.; Yaghi, O. M. The pervasive chemistry of metal-organic frameworks. *Chemical Society Reviews* 2009, 38, 1213-1214.

40. Schneemann, A.; Bon, V.; Schwedler, I.; Senkovska, I.; Kaskel, S.; Fischer, R. A. Flexible metal-organic frameworks. *Chemical Society Reviews* 2014, 43, 6062-6096.

41. Farha, O. K.; Eryazici, I.; Jeong, N. C.; Hauser, B. G.; Wilmer, C. E.; Sarjeant, A. A.; Snurr, R. Q.; Nguyen, S. T.; Yazaydın, A. Ö.; Hupp, J. T. Metal–Organic Framework Materials with Ultrahigh Surface Areas: Is the Sky the Limit? *Journal of the American Chemical Society* 2012, 134, 15016-15021.

42. Furukawa, H.; Ko, N.; Go, Y. B.; Aratani, N.; Choi, S. B.; Choi, E.; Yazaydin, A. Ö.; Snurr, R. Q.; O'Keeffe, M.; Kim, J.; Yaghi, O. M. Ultrahigh Porosity in Metal-Organic Frameworks. *Science* 2010, 329, 424-428.

43. Kabbour, H.; Baumann, T. F.; Satcher, J. H.; Saulnier, A.; Ahn, C. C. Toward New Candidates for Hydrogen Storage: High-Surface-Area Carbon Aerogels. *Chemistry of Materials* 2006, 18, 6085-6087.

44. Chester, A. W.; Clement, C. P.; Han, S. Faujasite zeolitic materials. Google Patents: 2000.
45. Murray, L. J.; Dinca, M.; Long, J. R. Hydrogen storage in metal-organic frameworks. *Chemical Society Reviews* 2009, 38, 1294-1314.
46. Makal, T. A.; Li, J. R.; Lu, W. G.; Zhou, H. C. Methane storage in advanced porous materials. *Chemical Society Reviews* 2012, 41, 7761-7779.
47. Chaemchuen, S.; Kabir, N. A.; Zhou, K.; Verpoort, F. Metal-organic frameworks for upgrading biogas via CO_2 adsorption to biogas green energy. *Chemical Society Reviews* 2013, 42, 9304-9332.
48. Barea, E.; Montoro, C.; Navarro, J. A. R. Toxic gas removal - metal-organic frameworks for the capture and degradation of toxic gases and vapours. *Chemical Society Reviews* 2014, 43, 5419-5430.
49. Dhakshinamoorthy, A.; Garcia, H. Catalysis by metal nanoparticles embedded on metal-organic frameworks. *Chemical Society Reviews* 2012, 41, 5262-5284.
50. Novio, F.; Simmchen, J.; Vazquez-Mera, N.; Amorin-Ferre, L.; Ruiz-Molina, D. Coordination polymer nanoparticles in medicine. *Coordination Chemistry Reviews* 2013, 257, 2839-2847.
51. Horcajada, P.; Gref, R.; Baati, T.; Allan, P. K.; Maurin, G.; Couvreur, P.; Ferey, G.; Morris, R. E.; Serre, C. Metal-Organic Frameworks in Biomedicine. *Chemical Reviews* 2012, 112, 1232-1268.
52. Deng, H. X.; Grunder, S.; Cordova, K. E.; Valente, C.; Furukawa, H.; Hmadeh, M.; Gandara, F.; Whalley, A. C.; Liu, Z.; Asahina, S.; Kazumori, H.; O'Keeffe, M.; Terasaki, O.; Stoddart, J. F.; Yaghi, O. M. Large-Pore Apertures in a Series of Metal-Organic Frameworks. *Science* 2012, 336, 1018-1023.
53. Liu, J. X.; Lukose, B.; Shekhah, O.; Arslan, H. K.; Weidler, P.; Gliemann, H.; Brase, S.; Grosjean, S.; Godt, A.; Feng, X. L.; Mullen, K.; Magdau, I. B.; Heine, T.; Wöll, C. A novel series of isoreticular metal organic frameworks: realizing metastable structures by liquid phase epitaxy. *Scientific Reports* 2012, 2, 921.
54. Deng, H.; Doonan, C. J.; Furukawa, H.; Ferreira, R. B.; Towne, J.; Knobler, C. B.; Wang, B.; Yaghi, O. M. Multiple Functional Groups of Varying Ratios in Metal-Organic Frameworks. *Science* 2010, 327, 846-850.
55. Cohen, S. M. Postsynthetic Methods for the Functionalization of Metal-Organic Frameworks. *Chemical Reviews* 2012, 112, 970-1000.
56. Liu, Y.; Xuan, W.; Cui, Y. Engineering Homochiral Metal-Organic Frameworks for Heterogeneous Asymmetric Catalysis and Enantioselective Separation. *Advanced Materials* 2010, 22, 4112-4135.
57. Yoon, M.; Srirambalaji, R.; Kim, K. Homochiral Metal-Organic Frameworks for Asymmetric Heterogeneous Catalysis. *Chemical Reviews* 2012, 112, 1196-1231.

58. Ma, L.; Abney, C.; Lin, W. Enantioselective catalysis with homochiral metal-organic frameworks. *Chemical Society Reviews* 2009, 38, 1248-1256.
59. Kesanli, B.; Lin, W. B. Chiral porous coordination networks: rational design and applications in enantioselective processes. *Coordination Chemistry Reviews* 2003, 246, 305-326.
60. Grunker, R.; Senkovska, I.; Biedermann, R.; Klein, N.; Klausch, A.; Baburin, I. A.; Mueller, U.; Kaskel, S. Topological Diversity, Adsorption and Fluorescence Properties of MOFs Based on a Tetracarboxylate Ligand. *European Journal of Inorganic Chemistry* 2010, 3835-3841.
61. Hu, Z.; Deibert, B. J.; Li, J. Luminescent metal-organic frameworks for chemical sensing and explosive detection. *Chemical Society Reviews* 2014, 43, 5815-5840.
62. Givaja, G.; Amo-Ochoa, P.; Gomez-Garcia, C. J.; Zamora, F. Electrical conductive coordination polymers. *Chemical Society Reviews* 2012, 41, 115-147.
63. Ramaswamy, P.; Wong, N. E.; Shimizu, G. K. H. MOFs as proton conductors - challenges and opportunities. *Chemical Society Reviews* 2014, 43, 5913-5932.
64. Yoon, M.; Suh, K.; Natarajan, S.; Kim, K. Proton Conduction in Metal-Organic Frameworks and Related Modularly Built Porous Solids. *Angewandte Chemie-International Edition* 2013, 52, 2688-2700.
65. Horike, S.; Shimomura, S.; Kitagawa, S. Soft porous crystals. *Nature Chemistry* 2009, 1, 695-704.
66. Fukushima, T.; Horike, S.; Inubushi, Y.; Nakagawa, K.; Kubota, Y.; Takata, M.; Kitagawa, S. Solid Solutions of Soft Porous Coordination Polymers: Fine-Tuning of Gas Adsorption Properties. *Angewandte Chemie International Edition* 2010, 49, 4820-4824.
67. Chen, B.; Liang, C.; Yang, J.; Contreras, D. S.; Clancy, Y. L.; Lobkovsky, E. B.; Yaghi, O. M.; Dai, S. A Microporous Metal–Organic Framework for Gas-Chromatographic Separation of Alkanes. *Angewandte Chemie International Edition* 2006, 45, 1390-1393.
68. Klein, N.; Herzog, C.; Sabo, M.; Senkovska, I.; Getzschmann, J.; Paasch, S.; Lohe, M. R.; Brunner, E.; Kaskel, S. Monitoring adsorption-induced switching by 129Xe NMR spectroscopy in a new metal-organic framework $Ni_2(2,6\text{-ndc})_2(dabco)$. *Physical Chemistry Chemical Physics* 2010, 12, 11778-11784.
69. Chen, Q.; Chang, Z.; Song, W.-C.; Song, H.; Song, H.-B.; Hu, T.-L.; Bu, X.-H. A Controllable Gate Effect in Cobalt(II) Organic Frameworks by Reversible Structure Transformations. *Angewandte Chemie International Edition* 2013, 52, 11550-11553.
70. Yanai, N.; Kitayama, K.; Hijikata, Y.; Sato, H.; Matsuda, R.; Kubota, Y.; Takata, M.; Mizuno, M.; Uemura, T.; Kitagawa, S. Gas detection by structural variations of fluorescent guest molecules in a flexible porous coordination polymer. *Nature Materials* 2011, 10, 787-793.
71. McKinlay, A. C.; Eubank, J. F.; Wuttke, S.; Xiao, B.; Wheatley, P. S.; Bazin, P.; Lavalley, J. C.; Daturi, M.; Vimont, A.; De Weireld, G.; Horcajada, P.; Serre, C.; Morris, R. E.

Nitric Oxide Adsorption and Delivery in Flexible MIL-88(Fe) Metal–Organic Frameworks. *Chemistry of Materials* 2013, 25, 1592-1599.
72. Horcajada, P.; Serre, C.; Maurin, G.; Ramsahye, N. A.; Balas, F.; Vallet-Regí, M.; Sebban, M.; Taulelle, F.; Férey, G. Flexible Porous Metal-Organic Frameworks for a Controlled Drug Delivery. *Journal of the American Chemical Society* 2008, 130, 6774-6780.
73. Ma, T.-Y.; Liu, L.; Yuan, Z.-Y. Direct synthesis of ordered mesoporous carbons. *Chemical Society Reviews* 2013, 42, 3977-4003.
74. Zhao, D.; Shui, J.-L.; Grabstanowicz, L. R.; Chen, C.; Commet, S. M.; Xu, T.; Lu, J.; Liu, D.-J. Highly Efficient Non-Precious Metal Electrocatalysts Prepared from One-Pot Synthesized Zeolitic Imidazolate Frameworks. *Advanced Materials* 2014, 26, 1093-1097.
75. Zhang, P.; Sun, F.; Xiang, Z.; Shen, Z.; Yun, J.; Cao, D. ZIF-derived in situ nitrogen-doped porous carbons as efficient metal-free electrocatalysts for oxygen reduction reaction. *Energy & Environmental Science* 2014, 7, 442-450.
76. Li, Q.; Xu, P.; Gao, W.; Ma, S.; Zhang, G.; Cao, R.; Cho, J.; Wang, H.-L.; Wu, G. Graphene/Graphene-Tube Nanocomposites Templated from Cage-Containing Metal-Organic Frameworks for Oxygen Reduction in Li–O_2 Batteries. *Advanced Materials* 2014, 26, 1378-1386.
77. Chaikittisilp, W.; Torad, N. L.; Li, C.; Imura, M.; Suzuki, N.; Ishihara, S.; Ariga, K.; Yamauchi, Y. Synthesis of Nanoporous Carbon–Cobalt-Oxide Hybrid Electrocatalysts by Thermal Conversion of Metal–Organic Frameworks. *Chemistry – A European Journal* 2014, 20, 4217-4221.
78. Li, S.-L.; Xu, Q. Metal-organic frameworks as platforms for clean energy. *Energy & Environmental Science* 2013, 6, 1656-1683.
79. Aiyappa, H. B.; Pachfule, P.; Banerjee, R.; Kurungot, S. Porous Carbons from Nonporous MOFs: Influence of Ligand Characteristics on Intrinsic Properties of End Carbon. *Crystal Growth & Design* 2013, 13, 4195-4199.
80. Zhao, D.; Shui, J.-L.; Chen, C.; Chen, X.; Reprogle, B. M.; Wang, D.; Liu, D.-J. Iron imidazolate framework as precursor for electrocatalysts in polymer electrolyte membrane fuel cells. *Chemical Science* 2012, 3, 3200-3205.
81. Morozan, A.; Jaouen, F. Metal organic frameworks for electrochemical applications. *Energy & Environmental Science* 2012, 5, 9269-9290.
82. Jahan, M.; Bao, Q.; Loh, K. P. Electrocatalytically Active Graphene–Porphyrin MOF Composite for Oxygen Reduction Reaction. *Journal of the American Chemical Society* 2012, 134, 6707-6713.
83. Proietti, E.; Jaouen, F.; Lefèvre, M.; Larouche, N.; Tian, J.; Herranz, J.; Dodelet, J.-P. Iron-based cathode catalyst with enhanced power density in polymer electrolyte membrane fuel cells. *Nature Communications* 2011, 2, 416.

84. Stavila, V.; Talin, A. A.; Allendorf, M. D. MOF-based electronic and optoelectronic devices. *Chemical Society Reviews* 2014, 43, 5994-6010.
85. Betard, A.; Fischer, R. A. Metal-Organic Framework Thin Films: From Fundamentals to Applications. *Chemical Reviews* 2012, 112, 1055-1083.
86. Hermes, S.; Schröder, F.; Chelmowski, R.; Wöll, C.; Fischer, R. A. Selective Nucleation and Growth of Metal−Organic Open Framework Thin Films on Patterned $COOH/CF_3$-Terminated Self-Assembled Monolayers on Au(111). *Journal of the American Chemical Society* 2005, 127, 13744-13745.
87. Guerrero, V. V.; Yoo, Y.; McCarthy, M. C.; Jeong, H.-K. HKUST-1 membranes on porous supports using secondary growth. *Journal of Materials Chemistry* 2010, 20, 3938-3943.
88. Ameloot, R.; Gobechiya, E.; Uji-i, H.; Martens, J. A.; Hofkens, J.; Alaerts, L.; Sels, B. F.; De Vos, D. E. Direct Patterning of Oriented Metal–Organic Framework Crystals via Control over Crystallization Kinetics in Clear Precursor Solutions. *Advanced Materials* 2010, 22, 2685-2688.
89. Carbonell, C.; Imaz, I.; Maspoch, D. Single-Crystal Metal−Organic Framework Arrays. *Journal of the American Chemical Society* 2011, 133, 2144-2147.
90. Zhuang, J.-L.; Ceglarek, D.; Pethuraj, S.; Terfort, A. Rapid Room-Temperature Synthesis of Metal–Organic Framework HKUST-1 Crystals in Bulk and as Oriented and Patterned Thin Films. *Advanced Functional Materials* 2011, 21, 1442-1447.
91. Ameloot, R.; Stappers, L.; Fransaer, J.; Alaerts, L.; Sels, B. F.; De Vos, D. E. Patterned Growth of Metal-Organic Framework Coatings by Electrochemical Synthesis. *Chemistry of Materials* 2009, 21, 2580-2582.
92. Schoedel, A.; Scherb, C.; Bein, T. Oriented Nanoscale Films of Metal–Organic Frameworks By Room-Temperature Gel-Layer Synthesis. *Angewandte Chemie International Edition* 2010, 49, 7225-7228.
93. Makiura, R.; Motoyama, S.; Umemura, Y.; Yamanaka, H.; Sakata, O.; Kitagawa, H. Surface nano-architecture of a metal-organic framework. *Nature Materials* 2010, 9, 565.
94. Motoyama, S.; Makiura, R.; Sakata, O.; Kitagawa, H. Highly Crystalline Nanofilm by Layering of Porphyrin Metal−Organic Framework Sheets. *Journal of the American Chemical Society* 2011, 133, 5640.
95. Mao, Y.; shi, L.; Huang, H.; Cao, W.; Li, J.; Sun, L.; Jin, X.; Peng, X. Room temperature synthesis of free-standing HKUST-1 membranes from copper hydroxide nanostrands for gas separation. *Chemical Communications* 2013, 49, 5666-5668.
96. Khaletskaya, K.; Turner, S.; Tu, M.; Wannapaiboon, S.; Schneemann, A.; Meyer, R.; Ludwig, A.; Van Tendeloo, G.; Fischer, R. A. Self-Directed Localization of ZIF-8 Thin Film Formation by Conversion of ZnO Nanolayers. *Advanced Functional Materials* 2014, 24, 4804-4811.

97. Reboul, J.; Furukawa, S.; Horike, N.; Tsotsalas, M.; Hirai, K.; Uehara, H.; Kondo, M.; Louvain, N.; Sakata, O.; Kitagawa, S. Mesoscopic architectures of porous coordination polymers fabricated by pseudomorphic replication. *Nature Materials* 2012, 11, 717-723.
98. Zhang, Y.; Gao, Q.; Lin, Z.; Zhang, T.; Xu, J.; Tan, Y.; Tian, W.; Jiang, L. Constructing Free Standing Metal Organic Framework MIL-53 Membrane Based on Anodized Aluminum Oxide Precursor. *Scientific Reports* 2014, 4, 4947.
99. Shekhah, O.; Liu, J.; Fischer, R. A.; Wöll, C. MOF thin films: existing and future applications. *Chemical Society Reviews* 2011, 40, 1081-1106.
100. Arslan, H. K.; Shekhah, O.; Wohlgemuth, J.; Franzreb, M.; Fischer, R. A.; Wöll, C. High-Throughput Fabrication of Uniform and Homogenous MOF Coatings. *Advanced Functional Materials* 2011, 21, 4228-4231.
101. Shekhah, O.; Wang, H.; Kowarik, S.; Schreiber, F.; Paulus, M.; Tolan, M.; Sternemann, C.; Evers, F.; Zacher, D.; Fischer, R. A.; Wöll, C. Step-by-Step Route for the Synthesis of Metal−Organic Frameworks. *Journal of the American Chemical Society* 2007, 129, 15118-15119.
102. Zhuang, J.-L.; Ar, D.; Yu, X.-J.; Liu, J.-X.; Terfort, A. Patterned Deposition of Metal-Organic Frameworks onto Plastic, Paper, and Textile Substrates by Inkjet Printing of a Precursor Solution. *Advanced Materials* 2013, 25, 4631-4635.
103. Arnold, R.; Azzam, W.; Terfort, A.; Wöll, C. Preparation, modification, and crystallinity of aliphatic and aromatic carboxylic acid terminated self-assembled monolayers. *Langmuir* 2002, 18, 3980-3992.
104. Liu, J. X.; Schupbach, B.; Bashir, A.; Shekhah, O.; Nefedov, A.; Kind, M.; Terfort, A.; Wöll, C. Structural characterization of self-assembled monolayers of pyridine-terminated thiolates on gold. *Physical Chemistry Chemical Physics* 2010, 12, 4459-4472.
105. Blodgett, K. B.; Langmuir, I. Built-Up Films of Barium Stearate and Their Optical Properties. *Physical Review* 1937, 51, 964-982.
106. Decher, G.; Hong, J.-D. Buildup of ultrathin multilayer films by a self-assembly process, 1 consecutive adsorption of anionic and cationic bipolar amphiphiles on charged surfaces. *Makromolekulare Chemie. Macromolecular Symposia* 1991, 46, 321-327.
107. Kotov, N. A.; Dekany, I.; Fendler, J. H. Layer-by-Layer Self-Assembly of Polyelectrolyte-Semiconductor Nanoparticle Composite Films. *The Journal of Physical Chemistry* 1995, 99, 13065-13069.
108. Jain, V.; Sahoo, R.; Jinschek, J. R.; Montazami, R.; Yochum, H. M.; Beyer, F. L.; Kumar, A.; Heflin, J. R. High contrast solid state electrochromic devices based on Ruthenium Purple nanocomposites fabricated by layer-by-layer assembly. *Chemical Communications* 2008, 3663-3665.
109. Hong, J. D.; Lowack, K.; Schmitt, J.; Decher, G. Layer-by-layer deposited multilayer assemblies of polyelectrolytes and proteins: from ultrathin films to protein arrays. In *Trends in*

Colloid and Interface Science VII, Laggner, P.; Glatter, O., Eds. Steinkopff: 1993; Vol. 93, pp 98-102.
110. Lu, L.-P.; Wang, S.-Q.; Lin, X.-Q. Fabrication of layer-by-layer deposited multilayer films containing DNA and gold nanoparticle for norepinephrine biosensor. *Analytica Chimica Acta* 2004, 519, 161-166.
111. Netzer, L.; Sagiv, J. A new approach to construction of artificial monolayer assemblies. *Journal of the American Chemical Society* 1983, 105, 674-676.
112. Falcaro, P.; Ricco, R.; Doherty, C. M.; Liang, K.; Hill, A. J.; Styles, M. J. MOF positioning technology and device fabrication. *Chemical Society Reviews* 2014, 43, 5513-5560.
113. Shekhah, O.; Liu, J.; Fischer, R. A.; Woell, C. MOF thin films: existing and future applications. *Chemical Society Reviews* 2011, 40, 1081-1106.
114. Zacher, D.; Shekhah, O.; Woell, C.; Fischer, R. A. Thin films of metal-organic frameworks. *Chemical Society Reviews* 2009, 38, 1418-1429.
115. Arslan, H. K.; Shekhah, O.; Wieland, D. C. F.; Paulus, M.; Sternemann, C.; Schroer, M. A.; Tiemeyer, S.; Tolan, M.; Fischer, R. A.; Wöll, C. Intercalation in Layered Metal-Organic Frameworks: Reversible Inclusion of an Extended pi-System. *Journal of the American Chemical Society* 2011, 133, 8158-8161.
116. Stavila, V.; Volponi, J.; Katzenmeyer, A. M.; Dixon, M. C.; Allendorf, M. D. Kinetics and mechanism of metal-organic framework thin film growth: systematic investigation of HKUST-1 deposition on QCM electrodes. *Chemical Science* 2012, 3, 1531-1540.
117. Curie, J.; Curie, P. Développement, par pression, de l'électricité polaire dans les cristaux hémièdres à faces inclinées. *Comptes Rendus* 1880, 91, 294-295.
118. Sauerbrey, G. Verwendung von Schwingquarzen zur Wägung dünner Schichten und zur Mikrowägung. *Z. Physik* 1959, 155, 206-222.
119. Shekhah, O.; Wang, H.; Zacher, D.; Fischer, R. A.; Wöll, C. Growth Mechanism of Metal-Organic Frameworks: Insights into the Nucleation by Employing a Step-by-Step Route. *Angewandte Chemie-International Edition* 2009, 48, 5038-5041.
120. Liu, B.; Tu, M.; Fischer, R. A. Metal-Organic Framework Thin Films: Crystallite Orientation Dependent Adsorption. *Angewandte Chemie-International Edition* 2013, 52, 3402-3405.
121. Zybaylo, O.; Shekhah, O.; Wang, H.; Tafipolsky, M.; Schmid, R.; Johannsmann, D.; Wöll, C. A novel method to measure diffusion coefficients in porous metal-organic frameworks. *Physical Chemistry Chemical Physics* 2010, 12, 8092-8097.
122. Shekhah, O.; Hirai, K.; Wang, H.; Uehara, H.; Kondo, M.; Diring, S.; Zacher, D.; Fischer, R. A.; Sakata, O.; Kitagawa, S.; Furukawa, S.; Wöll, C. MOF-on-MOF heteroepitaxy: perfectly oriented $[Zn_2(ndc)_2(dabco)]_n$ grown on $[Cu_2(ndc)_2(dabco)]_n$ thin films. *Dalton Transactions* 2011, 40, 4954-4958.

123. Liu, B.; Ma, M. Y.; Zacher, D.; Betard, A.; Yusenko, K.; Metzler-Nolte, N.; Wöll, C.; Fischer, R. A. Chemistry of SURMOFs: Layer-Selective Installation of Functional Groups and Post-synthetic Covalent Modification Probed by Fluorescence Microscopy. *Journal of the American Chemical Society* 2011, 133, 1734-1737.
124. Heinke, L.; Cakici, M.; Dommaschk, M.; Grosjean, S.; Herges, R.; Bräse, S.; Wöll, C. Photoswitching in Two-Component Surface-Mounted Metal–Organic Frameworks: Optically Triggered Release from a Molecular Container. *ACS Nano* 2014, 8, 1463-1467.
125. Allendorf, M. D.; Houk, R. J. T.; Andruszkiewicz, L.; Talin, A. A.; Pikarsky, J.; Choudhury, A.; Gall, K. A.; Hesketh, P. J. Stress-Induced Chemical Detection Using Flexible Metal−Organic Frameworks. *Journal of the American Chemical Society* 2008, 130, 14404-14405.
126. Liu, B.; Shekhah, O.; Arslan, H. K.; Liu, J. X.; Wöll, C.; Fischer, R. A. Enantiopure Metal-Organic Framework Thin Films: Oriented SURMOF Growth and Enantioselective Adsorption. *Angewandte Chemie-International Edition* 2012, 51, 807-810.
127. Streit, H. C.; Adlung, M.; Shekhah, O.; Stammer, X.; Arslan, H. K.; Zybaylo, O.; Ladnorg, T.; Gliemann, H.; Franzreb, M.; Wöll, C.; Wickleder, C. Surface-Anchored MOF-Based Photonic Antennae. *Chemphyschem* 2012, 13, 2699-2702.
128. Dragasser, A.; Shekhah, O.; Zybaylo, O.; Shen, C.; Buck, M.; Wöll, C.; Schlettwein, D. Redox mediation enabled by immobilised centres in the pores of a metal-organic framework grown by liquid phase epitaxy. *Chemical Communications* 2012, 48, 663-665.
129. Talin, A. A.; Centrone, A.; Ford, A. C.; Foster, M. E.; Stavila, V.; Haney, P.; Kinney, R. A.; Szalai, V.; El Gabaly, F.; Yoon, H. P.; Léonard, F.; Allendorf, M. D. Tunable Electrical Conductivity in Metal-Organic Framework Thin-Film Devices. *Science* 2014, 343, 66-69.
130. Seo, J. S.; Whang, D.; Lee, H.; Jun, S. I.; Oh, J.; Jeon, Y. J.; Kim, K. A homochiral metal-organic porous material for enantioselective separation and catalysis. *Nature* 2000, 404, 982-986.
131. Wang, Z.; Cohen, S. M. Postsynthetic modification of metal-organic frameworks. *Chemical Society Reviews* 2009, 38, 1315-1329.
132. Stavitski, E.; Pidko, E. A.; Couck, S.; Remy, T.; Hensen, E. J. M.; Weckhuysen, B. M.; Denayer, J.; Gascon, J.; Kapteijn, F. Complexity behind CO_2 Capture on NH_2-MIL-53(Al). *Langmuir* 2011, 27, 3970-3976.
133. Sun, D.; Fu, Y.; Liu, W.; Ye, L.; Wang, D.; Yang, L.; Fu, X.; Li, Z. Studies on Photocatalytic CO_2 Reduction over NH_2-Uio-66(Zr) and Its Derivatives: Towards a Better Understanding of Photocatalysis on Metal–Organic Frameworks. *Chemistry – A European Journal* 2013, 19, 14279-14285.
134. Peikert, K.; Hoffmann, F.; Froba, M. Amino substituted $Cu_3(btc)_2$: a new metal-organic framework with a versatile functionality. *Chemical Communications* 2012, 48, 11196-11198.

135. Wang, Z.; Tanabe, K. K.; Cohen, S. M. Accessing Postsynthetic Modification in a Series of Metal-Organic Frameworks and the Influence of Framework Topology on Reactivity. *Inorganic Chemistry* 2008, 48, 296-306.
136. Wang, Z.; Cohen, S. M. Postsynthetic Covalent Modification of a Neutral Metal−Organic Framework. *Journal of the American Chemical Society* 2007, 129, 12368-12369.
137. Savonnet, M.; Bazer-Bachi, D.; Bats, N.; Perez-Pellitero, J.; Jeanneau, E.; Lecocq, V.; Pinel, C.; Farrusseng, D. Generic Postfunctionalization Route from Amino-Derived Metal−Organic Frameworks. *Journal of the American Chemical Society* 2010, 132, 4518-4519.
138. Kolb, H. C.; Finn, M. G.; Sharpless, K. B. Click chemistry: Diverse chemical function from a few good reactions. *Angewandte Chemie-International Edition* 2001, 40, 2004-2021.
139. Meilikhov, M.; Yusenko, K.; Fischer, R. A. Turning MIL-53(Al) Redox-Active by Functionalization of the Bridging OH-Group with 1,1′-Ferrocenediyl-Dimethylsilane. *Journal of the American Chemical Society* 2009, 131, 9644-9645.
140. Valtchev, V.; Majano, G.; Mintova, S.; Perez-Ramirez, J. Tailored crystalline microporous materials by post-synthesis modification. *Chemical Society Reviews* 2013, 42, 263-290.
141. Tanabe, K. K.; Cohen, S. M. Postsynthetic modification of metal-organic frameworks-a progress report. *Chemical Society Reviews* 2011, 40, 498-519.
142. Shekhah, O.; Arslan, H. K.; Chen, K.; Schmittel, M.; Maul, R.; Wenzel, W.; Wöll, C. Post-synthetic modification of epitaxially grown, highly oriented functionalized MOF thin films. *Chemical Communications* 2011, 47, 11210-11212.
143. Meilikhov, M.; Furukawa, S.; Hirai, K.; Fischer, R. A.; Kitagawa, S. Binary Janus Porous Coordination Polymer Coating for Sensor Devices with Tunable Analyte Affinity. *Angewandte Chemie-International Edition* 2013, 52, 341-345.
144. Hebbar, K. R. Basics of X-Ray Diffraction and its Applications. *I.K.International Publishing House; 1st Edition* 2011, New Delhi.
145. Pease, R. S. An X-ray Study of Boron Nitride. *Acta Crystallographica* 1952, 5, 356-361.
146. Stuart, B. H. Infrared Spectroscopy: Fundamentals and Applications. *John Wiley & Sons, Inc.* 2004, Chichester.
147. St Petkov, P.; Vayssilov, G. N.; Liu, J. X.; Shekhah, O.; Wang, Y. M.; Wöll, C.; Heine, T. Defects in MOFs: A Thorough Characterization. *Chemphyschem* 2012, 13, 2025-2029.
148. Arnold, R.; Terfort, A.; Wöll, C. Determination of Molecular Orientation in Self-Assembled Monolayers Using IR Absorption Intensities: The Importance of Grinding Effects. *Langmuir* 2001, 17, 4980-4989.
149. Hoffmann, F. M. Infrared reflection-absorption spectroscopy of adsorbed molecules. *Surface Science Reports* 1983, 3, 107-192.

150. Mojet, B. L.; Ebbesen, S. D.; Lefferts, L. Light at the interface: the potential of attenuated total reflection infrared spectroscopy for understanding heterogeneous catalysis in water. *Chemical Society Reviews* 2010, 39, 4643-4655.
151. Wang, Y.; Glenz, A.; Muhler, M.; Wöll, C. A new dual-purpose ultrahigh vacuum infrared spectroscopy apparatus optimized for grazing-incidence reflection as well as for transmission geometries. *Review of Scientific Instruments* 2009, 80, 113108.
152. Hüfner, S. Photoelectron Spectroscopy: Principles and Applications. *Springer Series in Solid-State Sciences* 2003, Berlin.
153. Heide, P. v. d. X-ray Photoelectron Spectroscopy: An introduction to Principles and Practices. *Wiley* 2011, Hoboken.
154. Perkampus, H.-H. UV-VIS spectroscopy and its applications. *Springer-Verlag* 1992, Berlin.
155. Clarke, A. R.; Eberhardt, C. N. Microscopy Techniques for Materials Science. *Woodhead Publishing* 2002, Abington.
156. Kubitscheck, U. Fluorescence Microscopy: From Principles to Biological Applications. *Wiley-Blackwell* 2013, Weinheim.
157. http://en.wikipedia.org/wiki/Fluorescence_microscope. *wikipedia* Taken at 11/28/2014.
158. http://en.wikipedia.org/wiki/Scanning_electron_microscope. *Wikipedia* Taken at 11/28/2014.
159. Haugstad, G. Atomic Force Microscopy: Understanding Basic Modes and Advanced Applications. *Wiley* 2012, Hoboken.
160. Braga, P. C.; Ricci, D. Atomic Force Microscopy: Biomedical Methods and Applications. *Humana press* 2004, Totowa.
161. http://en.wikipedia.org/wiki/Atomic_force_microscopy. *Wikipedia* Taken at 11/28/2014.
162. Fujiwara, H. Spectroscopic Ellipsometry: Principles and Applications. *Wiley* 2007, Tokyo.
163. http://www.jawoollam.com/tutorial_2.html. Taken at 11/28/2014.
164. Zhechkov, L.; Heine, T.; Patchkovskii, S.; Seifert, G.; Duarte, H. A. An Efficient a Posteriori Treatment for Dispersion Interaction in Density-Functional-Based Tight Binding. *Journal of Chemical Theory and Computation* 2005, 1, 841-847.
165. Lukose, B.; Supronowicz, B.; St. Petkov, P.; Frenzel, J.; Kuc, A. B.; Seifert, G.; Vayssilov, G. N.; Heine, T. Structural properties of metal-organic frameworks within the density-functional based tight-binding method. *physica status solidi (b)* 2012, 249, 335-342.
166. Elstner, M.; Porezag, D.; Jungnickel, G.; Elsner, J.; Haugk, M.; Frauenheim, T.; Suhai, S.; Seifert, G. Self-consistent-charge density-functional tight-binding method for simulations of complex materials properties. *Physical Review B* 1998, 58, 7260-7268.

167. Becke, A. D. Density-functional exchange-energy approximation with correct asymptotic behavior. *Physical Review A* 1988, 38, 3098-3100.
168. Lee, C.; Yang, W.; Parr, R. G. Development of the Colle-Salvetti correlation-energy formula into a functional of the electron density. *Physical Review B* 1988, 37, 785-789.
169. Grimme, S.; Antony, J.; Ehrlich, S.; Krieg, H. A consistent and accurate ab initio parametrization of density functional dispersion correction (DFT-D) for the 94 elements H-Pu. *The Journal of Chemical Physics* 2010, 132, 154104.
170. Boys, S. F.; Bernardi, F. The calculation of small molecular interactions by the differences of separate total energies. Some procedures with reduced errors. *Molecular Physics* 1970, 19, 553-566.
171. Reed, A. E.; Weinstock, R. B.; Weinhold, F. Natural population analysis. *The Journal of Chemical Physics* 1985, 83, 735-746.
172. Meilikhov, M.; Furukawa, S.; Hirai, K.; Fischer, R. A.; Kitagawa, S. Binary Janus Porous Coordination Polymer Coatings for Sensor Devices with Tunable Analyte Affinity. *Angewandte Chemie* 2013, 125, 359-363.
173. Furukawa, S.; Hirai, K.; Nakagawa, K.; Takashima, Y.; Matsuda, R.; Tsuruoka, T.; Kondo, M.; Haruki, R.; Tanaka, D.; Sakamoto, H.; Shimomura, S.; Sakata, O.; Kitagawa, S. Heterogeneously Hybridized Porous Coordination Polymer Crystals: Fabrication of Heterometallic Core–Shell Single Crystals with an In-Plane Rotational Epitaxial Relationship. *Angewandte Chemie International Edition* 2009, 48, 1766-1770.
174. Furukawa, S.; Hirai, K.; Takashima, Y.; Nakagawa, K.; Kondo, M.; Tsuruoka, T.; Sakata, O.; Kitagawa, S. A block PCP crystal: anisotropic hybridization of porous coordination polymers by face-selective epitaxial growth. *Chemical Communications* 2009, 5097-5099.
175. Shekhah, O.; Hirai, K.; Wang, H.; Uehara, H.; Kondo, M.; Diring, S.; Zacher, D.; Fischer, R. A.; Sakata, O.; Kitagawa, S.; Furukawa, S.; Wöll, C. MOF-on-MOF heteroepitaxy: perfectly oriented $[Zn_2(ndc)_2(dabco)]_n$ grown on $[Cu_2(ndc)_2(dabco)]_n$ thin films. *Dalton Transactions* 2011, 40, 4954-4958.
176. Kreno, L. E.; Leong, K.; Farha, O. K.; Allendorf, M.; Van Duyne, R. P.; Hupp, J. T. Metal–Organic Framework Materials as Chemical Sensors. *Chemical Reviews* 2011, 112, 1105-1125.
177. Tang, S. J.; Lee, C. Y.; Huang, C. C.; Chang, T. R.; Cheng, C. M.; Tsuei, K. D.; Jeng, H. T.; Yeh, V.; Chiang, T. C. Electronic versus Lattice Match for Metal-Semiconductor Epitaxial Growth: Pb on Ge(111). *Physical Review Letters* 2011, 107.
178. Trent, J. S.; Scheinbeim, J. I.; Couchman, P. R. Ruthenium tetraoxide staining of polymers for electron microscopy. *Macromolecules* 1983, 16, 589-598.
179. Adrian, M.; Dubochet, J.; Fuller, S. D.; Harris, J. R. Cryo-negative staining. *Micron* 1998, 29, 145-160.

180. Kuc, A.; Enyashin, A.; Seifert, G. Metal−Organic Frameworks: Structural, Energetic, Electronic, and Mechanical Properties. *The Journal of Physical Chemistry B* 2007, 111, 8179-8186.
181. Bauer, C. A.; Timofeeva, T. V.; Settersten, T. B.; Patterson, B. D.; Liu, V. H.; Simmons, B. A.; Allendorf, M. D. Influence of connectivity and porosity on ligand-based luminescence in zinc metal-organic frameworks. *Journal of the American Chemical Society* 2007, 129, 7136-7144.
182. Wang, Z.; Liu, J.; Lukose, B.; Gu, Z.; Weidler, P. G.; Gliemann, H.; Heine, T.; Wöll, C. Nanoporous Designer Solids with Huge Lattice Constant Gradients: Multiheteroepitaxy of Metal–Organic Frameworks. *Nano Letters* 2014, 14, 1526-1529.
183. Cohen, S. M. Modifying MOFs: new chemistry, new materials. *Chemical Science* 2010, 1, 32-36.
184. Kreno, L. E.; Leong, K.; Farha, O. K.; Allendorf, M.; Van Duyne, R. P.; Hupp, J. T. Metal-Organic Framework Materials as Chemical Sensors. *Chemical Reviews* 2012, 112, 1105-1125.
185. Silva, C. G.; Corma, A.; Garcia, H. Metal-organic frameworks as semiconductors. *Journal of Materials Chemistry* 2010, 20, 3141-3156.
186. Li, Y. S.; Liang, F. Y.; Bux, H.; Feldhoff, A.; Yang, W. S.; Caro, J. Molecular Sieve Membrane: Supported Metal-Organic Framework with High Hydrogen Selectivity. *Angewandte Chemie-International Edition* 2010, 49, 548-551.
187. Rostovtsev, V. V.; Green, L. G.; Fokin, V. V.; Sharpless, K. B. A Stepwise Huisgen Cycloaddition Process: Copper(I)-Catalyzed Regioselective "Ligation" of Azides and Terminal Alkynes. *Angewandte Chemie International Edition* 2002, 41, 2596-2599.
188. Savonnet, M.; Kockrick, E.; Camarata, A.; Bazer-Bachi, D.; Bats, N.; Lecocq, V.; Pinel, C.; Farrusseng, D. Combinatorial synthesis of metal-organic frameworks libraries by click-chemistry. *New Journal of Chemistry* 2011, 35, 1892-1897.
189. Devic, T.; David, O.; Valls, M.; Marrot, J.; Couty, F.; Ferey, G. An illustration of the limit of the metal organic framework's isoreticular principle using a semirigid tritopic linker obtained by "Click" chemistry. *Journal of the American Chemical Society* 2007, 129, 12614-12615.
190. Gadzikwa, T.; Farha, O. K.; Malliakas, C. D.; Kanatzidis, M. G.; Hupp, J. T.; Nguyen, S. T. Selective Bifunctional Modification of a Non-catenated Metal−Organic Framework Material via "Click" Chemistry. *Journal of the American Chemical Society* 2009, 131, 13613-13615.
191. Goto, Y.; Sato, H.; Shinkai, S.; Sada, K. "Clickable" Metal−Organic Framework. *Journal of the American Chemical Society* 2008, 130, 14354-14355.
192. Horcajada, P.; Chalati, T.; Serre, C.; Gillet, B.; Sebrie, C.; Baati, T.; Eubank, J. F.; Heurtaux, D.; Clayette, P.; Kreuz, C.; Chang, J. S.; Hwang, Y. K.; Marsaud, V.; Bories, P. N.;

Cynober, L.; Gil, S.; Ferey, G.; Couvreur, P.; Gref, R. Porous metal-organic-framework nanoscale carriers as a potential platform for drug delivery and imaging. *Nature Materials* 2010, 9, 172-178.
193. Horcajada, P.; Gref, R.; Baati, T.; Allan, P. K.; Maurin, G.; Couvreur, P.; Férey, G.; Morris, R. E.; Serre, C. Metal–Organic Frameworks in Biomedicine. *Chemical Reviews* 2011, 112, 1232-1268.
194. McKinlay, A. C.; Morris, R. E.; Horcajada, P.; Férey, G.; Gref, R.; Couvreur, P.; Serre, C. BioMOFs: Metal–Organic Frameworks for Biological and Medical Applications. *Angewandte Chemie International Edition* 2010, 49, 6260-6266.
195. Hanke, M.; Arslan, H. K.; Bauer, S.; Zybaylo, O.; Christophis, C.; Gliemann, H.; Rosenhahn, A.; Wöll, C. The Biocompatibility of Metal–Organic Framework Coatings: An Investigation on the Stability of SURMOFs with Regard to Water and Selected Cell Culture Media. *Langmuir* 2012, 28, 6877-6884.
196. Yoon, M.; Suh, K.; Natarajan, S.; Kim, K. Proton Conduction in Metal–Organic Frameworks and Related Modularly Built Porous Solids. *Angewandte Chemie International Edition* 2013, 52, 2688-2700.
197. Agard, N. J.; Prescher, J. A.; Bertozzi, C. R. A Strain-Promoted [3 + 2] Azide−Alkyne Cycloaddition for Covalent Modification of Biomolecules in Living Systems. *Journal of the American Chemical Society* 2004, 126, 15046-15047.
198. Becer, C. R.; Hoogenboom, R.; Schubert, U. S. Click Chemistry beyond Metal-Catalyzed Cycloaddition. *Angewandte Chemie International Edition* 2009, 48, 4900-4908.
199. Liu, C.; Li, T.; Rosi, N. L. Strain-Promoted "Click" Modification of a Mesoporous Metal-Organic Framework. *Journal of the American Chemical Society* 2012, 134, 18886-18888.
200. Arslan, H. K.; Shekhah, O.; Wohlgemuth, J.; Franzreb, M.; Fischer, R. A.; Wöll, C. High-Throughput Fabrication of Uniform and Homogenous MOF Coatings. *Advanced Functional Materials* 2011, 21, 4228-4231.
201. Wang, Z.; Liu, J.; Arslan, H. K.; Grosjean, S.; Hagendorn, T.; Gliemann, H.; Bräse, S.; Wöll, C. Post-Synthetic Modification of Metal–Organic Framework Thin Films Using Click Chemistry: The Importance of Strained C–C Triple Bonds. *Langmuir* 2013, 29, 15958-15964.
202. Gadzikwa, T.; Lu, G.; Stern, C. L.; Wilson, S. R.; Hupp, J. T.; Nguyen, S. T. Covalent surface modification of a metal-organic framework: selective surface engineering via CuI-catalyzed Huisgen cycloaddition. *Chemical Communications* 2008, 0, 5493-5495.
203. Chen, C.; Allen, C. A.; Cohen, S. M. Tandem Postsynthetic Modification of Metal–Organic Frameworks Using an Inverse-Electron-Demand Diels–Alder Reaction. *Inorganic Chemistry* 2011, 50, 10534-10536.

204. Ning, X.; Guo, J.; Wolfert, M. A.; Boons, G.-J. Visualizing Metabolically Labeled Glycoconjugates of Living Cells by Copper-Free and Fast Huisgen Cycloadditions. *Angewandte Chemie International Edition* 2008, 47, 2253-2255.
205. Poloukhtine, A. A.; Mbua, N. E.; Wolfert, M. A.; Boons, G.-J.; Popik, V. V. Selective Labeling of Living Cells by a Photo-Triggered Click Reaction. *Journal of the American Chemical Society* 2009, 131, 15769-15776.
206. Sanders, B. C.; Friscourt, F.; Ledin, P. A.; Mbua, N. E.; Arumugam, S.; Guo, J.; Boltje, T. J.; Popik, V. V.; Boons, G.-J. Metal-Free Sequential [3 + 2]-Dipolar Cycloadditions using Cyclooctynes and 1,3-Dipoles of Different Reactivity. *Journal of the American Chemical Society* 2010, 133, 949-957.
207. Wittig, G.; Krebs, A. Zur Existenz niedergliedriger Cycloalkine, I. *Chemische Berichte* 1961, 94, 3260-3275.
208. Arpa Sancet, M.; Hanke, M.; Wang, Z.; Bauer, S.; Azucena, C.; Arslan, H.; Heinle, M.; Gliemann, H.; Wöll, C.; Rosenhahn, A. Surface anchored metal-organic frameworks as stimulus responsive antifouling coatings. *Biointerphases* 2013, 8, 1-8.
209. Wang, Z.; Tanabe, K. K.; Cohen, S. M. Tuning Hydrogen Sorption Properties of Metal-Organic Frameworks by Postsynthetic Covalent Modification. *Chemistry-a European Journal* 2010, 16, 212-217.
210. Savonnet, M.; Bazer-Bachi, D.; Bats, N.; Perez-Pellitero, J.; Jeanneau, E.; Lecocq, V.; Pinel, C.; Farrusseng, D. Generic Postfunctionalization Route from Amino-Derived Metal-Organic Frameworks. *Journal of the American Chemical Society* 2010, 132, 4518-4519.
211. Adzima, B. J.; Tao, Y.; Kloxin, C. J.; DeForest, C. A.; Anseth, K. S.; Bowman, C. N. Spatial and temporal control of the alkyne-azide cycloaddition by photoinitiated Cu(II) reduction. *Nature Chemistry* 2011, 3, 256-259.
212. Chen, R. T.; Marchesan, S.; Evans, R. A.; Styan, K. E.; Such, G. K.; Postma, A.; McLean, K. M.; Muir, B. W.; Caruso, F. Photoinitiated Alkyne-Azide Click and Radical Cross-Linking Reactions for the Patterning of PEG Hydrogels. *Biomacromolecules* 2012, 13, 889-895.
213. Gong, T.; Adzima, B. J.; Baker, N. H.; Bowman, C. N. Photopolymerization Reactions Using the Photoinitiated Copper (I)-Catalyzed Azide-Alkyne Cycloaddition (CuAAC) Reaction. *Advanced Materials* 2013, 25, 2024-2028.
214. Tasdelen, M. A.; Yagci, Y. Light-Induced Click Reactions. *Angewandte Chemie-International Edition* 2013, 52, 5930-5938.
215. Labbe, G. Decomposition and addition reactions of organic azides. *Chemical Reviews* 1969, 69, 345-363.
216. Zacher, D.; Shekhah, O.; Wöll, C.; Fischer, R. A. Thin films of metal-organic frameworks. *Chemical Society Reviews* 2009, 38, 1418-1429.

217. Whitesides, G. M.; Kriebel, J. K.; Love, J. C. Molecular engineering of surfaces using self-assembled monolayers. *Science progress* 2005, 88, 17-48.
218. Smith, R. K.; Lewis, P. A.; Weiss, P. S. Patterning self-assembled monolayers. *Progress in Surface Science* 2004, 75, 1-68.
219. Kumar, A.; Abbott, N. L.; Kim, E.; Biebuyck, H. A.; Whitesides, G. M. Patterned Self-Assembled Monolayers and Meso-Scale Phenomena. *Accounts of Chemical Research* 1995, 28, 219-226.
220. Tsotsalas, M.; Liu, J.; Tettmann, B.; Grosjean, S.; Shahnas, A.; Wang, Z.; Azucena, C.; Addicoat, M.; Heine, T.; Lahann, J.; Overhage, J.; Bräse, S.; Gliemann, H.; Wöll, C. Fabrication of Highly Uniform Gel Coatings by the Conversion of Surface-Anchored Metal–Organic Frameworks. *Journal of the American Chemical Society* 2014, 136, 8-11.
221. Xi, W.; Scott, T. F.; Kloxin, C. J.; Bowman, C. N. Click Chemistry in Materials Science. *Advanced Functional Materials* 2014, 24, 2572-2590.
222. Hoogenboom, R. Thiol–Yne Chemistry: A Powerful Tool for Creating Highly Functional Materials. *Angewandte Chemie International Edition* 2010, 49, 3415-3417.
223. Feng, W.; Li, L.; Ueda, E.; Li, J.; Heißler, S.; Welle, A.; Trapp, O.; Levkin, P. A. Surface Patterning via Thiol-Yne Click Chemistry: An Extremely Fast and Versatile Approach to Superhydrophilic-Superhydrophobic Micropatterns. *Advanced Materials Interfaces* 2014, 1, 1400269.
224. Mugnaini, V.; Tsotsalas, M.; Bebensee, F.; Grosjean, S.; Shahnas, A.; Braese, S.; Lahann, J.; Buck, M.; Woell, C. Electrochemical investigation of covalently post-synthetic modified SURGEL coatings. *Chemical Communications* 2014, 50, 11129-11131.
225. Zheng, S. T.; Zhao, X.; Lau, S.; Fuhr, A.; Feng, P. Y.; Bu, X. H. Entrapment of Metal Clusters in Metal-Organic Framework Channels by Extended Hooks Anchored at Open Metal Sites. *Journal of the American Chemical Society* 2013, 135, 10270-10273.
226. Supronowicz, B.; Mavrandonakis, A.; Heine, T. Interaction of Small Gases with the Unsaturated Metal Centers of the HKUST-1 Metal Organic Framework. *Journal of Physical Chemistry C* 2013, 117, 14570-14578.
227. Lin, L. C.; Kim, J.; Kong, X. Q.; Scott, E.; McDonald, T. M.; Long, J. R.; Reimer, J. A.; Smit, B. Understanding CO_2 Dynamics in Metal-Organic Frameworks with Open Metal Sites. *Angewandte Chemie-International Edition* 2013, 52, 4410-4413.
228. Wang, X.-S.; Ma, S.; Forster, P. M.; Yuan, D.; Eckert, J.; López, J. J.; Murphy, B. J.; Parise, J. B.; Zhou, H.-C. Enhancing H2 Uptake by "Close-Packing" Alignment of Open Copper Sites in Metal–Organic Frameworks. *Angewandte Chemie International Edition* 2008, 47, 7263-7266.

229. Wenzel, S. E.; Fischer, M.; Hoffmann, F.; Fröba, M. Highly Porous Metal-Organic Framework Containing a Novel Organosilicon Linker − A Promising Material for Hydrogen Storage. *Inorganic Chemistry* 2009, 48, 6559-6565.
230. Wenzel, S. E.; Fischer, M.; Hoffmann, F.; Froba, M. A new series of isoreticular copper-based metal-organic frameworks containing non-linear linkers with different group 14 central atoms. *Journal of Materials Chemistry* 2012, 22, 10294-10302.
231. Rubes, M.; Grajciar, L.; Bludsky, O.; Wiersum, A. D.; Llewellyn, P. L.; Nachtigall, P. Combined Theoretical and Experimental Investigation of CO Adsorption on Coordinatively Unsaturated Sites in CuBTC MOF. *Chemphyschem* 2012, 13, 488-495.
232. Qiu, W. G.; Wang, Y.; Li, C. Q.; Zhan, Z. C.; Zi, X. H.; Zhang, G. Z.; Wang, R.; He, H. Effect of Activation Temperature on Catalytic Performance of CuBTC for CO Oxidation. *Chinese Journal of Catalysis* 2012, 33, 986-992.
233. Zou, R. Q.; Sakurai, H.; Han, S.; Zhong, R. Q.; Xu, Q. Probing the lewis acid sites and CO catalytic oxidation activity of the porous metal-organic polymer Cu(5-methylisophthalate). *Journal of the American Chemical Society* 2007, 129, 8402-8403.
234. Thi-Thanh-Tam, N.; Tuerp, D.; Wang, D.; Noelscher, B.; Laquai, F.; Muellen, K. A Fluorescent, Shape-Persistent Dendritic Host with Photoswitchable Guest Encapsulation and Intramolecular Energy Transfer. *Journal of the American Chemical Society* 2011, 133, 11194-11204.
235. Wu, H.; Chua, Y. S.; Krungleviciute, V.; Tyagi, M.; Chen, P.; Yildirim, T.; Zhou, W. Unusual and Highly Tunable Missing-Linker Defects in Zirconium Metal-Organic Framework UiO-66 and Their Important Effects on Gas Adsorption. *Journal of the American Chemical Society* 2013, 135, 10525-10532.
236. Mao, Y.; Shi, L.; Huang, H.; Yu, Q.; Ye, Z.; Peng, X. Mesoporous separation membranes of $\{[Cu(BTC–H_2)_2\cdot(H_2O)_2]\cdot 3H_2O\}$ nanobelts synthesized by ultrasonication at room temperature. *Crystengcomm* 2013, 15, 265-270.
237. Blackburn, J. L.; Engtrakul, C.; Bult, J. B.; Hurst, K.; Zhao, Y.; Xu, Q.; Parilla, P. A.; Simpson, L. J.; Rocha, J.-D. R.; Hudson, M. R.; Brown, C. M.; Gennett, T. Spectroscopic Identification of Hydrogen Spillover Species in Ruthenium-Modified High Surface Area Carbons by Diffuse Reflectance Infrared Fourier Transform Spectroscopy. *Journal of Physical Chemistry C* 2012, 116, 26744-26755.
238. Vermoortele, F.; Ameloot, R.; Alaerts, L.; Matthessen, R.; Carlier, B.; Fernandez, E. V. R.; Gascon, J.; Kapteijn, F.; De Vos, D. E. Tuning the catalytic performance of metal-organic frameworks in fine chemistry by active site engineering. *Journal of Materials Chemistry* 2012, 22, 10313-10321.

239. Szanyi, J.; Daturi, M.; Clet, G.; Baer, D. R.; Peden, C. H. F. Well-studied Cu-BTC still serves surprises: evidence for facile Cu^{2+}/Cu^{+} interchange. *Physical Chemistry Chemical Physics* 2012, 14, 4383-4390.
240. Nijem, N.; Bluhm, H.; Ng, M. L.; Kunz, M.; Leone, S. R.; Gilles, M. K. Cu^{1+} in HKUST-1: selective gas adsorption in the presence of water. *Chemical Communications* 2014, 50, 10144-7.
241. Kung, S.-C.; van der Veer, W. E.; Yang, F.; Donavan, K. C.; Penner, R. M. 20 mu s Photocurrent Response from Lithographically Patterned Nanocrystalline Cadmium Selenide Nanowires. *Nano Letters* 2010, 10, 1481-1485.
242. Kaeding, W. W.; Kerlinger, H. O.; Collins, G. R. Oxidation of Aromatic Acids. VI. Reaction of Cupric Salts of Carboxylic Acids with Aromatic Aprotic Compounds. *The Journal of Organic Chemistry* 1965, 30, 3754-3759.
243. Chaffins, S.; Brettreich, M.; Wudl, F. An efficient synthesis of dibenzocycloocta-4a,6a,-diene-5,11-diyne and its precursors. *Synthesis-Stuttgart* 2002, 1191-1194.
244. Schultz, M. K.; Parameswarappa, S. G.; Pigge, F. C. Synthesis of a DOTA−Biotin Conjugate for Radionuclide Chelation via Cu-Free Click Chemistry. *Organic Letters* 2010, 12, 2398-2401.
245. Olkhovik, V. K.; Vasilevskii, D. A.; Pap, A. A.; Kalechyts, G. V.; Matveienko, Y. V.; Baran, A. G.; Halinouski, N. A.; Petushok, V. G. Synthesis of new polyconjugated molecules with biphenyl, dibenzothiophene, carbazole and phenanthrene units. *Arkivoc* 2008, 69-93.
246. Deshpande, R. K.; Minnaar, J. L.; Telfer, S. G. Thermolabile Groups in Metal–Organic Frameworks: Suppression of Network Interpenetration, Post-Synthetic Cavity Expansion, and Protection of Reactive Functional Groups. *Angewandte Chemie International Edition* 2010, 49, 4598-4602.
247. Liu, C.; Li, T.; Rosi, N. L. Strain-Promoted “Click” Modification of a Mesoporous Metal–Organic Framework. *Journal of the American Chemical Society* 2012, 134, 18886-18888.

8 Publications

1. Redel, E., **Wang, Z.**, Walheim, S., Liu, J., Gliemann, H., Wöll, C. On the dielectric and optical properties of surface-anchored metal-organic frameworks: A study on epitaxially grown thin films. *Applied Physics Letters* **2013**, 103.
2. Arpa Sancet, M., Hanke, M., **Wang, Z.**, Bauer, S., Azucena, C., Arslan, H., Heinle, M., Gliemann, H., Wöll, C., Rosenhahn, A. Surface anchored metal-organic frameworks as stimulus responsive antifouling coatings. *Biointerphases* **2013**, 8, 1-8.
3. **Wang, Z.**, Liu, J., Arslan, H. K., Grosjean, S., Hagendorn, T., Gliemann, H., Bräse, S., Wöll, C. Post-Synthetic Modification of Metal–Organic Framework Thin Films Using Click Chemistry: The Importance of Strained C–C Triple Bonds. *Langmuir* **2013**, 29, 15958-15964.
4. Tsotsalas, M., Liu, J., Tettmann, B., Grosjean, S., Shahnas, A., **Wang, Z.**, Azucena, C., Addicoat, M., Heine, T., Lahann, J., Overhage, J., Bräse, S., Gliemann, H., Wöll, C. Fabrication of Highly Uniform Gel Coatings by the Conversion of Surface-Anchored Metal–Organic Frameworks. *Journal of the American Chemical Society* **2014**, 136, 8-11.
5. **Wang, Z.**, Liu, J., Lukose, B., Gu, Z., Weidler, P. G., Gliemann, H., Heine, T., Wöll, C. Nanoporous Designer Solids with Huge Lattice Constant Gradients: Multiheteroepitaxy of Metal–Organic Frameworks. *Nano Letters* **2014**, 14, 1526-1529.
6. Gu, Z.-G., Bürck, J., Bihlmeier, A., Liu, J., Shekhah, O., Weidler, P. G., Azucena, C., **Wang, Z.**, Heissler, S., Gliemann, H., Klopper, W., Ulrich, A. S., and Wöll, C. Oriented Circular Dichroism Analysis of Chiral Surface-Anchored Metal–Organic Frameworks Grown by Liquid-Phase Epitaxy and upon Loading with Chiral Guest Compounds. *Chemistry – A European Journal* **2014**, 20, 9879-9882.
7. **Wang, Z.**, Sezen, H., Liu. J., Yang. C, Roggenbuck, S. E., Peikert, K., Fröba. M, Mavrantonakis, A., Supronowiczc, B., Heine T., Gliemann H. and Wöll, C., Tunable Coordinative Defects in UHM-3 Surface-Mounted MOFs for Gas Adsorption and Separation: A Combined Experimental and Theoretical Study. *Microporous and Mesoporous Materials* **2015**, 207, 53.
8. Liu, J., Redel, E., Walheim, S., **Wang, Z.**, Oberst, V., Liu, J., Heissler, S., Welle, A., Moosmann, M., Scherer, T., Bruns, M., Gliemann, H., Wöll, C., Monolithic high performance SURMOF Bragg Reflector for Optical Sensing. **Submitted**.
9. Stavila, V., Robinson, A. L., Zeitler, T. R., Greathouse, J. A., Denning, J. M., Volponi, J., Leong, K., Quan, W., White, M. I., **Wang, Z.**, Gliemann, H., Wöll, C., Tu, M., Fischer, R.

A., Allendorf, M. D., Tunable Suite of Copper(II) Paddlewheel MOF Thin Films for Small-Molecule Chemical Detection. **Submitted**.

10. **Wang, Z.**, Weidler, P.G., Heinke, L. and Wöll, C., Anisotropic Thermal Expansion of Surface Mounted HKUST-1 MOF Thin Films. **To be submitted**.
11. **Wang, Z.**, Heinke, L., Jelic, J., Cakici, M., Dommaschk, M., Reinha, R. J. Maurer, R. J., Oberhofer, H., Grosjean, S., Bräse, S., Herges, R., Reuter, K. and Wöll, C., Photoswitching in nanoporous, crystalline solids: An experimental and theoretical study for azobenzene linkers incorporated in metal-organic frameworks. **To be submitted**.
12. **Wang, Z.**, Liu, J., Grosjean, S., Guo, W., Gu, Z., Heinke, L. Gliemann, H., Bräse, S., and Wöll, C., Monolithic, Crystalline MOF Coating: An Excellent Patterning and Photoresist Material. **To be submitted**.
13. Liu, J., Zhou, W., Walheim, S., **Wang, Z.**, Lindemann, P., Heissler, S., Liu, J. Weidler, P. G. Schimmel, T., Wöll, C., Redel, E., Electrochromic Switching of a Monolithic Prussian Blue Thin Film Device. **To be submitted**.
14. Liu, J., Zhou, W., Liu, J., Howard, I., Kilibarda, G., Schlabach, S., Coupry, D., Addicoat, M., **Wang, Z.**, Lindemann, P., Redel, E., Heine, T., Wöll, C., Crystalline, Highly Oriented, Surface-grafted Arrays of Porphyrins: Realization of an indirect band gap organic semiconductor? **To be submitted**.
15. **Wang, Z.**, Nminibapiel, D., Shrestha, P., Baumgart, H., Redel, E. and Wöll, C. Resistive Switching Effects in Metal-SURMOF-Metal Structure with Nano-meter thin Crystalline HKUST-1 SURMOF films. **To be submitted**.
16. **Wang, Z.**, Heinke, L. Grosjean, S., Bräse, S., and Wöll, C., Photo-Switchable Gas Adsorption in Designed Metal-Organic Framework Thin Films. **To be submitted**.

9 Acknowledgements

First of all, I would like to thank my supervisor, Prof. Dr. Christof Wöll, for offering me the opportunity to work on many interesting projects, for giving me a lot of help and supports in performing these projects, and for providing critical feedback to me for the experimental design and results through our discussions. Without his supervision and kind help, I could not finish my PhD thesis. I really appreciate the time and effort he contributed to my study. Thanks a lot.

I would like to thank Prof. Dr. Stefan Bräse for accepting to be the co-referee of my thesis and appreciate the time he contributed for reviewing my thesis.

I would like to thank Dr. Hartmut Gliemann and Dr. Peter Weidler for offering me a lot of kind help and valuable suggestions during my study in IFG.

I would like to thank Dr. Peter Weidler, Stefan Heissler, Dr. Carlos Azucena, Peter Krolla-Sidenstein, Dr. Jinxuan Liu, Dr. Xia Stammer, Dr. Lars Heinke, Dr. Veronica Mugnaini and Peter Lindemann for offering me the training of characterization methods and also for a lot of helpful discussion on my projects.

I would like to thank Dr. Pierre Tremouilhac, Dr. Jinxuan Liu and Dr. Hartmut Gliemann for their help on the proof-reading and correction of my thesis. I would like to thank Dr. Lars Heinke for editing the abstract in German version.

I would like to thank my colleagues: Dr. Engelbert Redel, Dr. Hikmet Sezen, Dr. Manuel Tsotsalas, Dr. Zhigang Gu, Weiwei Qin, Chengwu Yang, Wei Guo, Jianxi Liu, Wencai Zhou, Sophia Schmitt, Dr. Alexander Welle, Dr. Alexei Nefedov, Dr. Maria Buchholz and Dr. Fabian Bebensee for their kind help during my study in IFG and I am very appreciative to have opportunity to work together with them.

I would like to thank my collaborator: Prof. Dr. Stefan Bräse, Dr. Sylvain Grosjean and Dr. Tobias Hagendorn for providing me the organic ligands. Without their help and support, a lot of interesting projects could not be carried out.

I would like to thank my collaborator: Prof. Dr. Thomas Heine, Dr. Binit Lukose, Dr. Andreas Mavrantonakis and Dr. Barbara Supronowicz for the supports of theoretical calculations. Their efforts help us to understand the experimental results.

I would like to thank my collaborator: Prof. Dr. Michael Fröba, Dr. Stephanie E. Roggenbuck and Dr. Katharina Peikert for synthesizing the organic ligands for the UHM-3 project.

I would like to thank Dr. Junsheng Li and Silke Kirchen for the help of the water contact angle measurement and the fluorescence measurements. I would like to thank Dr. Pavel Levkin for allowing me to carry out experiments in his lab in ITG.

I would like to give the special thanks to my supervisor for myMaster study, Prof. Dr. Haolin Tang. He is my first supervisor to guild me how to find the direction and interesting during the research study in my life. Thank him for the support and help all the time.

I would like to thank the China Scholarship Council and Deutsche Forschungsgemeinschaft (DFG) within the Priority Program Metal−Organic Frameworks (SPP 1362) for providing the financial support for this PHD study.

I would like to thank Dr. Jinxuan Liu and Dr. Xia Stammer for a lot of kind help and encouragement when I was a newcomer in Karlsruhe.

Finally, I would like to express my happy gratitude to my family, especially to my parents for giving me lots of love and support all the time. I great thank my wife not only because she gave the birth of my lovely daughter but also she is my beauty girl who always stays with me in full of love, support and encouragement. And also under her care, our daughter grows up happy and healthy day by day. I also would like to thank my litter daughter; her smile and every step of growth inspire me to move forward every day.